



Electrochemical and Spectroelectrochemical Characterization of Electrocatalysts for the Alkaline Water Electrolysis

Gellrich, Florian

Publication date:
2021

Document Version
Publisher's PDF, also known as Version of record

[Link back to DTU Orbit](#)

Citation (APA):
Gellrich, F. (2021). *Electrochemical and Spectroelectrochemical Characterization of Electrocatalysts for the Alkaline Water Electrolysis*. DTU Energy.

General rights

Copyright and moral rights for the publications made accessible in the public portal are retained by the authors and/or other copyright owners and it is a condition of accessing publications that users recognise and abide by the legal requirements associated with these rights.

- Users may download and print one copy of any publication from the public portal for the purpose of private study or research.
- You may not further distribute the material or use it for any profit-making activity or commercial gain
- You may freely distribute the URL identifying the publication in the public portal

If you believe that this document breaches copyright please contact us providing details, and we will remove access to the work immediately and investigate your claim.



**Electrochemical and
Spectroelectrochemical
Characterization of Electrocatalysts
for the
Alkaline Water Electrolysis**

Ph.D. thesis

Florian Gellrich

April 2021

*In the realm of ideas everything depends on enthusiasm ...
in the real world all rests on perseverance.*

Johann Wolfgang von Goethe

DTU Energy
Department of Energy Conversion and Storage
Technical University of Denmark

Fysikvej
2800 Lyngby, Denmark
www.energy.dtu.dk

DTU Energy
Department of Energy Conversion and Storage

Preface

This thesis is submitted in candidacy for the Ph.D. degree from the Technical University of Denmark (DTU) and it is based on the work carried out at the Department of Energy Conversion and Storage in the period from February 1st 2018 to April 30th 2021. The project was mainly supervised by Professor Jens Oluf Jensen and co-supervised by Assistant Professor Marie Lund Traulsen and by Senior Researcher Christodoulos Chatzichristodoulou.

The work was partly funded by the "BEEST" (EUDP17-I: 12542) project, by the "EEEHy" (Innovation Fund Denmark 7046-00016B) project, and by internal funding.

The Ph.D. project was conducted during the relocation of DTU Energy and during the covid-19 pandemic, and it was greatly impacted by this. A planned external stay at the University of Chemistry and Technology (Prague) under supervision of Professor Karel Bouzek had to be canceled due to the pandemic.

Lyngby Campus, April 30, 2021

Florian Gellrich

Acknowledgements

A Ph.D. thesis is basically a lonely endeavor, where one might find himself isolated from the world in his apartment during a worldwide pandemic. Yet the path leading to this climax cannot be managed by a single person alone.

I would like to thank my supervisors Jens Oluf Jensen, Marie Lund Traulsen, and Christodoulos Chatzichristodoulou. Also thanks to Peter Holtappels, Søren Bredmose Simonsen and Lars Nilausen Cleemann for all the support. Be it the funding, new ideas, the help with unforeseen issues or simply bringing the Ph.D. studies on a track that made it possible to write this thesis. It is fair to say that it would not have come to this point without you.

I would also like to express my gratitude to my unofficial co-supervisor Mikkel Rykær Kraglund, whose feedback and all the constructive discussions have led to so much more beyond the Ph.D. work.

Thanks further to Rune, Christophe, Peyman, and Ragnar for more than just scientific advice in project groups.

A huge thanks also goes to the technicians and secretaries of DTU Energy. The scientific part is only one part of a Ph.D. Thank you Bent, Jens Ø., Jens B., Jens H., Henrik, Ole, Ebtisam, Larisa, John, June, Mike, Anders, Anne H., Anita and everybody else for keeping everything running. A Ph.D. can really only be as good as the laboratories, the workshops, and the structures she or he is able to work with. The fact that this thesis exists in the way it is, despite a relocation of the whole department and a pandemic, is the proof for the quality of your tireless work and collaborative approach.

To all my friends, colleagues and flatmates who supported me. At work, in the friday bar, at festivals and concerts, and basically anywhere else, not at last online. Thank you Hendrik, Elena, Nicola, Filippo, Alex P., Alex K.R., Efi, Benedikt, Sofie, Daniel, Elise,

Florian E., Dillen, Natalie, Michael, Jens, Thorben, Xanthi, Nedo and everybody I forgot to mention. I specially would like to thank Joe and Mohamad for the awesome time and the - quite literal - support during tough times. More than anybody else, I want to express my gratefulness to Simon and Doris. You have accompanied me all the way long at work and beyond. Both of you have such a big share of the past three and a half years that I cannot imagine how it would have looked like without you. For everything that could probably fill a book by itself, thanks to all of you.

Lastly, I owe my family the deepest gratitude. There is so much to it that it cannot be expressed by words alone, and unfortunately I cannot express it to all of you anymore. But if I have to choose just one thing: Thanks for making anything possible by being my backbone - no matter where my way is going. And no matter what happens, remember that it is always for something better. Et hätt noch emmer joot jejange.

Danke. Tak. Thanks.

Abstract

Green hydrogen will be a key component for the decarbonization of Europe. The combination of renewable energies with water electrolysis offers a sustainable source of hydrogen. Alkaline water electrolysis is the most mature technology, despite having the lowest production rate amongst competing technologies. One key component to improve it to a competitive level lies within the optimization of electrocatalysts.

This Ph.D. project therefore investigated high-performing nickel-molybdenum electrocatalysts for the hydrogen evolution reaction and nickel-iron electrocatalysts for the oxygen evolution reaction for the alkaline water electrolysis. Since focused work on the origin of the high performance and the stability of these electrocatalysts under technologically relevant conditions is of major interest for the industrial application, the Ph.D. project combined electrocatalyst studies with stability testing under technologically relevant conditions. The electrochemical tests were furthermore extended with spectroelectrochemical Raman and X-ray diffraction studies, which were conducted with a self-developed setup called FeliS.

The electrochemical active surface area of nickel and nickel-molybdenum HER electrocatalysts was studied to understand performance descriptors. It was seen that an *in situ* impedance method can be applied. Based on this method, it could be hypothesized that nickel is the active site in nickel-molybdenum electrocatalysts. This hypothesis is based on the congruent trends in decreasing the overpotential at 10 mA/cm² with surface roughness between nickel-molybdenum and active nickel electrocatalysts. Furthermore, it guides to additional studies, which have to address the chemical oxidation state of nickel in nickel-molybdenum.

Stability studies were conducted to address the necessity for durable electrocatalysts under technologically relevant conditions. The long-term investigated molybdenum oxide supported Ni₄Mo electrocatalyst displayed stable operation during uninterrupted polariza-

tion. However, it was sensitive to intermittent operation. Spectroelectrochemical Raman indicated that between 0.1-0.55 V vs RHE irreducible NiO forms, which decreases the apparent kinetics. At potentials greater than 0.55 V vs RHE, the molybdenum oxide supporting structure oxidizes to permolybdates, which irreversibly degrades the electrocatalyst.

For a bulk Ni₈Fe₂ layered double hydroxide electrocatalyst, stability testing revealed that it is sensitive to the entire operational window. It coagulated and depleted iron irrespective of its potential during uninterrupted polarization. It is therefore expected to degrade to a form close to a surface specific electrocatalyst. Spectroelectrochemical X-ray diffraction showed that an exfoliated Ni₈Fe₂ layered double hydroxide electrocatalyst crystallizes with potential and time under technologically relevant conditions. In contrast to the bulk electrocatalyst, it was found that the exfoliated electrocatalyst is stable. The observed apparent performance loss of the exfoliated electrocatalyst was due to a reduced electrochemical active surface area as a consequence of the crystallization process.

Dansk Resumé

Grønt brint vil være en nøglekomponent for dekarboniseringen af Europa. Kombinationen af vedvarende energi med vandelegktrolyse giver en bæredygtig brintkilde. Den alkaliske vandelegktrolyse er den mest modne teknologi, mens den tilbyder den laveste produktionshastighed blandt konkurrerende teknologier. En nøglekomponent for at forbedre det til et konkurrencepræget niveau ligger inden for optimering af elektrokatalysatorer.

Dette Ph.D. projekt undersøgte derfor højt ydende nikkel-molybdæn elektrokatalysatorer til brintudviklingsreaktionen og nikkel-jern elektrokatalysatorer til iltudviklingsreaktionen til alkalisk vandelegktrolyse. Da fokuseret arbejde på oprindelsen af den høje ydeevne og stabiliteten af disse elektrokatalysatorer under teknologisk relevante forhold er af stor interesse for den industrielle anvendelse, har Ph.D. projektet kombineret elektrokatalysatorundersøgelser med stabilitetstest under teknologisk relevante forhold. De elektrokemiske tests blev desuden udvidet med spektroelektrokemiske Raman og røntgen-diffraktionsundersøgelser, som blev udført med et selvudviklet setup kaldet FeliS.

Det elektrokemisk aktive overfladeareal af nikkel og nikkel-molybdæn HER elektrokatalysatorer blev undersøgt for at forstå præstationsindikatorer. Der blev set, at en *in situ* impedansmetode kan anvendes. Baseret på denne metode kunne der antages, at nikkel er det aktive sted i nikkel-molybdæn elektrokatalysatorer. Denne hypotese er baseret på de kongruente tendenser i faldende overpotentiale ved 10 mA/cm^2 med overfladeruhed mellem nikkel-molybdæn og aktive nikkel elektrokatalysatorer. Desuden leder den til yderligere undersøgelser, der skal adressere den kemiske oxidationstilstand for nikkel i nikkel-molybdæn.

Stabilitetsundersøgelser blev udført for at imødegå nødvendigheden af holdbare elektrokatalysatorer under teknologisk relevante forhold. Den langvarigt undersøgte molybdænoxid understøttede Ni_4Mo elektrokatalysator viste stabil drift under uafbrudt polarisering. Den var imidlertid følsom overfor periodisk drift. Spektroelektrokemisk Raman

antydede, at der formes ikke-reducerbar NiO mellem 0,1-0,55 V vs RHE, som nedsætter den tilsyneladende kinetik. Ved potentialer større end 0,55 V vs RHE oxiderer den molybdænoxid-understøtte strukturen til permolybdate, hvilket irreversibelt nedbryder elektrokatalysatoren.

For en bulk Ni₈Fe₂ lagdelt dobbelthydroxid elektrokatalysator viste stabilitestest, at den er følsom overfor hele driftsvinduet. Den koagulerede og tabte jern uanset dens potentiale under uafbrudt polarisering. Den forventes derfor at nedbrydes til en form tæt på en overfladespecifik elektrokatalysator. Spektroelektrokemisk røntgendiffraction viste, at en eksfolieret Ni₈Fe₂ lagdelt dobbelthydroxid elektrokatalysator krystalliserer med potentiale og tid under teknologisk relevante forhold. I modsætning til bulk-elektrokatalysatoren blev der fundet, at den eksfolierede elektrokatalysator er stabil. Det observerede tilsyneladende præstationstab for den eksfolierede elektrokatalysator skyldtes et reduceret elektrokemisk aktivt overfladeareal som en konsekvens af krystallisationsprocessen.

Abbreviations, Terminologies and Symbols

Abbreviations

AWE	alkaline water electrolysis
A.C.	alternating current
APXPS	ambient-pressure X-ray photoelectron spectroscopy
CAD	computer-aided design
CPE	constant-phase element
CE	counter electrode
CV	cyclic voltammetry
D.C.	direct current
DFT	density-functional theory
DRT	distribution of relaxation times
ECSA	electrochemically active surface area
EDS	energy dispersive X-ray spectroscopy
EIS	electrochemical impedance spectroscopy
EPDM	ethylene propylene diene monomer rubber
EQCM	electrochemical quartz crystal microbalance
GIXRD	grazing incidence X-ray diffraction
HBE	hydrogen binding energy theory
HER	hydrogen evolution reaction
KK	Kramers-Kronik
LDH	layered double hydroxide
LSV	linear sweep voltammetry

OCV	open circuit potential
OER	oxygen evolution reaction
PEEK	polyether ether keton
PEMEC	proton exchange membrane electrolysis
PFA	perfluoroalkoxy alkane
PGM	platinum group metals
PP	perforated plate
PTFE	polytetrafluoroethylen
PZFC	potential of zero free charge
RDE	rotating disc electrode
RDS	rate-determining step
RE	reference electrode
RHE	reversible hydrogen electrode
RS	Raman spectroscopy
SEM	scanning electron microscope
SHE	standard hydrogen electrode
SOEC	solid oxide electrolysis
TOF	turnover frequency
WE	working electrode
XPS	X-ray photoelectron spectroscopy
XRD	X-ray diffraction
YSZ	yttrium-stabilized zirconia

Terminologies

<i>ex situ</i>	outside or away from a subject's intended operating environment. Applied for measurements without simultaneous electrochemical tests.
<i>in situ</i>	on site or on the premises. Applied for a broad range of measurements, where a reaction is observed in simulated operational conditions.
<i>operando</i>	in operation under real operating conditions. Applied for measurements taking place simultaneously with electrochemical tests.

<i>spectro- electro- chemical</i>	terminology for the combination of <i>in situ</i> and <i>operando</i> , as the transition is debatable. Applied for all spectroscopic measurements in combination with electrochemical testing.
<i>FeliS</i>	F lorian's cell for l iquid S pectroelectrochemistry. The name for the self-developed spectroelectrochemical setup.

Symbols

α	transfer coefficient / polarization tensor
γ	activity coefficient / surface tension
ϵ	dielectric constant
η	overpotential
Θ_{hkl}	X-ray angle
θ_i	coverage of a species i
κ	conductivity
λ	X-ray wavelength
μ	chemical potential
μ^*	electrochemical potential
ν	scan rate
σ	Warburg coefficient
ϕ	electrostatic potential / phase-shift
φ	galvani potential
ω	angular frequency
A	area
b	Tafel-slope
C	capacity
C_{dl}	double layer capacity
D	diffusion coefficient
E	potential of an electrode versus a reference electrode / energy / electric field
e	electronic charge
E^0	standard potential of a half cell reaction
E_{eq}	equilibrium potential of an electrode

E_A	activation energy of a reaction
E_F	Fermi level
E_p	peak potential
e	electronic charge
F	Faraday's constant
f	frequency
G	Gibbs free energy
g	gravitational acceleration
H	enthalpy
H_{opd}	hydrogen overpotential deposition
H_{upd}	hydrogen underpotential deposition
h	Planck's constant
I	current
i	current density
i_p	peak current
i_0	exchange current density
iR	voltage drop over the series resistance
iV	current voltage correlation
K	equilibrium constant
k	rate constant
L	inductor
N_A	Avogadro's number
ox	oxidized redox species
p	pressure
Q_0	constant-phase element
R	gas constant / resistance
R_{ct}	charge transfer resistance
R_f	surface roughness factor
R_p	resistance of a pseudo-process
R_s	series resistance
red	reduced redox species

ΔS	entropy change of a chemical reaction
t	time
T	temperature
U	voltage
Y	admittance
z	number of electrons
Z	impedance
Z_C	impedance of a capacitor
Z_{Im}	imaginary part of impedance
Z_L	impedance of an inductor
Z_Q	impedance of a constant-phase element
Z_R	impedance of a resistor
Z_{Re}	real part of impedance
Z_W	Warburg impedance

Contents

Preface	i
Acknowledgements	iii
Abstract	v
Dansk Resumé	vii
Abbreviations, Terminologies and Symbols	ix
1 Introduction	1
1.1 Water electrolysis	2
1.2 Electrocatalysts for the alkaline water electrolysis	4
1.3 Motivation and scope of the thesis	6
2 Water splitting in alkaline electrolyte	9
2.1 Theoretical electrochemical background	9
2.2 Nickel in alkaline media	15
2.3 The mechanism of the hydrogen evolution reaction	16
2.4 Alkaline HER on Ni	17
2.5 Alkaline HER on NiMo	25
2.5.1 The role of the molybdenum content	25
2.5.2 Proposed reasons for the high performance of NiMo	27
2.5.3 The stability of NiMo in alkaline electrolyte	30
2.6 The mechanism of the oxygen evolution reaction	35

2.7	Alkaline OER on Ni and on NiFe layered double hydroxides	38
2.7.1	The influence of Fe on the alkaline OER	39
2.7.2	Understandings about the mechanisms on Ni OER electrocatalysts . .	42
2.7.3	On the stability of NiFe layered double hydroxides in alkaline electrolyte	44
2.8	Concluding remarks on the hydrogen and oxygen evolution in alkaline electrolyte	46
3	Experimental Methods and Setups	47
3.1	Electrochemical impedance spectroscopy	47
3.2	Cyclic voltammetry	52
3.3	Scanning electron microscope and electron dispersive X-ray spectroscopy . . .	53
3.4	Raman spectroscopy	54
3.5	X-ray diffraction	56
3.6	X-ray photoelectron spectroscopy	57
3.7	Testing setups	58
3.7.1	The FlexCell	58
3.7.2	Zero-gap electrolyzer	59
4	Development of a spectroelectrochemical cell for Raman spectroscopy and X-ray analysis techniques	61
4.1	Stipulations for a spectroelectrochemical cell with liquid electrolyte at strong pH and high polarizations	61
4.2	Setups published in the literature	63
4.3	Approaches towards spectroelectrochemistry in alkaline electrolyte	66
4.4	The inhouse developed, modular, spectroelectrochemical cell FeliS	70
4.4.1	Electrochemical verification of FeliS with platinum	72
4.4.2	FeliS in Raman configuration	75
4.4.3	FeliS in X-ray configuration	79
4.5	Conceptions for the prospective applications of FeliS	85
4.5.1	FeliS in a flowcell configuration	85
4.5.2	Improving the assembly of FeliS with a mounting-tool	88
4.6	Conclusions on the spectroelectrochemical cell FeliS	88

5 Influence of the electrochemical active surface area and partial oxidation of Ni and NiMo electrocatalysts	91
5.1 Experimental details	92
5.1.1 Electrochemical characterization	92
5.1.2 Electrocatalyst preparation	92
5.2 Electrochemical impedance studies in the HER overpotential region	94
5.2.1 Modeling with a simple R(RQ) equivalent circuit	95
5.2.2 Kramers-Kronig tests	99
5.2.3 Advanced impedance modeling with Armstrong’s electric circuit	101
5.3 Electrochemical active surface area	103
5.3.1 Correlating the electrochemical active surface area obtained by EIS, the formation of alpha nickel hydroxide and non-faradaic cyclic voltammetry	103
5.3.2 Interdependency between electrochemical active surface area, partial oxidation and kinetics	109
5.3.3 Statistical evaluation of the importance of the electrochemical surface area	123
5.4 Conclusions and discussions on performance descriptors for Ni and NiMo electrocatalysts	127
6 Stability testing of NiMo and NiFe LDH electrocatalysts	131
6.1 Experimental details	132
6.1.1 Sample preparation	132
6.1.2 Effects of polarization and potential-distribution	134
6.1.3 Single electrode kinetics by electrochemical impedance spectroscopy	136
6.1.4 Single electrode kinetics by reference electrode measurements	140
6.2 Cell performance in zero-gap configuration	144
6.3 Voltammetry and open-circuit as tools for accelerated degradation studies	148
6.3.1 Cyclic voltammetry on perforated plate supported electrodes	148
6.3.2 Open-circuit voltage simulating the shutdown response	153
6.3.3 Influence of cyclic voltammetry and open-circuit voltage on the cell and electrode kinetics	155

6.3.4	Pre- and post-mortem characterization of electrodes from accelerated degradation testing	166
6.3.5	Results from accelerated degradation testing	170
6.4	Dynamic long-term operation simulating the industrial application under fluctuating energy supply	172
6.4.1	Dynamic operation over 357 h on felt supported electrodes	173
6.4.2	Results from polarization curves and electrochemical impedance spectroscopy of the 357 h test	179
6.4.3	Pre- and post-mortem characterization of electrodes from long-term dynamic operation	185
6.5	Conclusions and discussions on the operational domains of NiMo and NiFe LDH electrocatalysts	192
7	Spectroelectrochemical Raman and X-ray diffraction studies of NiMo and NiFe LDH electrocatalysts	201
7.1	Experimental details	202
7.2	NiMo in the cathode operational window	204
7.2.1	Results from cyclic voltammetry	204
7.2.2	Results from spectroelectrochemical Raman	208
7.2.3	Importance of spectroelectrochemical Raman studies of NiMo electrocatalysts	212
7.2.4	Conclusions on the redox processes of a molybdenum oxide supported Ni ₄ Mo electrocatalysts	214
7.3	Spectroelectrochemical X-ray diffraction of NiFe LDH in the anode operational window	217
7.3.1	Stability and performance evolution with temperature	217
7.3.2	Accelerated degradation at 85°C	220
7.3.3	Conclusions on the stability and the active phase of a Ni ₈ Fe ₂ LDH electrocatalysts	224
7.4	Discussions on the spectroelectrochemical studies	227
8	General Conclusions and Outlook	229

Bibliography	I
List of Figures	XV
List of Tables	XXI
A Drawings of the spectroelectrochemical cell FeliS	XXIII
B Supplementary Raman results	XXXIII
C Supplementary X-ray diffraction results	XXXV

Chapter 1

Introduction

Hydrogen is a vital component to a carbon neutral future. The European Commission has recently formulated a strategy to implement a hydrogen ecosystem in Europe by the European Green Deal to decarbonize Europe. In the roadmap for the EU, the European Commission prioritizes hydrogen from renewable sources, which is also known as green hydrogen [1]. As for today, the main sources for the production of hydrogen are of fossil origin, with the result that more than 94% of the today produced hydrogen is grey hydrogen [2, 3]. However, the potential to replace grey with green hydrogen in the EU is given [2].

The possibilities of hydrogen as a major future energy vector are vast, as it can replace fossil sources in transportation, district heating, energy systems, the chemical, cement, fertilizer, and steel industry [3]. For a carbon-neutral implementation of the hydrogen ecosystem, the EU plans to scale up the production of hydrogen through the electrolysis of water with renewable energies [1]. This would not only be a viable solution for the production of green hydrogen, but also addresses the well-known issues associated with renewable energies. Their production fluctuations are challenging with a view towards the stabilization of power grids in the future. The divergence between energy supply from renewable energies and the energy demand by industries and urban areas increases the complexity, which requires novel solutions to avert inevitable grid blackouts. One possible approach is water electrolysis, which can combine grid-stabilization with the demand for green hydrogen [1].

In fact, the history of water electrolysis displays that it reached industrial maturity prior to fossil energies [4]. Thus, a combination of policies with century long knowledge and recent scientific advancements in water electrolysis are promising to reach the EU climate goals of 2050 with hydrogen from electrolysis as a major player [1].

1.1 Water electrolysis

The electrolysis of water is technically realized with three different techniques. These comprise of proton exchange membrane electrolysis (PEMEC), solid oxide electrolysis (SOEC), and alkaline water electrolysis (AWE), which are shown in Fig. 1.1.

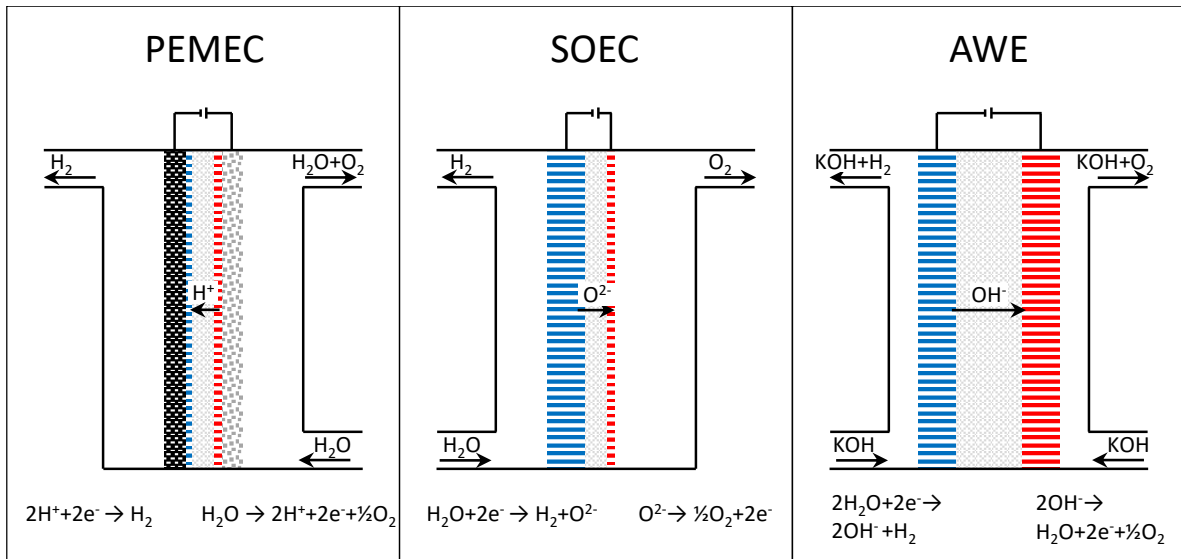


Fig. 1.1: The three different types of water electrolyzers: PEMEC, SOEC, and AWE.

PEMEC uses a proton conducting membrane, which allows the cell to be run at high differential pressure. Due to the low ohmic resistance, PEMEC can run at high current densities and thus low operational costs. However, the harsh acidic conditions in combination with high voltages in PEMEC require expensive and scarce precious metals, more specifically platinum and iridium, which significantly increase investment costs. Another disadvantage of PEMEC is that it is susceptible towards water-impurities. In addition, the gas-crossover at low current densities often causes a safety shutdown of PEMEC [5].

SOEC operates at high temperatures of typically 700-850 °C. This allows the use of comparably cheap and abundant ceramic electrodes without noble metals and results in a high efficiency. On the other hand, SOEC requires high temperature steam, which decreases its overall efficiency if it does not run on waste heat. Furthermore, SOEC suffers from severe degradation, especially when subjected to intermittent operation. As a consequence, SOEC has to this date not reached full market maturity in the order of MW yet [5].

AWE is the oldest electrolysis technology, which dates back more than 200 years [4]. It can run with inexpensive transition metals as catalysts, e.g. nickel and iron, as the alkaline environment allows for a larger amount of corrosion resistant metals compared to PEMEC. This enables the manufacturing of high surface area electrodes of up to $3 \text{ m}^2_{\text{geometric}}$ at comparably low investment cost, which leads to high volume production and reliable operation over several decades. Similar to PEMEC, low current densities cause gas-intermixing, which on the other hand is less significant in AWE. A major disadvantage of AWE is a high ohmic loss, which primarily originates from a $500 \mu\text{m}$ thick diaphragm to avoid the intermixing of hydrogen and oxygen. Furthermore, the electrocatalytic activity of the transition metal electrocatalysts is typically lower than the precious metal electrocatalysts in PEMEC [5].

With a view on the investment costs, the maturity of the technology, the reliability, and the abundance of transition metals [6], the AWE is of high interest for the large scale hydrogen production. However, Fig. 1.2 displays the major challenge of AWE compared to PEMEC and SOEC. Due to the high ohmic loss and the lower activity of the electrocatalysts, the losses of AWE at the same current density are higher than for PEMEC and SOEC resulting in a higher cell voltage. Accordingly, AWE operates at a to PEMEC comparable efficiency, but at much reduced production rate [7].

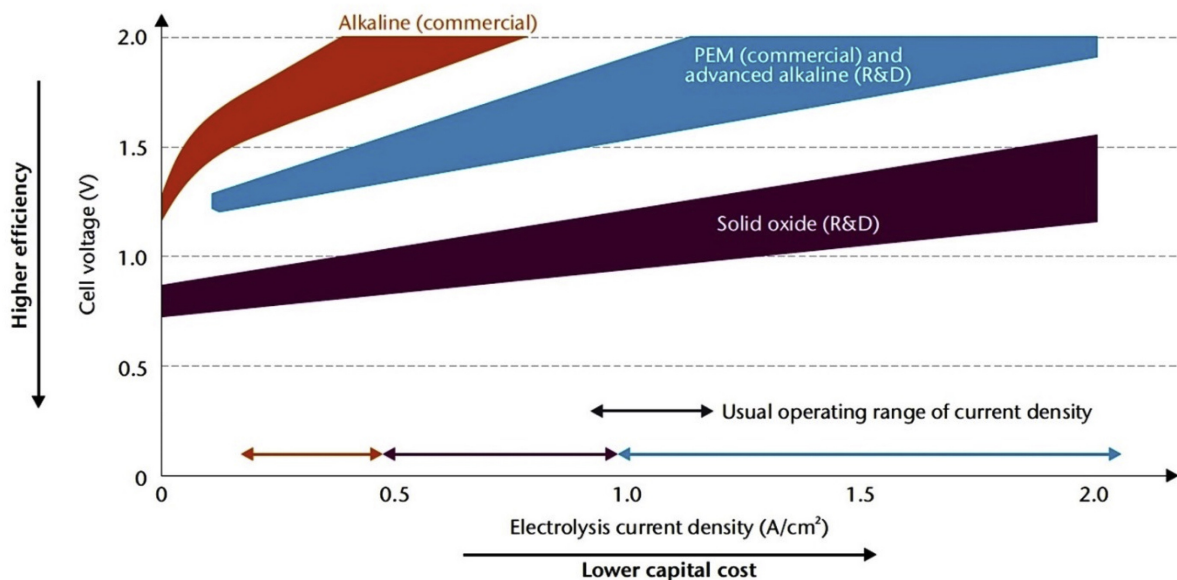


Fig. 1.2: Comparison of the current status and the development potential of water electrolysis between AWE, PEMEC, and SOEC. Reproduced from [3].

Thus, the main working objective in the improvement of AWE is the focus on producing electrolysis stacks with high efficiency through the reduction of these losses. One part of these improvements is focused on the manufacturing of new separators and membranes, which would effectively reduce the ohmic losses. Another part is the view on new electrocatalysts. High performance electrocatalysts made of earth abundant transition metals, which have a comparable activity to precious metals, allow for highly effective and high volume production of hydrogen. However, electrocatalysts at competing efficiency at similar production rate to PEMEC would only enter market maturity in AWE if this performance is durable.

In other words, the AWE is the favorable large volume hydrogen production technology if it can combine its low investment costs and decade long stable operation with the high effectiveness of PEMEC.

1.2 Electrocatalysts for the alkaline water electrolysis

The literature consists of a vast variety of highly active electrocatalysts for the alkaline water electrolysis. Most of the work on electrocatalysts for the hydrogen evolution reaction (HER), which do not belong to the platinum group metals (PGM), has been conducted on nickel-based electrocatalysts. Besides raney-nickel, nickel-molybdenum electrocatalysts appear on top of all other reported electrocatalysts in terms of activity for the hydrogen evolution reaction [8, 9].

The work on electrocatalysts for the oxygen evolution reaction (OER) is mostly on comparatively low active perovskites, as well as spinels and hydroxides. Precious metal free electrocatalysts for the oxygen evolution reaction show the most promising activity for nickel-based spinels and hydroxides, when the electrocatalyst contains iron [8, 10].

McCroly et al. [8] conducted a screening study in 1 M NaOH (and 1 M H₂SO₄) for a large collection of electrocatalysts. The authors compared the overpotential at a geometric current density of 10 mA/cm² after 2 hours of polarization for the different electrocatalysts. The results of this study are represented in Fig. 1.3 and are well in agreement with the aforementioned observations in the literature; nickel-molybdenum electrocatalysts for the

hydrogen evolution reaction and nickel-iron electrocatalysts for the oxygen evolution reaction stick out on top of the reported electrocatalysts.

Therefore, this work focuses on the characterization of nickel-molybdenum and nickel-iron electrocatalysts for the alkaline water electrolysis. As a general convention throughout this work, the different types of electrocatalysts are abbreviated. The abbreviations for nickel (Ni), nickel-molybdenum (NiMo), and nickel-iron (NiFe) electrocatalysts do not represent stoichiometric ratios of the elements. In case of specific stoichiometries in parts of this work, the ratios between the elements are indexed.

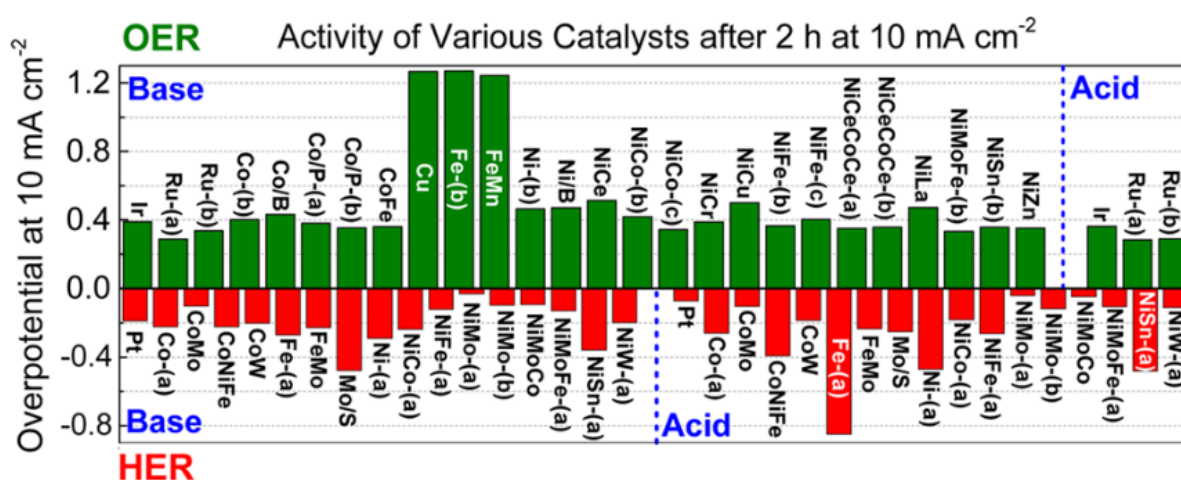


Fig. 1.3: The overpotential of various electrocatalysts at a geometric current density of 10 mA/cm² after a polarization time of 2 hours. The given values for the oxygen evolution reaction (OER - top of the figure) and the hydrogen evolution reaction (HER - bottom of the figure) are measured in 1 M H₂SO₄ (denoted as Acid) or 1 M NaOH (denoted as Base). Reproduced from [8].

1.3 Motivation and scope of the thesis

The water-splitting reactions, the HER and the OER, are well-studied electrochemical reactions. They have served in lectures and textbooks to teach electrochemistry for decades [11]. However, these intensively studied reactions are not fully understood yet.

Besides open questions about the reaction mechanisms of the water-splitting reactions, the literature on electrocatalysts for alkaline water splitting focuses on low electrolyte concentrations and low temperatures, while industrial electrolyzers work at pH 14–15 and up to 100 °C. Studies about the stability of alkaline electrocatalysts under technologically relevant conditions are not sufficiently represented, although these are required to ensure long-term reliability in industrial applications.

The uncertainty about the reaction mechanisms, e.g. about active sites, and the open questions in terms of catalyst stability and reliability query the economical and ecological benefits of AWE; a deeper understanding of these mechanisms in alkaline media are crucial to demonstrate the durability of AWE at competing performance.

In this perspective, this work focuses on characterizing well-performing NiMo and NiFe electrocatalysts for the HER and the OER, respectively, in alkaline media. It investigates electrochemical kinetics and degradation mechanisms, which are associated with pre- and post-mortem characterizations of the electrocatalysts. In addition, spectroelectrochemical techniques, which characterize electrocatalysts with spectroscopic techniques during electrochemical measurements, are applied to shed light on the degradation mechanisms occurring in electrocatalysts under technologically relevant operating conditions. Spectroelectrochemical measurements, in contrast to pre- and post-mortem characterizations, avoid changes of the environment with regards to e.g. pH, temperature and polarization between electrochemical operation and characterization. While these changes may lead to conclusions dissociated from the operational processes of electrocatalysts, spectroelectrochemical techniques characterize electrocatalysts in the operational environment.

To conclude, the thesis aims to shed light on open questions about alkaline water electrocatalysts through the application of electrochemical and spectroelectrochemical techniques. The contents of this work on the path of answering these questions are structured as follows.

Chapter 1: An introduction to the background of alkaline water electrolysis and the motivation of the Ph.D. thesis.

Chapter 2: Theory and the literature background on the water splitting electrochemical reactions in alkaline electrolyte, ending with a conclusion about open working questions.

Chapter 3: Overview of the core methods and the testing setups applied throughout the Ph.D. studies.

Chapter 4: The route of developing a novel spectroelectrochemical testing setup, which is capable of working at technical relevant conditions with electrolytes at strong pH, at high polarizations and at elevated temperatures.

Chapter 5: Studies on the influence of the surface area and partial oxidation in nickel and nickel-molybdenum electrocatalysts by means of electrochemical impedance spectroscopy and cyclic voltammetry, in order to address the open question about the origin of the high electrocatalytic activity of nickel-molybdenum electrocatalysts.

Chapter 6: Investigations of the kinetics and the stability of high-performance electrocatalysts under industrial relevant conditions. Accelerated degradation and long-term testing for zero-gap alkaline electrolysis (atmospheric pressure and 80°C) address the open question of the applicability of high-performing non-noble nickel-molybdenum and nickel-iron electrocatalysts for the industrial application.

Chapter 7: Spectroelectrochemical studies on the dependence of the electrochemical potential and the stability of nickel-molybdenum and nickel-iron electrocatalysts in alkaline water electrolysis. Raman spectroscopy and X-ray diffraction are applied to address the open question about redox and degradation processes.

Chapter 8: The general conclusion and outlook of the Ph.D. thesis.

Chapter 2

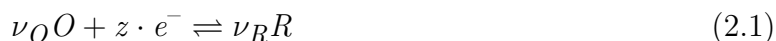
Water splitting in alkaline electrolyte

In this chapter the background to water electrolysis is reported. It covers the general theoretical electrochemical background, the reaction mechanisms of the hydrogen and oxygen evolution, and a literature overview about the hydrogen evolution on nickel and nickel-molybdenum electrocatalysts, as well as about the oxygen evolution on nickel and nickel-iron layered double hydroxide electrocatalysts. It finishes with concluding remarks, which set the working objects of the thesis.

2.1 Theoretical electrochemical background

Nernst equation

When a metal electrode is immersed into an electrolyte, an electrochemical double layer forms at the electrode-electrolyte interface. On the electrode, the metal-cation is adsorbed and accessible for free electrons, while the metal-cation in solution is hydrated and surrounded by the electrolyte. The work required to deliver a unit of positive charge from an infinite distance is called the galvanic potential φ . For the case of a reaction at the electrode-electrolyte interface, formally following Eq. (2.1), the thermodynamically required potential to drive the reaction depends on a reference point. In electrochemistry, the reference point is defined as the equilibrium potential E^0 of the reaction of hydrogen on a platinum electrode, also known as the standard hydrogen electrode (SHE). As a convention, the equilibrium potential of all electrochemical reactions is measured versus this reference point [11].

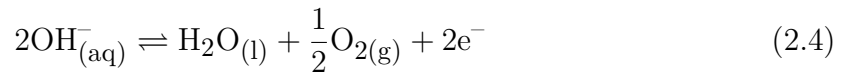
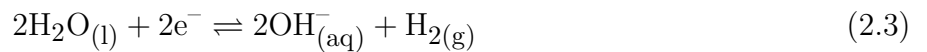


The equilibrium potential is measured in ideal conditions of 298 K, 1 atm, and an activity of all reactants of $\alpha = 1$. Deviations from these cause a shift of the equilibrium potential. With the gas constant R , the temperature T , the associated electrons of the electrochemical reaction z , the Faraday constant F , and the activities of the oxidized α_O and reduced α_R species, the Nernst equation in Eq. (2.2) describes the deviation from the equilibrium potential. The activity of the oxidized and reduced species depends on the concentration c of the species and an individual activity coefficient γ . Practically, the Nernst equation is often applied under negligence of the activity coefficients, as the difference between the activity coefficients of a redox couple is often marginal [11].

$$E = E^0 + \frac{RT}{zF} \cdot \ln \left(\frac{\alpha_O^{\nu_O}}{\alpha_R^{\nu_R}} \right) \quad ; \quad E = E^0 + \frac{RT}{zF} \cdot \ln \left(\frac{\gamma_O \cdot c_O^{\nu_O}}{\gamma_R \cdot c_R^{\nu_R}} \right) \quad (2.2)$$

Water electrolysis

This process describes the situation at one electrode. In an electrochemical cell, the electrochemical reaction requires a second electrode, an ion-conducting electrolyte between both, and an electric circuit for the exchange of electrons. Splitting water into its components hydrogen and oxygen is known as water electrolysis. The reactions at both electrodes, which are known as half-cell reactions, at pH 14 follow Eq. (2.3) and (2.4) at equilibrium potentials of $E_{H_2O/H_2}^0 = -0.828 \text{ V}$ and $E_{O_2/OH^-}^0 = 0.401 \text{ V}$, respectively. Overall, the alkaline water splitting occurs with a net reaction according to Eq. (2.5) [11–13].



Reversible cell voltage

The overall electrochemical reaction happens either spontaneously with or forced under application of a reversible cell voltage U_{rev} . It depends on the equilibrium potential of the half-cell reactions, following Eq. (2.6). The electrode with the reduction reaction is also known as cathode, and the electrode with the oxidation reaction is known as anode [11, 12].

$$U_{rev} = E_{rev,cathode} - E_{rev,anode} \quad (2.6)$$

When the reversible cell voltage is positive, one speaks of a galvanic cell, or more commonly known of a battery or fuel cell, where the electrochemical reactions happen spontaneously and thereby generate a cell voltage. In case of a negative reversible cell voltage, the reactions can only occur if an outer voltage is applied. This situation is known as electrolysis. In water electrolysis, the reversible cell voltage at room temperature and atmospheric pressure can be calculated according to Eq. (2.7) [11, 12].

$$U_{H_2O/H_2/O_2} = -0.828 \text{ V} - 0.401 \text{ V} = -1.229 \text{ V} \quad (2.7)$$

Operating cell voltage

The reversible cell voltage describes the thermodynamically required minimum potential difference between both electrodes to drive the electrolysis reaction. The operating cell voltage U_{cell} depends further on losses in the cell. Ohmic losses $\eta_{ohmic} = iR$ result from the electrolyte, from the separator, and from the anode and the cathode. Another loss stems from the current density depending transport resistances $\eta_{transport}$. In addition, the overpotentials from the HER and OER contribute to the operating cell voltage in dependence of the current density. Overall, the operating cell voltage can be calculated according to Eq. (2.8). Accordingly, improving the efficiency of a water electrolyzer requires the reduction of these losses [11–13]. The correlation between the different contributions on the operating cell voltage of a water electrolyzer is schematically illustrated in Fig. 2.1.

$$U_{cell}(T, i) = U_{rev}(T) + i \cdot R(T, i) + \eta_{transport}(T, i) + \eta_{HER}(T, i) + \eta_{OER}(T, i) \quad (2.8)$$

Gibbs free energy

The reversible cell voltage depends on the Gibbs free energy of the components, as described in Eq. (2.9). The reversible cell voltage and the Gibbs free energy correlate following Eq. (2.10). For water electrolysis, with the change of the enthalpy ΔH and the change of the entropy ΔS , it is possible to calculate the reversible cell voltage depending on the temperature, along with the thermoneutral voltage U_{tn} in Eq. (2.11). The thermoneutral voltage represents the isothermal operation of the cell. Consequentially, the operation above this voltage is exothermic and endothermic below this voltage [11–13].

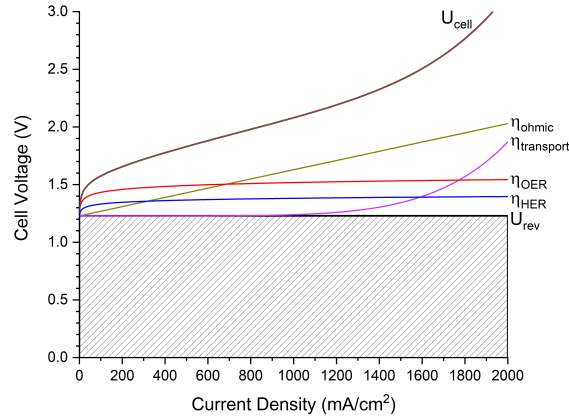


Fig. 2.1: Schematic illustration of the losses in a water electrolyzer on the reversible cell voltage summing up to the operating cell voltage.

$$\Delta G = \Delta H - T\Delta S \quad (2.9)$$

$$U_{rev} = -\frac{\Delta G}{zF} \quad (2.10)$$

$$U_{tn} = -\frac{\Delta H}{zF} \quad (2.11)$$

Faraday equation

During an electrochemical reaction, the number of electrons exchanged with a species and the current are proportional to the produced or consumed amount of the species. This proportionality was first described by Faraday and the describing equation in Eq. (2.12) was thus named after him. The equation describes the amount n of a species in proportionality to the current I , the elapsed time t , the number of exchanged electrons in the electrochemical reaction z , and the Faraday constant F [11].

$$n = \frac{I \cdot t}{z \cdot F} \quad (2.12)$$

Reference electrodes

As aforementioned equilibrium potentials are reported versus the SHE. It is moreover possible to measure potentials against other reference electrodes. A prerequisite for the choice of reference electrodes is that the electrochemical reaction of the reference electrode is stable and unaffected by the measurement. Furthermore, the deviation to the SHE has to be known. For

the alkaline water electrolysis, a Hg/HgO reference electrode as well as a reversible hydrogen electrode (RHE) are often applied. The RHE is a pH-relaxed variation of the SHE. While the latter requires a pH 0, the RHE operates at the electrolyte pH. By definition, the reference electrode potential of the RHE is the equilibrium potential of the hydrogen evolution reaction at any given pH [11].

Activation energy

The rate of a chemical reaction is temperature-dependent. The same applies for an electrochemical reaction. In both cases, the rate of the reaction k depends on a frequency factor A , the activation energy E_A , the gas constant R and the temperature T according to Eq. (2.13). Experimentally, the activation energy can be obtained through a logarithmic fitting of a rate-determining constant k over $1/T$. In an electrochemical system, the rate-determining constant is generally potential-dependent [11].

$$k = A \cdot e^{-E_A/RT} \quad (2.13)$$

Fermi level

The Fermi level describes the electrochemical potential μ_e^* of electrons in a phase. It depends e.g. on the electrode material or on the electrochemical potentials of oxidized as well as reduced species in a solution. In electrocatalysis, it describes an important characteristic; in an efficient electrocatalyst, the Fermi level has to match with the electrochemical potentials of the reactants to catalyze the electrochemical reaction [11].

Butler-Volmer equation

The kinetics of an electrode are influenced by its potential. With an increased difference to the equilibrium potential of an electrochemical reaction, which is defined as the overpotential η , the rate of the reaction increases. The rate of the reaction k^0 depends on the forward as well as on the backward electrochemical reaction. For a one-step process, as described in Eq. (2.1), with the transfer coefficient α , the area A , the Faraday constant F , the number of exchanged electrons z , the gas constant R , and the temperature T , the current-potential characteristics follow Eq. (2.14) [11, 13].

$$i = F A k^0 \left[C_{ox}(\theta, t) \cdot e^{-\alpha z F (E - E^0) / RT} - C_{red}(\theta, t) \cdot e^{(1-\alpha) z F (E - E^0) / RT} \right] \quad (2.14)$$

When the forward and backward electrochemical reactions are equal, the overall reaction is at equilibrium and the net current is zero. This situation is described by the exchange current density i_0 . When the terms reported in parentheses in Eq. (2.14) are set equally and no mass transfer effects occur, one can obtain the correlation of overpotential and current density in Eq. (2.15), which was named after Butler and Volmer (see also Fig. 2.2A). This equation can further be linearized in two different sections. Firstly, at sufficiently small overpotentials η , the current can be described with Eq. (2.16). It can further be rewritten into the correlation of current and overpotential known as the charge transfer resistance R_{ct} , which can be calculated following Eq. (2.17). Secondly, at sufficiently large overpotentials of $\eta > 118$ mV, the term of the backward electrochemical reaction described in parentheses in Eq. (2.15) is negligible in correlation to the forward electrochemical reaction. A so obtained equation following Eq. (2.18) (see also Fig. 2.2B) is named Tafel equation [11, 13].

$$i = i_0 \left[e^{-\alpha zF\eta/RT} - e^{(1-\alpha)zF\eta/RT} \right] \quad (2.15)$$

$$i = -i_0 \frac{zF\eta}{RT} \quad (2.16)$$

$$R_{ct} = \frac{RT}{zFi_0} \quad (2.17)$$

$$\eta = \frac{2.3 \cdot RT}{\alpha zF} \log(i_0) - \frac{2.3 \cdot RT}{\alpha zF} \log(i) \quad (2.18)$$

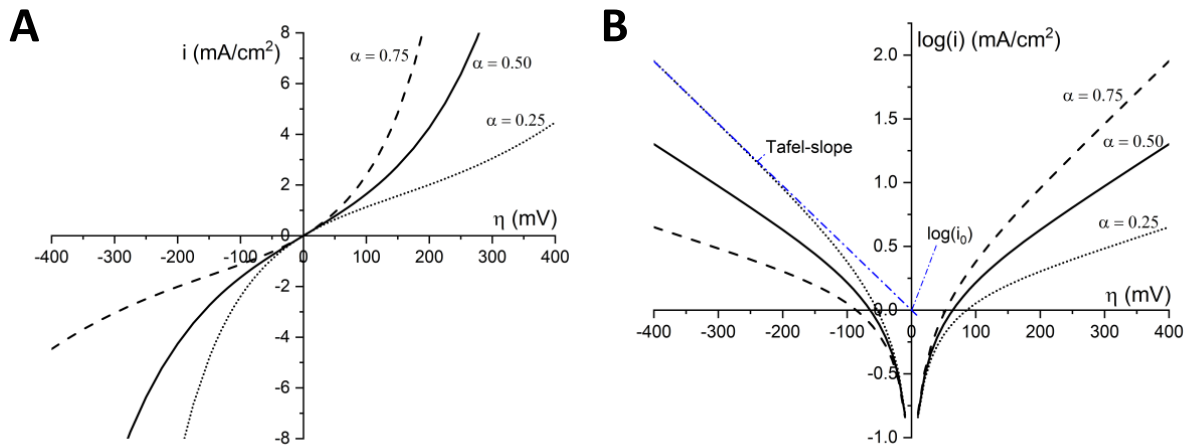


Fig. 2.2: Illustration of **A:** The Butler-Volmer and **B:** The Tafel equation.

2.2 Nickel in alkaline media

Nickel is the state-of-the-art transition metal electrocatalyst for the alkaline water electrolysis. The first description of the different oxidation states of Nickel in alkaline media was made by Bode et al. in the 1960s [14]. The correlation between the two different hydroxides and the two different oxyhydroxides are visualized in the Bode diagram (Fig. 2.3). The turbostratic α -Ni(OH)₂ consists of intercalated water molecules between its hydroxide-layers. This form can reversibly convert to γ -NiOOH. The more crystalline form β -Ni(OH)₂ forms irreversibly through aging out of the α -form by the loss of the intercalated water molecules. The corresponding β -NiOOH can, through an overcharging process, intercalate water molecules and thus transform to the γ -form.

The Bode diagram is applied as a general descriptor for the redox-transitions of nickel. However, the redox reactions of nickel are the subject of recent studies as the correlation between electrode potential, time and temperature draws a more complex picture about the redox states of nickel [15–20].

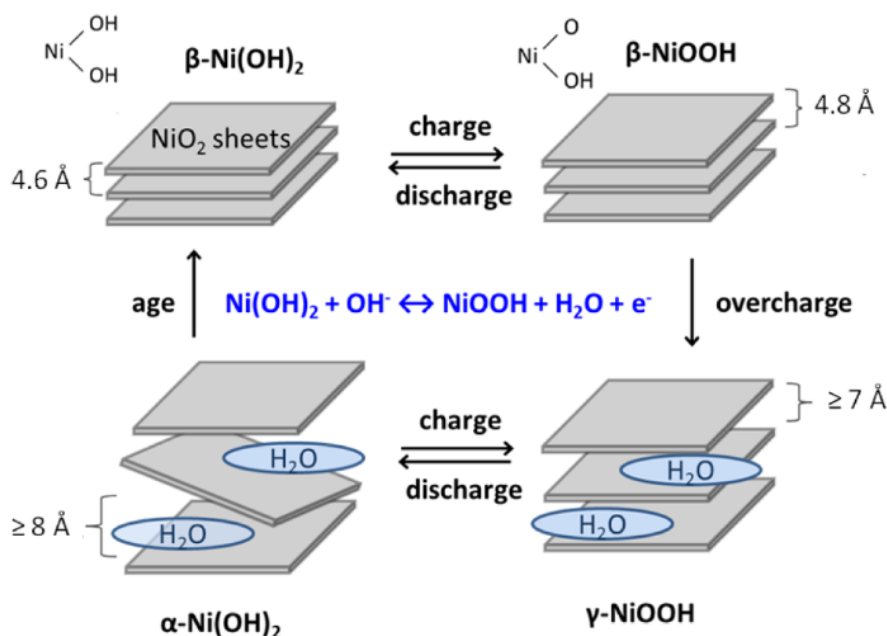


Fig. 2.3: The hydroxides and oxyhydroxides of nickel according to the Bode diagram [14]. Reproduced from [21].

2.3 The mechanism of the hydrogen evolution reaction

The hydrogen evolution reaction proceeds with three fundamental reaction steps. At first, the splitting of the water molecule into the hydroxide-anion OH^- and adsorbed hydrogen H^* on an active site of the electrocatalyst is known as the Volmer step (Eq. (2.19)). In a second and final step, two possible pathways exist. The Tafel step combining two adsorbed hydrogen atoms H^* (Eq. (2.20)) or the Heyrovsky step combining the dissociation of a water molecule with the adsorbed hydrogen atom H^* (Eq. (2.21)) produce molecular hydrogen H_2 . Thus, the HER occurs via the Volmer-Tafel or the Volmer-Heyrovsky pathways. The rate-determining step (RDS) of the HER is often determined through a Tafel-analysis. While the water dissociating Volmer step is characterized by a Tafel-slope of 120 mV/dec, the Tafel and Heyrovsky steps are associated with a Tafel-slope of 30 mV/dec and 40 mV/dec, respectively [22–24].

However, recent literature questions the validity of concluding on the RDS based on a Tafel-analysis. It was shown by Shinagawa et al. [25] through kinetic modeling that the Volmer step is not always solely responsible for a Tafel-slope of 120 mV/dec. In case the surface coverage of adsorbed hydrogen exceeds 0.6, the Heyrovsky step becomes the RDS of the HER associated with a Tafel-slope of 120 mV/dec. The authors furthermore declare that, based on theoretical modeling, the electron transfer reaction does not represent the majority of the RDS. Hence, the applicability of the Butler-Volmer equation for the HER is not always given. Therefore, the model of the Tafel-slope might not be suitable to describe the HER, which requires other kinetic models to describe it.

Tab. 2.1: The reaction steps of the HER in alkaline electrolyte and the correlated Tafel-slopes.

step	reaction	Tafel-slope [mV/dec]
Volmer	$\text{H}_2\text{O}_{(l)} + e^- \longrightarrow \text{H}^* + \text{OH}^-_{(aq)}$ (2.19)	120
Tafel	$\text{H}^* + \text{H}^* \longrightarrow \text{H}_{2(g)}$ (2.20)	30
Heyrovsky	$\text{H}_2\text{O}_{(l)} + e^- + \text{H}^* \longrightarrow \text{H}_{2(g)} + \text{OH}^-_{(aq)}$ (2.21)	40&120

Electrocatalysts for the HER are often classified by their ability to bind the hydrogen intermediate, as the reaction pathways clearly indicate a correlation of the HER with the strength of the metal-hydrogen bond. A volcano plot expresses the exchange current density over the strength of the metal hydride bond to represent an optimal hydrogen binding strength. The Sabatier principle, which is visualized by the volcano plot, is a balance between strong binding to adsorb the reactant and a weak bonding to let go the product [22–24].

However, a volcano plot is not presented here. It originates from the HER in acidic electrolyte, where its application has proven to be useful. Besides, it only considers the formation of metal hydrides. A distinction between strongly adsorbed hydrogen from the HER underpotential region (positive to E_{HER}^0) H_{upd} and more weakly but higher reactive overpotentially adsorbed (negative to E_{HER}^0) H_{opd} is lacking. Also, the HER in alkaline water electrolysis requires the breakage of the strong covalent bond in H_2O . Compared to the Volmer step proceeding via H_3O^+ in acidic electrolyte, additional performance descriptors besides the hydrogen binding strength determine the activity of an HER electrocatalyst in alkaline electrolyte. For instance, the adsorption of hydroxide-anions is another important descriptor. The presence of OH^* on the electrocatalyst surface can be a vital step in the water-dissociating step. On the contrary, it can influence the hydrogen binding strength of neighboring active sites and block an active site for a hydrogen adsorbent [22–24, 26, 27].

2.4 Alkaline HER on Ni

The obtainable kinetic values in the literature for smooth nickel electrodes are reported for NaOH and KOH in different electrolyte concentrations. The values that were taken in this work for a comparative overview reach from 0.01 M up to 34 w% (~ 8 M). To accommodate the different electrolyte concentrations, Fig. 2.4, 2.5 and 2.6 represent the reported values for Tafel-slopes, exchange current densities and the overpotential at 10 mA/cm^2 , respectively, for polycrystalline nickel at room temperature with regards to the measurement pH. The overpotential at 10 mA/cm^2 is chosen as a standard comparison for electrocatalysts, as it refers to the current density of a water-splitting photoelectrochemical device [28, 29]. The presented values were taken for smooth nickel surfaces to get an overview of intrinsic kinetic properties. Values are marked in black when the authors made an effort to assess intrinsic

kinetics by correcting for the electrochemical active surface area (ECSA). The kinetic values of nickel are further summarized in Tab. 2.2, where the sources considering the ECSA are represented in bold.

The figures reveal a great variety over several orders of magnitude in reported literature values. If only the ECSA corrected intrinsic values are considered, the Tafel-slope (Fig. 2.4) can reach from 95 - 145 mV/Dec, the exchange current density (Fig. 2.5) from $7 - 344 \cdot 10^{-5} \text{ mA/cm}^2$ and the overpotential at 10 mA/cm^2 (Fig. 2.6) from 409 - 563 mV.

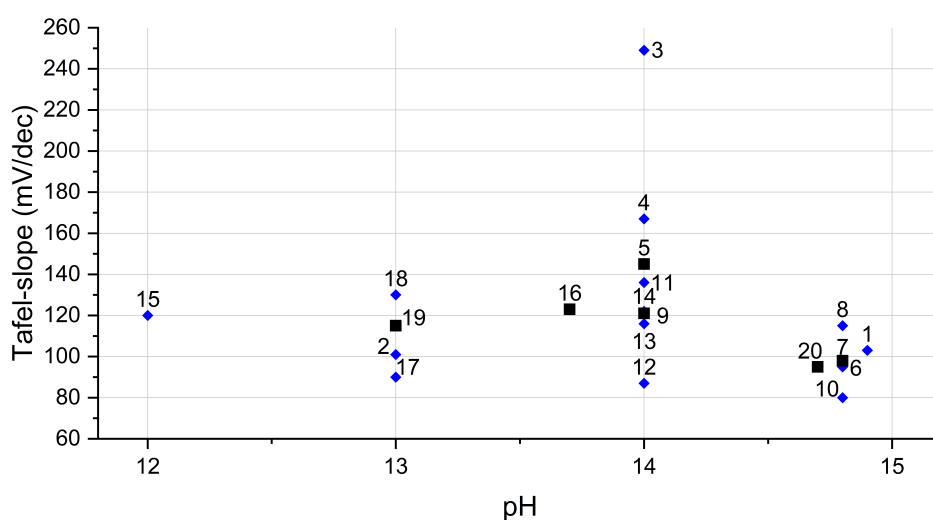


Fig. 2.4: Reported Tafel-slopes for the HER on polycrystalline nickel in alkaline electrolyte at room temperature with respect to the measurement pH [30–45]. Values summarized in Tab. 2.2. Black marked values represent literature sources that considered the electrochemical active surface area.

This scatter raises the question why the kinetics of polycrystalline nickel differ remarkably between different studies. Summing up the literature knowledge on this artifact, it can be concluded that the surface state of nickel and its kinetic response are depending on the electrode preparation and pretreatment, as well as the electrode’s history [42, 44–49].

Oshchepkov et al. [45, 47, 48] show that a partially oxidized nickel surface enhances the HER performance drastically. Through kinetic modeling, the authors claim that the HER on pure nickel proceeds with the Volmer-Heyrovsky mechanism, which is indicative for

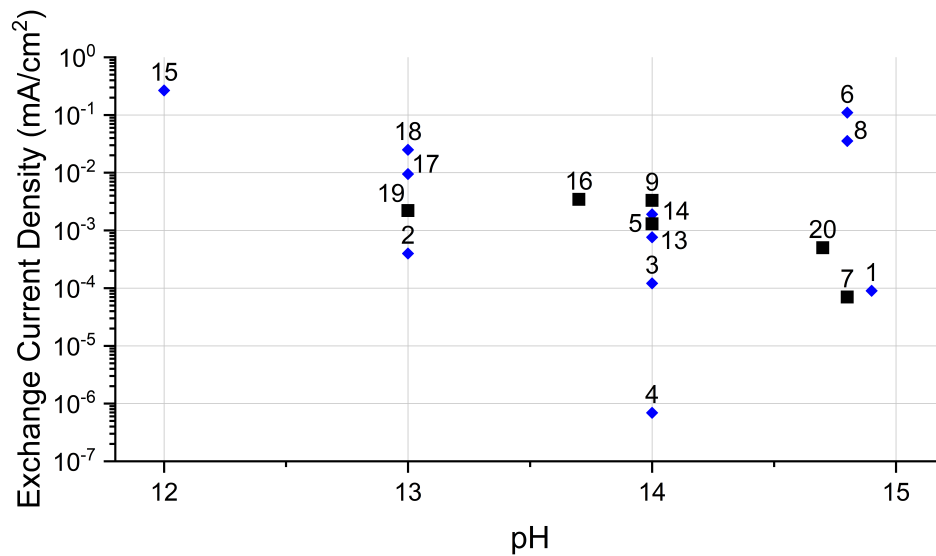


Fig. 2.5: Reported exchange current densities for the HER on polycrystalline nickel in alkaline electrolyte at room temperature with respect to the measurement pH [30–45]. Values summarized in Tab. 2.2. Black marked values represent literature sources that considered the electrochemical active surface area.

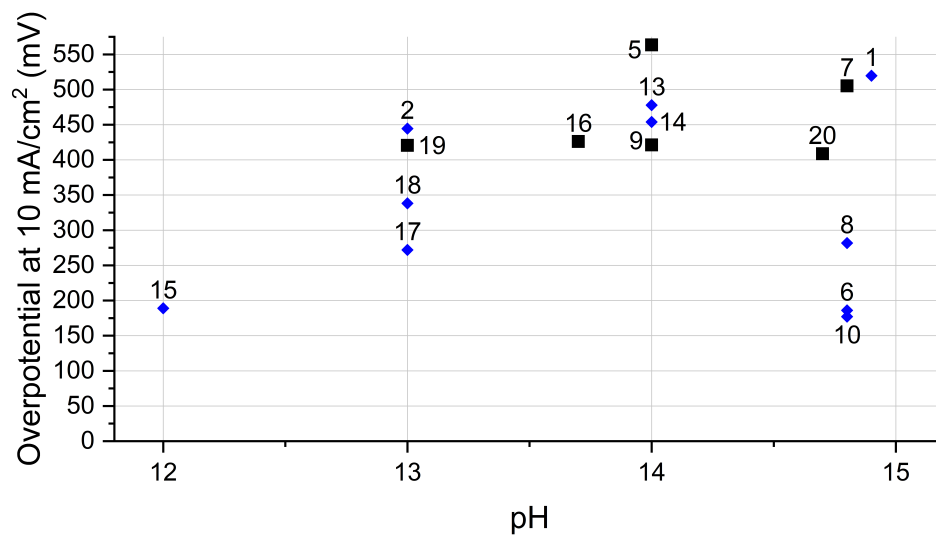


Fig. 2.6: Overpotential at 10 mA/cm² for the HER on polycrystalline nickel in alkaline electrolyte at room temperature with respect to the measurement pH [30–45]. Values summarized in Tab. 2.2. Black marked values represent literature sources that considered the electrochemical active surface area.

Tab. 2.2: Kinetic values for the alkaline HER on nickel, obtained from the literature and used in Fig. 2.4, 2.5, and 2.6. Bold marked values represent literature sources that considered the electrochemical active surface area.

No.	Electrolyte	Concentration	pH	Tafel-slope [mV/dec]	i_0 [mA/cm ²]	η_{10} [mV]	Source
1	KOH	34 %	14.9	103	$9 \cdot 10^{-5}$	520	[31]
2	NaOH	0.1 M	13.0	101	$3.98 \cdot 10^{-4}$	444	[32]
3	KOH	1 M	14.0	249	$1.21 \cdot 10^{-4}$	-	[33]
4	KOH	1 M	14.0	167	$6.91 \cdot 10^{-7}$	-	[33]
5	NaOH	1 M	14.0	145	$1.3 \cdot 10^{-3}$	563	[34]
6	KOH	30 %	14.8	95	$1.1 \cdot 10^{-1}$	186	[35]
7	KOH	30 %	14.8	98	$7 \cdot 10^{-5}$	505	[36]
8	KOH	30 %	14.8	115	$3.55 \cdot 10^{-2}$	282	[37]
9	NaOH	1 M	14.0	121	$3.3 \cdot 10^{-3}$	421	[38]
10	KOH	30 %	14.8	80	-	177	[39]
11	KOH	1 M	14.0	136	-	-	[40]
12	KOH	1 M	14.0	87	-	-	[40]
13	NaOH	1 M	14.0	116	$7.6 \cdot 10^{-4}$	478	[41]
14	NaOH	1 M	14.0	122	$1.9 \cdot 10^{-3}$	454	[41]
15	KOH	0.01 M	12.0	120	$2.66 \cdot 10^{-1}$	189	[42]
16	NaOH	0.5 M	13.7	123	$3.44 \cdot 10^{-3}$	426	[43]
17	NaOH	0.1 M	13.0	90	$9.5 \cdot 10^{-3}$	272	[44]
18	NaOH	0.1 M	13.0	130	$2.5 \cdot 10^{-2}$	338	[44]
19	NaOH	0.1 M	13.0	115	$2.2 \cdot 10^{-3}$	421	[45]
20	KOH	5 M	14.7	95	$5 \cdot 10^{-4}$	409	[30]

a strong adsorption of the hydrogen intermediate and thus a low reaction rate. The partial oxidation of the surface with a nickel oxide species reduces the strength of the hydrogen adsorption. Accordingly, the rate of the Volmer step and the overall reaction rate increases significantly. A comparison of the exchange current densities with respect to the temperature for a pure and partially oxidized nickel electrode is given in Fig. 2.7. The increase of the exchange current density through the partial oxidation (EC-activated Ni) over plain Ni (Non-activated Ni) irrespective of the temperature confirms the activating effect.

The findings of Oshchepkov et al. are well in agreement with Liang et al. [42]. Liang et al. applied the scanning electrochemical microscopy technique to unambiguously determine the amount of hydrogen produced during the HER on partially oxidized nickel electrodes. Through a combination of electrochemical measurements with surface titration, the authors could divide the electrochemically measured reduction current into nickel hydroxide/oxide reduction and hydrogen evolution. It was found that a partially oxidized surface, when the electrode potential was scanned up to 1 V vs RHE¹, could enhance the performance of the HER on nickel. When scanned at higher potentials than 1 V vs RHE, the HER performance drastically decreased (see Fig. 2.8). The authors also express a warning, as great amounts of the electrochemically measured reduction current had to be correlated to the reduction of nickel hydroxide/oxide. Therefore, some reported values for partially oxidized nickel electrodes can be considered erroneous.

The impact of the partial oxidation of nickel is further potential depending. As it can be seen in Fig. 2.9, the influence of the partial oxidation on the HER kinetics requires a minimum potential of +500 mV vs RHE (-438 mV vs Ag/AgCl). This refers to the potential window of alpha nickel hydroxide, which is reported to be a reversible electrochemical reaction [18, 43, 50]. The figure further indicates that potential cycling in the alpha nickel hydroxide region does not influence the performance of the HER on nickel, confirming that this transition is electrochemically reversible.

The influence of nickel oxide on nickel is of great importance. Medway et al. [49] show that nickel oxide is formed in air on Ni(111) single-crystal surfaces. Upon immersion into 1 M KOH, additional nickel hydroxide is formed on top of the nickel oxide. The nickel oxide

¹The authors report the potentials vs Ag/AgCl and 0.01 M KOH. The values were recalculated to the RHE scale to allow for comparison

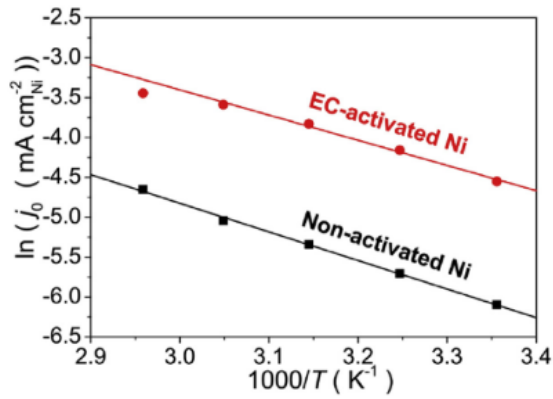


Fig. 2.7: Calculated exchange current densities of the HER over reciprocal temperature for bare and partially oxidized nickel. The potential of the partial oxidation is identical to 0.062 V in Fig. 2.8. Reproduced from [45].

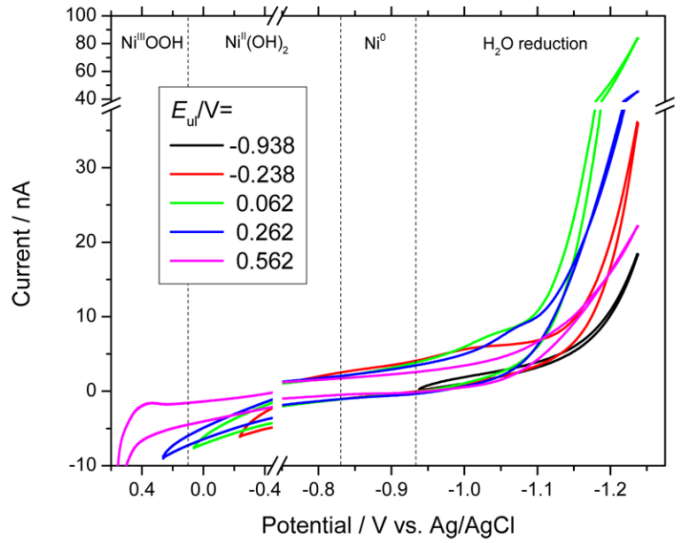


Fig. 2.8: Cyclic voltammograms of a nickel electrode with increasing upper potential limit, reported vs Ag/AgCl (1 M KCl) in 0.01 M KOH. Reproduced from [42].

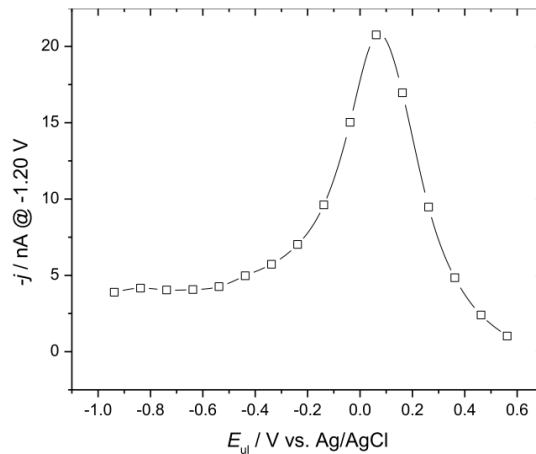


Fig. 2.9: The measured current of the hydrogen evolution reaction at -1.20 V by Surface Interrogation Scanning Electrochemical Microscopy in relation to the upper potential limit from Fig. 2.8. Results from voltammetry at 50 mV/s in 0.01 M KOH. The Equilibrium potential for the HER is -938 mV vs the Ag/AgCl reference. Reproduced from [51].

cannot be reduced electrochemically, as hydrogen is only absorbed into the nickel oxide layer. This finding is well in agreement with a previous study by Visscher and Barendrecht [52].

Another finding for a history-dependence of nickel was made by Pătru et al. [53]. Pătru et al. claim that the intrinsic performance of nickel is depending on its morphology and its internal mechanical stress. By comparing different nickel nanoparticle catalysts, the highest activity was found in small particles with high internal stress and a monotone correlation between high material strain and a high performance could be drawn.

A further mechanical effect on nickel at HER potentials was seen in the initiation of cracks, which is changing the mechanical nature of nickel [54]. Evaluating nickel single-crystals, the authors find that a nickel α -phase transforms into a hydride, which initiates cracks and influences the performance. These findings are in line with the findings of Soares et al. and Hall et al. [55–57].

Both groups, Soares et al. [55, 56] and Hall et al. [57], applied X-ray diffraction on previously strongly negative polarized nickel electrodes with roughly 1000 mV of HER overpotential. For both, nickel hydrides are found to be produced during the HER, as visible in the XRD patterns in Fig. 2.10 and 2.11. It is a matter of debate, if this hydride phase is present in the surface and subsurface, if it can be present in the bulk or only in the grain boundaries [58]. Only surface or subsurface hydrides would influence the kinetic response of nickel. The results from X-ray diffraction, which are greatly influenced by the bulk, cannot address this point. Furthermore, the high overpotential reached in both studies allows to question their correlation to the technical application.

Finally, a time-dependending altering effect of nickel can be found in the literature. The kinetics of the HER on nickel decrease, which is visible by the increase of the overpotential at identical current densities with electrolysis time [33, 57, 59]. This altering effect was ascribed to the formation of nickel hydride [33, 57, 60, 61], but remains elusive due to the unresolved question about the presence of surface and subsurface hydrides.

In summary, the unambiguous correlation between the kinetics on nickel and its surface state has yet to be resolved. However, it is known that the pretreatment of a nickel electrode greatly influences its kinetic performance, as the surface state, the roughness, and the material strain each impact it. Hence, the above illustrated scatter of obtainable kinetic

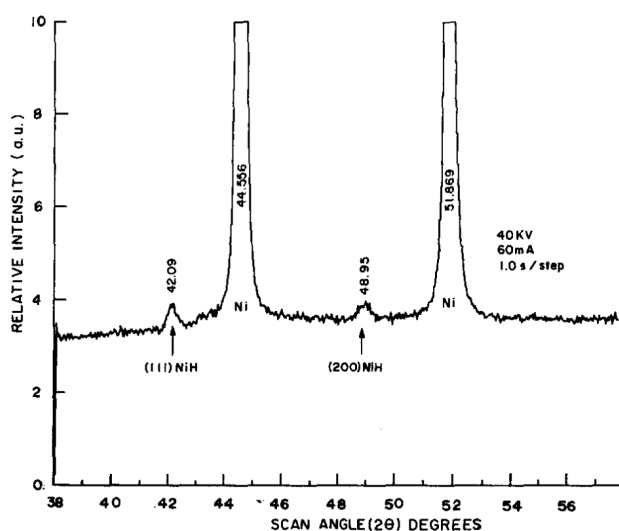


Fig. 2.10: XRD pattern of a nickel electrode, 20 minutes after being polarized at 300 mA/cm^2 for 2 h. Reproduced from [56].

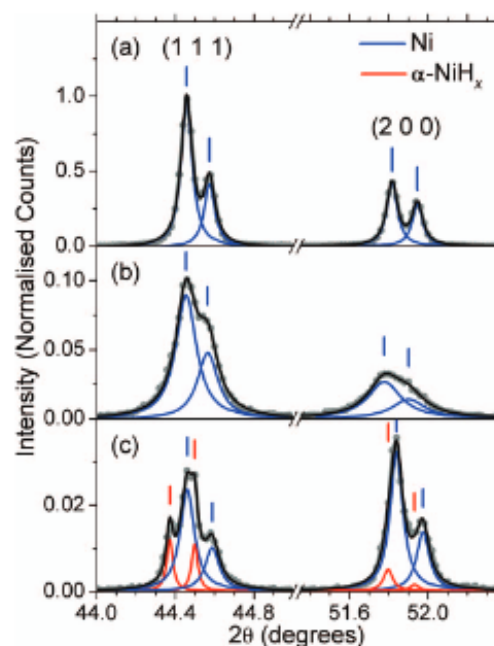


Fig. 2.11: XRD pattern of a) fresh nickel, b) after 141 h at 500 mA/cm^2 in 1 M NaOH, c) after 66.5 h at 500 mA/cm^2 in 30 % KOH. Reproduced from [57].

data for nickel is certainly a consequence of unstandardized or the lack of pretreatments of the nickel electrode.

In order to evaluate the intrinsic kinetic properties of nickel, it is necessary to assess the ECSA. One approach is to correct for the ECSA by measuring the double layer capacitance with EIS. Depending on the literature source, the double layer capacitance and the ECSA are equal by a value between 20 and $40 \mu\text{F/cm}^2$ for a metallic electrode [8, 15, 36, 62].

The weak point of this procedure lies in the uncertainty if EIS is indeed only measuring the electrochemical double layer capacitance, or if side processes influence the obtainable value. Conway and Bai [63] found a pseudocapacitive influence at overpotentials close to the equilibrium potential of the HER. Out of this observation, Conway and Bai proposed a model for the pseudocapacitive influence of overpotentially adsorbed hydrogen on nickel electrodes in alkaline electrolytes. Depending on the predominant HER mechanism, three

overpotentially depending pseudocapacitance-curves are gathered, as shown in Fig. 2.12. These curves, however, become negligible for overpotentials higher than 200 mV, where the capacitance measurement delivers the double layer capacitance free of a pseudocapacitance. An additional way to assess the ECSA is based on the formation of a monolayer of α -nickel hydroxide. Scanning between the onset of the HER and +500 mV vs RHE results in the formation of a monolayer of α -Ni(OH)₂. The charge of this process equals 514 $\mu\text{C}/\text{cm}^2$ [18, 43]. Consequentially, the estimation of the ECSA delivers reliable values if the results of both methods are akin.

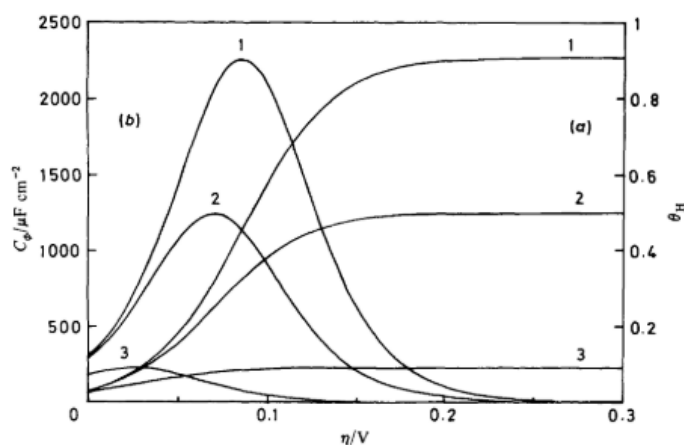


Fig. 2.12: Model of the influence from overpotentially deposited hydrogen on the total capacitance of a nickel electrode in the HER region. Reproduced from [63].

2.5 Alkaline HER on NiMo

Nickel-molybdenum electrocatalysts for the HER display high performances in the literature [8, 64, 65]. However, the literature is not unequivocal about their optimal composition, the origin of their high performance, the influence of the ECSA, and about their stability.

2.5.1 The role of the molybdenum content

The ratio between nickel and molybdenum is one focus point in the literature. For instance, Jaksic et al. [38] studied metallurgically prepared samples with Mo contents of 50 %, 33 %, 25 %, and 20 %. Although a correction for the electrochemical surface area is absent, the

measurements of these polished electrodes with smooth surfaces allow to conclude on intrinsic properties. For the evaluation of the optimal composition, potentiostatic measurements in 1 M NaOH resulted in the in Fig. 2.13 represented correlation, in which the current density at an HER overpotential of 400 mV is displayed as a function of the molybdenum content. For these metallurgically prepared samples, the authors find a 6-times increase of the activity for a 50:50-composition in comparison to pure nickel and pure molybdenum, and more than a twofold increase in comparison to the other nickel-molybdenum electrocatalysts.

In another study, McKone et al. [65] investigated nickel-molybdenum electrocatalysts made by a coprecipitation synthesis. By changing the ratio of the precursors, different Ni-to-Mo ratios could be obtained from this synthesis. These in Mo-content varying electrocatalysts were then evaluated with respect to the overpotential at a current density of 10 mA/cm^2 in 1 M NaOH. Fig. 2.14 illustrates the correlation between the Mo-content in the precursor (top of the figure) to the Mo-content in the final electrocatalyst, including the overpotential measured at 10 mA/cm^2 (bottom of the figure). For these similarly prepared samples, a significant performance-difference for Mo-contents between 20-40% cannot be deduced from the figure². These results are not directly in line with the findings of Jaksic et al. In addition to activities of different nickel-molybdenum electrocatalysts reported elsewhere [66–68], Mo-contents between 20-50% are therefore of highest interest with regards to the performance of nickel-molybdenum electrocatalysts [69].

Furthermore, the effect of present oxide phases was addressed. Danilovic et al. [70] demonstrate the importance of present hydroxide phases, which can greatly enhance the hydrogen evolution reaction in alkaline media. This effect was described as a result of a bifunctional mechanism, in which the presence of an oxidized species promotes the water-dissociating Volmer-step on a platinum electrocatalyst. In this perspective, Cao et al. [71] calculated the Gibbs free energy of the hydrogen adsorption on Ni_{10}Mo , Ni_4Mo and Ni_3Mo , which were supported on MoO_3 . The highest activity among these electrocatalysts was found for the Ni_{10}Mo electrocatalyst, which is ascribed to the MoO_3 induced lowest hydrogen adsorption energy.

Complementary, Gomez Vidales et al. [34] investigated oxide supported nickel-molybdenum electrocatalysts. In this study, the effect of different surface roughnesses was

²The authors claim to observe similar performance between 10-50%. However, the data from Fig. 2.14 display a more narrow window between 20-40%.

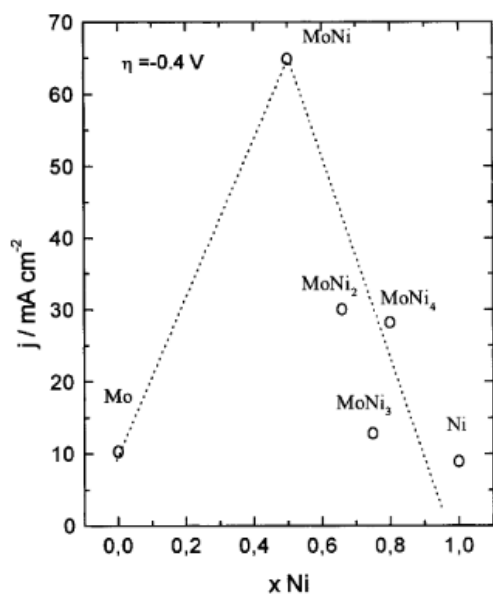


Fig. 2.13: Current densities of various Ni_xMo_y electrocatalysts at an HER overpotential of 400 mV in 1 M NaOH at room temperature. Reproduced from [38].

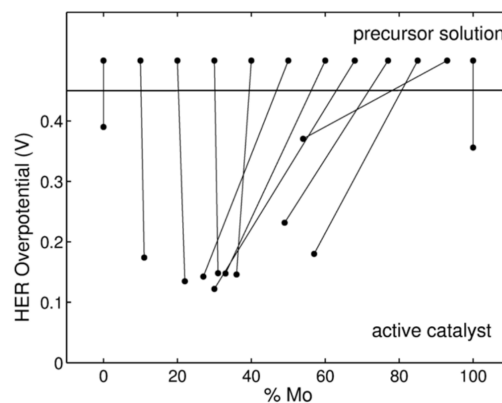


Fig. 2.14: Ni/Mo-ratio in the precursor solution (top) and the resulting Ni/Mo-ratio in the electrocatalyst with the respective overpotential at 10 mA/cm^2 in 1 M NaOH (bottom). Reproduced from [65].

addressed by the evaluation of the ECSA through the hexaaminruthenium (II/III) redox couple. The prepared electrocatalysts consist of pure nickel and pure molybdenum phases, which are accompanied by various nickel oxides and molybdenum oxides. Fig. 2.15 demonstrates the current densities with respect to the surface area (gathered from the hexaaminruthenium (II/III) redox couple) in 1 M NaOH at an HER overpotential of 300 mV. The results clearly show the importance of present oxide phases, as the oxide supported nickel and molybdenum phases, which are not present as nickel-molybdenum alloys, outperform a pure nickel electrocatalyst.

2.5.2 Proposed reasons for the high performance of NiMo

Although nickel-molybdenum electrocatalysts display promisingly high performances, it is debated if this effect has an intrinsic origin. Some authors propose that the performance increase is solely attributed to an increase of the electrochemical surface area of nickel [72, 73]. On the other hand, other sources ascribe an intrinsic effect from the presence of molybdenum

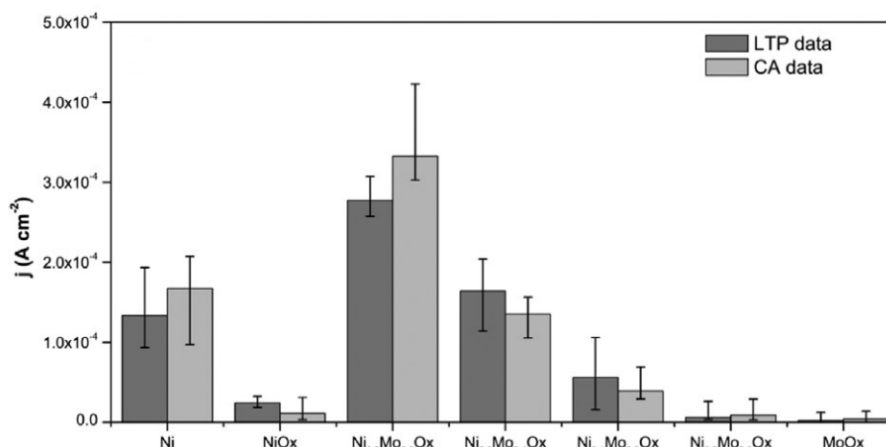


Fig. 2.15: Current density per true electrochemical surface area, evaluated through the hexaaminruthenium (II/III) redox couple, at -300 mV in 1 M NaOH. "LTP data" correspond to *iV* curves obtained at 1 mV/s, "CA data" to a 300 s long chronoamperometry, in which the last 100 s were averaged. Reproduced from [34].

to the performance increase, as e.g. nickel-molybdenum facets display almost thermoneutral hydrogen adsorption free energies according to density functional theory (DFT) calculations, indicating an optimal bond of the metal-hydrogen bond [69].

A further intrinsic effect was described by Liu et al. [74]. Liu et al. demonstrate a highly performing MoO₂ – Ni nanowire electrocatalyst. Supported by DFT calculations, an intrinsic effect through the raise of the 2p orbitals of oxygen in MoO₂ leads to the conclusion that oxygen is the active site in the MoO₂ – Ni electrocatalyst. Fig. 2.16 illustrates the effect of the heterostructure of MoO₂ – Ni in comparison to the single structures. The heterostructure, according to DFT, results in an optimal hydrogen binding energy on the oxygen atom, which is responsible for the observed performance. This is partly in accordance to Cao et al. [71] who find an intrinsic effect through the presence of MoO₃ sites, which lower the hydrogen adsorption energy on the alloy sites, but not on the oxide site.

In addition, Kabir et al. [75] investigated on the increased performance of nickel-molybdenum electrocatalysts in fuel cell applications. Despite the focus on the hydrogen oxidation reaction, a similarity to the hydrogen evolution can easily be made from this study, as the combined *in situ* XPS and XAS studies were conducted without applied potential. The study, as shown in Fig. 2.17, focused on the hydrogen adsorption in changing atmospheres.

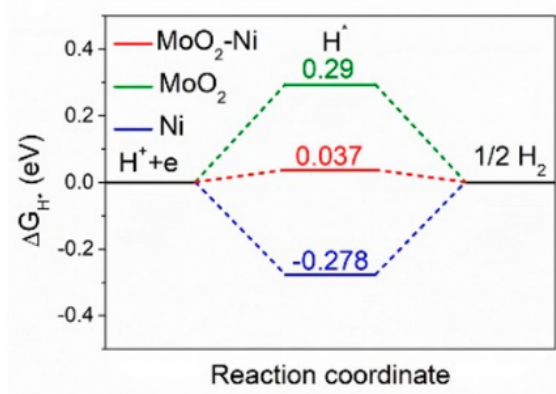


Fig. 2.16: Calculated hydrogen adsorption energy at the equilibrium potential of MoO₂-Ni, MoO₂, and Ni. Reproduced from [74].

Specifically, the studies were conducted in ultra high vacuum (UHV) and with pure hydrogen (H₂) and humidified hydrogen (H₂/H₂O) at 70 °C.

Upon exposure to hydrogen and humidified hydrogen, the binding energy changes for the Ni 3P sites in a Ni and a NiMo electrocatalyst, associated with the participation of -OH groups. Notably, the binding energy of Mo 3d in NiMo is not affected. Based on these results, microkinetic modeling directs to an intrinsic effect from molybdenum. This effect originates from a decreased binding energy of the hydrogen intermediate on the nickel site. These findings, although conducted in a gaseous atmosphere, enforce the importance of molybdenum in nickel-molybdenum HER electrocatalysts, although nickel appears to be the active site according to this study [75].

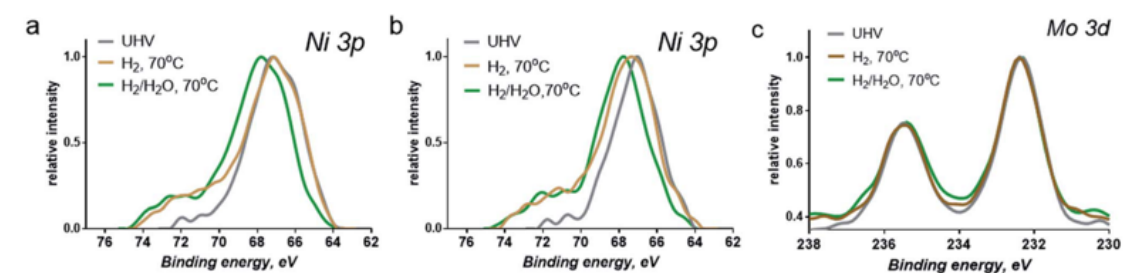


Fig. 2.17: High resolution XPS spectra at UHV, as well as in hydrogen and in humidified hydrogen environment at 70 °C. **a:** Ni 3p spectra of a Ni electrocatalyst. **b:** Ni 3p spectra of a NiMo electrocatalyst. **c:** Mo 3d spectra of a NiMo electrocatalyst. Reproduced from [75].

molybdenum and a nickel electrocatalyst in 1 M KOH around 0 V vs RHE from this study are illustrated in Fig. 2.19. It is apparent that, up to 80 mV above the HER equilibrium potential, the nickel-molybdenum electrocatalysts displays a non-negligible capacitive hysteresis. Further supported by EIS measurements, it is deduced that molybdenum is redox active at potentials near the hydrogen equilibrium potential, which ultimately causes a significant pseudocapacitance. Another possible source of a pseudocapacitance from hydrogen adsorption, as shown by Conway and Bai [63], was mentioned, but can neither be verified nor ruled out in this study.

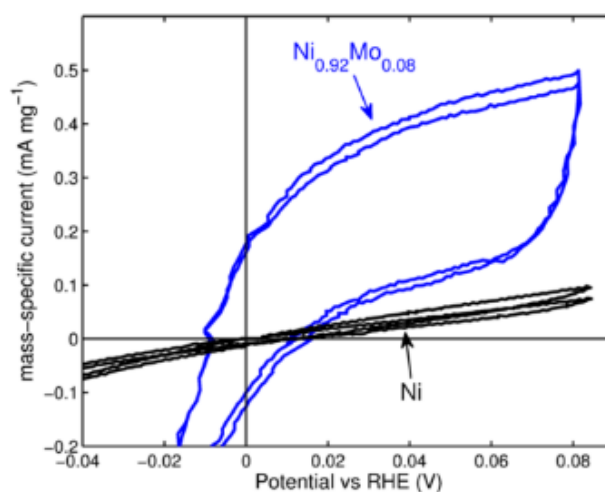
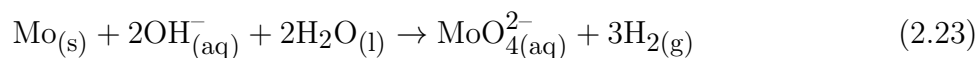


Fig. 2.19: Cyclic voltammograms close to the HER equilibrium potential of a Ni and a Ni_{0.92}Mo_{0.08} electrocatalyst. Reproduced from [77].

Complementary to this work, Davydova et al. [78] and Schalenbach et al. [73] investigated the effect of molybdenum leaching in 0.05 M KOH and NaOH, respectively, with online inductively coupled plasma mass spectrometry (ICP-MS) in respect to the applied potential. The selected electrocatalysts cover molybdenum contents from 14-50 %, as well as pure nickel and pure molybdenum. Both studies are illustrated in Fig. 2.20 and 2.21, respectively. In both cases, molybdenum displays high dissolution rates at potentials at OCV and above 0 V vs RHE. Davydova et al. further claim that the dissolution of molybdenum led to the decision to discard this electrocatalyst for measurements of the hydrogen oxidation in favor of more stable Ni₃Cu, Ni, Ni₃Co, and Ni₃Fe. However, it is questionable if the shown dissolution of molybdenum results in a destructed electrocatalyst, or if the molybdenum-

dissolution reached an equilibrium, which would then result in a stabilized electrocatalyst. Schalenbach et al. further studied NiMo electrocatalysts with varying molybdenum contents at potentials up to 400 mV vs RHE. The authors display that molybdenum dissolves from the alloys irrespective of the molybdenum content. Upon increasing the electrode potential, the rate of dissolution increases, which leads the authors to assume that the NiMo electrocatalysts are unstable in alkaline media.

Wijten et al.[69] confirm the segregation of molybdenum in a nickel-molybdenum electrocatalyst (Ni/Mo-ratio 3:1) by ICP-AES in 1 M KOH. Furthermore, a leaching mechanism, according to Eq. (2.23), is proposed. Following this mechanism, the dissolution of molybdenum is causing hydrogen evolution and thereby an overestimation of the activity of the nickel-molybdenum electrocatalysts, as a part of the generated hydrogen results from the dissolution of molybdenum. Despite this electrocatalyst instability, a steady-state can be observed in the chronopotentiometry at 10 mA/cm² after 30 h of operation, suggesting a stabilizing behavior of the electrocatalyst.



Another destabilizing effect of nickel-molybdenum electrocatalysts was calculated by Yu et al. [79]. If oxygen is chemisorbed on a MoNi(111) surface, its amount can greatly influence the segregation of molybdenum. As shown in Fig. 2.22, more than 1/9 of a monolayer of chemisorbed atomic oxygen can cause segregation of molybdenum by causing a free segregation energy of molybdenum in nickel. Notably, the segregation takes place in the surface layer, and is absent in the second atomic layer irrespective of the degree of chemisorbed oxygen. Although this effect might be less pronounced in HER electrocatalysts, it has to be taken into consideration due to the possibility of oxygen gas crossover in a technical electrolyzer.

In contrast to the studies on the instability of nickel-molybdenum electrocatalysts, several studies demonstrate their stability. For instance, Fernández-Valverde et al. [66] report stable operation of a nickel-molybdenum electrocatalyst (Ni/Mo-ratio 1:1) for the oxygen evolution in 0.5 M KOH for 1000 minutes. In another study, a two week long measurement of an electrodeposited nickel-molybdenum electrocatalyst in 6 M KOH at 60 °C displays a promisingly high stability at 100 mA/cm² [80].

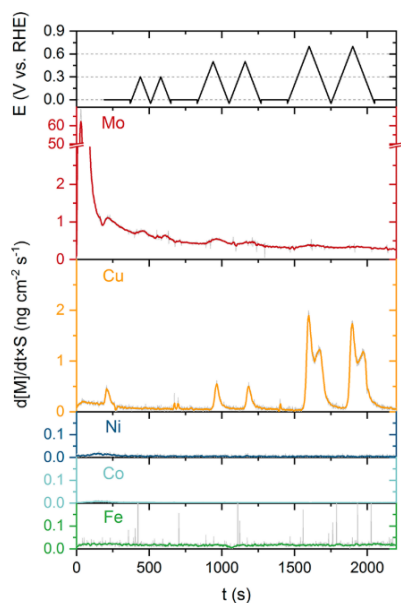


Fig. 2.20: Leaching of Mo from Ni_3Mo with respect to the applied potential and in comparison to Ni_3Cu , Ni, Ni_3Co and Ni_3Fe . Measurements in 0.05 M KOH. Reproduced from [78].

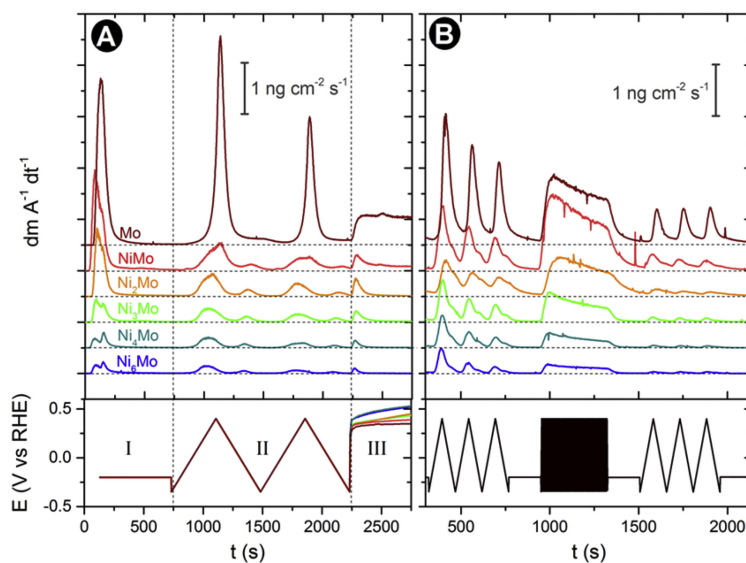


Fig. 2.21: Dissolution of molybdenum in Mo, NiMo, Ni_2Mo , Ni_3Mo , Ni_4Mo , and Ni_6Mo in correlation to the applied potential and the elapsed time. Measurement results from on-line ICP-MS in 0.05 M NaOH. Reproduced from [73].

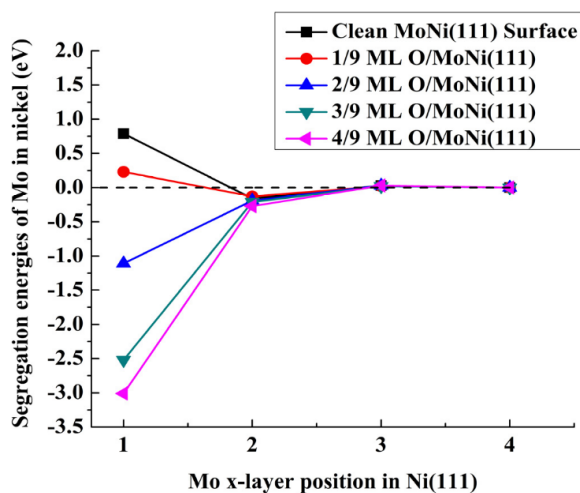


Fig. 2.22: Segregation energies of Mo in NiMo (111) with regards to the atomic layers (from 1: surface, to 4: bulk), with respect to the degree of chemisorbed monolayers (ML) of atomic oxygen. Reproduced from [79].

These observations are in agreement with a study conducted by Brown et al. [81]. The authors measured the overpotential of a nickel-molybdenum electrocatalyst (Ni/Mo-ratio 6:4) at a constant current density of 500 mA/cm^2 at 70°C in 30% KOH for 11000 h (equal to ≈ 1 year and 3 months). After an initial increase of the overpotential, a stabilization close to the initial overpotential is observed after ≈ 3000 hours of operation. From there onward, the nickel-molybdenum electrocatalyst operates at a stable overpotential. This measurement, conducted under industrial relevant conditions, demonstrates the feasibility of using nickel-molybdenum as HER electrocatalyst in technical applications.

Another publication contradicting the instability of nickel-molybdenum electrocatalysts was made by Bau et al. [82]. Conducting operando Raman spectroscopy between the OCV and 0 V vs RHE, as illustrated in Fig. 2.23, the redeposition of nickel-molybdenum oxides can be observed over time, when a potential is applied. Despite the above demonstrated instability of molybdenum at these conditions, Bau et al. show that molybdenum oxide supported electrocatalyst can be reconstructed, and hence be stabilized, in 0.1 M KOH at potentials around the equilibrium potential of the HER.

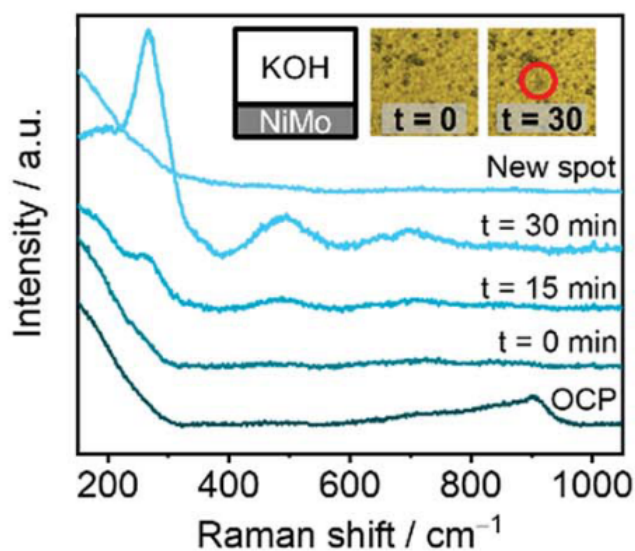


Fig. 2.23: Operando Raman spectra recorded at 0 V vs RHE and at OCV on a NiMo electrode in 0.1 M KOH. The spectra display the redeposition of molybdenum oxide. Reproduced from [82].

2.6 The mechanism of the oxygen evolution reaction

The mechanism of the oxygen evolution reaction in alkaline media is part of ongoing studies. First proposed mechanistic pathways date back into the 1950s. Bockris proposed several two-electron pathways, including the oxide, the electrochemical oxide, the hydrogen peroxide, the electrochemical metal peroxide, and the metal peroxide path [83]. Since then, the literature debates on the exact mechanistic understandings of the OER, which includes several possible two- and four-electron pathways [84–88], including e.g. the hypothesis that lattice oxygen in the form of O^{2-} anions dominate the OER [88]. Noteworthy, the OER appears to proceed with an intrinsic overpotential, which seems to be a natural cause of the reaction mechanism. This assumption was made elsewhere and is based on an overview from in the literature obtainable OER kinetics and a DFT study conducted for metal oxide electrocatalysts [86].

Despite ongoing discussions on the mechanism, the OER on nickel-based oxides, hydroxides, and oxyhydroxides is often reported to occur with either a single catalytic site and thus four one-electron steps [25], with an RDS in the OOH^* -forming step [87], or with a dual catalytic site mechanism consisting of two two-electron steps [85]. Despite the alkaline environment, the OER is further often modeled using the acidic four-electron pathway [89, 90]. The mechanisms and associated Tafel-slopes are summarized in Tab. 2.3.

The single site mechanism proceeds via the adsorption of hydroxide, which in further steps requires oxide and peroxide reaction intermediates. As a consequence, the electrocatalyst needs to have a favorable adsorption energy for both intermediates. The dual site mechanism differs by the absence of the peroxide reaction intermediate on a single site, as the oxide intermediate combines with a second oxide intermediate from the other reaction site. Both mechanisms are visualized in Fig. 2.24, where (a) describes the single and (b) the dual site mechanism. For the acidic pathway, the electrocatalyst has to stabilize the oxide and peroxide intermediate similar to the single site mechanism. The difference lies in the oxidation of water for the acidic pathway, instead of hydroxide-oxidation for the single site mechanism. Furthermore, the acidic pathway requires proton-acceptors.

Tab. 2.3: The reaction steps of the OER in alkaline electrolyte and the correlated Tafel-slopes.

step	reaction	Tafel-slope [mV/dec]
single site mechanism	(1) $\text{OH}_{(\text{aq})}^- \longrightarrow \text{OH}^* + \text{e}^-$ (2.24)	120
	(2) $\text{OH}^* + \text{OH}_{(\text{aq})}^- \longrightarrow \text{O}^* + \text{H}_2\text{O}_{(\text{l})} + \text{e}^-$ (2.25)	30&120
	(3) $\text{O}^* + \text{OH}_{(\text{aq})}^- \longrightarrow \text{OOH}^* + \text{e}^-$ (2.26)	21&40&120
	(4) $\text{OOH}^* + \text{OH}_{(\text{aq})}^- \longrightarrow \text{OO}^- * + \text{H}_2\text{O}_{(\text{l})}$ (2.27)	22&30&60&120
	(5) $\text{OO}^- * \longrightarrow \text{O}_{2(\text{g})} + \text{e}^-$ (2.28)	22&120/40&120
dual site mechanism	(1) $2\text{OH}_{(\text{aq})}^- \longrightarrow 2\text{OH}^* + 2\text{e}^-$ (2.29)	120
	(2) $2\text{OH}^* + 2\text{OH}_{(\text{aq})}^- \longrightarrow 2\text{O}^* + 2\text{H}_2\text{O}_{(\text{l})} + 2\text{e}^-$ (2.30)	30&120
	(3) $2\text{O}^* \longrightarrow \text{OO}^*$ (2.31)	–
	(4) $\text{OO}^* \longrightarrow \text{O}_{2(\text{g})}$ (2.32)	–
acidic pathway	(1) $\text{H}_2\text{O}_{(\text{l})} \longrightarrow \text{OH}^* + \text{e}^- + \text{H}_{(\text{aq})}^+$ (2.33)	120
	(2) $\text{OH}^* \longrightarrow \text{O}^* + \text{e}^- + \text{H}_{(\text{aq})}^+$ (2.34)	30&120
	(3) $\text{O}^* + \text{H}_2\text{O}_{(\text{l})} \longrightarrow \text{OOH}^* + \text{e}^- + \text{H}_{(\text{aq})}^+$ (2.35)	21&40&120
	(4) $\text{OOH}^* \longrightarrow \text{O}_{2(\text{g})} + \text{e}^- + \text{H}_{(\text{aq})}^+$ (2.36)	22&30&60&120

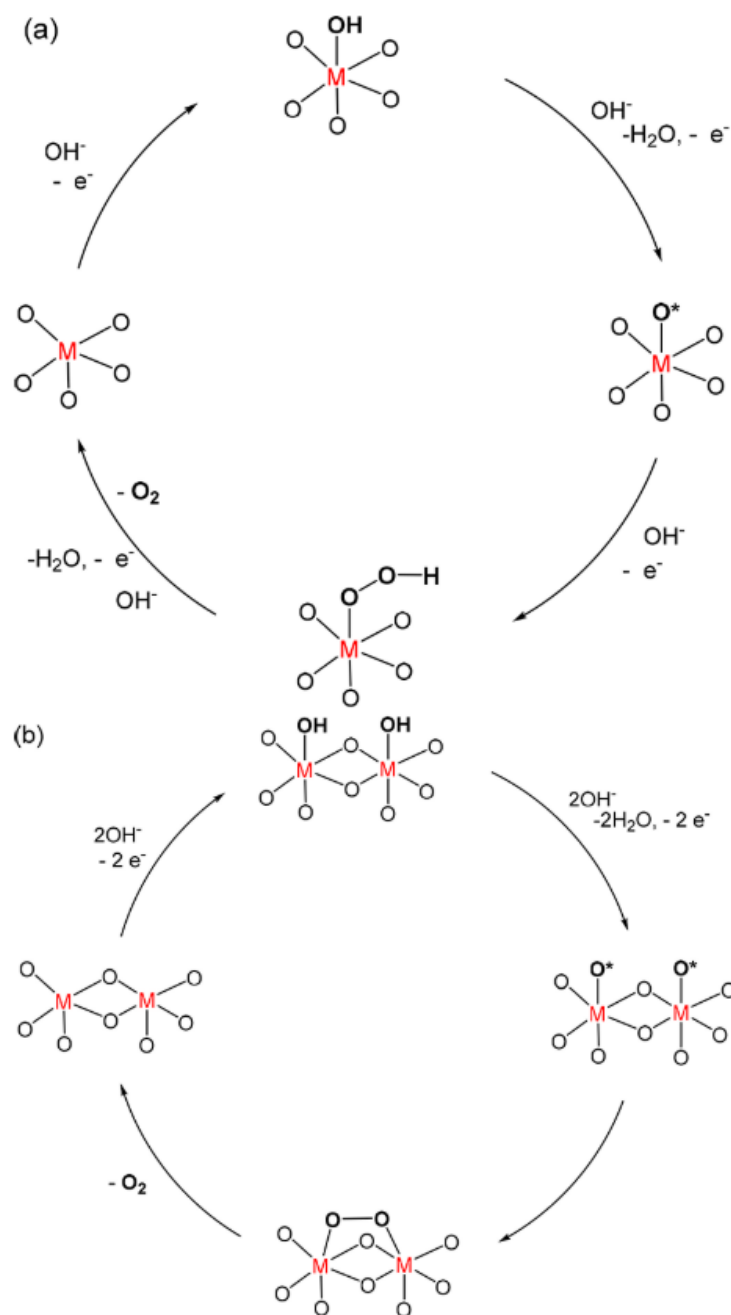


Fig. 2.24: Mechanism of the alkaline OER. (a): Single site mechanism. (b): Dual site mechanism. Reproduced from [85].

2.7 Alkaline OER on Ni and on NiFe layered double hydroxides

The in the literature obtainable kinetics for the OER on Ni vary remarkably. For instance, the Tafel-slope can be as low as 37 mV/dec [87] and 38 mV/dec [91], as well as high as 54 mV/dec [92], 72 mV/dec [93], and 82 mV/dec [94]. One possible explanation can be found in the different surface states of Ni according to the Bode diagram [14, 21], as differences in the surface roughness and the surface state due to different treatments influence the possible OER reaction pathways [87, 91, 94–97].

Besides Ni, the literature studies an abundance of different electrocatalysts for the OER. They cover, for example, perovskites, metal oxides, hydroxides, spinels, and layered double hydroxides (LDH) [8, 28, 88, 98–102]. Among all, NiFe LDH electrocatalyst come out on top as favorable OER electrocatalysts [8]. NiFe LDH electrocatalysts consist of sheets of β -Ni(OH)₂, in which some Ni²⁺ are substituted by Fe³⁺ ions. Due to the increased positive charge, charge-balancing anions are required. As a consequence, positively charged sheets of nickel-iron hydroxide stack with intercalated charge-balancing anions and water. This structure, illustrated in Fig. 2.25, is called the LDH structure [28, 103, 104].

Brucite β -Ni(OH)₂ and NiFe LDH are shown in Fig. 2.25a) and Fig. 2.25b), respectively. The layer stacking of NiFe LDH follows either a tetrahedral/monoclinic C2/m [105] (Fig. 2.25c)) or a trigonal R3m [106] (Fig. 2.25d)) structure. NiFe LDH electrocatalysts have different types of OH sites, which can be classified to edge sites μ_1 and μ_2 and center sites μ_3 . Due to the different possibilities in stacking, types of hydroxides and other aspects, LDH electrocatalysts are of high interest for research [28, 103, 104].

NiFe LDH in their as synthesized state are electric insulators, which activate upon polarization through the transition of Ni²⁺ → Ni³⁺ [99, 107]. They exhibit benchmarking OER kinetics with Tafel-slopes as low as 21–41 mV/dec [99, 107–111]. The kinetics of NiFe LDH electrocatalysts depend on the type of substrate [112], morphological aspects as the crystallinity and bulk or surface specific electrocatalysts [111, 113–115], the incorporation of a third metal [102, 116], the type of the intercalated anion [106, 113, 117], and the iron content [90, 93, 106, 118–120].

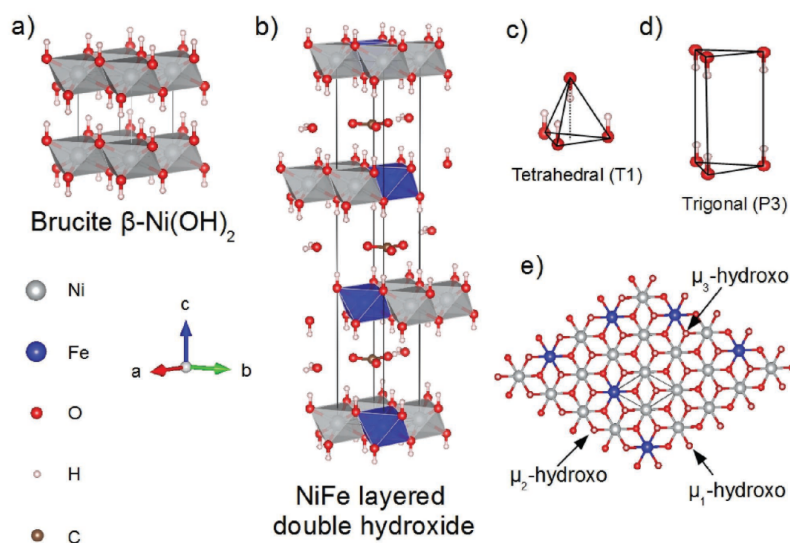


Fig. 2.25: Crystal structures of brucite β -Ni(OH)₂ and NiFe LDH. **a)**: Brucite β -Ni(OH)₂. **b)**: NiFe LDH. **c, d)**: Stacking of LDH following a tetrahedral/monoclinic C2/m or a trigonal R3m crystal system, respectively. **e)**: The different types of hydroxides in LDH. Reproduced from [28].

2.7.1 The influence of Fe on the alkaline OER

Iron plays a major role in the alkaline OER. In NiFe LDH electrocatalysts, the amount of iron is an important aspect for a highly active electrocatalyst. For instance, Klaus et al. [21] studied the impacts of the iron content of 0 – 25 % in electrodeposited NiFe LDH on the kinetics. As displayed in Fig. 2.26, the current density at an overpotential of 300 mV is highest and the overpotential at 10 mA/cm² is lowest for an iron content of roughly 11 %. On the other hand, other sources report different optimal iron contents. Diongi and Strasser attempted to normalize the results of different literature sources [28]. The authors first subtracted the lowest reported overpotential from all reported overpotentials within one literature source. The resulting plot of this figure of merit over the iron content is shown in Fig. 2.27. The combination of five literature sources provides the overview that iron contents of 10 – 50 % are required for a highly active NiFe LDH electrocatalyst.

Contrarily, the limit to which iron can be incorporated into NiFe LDH is reported to be below 50 %. In particular, Friebel et al. [90] show that iron contents above \approx 25 % result in the presence of iron-rich side phases in the form of γ -FeOOH besides the NiFe LDH structure. This finding is well in agreement with Manohara et al. [106] who find that the amount of Fe³⁺ in a MgFe LDH faces a limit of 20 %. Furthermore, it agrees with the observation that

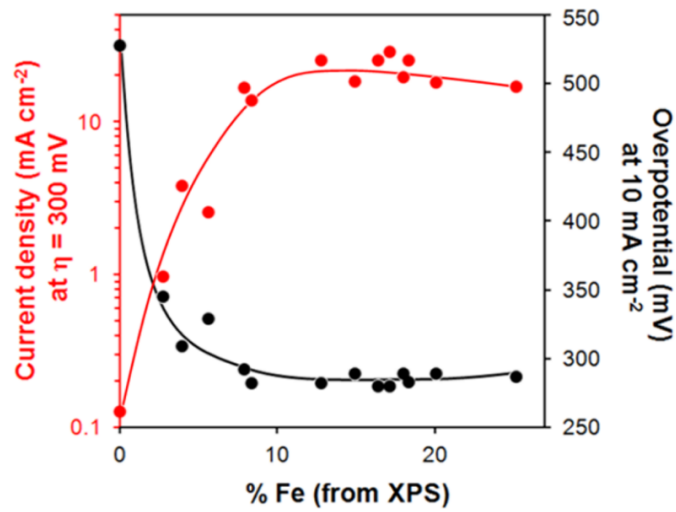


Fig. 2.26: Influence of the Fe content in electrodeposited NiFe LDH on the kinetics of the alkaline OER. Current density at an OER overpotential of 300 mV and the OER overpotential at 10 mA/cm². Reproduced from [21].

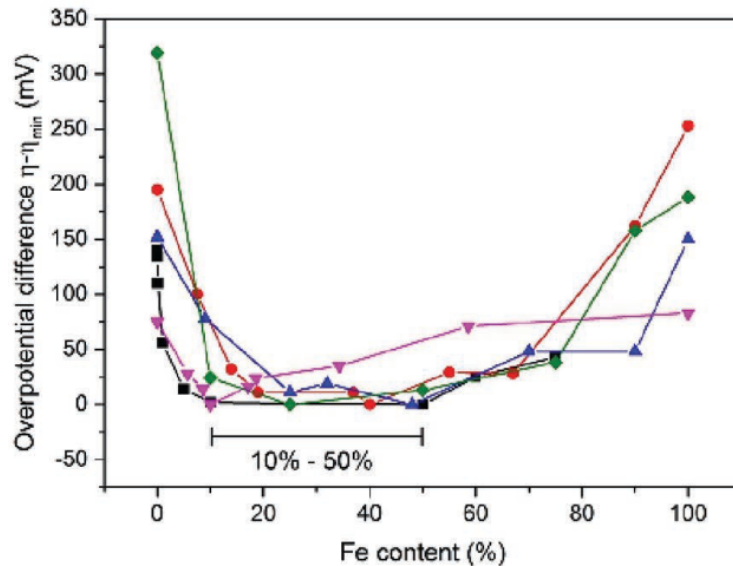


Fig. 2.27: OER overpotentials subtracted with the minimum reported overpotential in a literature source in regards to the iron content of NiFe LDH. Reproduced from [28].

iron-rich surfaces on a 50 % Fe sputter deposited LDH exhibited significantly reduced OER activity [121]. Hence, an optimal iron content around 10 – 20 % appears to be an optimal level between OER kinetics and phase purity [21, 90, 109, 121].

In addition, iron has a pivotal role in nickel based OER electrocatalysts. Corrigan demonstrates that an iron impurity of 1 ppm in the electrolyte drastically increases the OER kinetics of a nickel electrode [93]. A similar conclusion was made by Trotochaud et al. [118], as illustrated in Fig. 2.28. In an iron free electrolyte, a $\text{Ni}(\text{OH})_2/\text{NiOOH}$ electrocatalyst displays a high OER onset potential at an overpotential of roughly 400 mV. A repetition of the measurement in unpurified electrolyte resulted in the incorporation of 2 % of iron into the electrocatalyst film, which reduced the OER onset potential by more than 100 mV. The authors further show that co-deposited nickel-iron films with 25 % iron display the highest performance [118]. In addition, it was shown that nickel and iron containing electrocatalyst films experience an *in situ* oxidation into highly active LDH or oxyhydroxide films [21, 92, 122].

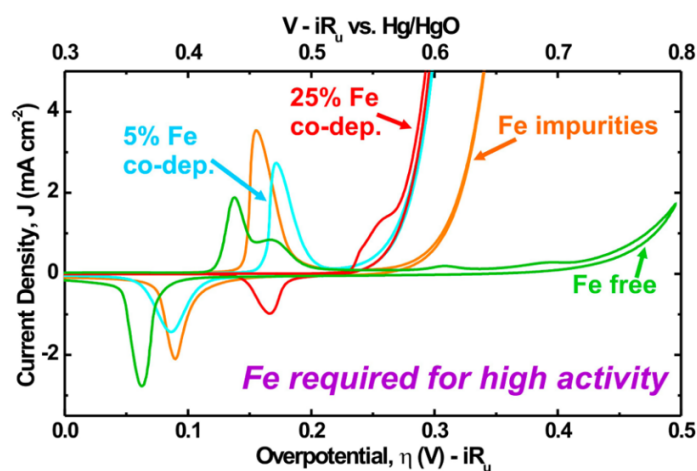


Fig. 2.28: The influence of Fe impurities and co-deposited Fe on the OER kinetics of $\text{Ni}(\text{OH})_2/\text{NiOOH}$ electrocatalyst films. Reproduced from [118].

The role of iron is further part of recent studies. To this date, it is elusive which effect can be ascribed to the increased OER kinetics of nickel electrocatalysts upon iron incorporation. As such, some claim that iron is the active site [120, 123]. Others indicate that iron increases the conductivity of the nearly insulating nickel electrocatalyst [118, 120]. Furthermore, impacts by the presence of iron on the redox chemistry are hypothesized,

which e.g. prevents nickel from further oxidation or assists in the formation of highly active Ni^{4+} [99, 124, 125]. A further discussion about each of the hypotheses is omitted and the reader is referred to the literature [119, 126].

To conclude, the presence of iron is crucial for a high-performing nickel OER electrocatalyst. Reported Tafel-slopes for Ni as low as values reported for NiFe LDH OER electrocatalysts may therefore originate from iron impurities in the electrolyte.

2.7.2 Understandings about the mechanisms on Ni OER electrocatalysts

As aforementioned, the mechanism of the oxygen evolution reaction is not fully understood yet. In addition, the complexity of the different phases of nickel increases the need for studies understanding the OER on nickel to develop highly performing and stable electrocatalysts.

In this regards, Mellsoop et al. [96] studied the redox reactions of a nickel electrode, hypothesizing that a second and more compact form of $\alpha\text{-Ni(OH)}_2$ (α_{compact}) forms from metallic nickel, and is solely formed from it. After extended periods of time under oxygen evolving conditions, this phase is expected to form a second form of $\gamma_{\text{aged}}\text{-NiOOH}$ with higher charge than the by the Bode diagram described phase. The γ_{aged} -NiOOH phase can partly recover to $\gamma\text{-NiOOH}$, which then follows the Bode diagram. The authors further consider electrochemical quartz crystal microbalance (EQCM) studies by Ohligschläger and Schwitzgebel [127] as well as *in situ* Raman studies by Yeo and Bell [128]. EQCM shows that an unexpected mass loss during cycling of a β/β Ni electrode occurs, which underlines an additional process forming a β^* phase. *In situ* Raman shows that a β/β Ni electrode forms an additional phase different to $\beta\text{-NiOOH}$ with cycling, which is not $\gamma\text{-NiOOH}$. It is described as $\beta_{\text{O}_2\text{evolution}}$. The overview of these phases in an updated Bode diagram is shown in Fig. 2.29. Mellsoop et al. further indicate that this diagram may not be encompassing, as additional phases of nickel are considerable [96].

The different types of phases in nickel raise the question about the so-called "right type of oxide" [87, 91, 129]. As mentioned before, Yeo and Bell [128] observed changes in $\beta\text{-NiOOH}$ with cycling which are ascribed to the formation of the $\beta_{\text{O}_2\text{evolution}}$ phase. The authors deduct this process as the peak-ratios of the main vibrations 485 cm^{-1} and 560 cm^{-1} experience an opposite trend than it would have been expected for the formation of $\gamma\text{-NiOOH}$.

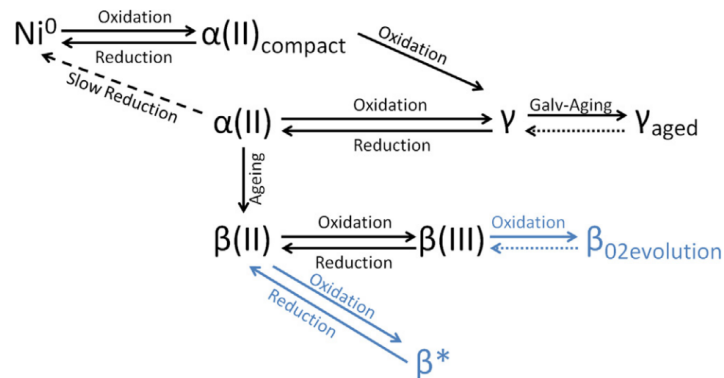


Fig. 2.29: Extended model of the nickel phases in alkaline media describing to the Bode diagram additional α and β phases. Reproduced from [96].

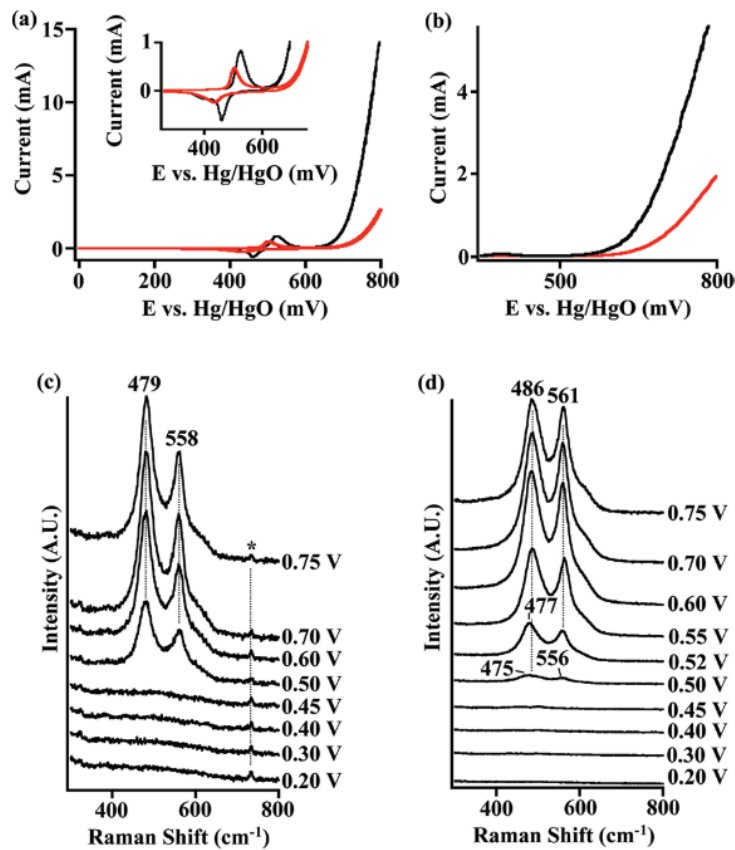


Fig. 2.30: (a): Cyclic voltammograms and (b): Linear sweep voltammetry at 1 mV/s of α/γ Ni (red trace) and β/β Ni (black trace). Raman spectra at polarization during LSV of (c): α/γ Ni and (d): β/β Ni. Reproduced from [128].

NiOOH. Furthermore, the authors compared an α/γ Ni to a β/β Ni electrode by CV, linear sweep voltammetry (LSV), and *in situ* Raman. The results are illustrated in Fig. 2.30. With increasing electrode potential, both electrodes display the expected formation of β - and γ -NiOOH. The results from CV and LSV indicate that the β/β outperforms the α/γ Ni electrode. This is further confirmed by the turnover frequency (TOF) of 0.68 s^{-1} for the β/β and 0.23 s^{-1} for the α/γ Ni electrode. Thus, the difference originates from an intrinsic superiority of the β/β Ni electrode.

In conclusion, a type of β -NiOOH seems to be the "right type of oxide" for a nickel OER electrocatalyst, although it varies from the pure phase [87, 91, 127–129]. This is further important to consider in studies on the understandings of NiFe LDH OER electrocatalysts.

2.7.3 On the stability of NiFe layered double hydroxides in alkaline electrolyte

Studies in the literature about the stability of LDH electrocatalysts are, in comparison to other studied aspects, comparably rare. This is particular the case for studies under technologically relevant conditions.

More recently, Andronescu et al. [130] aged a NiFe LDH electrocatalyst in 1 M KOH and in 7.5 M KOH at room temperature and at 80°C for 60 h. By conducting pre- and post-mortem X-ray diffraction (XRD) and Raman spectroscopy, as shown in Fig. 2.31, they conclude that the as prepared NiFe LDH is phase-stable during the 1 M KOH room temperature measurement. A similar observation was made in 1 M KOH at 80°C , and in 7.5 M KOH at room temperature. However, the at 80°C in 7.5 M KOH aged electrocatalyst phase changes into brucite β -Ni(OH)₂, amorphous γ -FeOOH, and minor amounts of α -FeOOH. Chemical aging further results in decreased electrochemical kinetics. These results indicate that measurements at technologically relevant conditions are necessary, as the electrocatalyst did not experience degradation at room temperature or in the lower electrolyte concentration of 1 M KOH. They further conclude that iron is still present in the surface, as iron leaching was not found to occur remarkably.

Contrary to Andronescu et al., Etzi Coller Pascuzzi et al. [131] found that iron leaching is of major impact at technologically relevant conditions and under polarization in NiFe LDH electrocatalysts. Supported by X-ray photoelectron and electron dispersive spectroscopy,

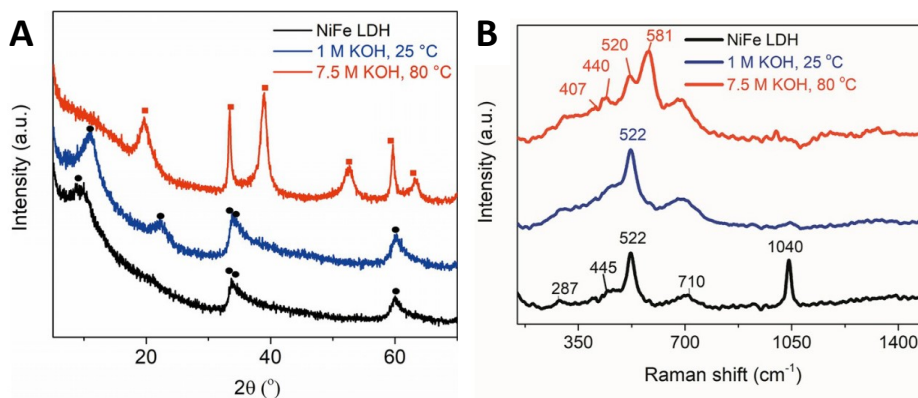


Fig. 2.31: **A:** XRD patterns and **B:** Raman spectra of a NiFe LDH electrocatalyst before and after aging for 60 h in 1 M and in 7.5 M KOH. Reproduced from [130].

iron leaches with increasing temperature and electrolyte concentration at a current density of $100 \text{ mA}/\text{cm}^2$. Similar to Andronescu et al., an electrolyte concentration of 1 M KOH has no impact on the leaching irrespective of the temperature. Besides, exposure to 10 M KOH and 75°C resulted in an almost iron-free electrocatalyst. They additionally conclude that iron leaching is a result of the electrochemical treatment at these conditions. Chemical dissolution does not occur according to the authors. Therefore, the contradiction between the results from Andronescu et al. [130] and Etzi Coller Pascuzzi et al. [131] appears to originate from the polarization of the electrocatalyst.

The understandings about the necessity of technological relevant conditions allow to question findings made at room temperature and made in 1 M KOH. For example, Liu et al. [132] demonstrate stable performance of a NiFe LDH electrocatalyst over more than 1000 h in 10 M KOH at $1000 \text{ mA}/\text{cm}^2$, but at room temperature. In addition, Chen et al. [114] show that a NiFe LDH electrocatalyst is stable for 20 h at 80°C and $500 \text{ mA}/\text{cm}^2$, but in 1 M KOH. Although both studied surface specific electrocatalysts, which might lead to the assumption that bulk NiFe LDH is unstable [114], it is elusive whether the shown stability remains valid at full technologically relevant conditions under polarization.

2.8 Concluding remarks on the hydrogen and oxygen evolution in alkaline electrolyte

Summing up the literature review, it is to this date elusive what determines the high performance of NiMo electrocatalysts for the HER. Furthermore, studies addressing technologically relevant conditions, intermittent operation, and degradation mechanisms are rare yet needed for NiMo HER and NiFe LDH OER electrocatalysts. The open questions that are in the focus of this thesis can therefore be summarized as following.

- What are the performance descriptors in Ni and NiMo electrocatalysts for the HER?
 - Which impact does the electrochemical active surface area have?
 - How do the intrinsic kinetics of these electrocatalysts correlate, when the effects of the electrochemical active surface area are considered?
 - What role does the presence of a partially oxidized surface and the presence of hydroxides or oxides have with regards to the intrinsic kinetics of these electrocatalysts?
 - What is the active site in NiMo electrocatalysts?
- How stable are NiMo HER and NiFe LDH OER electrocatalysts?
 - Are these electrocatalysts long-term stable under technologically relevant conditions?
 - What are the operational windows, with regards to the electrocatalyst's potential, during the industrial operation with intermittent energy supply?
 - What are the redox and degradation processes of these electrocatalysts in the operational windows?
 - Are the redox processes reversible or do they cause degradation of the electrocatalysts?

Chapter 3

Experimental Methods and Setups

This chapter describes the main applied techniques as well as the electrochemical setups used in this work.

3.1 Electrochemical impedance spectroscopy

Electrochemical impedance spectroscopy (EIS) combines direct current (D.C.) techniques with alternating current (A.C.). By the application of an A.C. perturbation on a D.C. signal, EIS adds the dimension of time to the measurements. Through different A.C. frequency responses of the studied system, it is possible to divide occurring processes on different time scales [133].

This differentiation is based on the phase-shift ϕ between the potential $E(t)$ and the current $I(t)$, according to Eq. (3.1) and (3.2), with the peak potential E_0 , the peak current I_0 and the angular frequency ω , described as a function of the frequency f according to Eq. (3.3) [133].

The different time responses of potential and current then form, similar to Ohm's law, the impedance Z as a function of the angular frequency, as given in Eq. (3.4) [133].

$$E(t) = E_0 \cdot \sin(\omega t) \quad (3.1)$$

$$I(t) = I_0 \cdot \sin(\omega t + \phi) \quad (3.2)$$

$$\omega = 2\pi f \quad (3.3)$$

$$Z(\omega) = \frac{E(t)}{I(t)} = \frac{E_0 \cdot \sin(\omega t)}{I_0 \cdot \sin(\omega t + \phi)} \quad (3.4)$$

The impedance is defined as a complex number, which can be described by a real part Z_{Re} and an imaginary part Z_{Im} (Eq. (3.5)). In the complex plane, as shown in Fig. 3.1 (left), the real and the imaginary part of the impedance can be described by the modulus $|Z|$ of the impedance, following Eq. (3.6) and (3.7) [133].

$$Z(\omega) = Z_{Re} + j \cdot Z_{Im} \quad (3.5)$$

$$Z_{Re} = |Z| \cdot \cos(\phi) \quad (3.6)$$

$$Z_{Im} = |Z| \cdot \sin(\phi) \quad (3.7)$$

The modulus of the impedance defines the length of the impedance vector. Therefore, it is possible to write it according to Eq. (3.8). The frequency dependent differentiating time responses of the impedance are gathered from the perturbing A.C. signals, which result in Lissajous curves as illustrated in Fig. 3.1 (right). The amplitudes of the ordinate and the abscissa in a Lissajous curve define the modulus of the impedance, while the tilt-angle of the ellipse defines the phase-shift [133].

$$|Z| = \sqrt{(Z_{Re})^2 + (Z_{Im})^2} \quad (3.8)$$

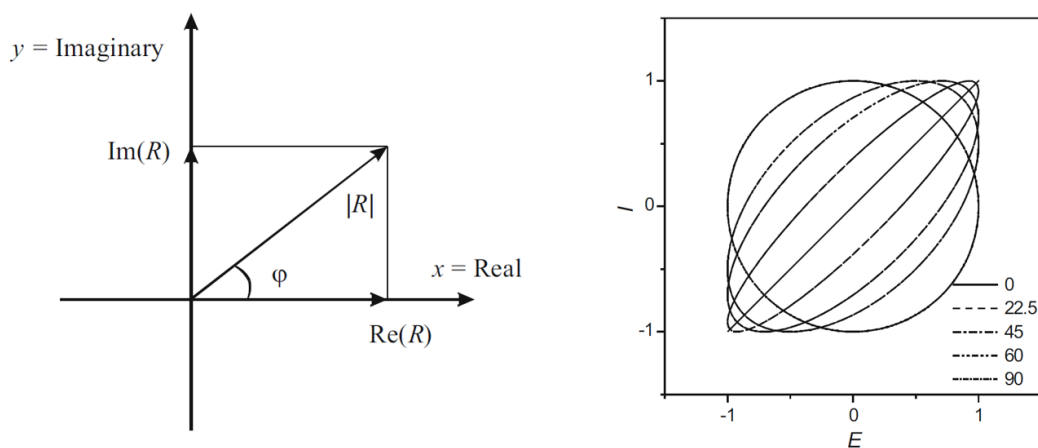


Fig. 3.1: Left: Illustrating the correlation of the imaginary and real part of impedance by a vector R and its modulus $|R|$ in the complex plane. Reproduced from [133]. Right: The Lissajous curves. The A.C. perturbation results in different degrees (shown on the bottom right) of the phase-shift between current and voltage. The Lissajous curve represents the modulus of the impedance by the axes-amplitudes, and the phase-shift by the tilt-angle of the ellipse. Reproduced from [133].

The resulting values of impedance spectroscopy, the real part, the imaginary part, the phase-shift and the frequency of the A.C. signal, can be plotted in different ways. A three-dimensional impedance plotting, as shown in Fig. 3.2, reveals the affiliations between Z_{Im} , Z_{Re} , and f . It is important to note that impedance plotting requires equal scaling for the real and imaginary part of the impedance. Most commonly, impedance plots are two-dimensional. The two-dimensional correlation between the negative imaginary part and the real part is known as Nyquist plot. Nyquist plots do not represent the corresponding frequency, which can be a necessary detail in analyses. This obstacle can be amended by adding frequency notations to the respective measurement points, or by additional plotting of the correlation of the imaginary part of impedance over the logarithm of the frequency [133].

Analyzing impedance plots requires modeling with equivalent electrical circuits. Therefore, it is necessary to understand the mechanisms of the investigated system, as it is otherwise possible to fit any kind of equivalent circuit to the obtained impedance data, which leads to misinterpretations. The most common elements for equivalent models are a resistor R , a capacitor C , a constant-phase element (CPE) Q_0 , an inductor L , and a Warburg element Z_W [133].

Equivalent circuits are either displayed as shown in Fig. 3.3, or written in Boukamp notation. A series connection is denoted as e.g. RC, while parentheses show a parallel connection, e.g. (RC). The combination, e.g. a resistor in series to a parallel connection of a resistor and a capacitor, is denoted as a combination, such as R(RC) [133].

A resistor is an element, which only consists of a frequency independent real part of the impedance. A capacitor reflects electrolytic double layers in the electrode-electrolyte interface. Electrochemical systems often show a deviation from a perfect capacitive behavior, which is caused by, for instance, impurities or side-reactions. The electrode capacitance is replaced by a constant-phase element (CPE) Q_0 , with the dimensionless exponent n . Q_0 can then be used to calculate an equivalent double layer capacity C_{eq} , with two subdivisions for blocking and non-blocking electrodes. An inductor induces a magnetic field, which causes a positive imaginary impedance. Thus, neglecting inductive aspects can lead to wrong interpretations of EIS spectra. Diffusion can influence the impedance results as well, as diffusion limitations inhibit the electron transfer between the electrode and the redox active species. The prevalent situation is described by a semi-infinite linear diffusion, represented by

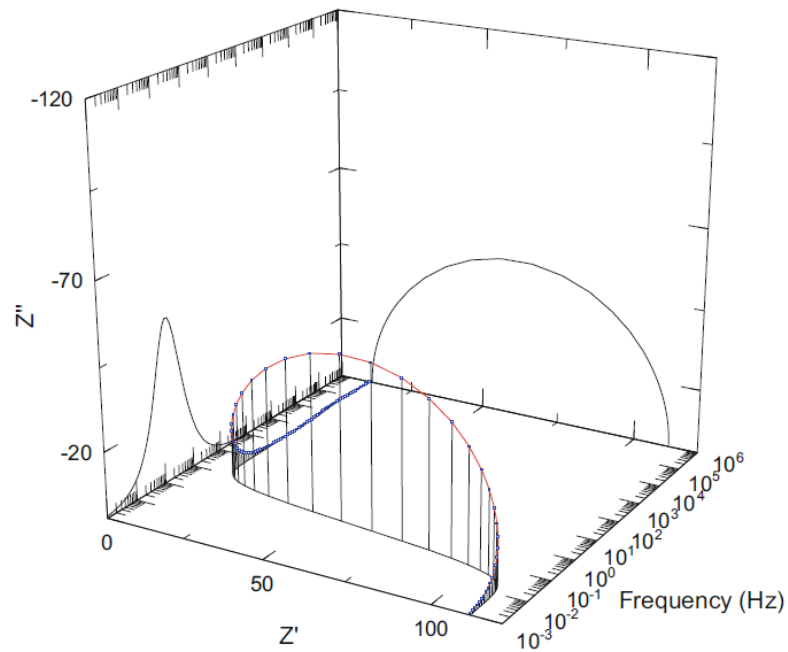


Fig. 3.2: The three-dimensional plotting of impedance. Z' represents the real part of the impedance Z_{Re} , Z'' the imaginary part Z_{Im} . The two-dimensional plot Z'' over Z' is known as Nyquist-plot. Reproduced from [133].

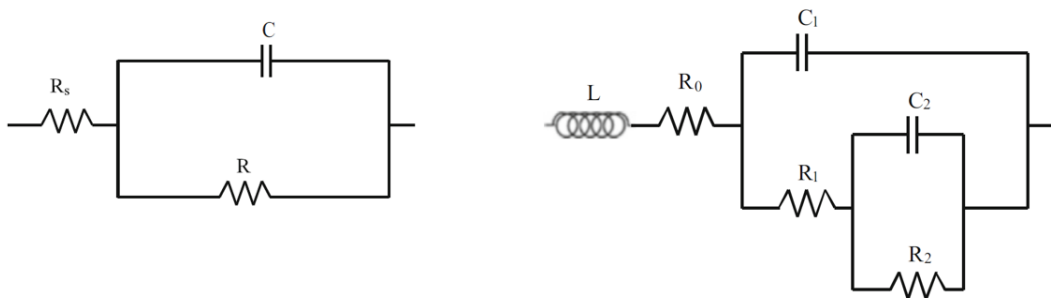


Fig. 3.3: Left: Electric circuit model with two resistance and one capacitive element, denoted as $R_s(RC)$ in Boukamp notation. Reproduced from [133]. Right: Electric circuit model considering an inductive impedance, three resistive and two capacitive contributions, denoted as $LR_0(C_1(R_1(R_2C_2)))$ in Boukamp notation. Reproduced from [133].

a Warburg element Z_W . The above described circuit elements and their impedance functions, as well as the equivalent capacity functions for the CPE, are summarized in Tab. 3.1 [133].

Impedance elements produce a distribution of time constants. It is therefore possible to obtain knowledge about the time-dependence of processes without fitting the impedance. The process, which is called distribution of relaxation times (DRT), calculates the time constant distribution function of impedance. Plots in relation to the measurement frequency thereby allow to deduct processes or changes in such [133].

Tab. 3.1: Elements for equivalent electric circuits and their impedance function and equivalent/coefficient functions. Reproduced from [133].

element/equivalent/ coefficient	symbol	function
resistor	R	$Z_R(\omega) = R$ (3.9)
capacitor	C	$Z_C(\omega) = \frac{1}{j\omega C}$ (3.10)
constant-phase element	Q_0	$Z_Q(\omega) = \frac{1}{(j\omega)^n \cdot Q_0}$ (3.11)
equivalent capacity (blocking electrode)	C_{eq}	$C_{eq} = Q_0^{1/n} \cdot \left(\frac{1}{R_s}\right)^{(1-1/n)}$ (3.12)
equivalent capacity (non-blocking electrode)	C_{eq}	$C_{eq} = Q_0^{1/n} \cdot \left(\frac{1}{R_s} + \frac{1}{R_{ct}}\right)^{1-1/n}$ (3.13)
inductor	L	$Z_L(\omega) = j\omega L$ (3.14)
Warburg impedance	Z_W	$Z_W(\omega) = \frac{\sigma}{\sqrt{\omega}} + \frac{\sigma}{j \cdot \sqrt{\omega}}$ (3.15)
Warburg coefficient	σ	$\sigma = \frac{RT}{z^2 F^2 A \sqrt{2}} \cdot \left(\frac{1}{D_{ox}^{1/2} \cdot c_{ox}^*} + \frac{1}{D_{red}^{1/2} \cdot c_{red}^*} \right)$ (3.16)

3.2 Cyclic voltammetry

Besides EIS, another time-resolved technique is based on the relation between current and electrode potential. In this three dimensional correlation, the potential of an electrode is varied linearly and the resulting current is measured. This process, called linear sweep voltammetry (LSV), aims to gradually increase the electrode potential from more negative values where no faradaic reactions occur towards and above E^0 of a redox process. Due to the changing concentration of the redox active species with increasing potential, eventually reaching depletion above E^0 , a peaked current-potential correlation is obtained. The potential at the peak is the peak potential E_p , which is linked but not necessarily congruent to E^0 . The current density at the peak i_p can be described with Eq. (3.17), where D is the diffusion coefficient and C the concentration of the redox species, and ν is the scan rate of the potential per time unit [11].

When the potential scan is reversed, the opposite process takes place if the electrochemical reaction is reversible. The concentration of the species gradually increases and eventually reaches the initial value, which gives rise to a peaked current-potential correlation similar to the first process but with reversed current flow. This repeating process is known as cyclic voltammetry (CV). The evolution of the electrode potential with time and the correlated CV, which essentially are two dimensional planes in the three dimensional correlation i - t - E , are shown in Fig. 3.4 [11].

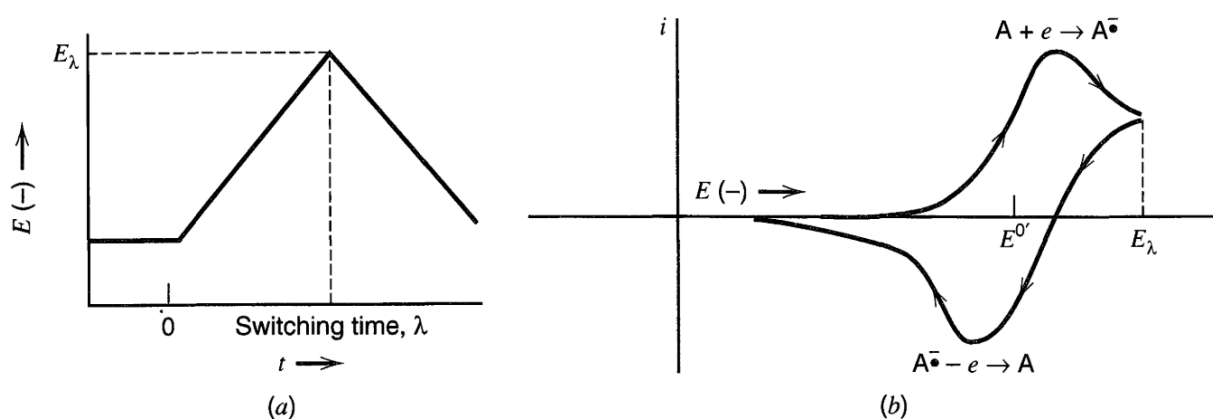


Fig. 3.4: (a): Cyclic sweeping of the electrode potential with time. (b): Resulting cyclic voltammogram as current over electrode potential. Reproduced from [11].

Noteworthy, CVs start in the non-faradaic region. Since no electrochemical reactions take place at these electrode potentials, the charging of the double layer can be observed. The linear correlation between the charging current density i_c , the electrode area A , and the scan rate ν , which follows Eq. (3.18), is often applied to measure the double layer capacitance C_{dl} in the non-faradaic region. By varying the scan rate and plotting the obtained charging currents over the scan rate, the double layer capacitance is obtained through a linear fit [11].

$$i_p = 0.4463 \cdot \left(\frac{F^3}{RT} \right)^{1/2} z^{3/2} AD^{1/2} C^* \nu^{1/2} \quad (3.17)$$

$$|i_c| = AC_{dl}\nu \quad (3.18)$$

3.3 Scanning electron microscope and electron dispersive X-ray spectroscopy

In scanning electron microscope (SEM) a beam of electrons, which is generated by an electron gun, is focused onto a sample surface. However, the electron beam interacts with the sample deeper than the surface and thus creates an interaction volume. The emitted electrons from the sample are detected with various types of detectors to generate a high resolution image. The magnification of the image is greater than for a light microscope. The type of the detector depends on the type of emitted electrons from the sample [134].

When the electrons from the sample scatter into the same direction as the incoming electrons of the electron gun, one speaks of backscattered electrons. The amount of backscattered electrons correlate with the atomic mass of the sample. Hence, the contrast of the obtained image reflects relations between different atoms of the sample, where atoms with higher mass are brighter. A second type of electrons emitted from the surface are secondary electrons. These are spontaneously given off surface atoms interacting with the electron beam. As the edges of a sample are the predominant emitters of secondary electrons, the obtained image gives a topological and morphological overview of the sample [134].

Another spectroscopic technique that is generally combined with SEM is electron dispersive X-ray spectroscopy (EDS). The sample surface exposed to the electron beam gives off electrons as well as element-characteristic X-rays. The energy of these X-rays can be analyzed to correlate them to element-characteristic wavelengths and thereby allows to

determine which and in which quantity to another elements are present within the interaction volume of the electron beam [134].

In this work, SEM and EDS are conducted with a Zeiss Ultra microscope and a Bruker EDS detector. EDS was analyzed with the software Bruker Esprit 2.1.

3.4 Raman spectroscopy

The energy E of a radiation depends on its frequency f following the Planck-Einstein relation with Planck's constant h according to Eq. (3.19).

$$E = h \cdot f \tag{3.19}$$

When a radiation is focused on a sample, the energy of the radiation can excite the sample to the electronic state. However, the sample can further be excited from the ground state to a virtual vibrational state, which is below the electronic state. The light predominantly scatters back from the virtual state to the ground state, which is known as Rayleigh scattering. However, a part (of about 10^{-8}) of the light scatters back to a higher ground state, giving rise to a frequency shift of the photons, which is denoted as Stokes scattering. Consequentially, Stokes scattering is accompanied by an energy loss causing a red-shift. When the sample is at the higher ground state prior to radiation-exposure and scatters back to the nominal ground state, Anti Stokes scattering occurs. Anti Stokes scattering causes a blue-shift, but is less pronounced than Stokes scattering. This is especially the case at room temperature, as the probability of higher ground states is a function of the temperature. The effect of an observable frequency shift was first described by Raman and Krishnan in 1928 and was named Raman scattering [135, 136]. The correlation between the ground state, the virtual state, the electronic state and the energy of incoming photons is shown in Fig. 3.5.

Raman scattering is characteristic for chemical bonds in the surface of a sample. The requirement for a Raman active vibration is the polarizability of a sample through the induction of a dipole moment P . The excitation with light needs to distort the electronic nature of the sample, which causes the development of the dipole. With a polarization tensor $\nabla\alpha$ and an electric field E , the polarization of a sample can be obtained with Eq. (3.20).

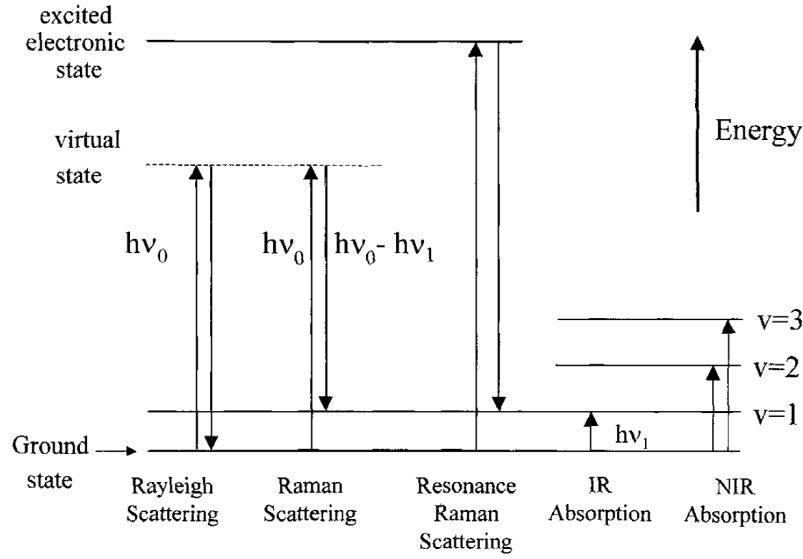


Fig. 3.5: Correlation between the energy of incoming photons, the excited electronic state and the virtual state. Reproduced from [136].

The polarization tensor can be a source of Raman activity if one or more of the nine elements of the tensor experience a change [136].

$$\vec{P} = \begin{bmatrix} \alpha_{xx} & \alpha_{xy} & \alpha_{xz} \\ \alpha_{yx} & \alpha_{yy} & \alpha_{yz} \\ \alpha_{zx} & \alpha_{zy} & \alpha_{zz} \end{bmatrix} \cdot \vec{E} \quad (3.20)$$

One challenge in Raman spectroscopy is fluorescence. When the photons reach the electronic state, the emitted fluorescence from the reversal to the ground state is at higher intensity than Raman scattering. As a consequence, the intensity of the Raman vibrations are overlapped by fluorescence. Hence, the chosen source of radiation has to match with the energy required for the vibrational states while simultaneously being too small for the excitement of the electronic state. The chosen sources of radiation are monochromatic light sources realized with lasers [136].

In this work, Raman spectroscopy is conducted with a Renishaw InVia Raman spectrometer and a 100 mW / 532 nm green laser.

3.5 X-ray diffraction

The crystal structure of a material is analyzed by X-ray diffraction (XRD). The sample is probed with a monochromatic X-ray beam and the amount of reflected or transmitted photons from the sample is detected as a function of the incidence and the reflection angle. This occurs either by varying the X-ray source and the detector angles (Θ – 2Θ scan or Bragg-Brentano scan) or with a fixed incidence angle and a moving detector (grazing incidence X-ray diffraction (GIXRD)). For XRD measurements of powders, the sample is often rotated to increase the statistical variability [137].

The emitted photons form constructive interference when the measurement-angle meets Bragg's law, as given by Eq. (3.21). The plane spacing is represented by d_{hkl} , the X-ray angle by Θ_{hkl} , the wavelength of the X-ray source by λ , and the integer number describing the order of the reflection by n [137].

$$2d_{hkl} \cdot \sin(\Theta_{hkl}) = n\lambda \quad (3.21)$$

The analysis of crystal structures is based on the Miller indices (hkl) as well as the interplanar spacing d and the lattice parameters a , b , c , α , β , γ . Their correlation irrespective of the type of unit cell is shown in Eq. (3.22) and (3.23) [137].

$$d_{hkl} = \frac{1}{|ha^* + kb^* + lc^*|} \quad (3.22)$$

$$\begin{aligned} |ha^* + kb^* + lc^*|^2 &= h^2 a^{*2} + k^2 b^{*2} + l^2 c^{*2} \\ &+ 2klb^*c^* \cos(\alpha^*) + 2lhc^*a^* \cos(\beta^*) + 2hka^*b^* \cos(\gamma^*) \end{aligned} \quad (3.23)$$

For a monoclinic structure, where $\alpha^* = \alpha = 90^\circ$ and $\gamma^* = \gamma = 90^\circ$ and $\beta^* = 180^\circ - \beta$, the calculation of the unit cell parameters shortens to Eq. (3.24). For planes of the $00l$ direction, it simplifies to Eq. (3.25) [137].

$$d_{hkl}^2 = \frac{1}{h^2 a^{*2} + k^2 b^{*2} + l^2 c^{*2} + 2lhc^*a^* \cos(\beta^*)} \quad (3.24)$$

$$d_{00l} = \frac{c \sin(\beta)}{l} \quad (3.25)$$

XRD measurements require an optimal alignment of the sample to the X-ray beam. If the sample-height does not match with the calibrated spot for the beam, a tilting of the peak positions in the XRD patterns is observed. This shift can be corrected using a certain peak position of the sample material, the resulting offset $\Delta 2\Theta$ and the geometry of the diffractometer s and R following Eq. (3.26) [137].

$$\Delta 2\Theta = -\frac{2s \cdot \cos(\Theta)}{R} \quad (3.26)$$

In this work, powder XRD is conducted with a Rigaku Miniflex diffractometer and Bragg-Brentano as well as GIXRD on solid samples with a Rigaku Smartlab diffractometer. For both, a Cu $K\alpha$ anode serves as the X-ray source.

3.6 X-ray photoelectron spectroscopy

X-ray photoelectron spectroscopy (XPS) studies the outer atomic layers of a sample. Monochromatic X-rays are focused on the sample, which induces the emission of electrons from it. These electrons are collected and selected over a hemisphere electron analyzer as a function of their energy. The measured kinetic energy KE of the emitted electrons is related to the energy of the incidence X-rays $h\nu$, the work function of the spectrometer ϕ , and to the binding energy BE following Eq. (3.27). The binding energy is quantified by the type of element, the orbital and the chemical environment. Since these correlations are element-specific, XPS delivers the atomic composition as well as the chemical state of the sample-surface. The greatest disadvantage of XPS is the need for ultra high vacuum due to the interaction of photoelectrons with gasses, which limits possible applications [138].

$$KE = h\nu - BE - \phi \quad (3.27)$$

In this work, a ThermoFisher Escalab 250 Xi spectrometer with an Al $K\alpha$ X-ray source is used for XPS. The measurements are analyzed with the software CasaXPS and a Shirley model. All binding energies were referenced to the Au 4f peak at 84.0 eV.

3.7 Testing setups

The electrochemical tests are conducted in two different setups described in this section. For the spectroelectrochemical tests, a homebuilt setup described in Chap. 4 is used.

For all measurements, the electrolyte is pre-electrolyzed between two nickel wires at a polarization of 1.8 V for 16 – 20 h. The wires are removed from the electrolyte without removing the potential to keep deposited impurities on the electrodes.

All electrolyte contacting materials in the setups applied in this work are made of polytetrafluorethylen (PTFE), polyether ether keton (PEEK), perfluoroalkoxy alkane (PFA), or ethylene propylene diene monomer rubber (EPDM). These are well-known corrosion resistant polymers, which are, in contrast to glass, not polluting alkaline solutions [139].

3.7.1 The FlexCell

The electrocatalysts were tested in a three-electrode configuration made of PTFE. The cell house, which was purchased from Gaskatel, is constructed in a three-compartment filterpress-configuration. The working electrode compartment was replaced by a homemade PTFE-compartment, which allows to heat up the compartment with six heating elements connected to a heating controller. The compartments are sealed with EPDM sealings to another. The working electrode compartment, with a circular electrode area of $A = 3.14 \text{ cm}^2$, and the counter electrode compartment are separated by a Zirfon separator to avoid gas-crossover.

A coiled nickel-wire serves as the counter electrode. Platinum, as often reported in the literature as counter electrode, was excluded as counter electrode material for the measurement of nickel-based working electrodes. It is known that high oxidation potentials on platinum can pollute alkaline electrolytes and thus overestimate kinetic measurements [139]. Nickel, on the other hand, is known to be an alkaline stable material [76]. The reference electrode is a commercial reversible hydrogen electrode (RHE), which was purchased from Gaskatel.

The FlexCell setup, as shown in Fig. 3.6, was placed in a protective housing, which is inertized by nitrogen to avoid the influence of oxygen from air intake.

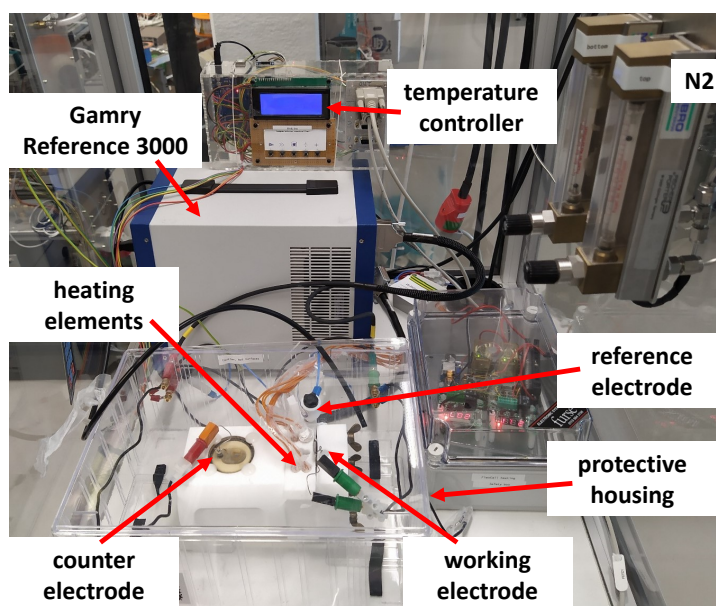


Fig. 3.6: The electrocatalyst testing setup FlexCell at DTU Energy. The cellhouse, made of PTFE, is placed in a nitrogen flushed protective housing.

3.7.2 Zero-gap electrolyzer

Electrode testing was carried out in a flowcell setup illustrated in Fig. 3.7, which was described previously [140].

The cell is made of nickel with an active circular electrode area of $A = 10 \text{ cm}^2$. The electrodes are pressed together with a Zirfon separator in a zero-gap geometry, which resembles a unit alike but not identical to a membrane-electrode-assembly (MEA). Both electrodes rest on flow fields, which are electrically connected to the cell bodies, where the connections to a DC power supply and to potentiostats are made. The cell bodies are heated with heating elements and are held together with M8 bolts and two steel endplates, which are electrically insulated from the cell bodies. All sealings are made of PTFE and vary in thickness to match with the thickness of the MEA-type unit.

The electrolyte is pumped via PFA tubes through both sides from and back to two PTFE reservoirs, which further serve as gas-liquid separators. The cathode side has the possibility to add water during a test. For a sufficient concentration equilibration of the electrolyte, both reservoirs are connected with an on-off hand valve. At both electrolyte-inlets to the cell, a mini RHE, which was purchased from Gaskatel, is mounted facing the backside of the electrodes.

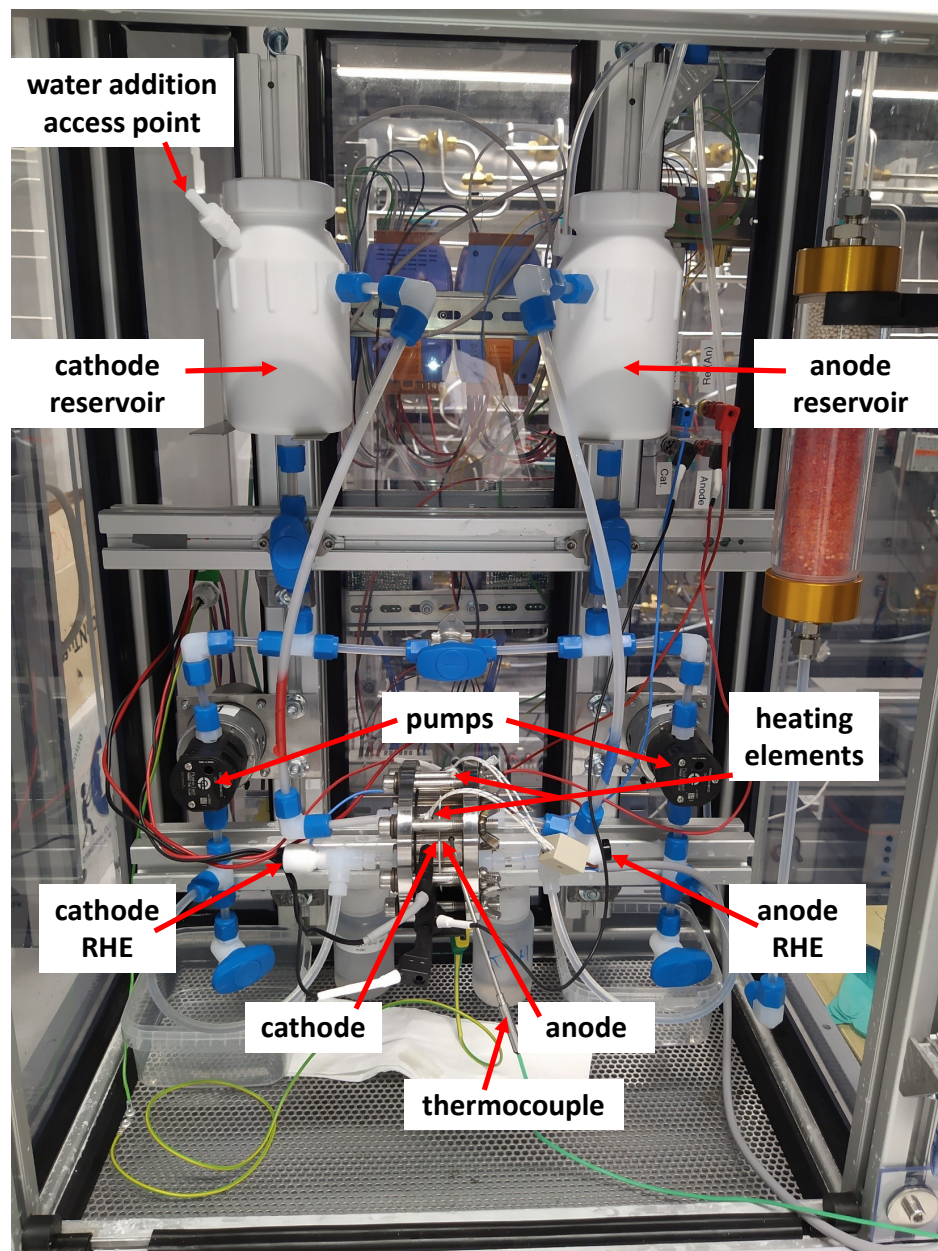


Fig. 3.7: The laboratory flowcell setup at DTU Energy. The cathode (left side) and anode (right side) have an active area of 10 cm^2 . The electrolyte is circulated on both sides through pumps from a reservoir through the cell. The reservoirs serve as gas/liquid-separators. A mini RHE reference electrode is mounted at the electrolyte-inlet of both sides.

Chapter 4

Development of a spectroelectrochemical cell for Raman spectroscopy and X-ray analysis techniques

This chapter illustrates the development of the testing setup for spectroelectrochemical measurements with liquid electrolyte, which is capable of working under operando conditions at strong pH and at elevated temperatures. Starting with the requirements and an overview of some published setups in the literature, the chapter leads from non-working approaches over to the final setup. In order to simplify communication, the final setup was given the name "Florian's cell for liquid Spectroelectrochemistry", in short *FeliS*. The drawings for reproducing the final spectroelectrochemical cell are added to the appendices in Chap. A.

4.1 Stipulations for a spectroelectrochemical cell with liquid electrolyte at strong pH and high polarizations

Spectroelectrochemistry is the combination of two worlds, which each have their specific requirements for a successful measurement. Accordingly, a spectroelectrochemical setup has to satisfy several stipulations.

As a general demand towards such a setup, it has to be granted that the electrocatalyst-measurements reflect real operating conditions. As such, it is of importance

that the electrocatalyst in the setup does not suffer from pollution, poor potential distribution or inadequate wetting. Furthermore, single electrode potentials have to be acquired by a reference electrode. To avoid electrolyte polarization and to ease potentiostatic operation, the series resistance should be comparably low, which is, based on practical experience, $5\ \Omega\text{cm}^2$ at maximum. From a user point of view, it is desirable that the setup is not limited to any spectroscopic instrument, and can be used with electrolyte flow and heating to resemble real operating conditions at best.

An overview of these stipulations is given in Tab. 4.1. Although the setup should satisfy all these conditions, a sub-priority is given to the electrolyte flow and the heating. A stationary application at room temperature, at least in an initial state of the setup, is deemed sufficient for the purpose of this work. Nevertheless, the setup should prospectively be capable of working with both.

Tab. 4.1: Summarized stipulations for the spectroelectrochemical cell.

No.	stipulation
1	agreement between electrocatalyst testing and spectroelectrochemical samples
2	no electrocatalyst pollution (e.g. from window materials) through electrolyte resistant materials
3	homogeneous potential distribution over the working electrode
4	reliable wetting of the working electrode
6	stable and consistent wetting film on the electrocatalyst
7	three-electrode configuration with low series resistance
8	accessibility for in- and outgoing radiation from lab scale instruments
9	versatility for the application with different spectroscopic techniques
10	optional possibility for electrolyte flow
11	optional possibility to heat

4.2 Setups published in the literature

As a starting point for building a spectroelectrochemical setup, a summary of published setups in the literature will be presented in this section. These setups have been applied for several techniques, such as XPS, XRD (including synchrotron applications), and Raman. The overview of such setups serves as an important guidance for a self-built setup, which combines X-ray based techniques and Raman within a single spectroelectrochemical setup.

A compilation of a choice of different setups, illustrated in Fig. 4.1 and summarized in Tab. 4.2, may not represent every concept that has been followed within the literature. Nevertheless, the choice represents a broad range of and preponderantly applied approaches for X-ray based techniques and Raman spectroscopy.

The first concept relies on a thin electrolyte film. As shown in Fig. 4.1A, the working electrode is covered with a thin electrolyte film by the dip-and-pull technique. The surface of the working electrode is spectroscopically analyzed from its backside. Similarly to this reflective method, a transmissive method with a thin reaction chamber was realized in Fig. 4.1C. The advantage of the dip-and-pull technique is the absence of disrupting window materials, while the technique itself requires high precision to ensure a constant electrolyte film. The transmissive concept secures a constant wetting of the working electrode. On the other hand, the use of window materials and the amount of electrolyte can negatively influence the transmitted signal. Furthermore, an electrolyte resistant window, which neither pollutes the electrolyte nor goes blind by it, is a major challenge, especially with concentrated KOH.

The thin electrolyte film concept can also be found in concepts Fig. 4.1E, Fig. 4.1G, and Fig. 4.1H. All three concepts are based on reflective radiation and the use of window materials, but differ in the placement of the counter electrode. In Fig. 4.1E, the sample is probed from the backside of the electrode, while Fig. 4.1G and Fig. 4.1H probe the frontside. Due to the placement of the counter electrode, it is questionable if the potential over the working electrode is equally distributed in Fig. 4.1G. Among these concepts, Fig. 4.1H appears to provide the most reliable working electrode potential by probing through, or rather in between, the counter electrode. However, all three concepts are based on electrolyte-contacting windows, which might pose a challenge in respect to the handling of evolving gases, if the electrolyte flow across the working electrode is improper.

For operando Raman measurements, the literature principally divides into two con-

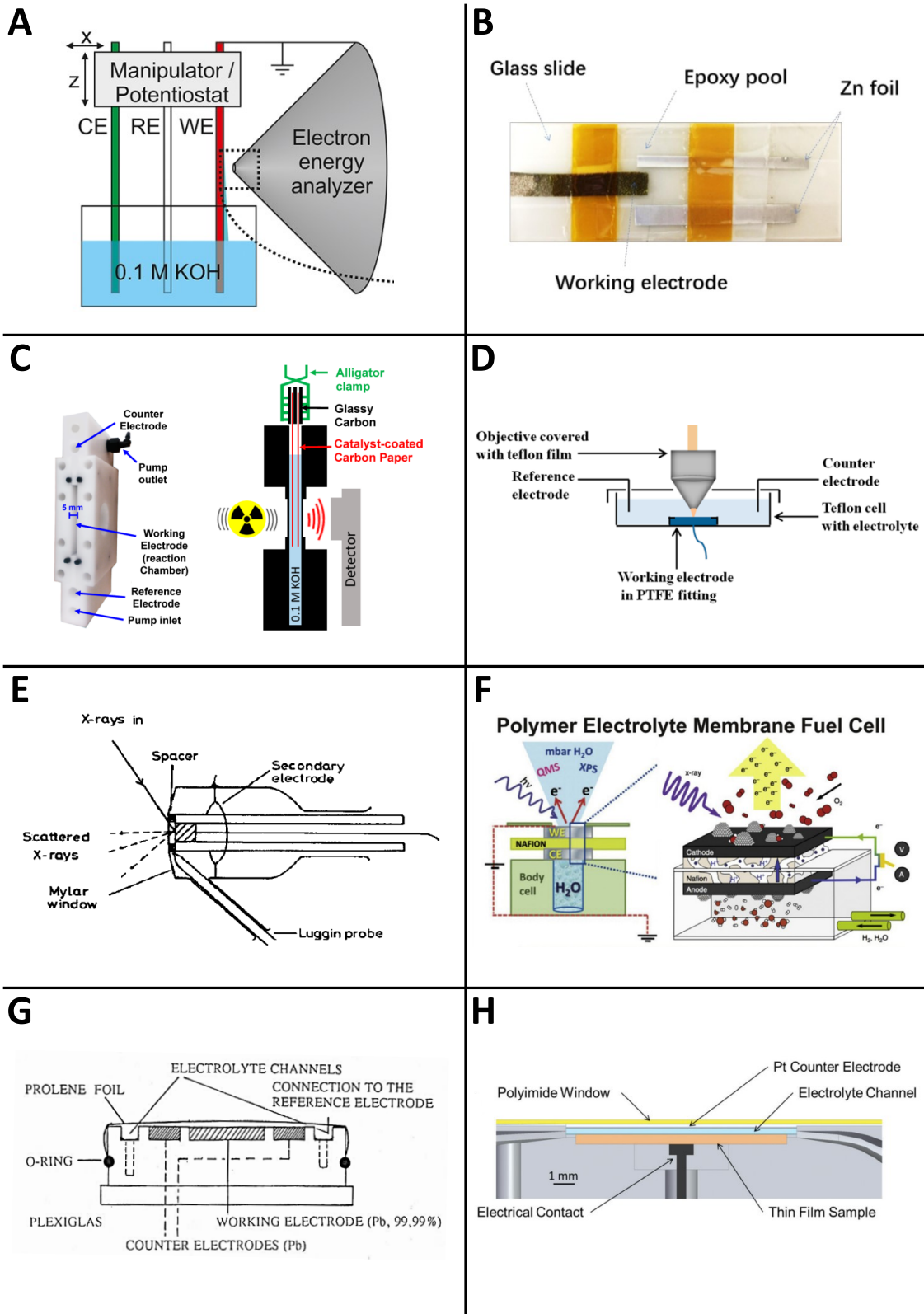


Fig. 4.1: A choice of setups for different spectroelectrochemical approaches published in the literature. See Tab. 4.2 for description and references.

Tab. 4.2: A choice of setups published in the literature and represented in Fig. 4.1.

No.	technique	concept	source
A	XPS	dip and pull; thin-electrolyte film	[29]
B	Raman	epoxy-pool with glass slide	[141]
C	Moessbauer	window-covered chamber for transmissive radiation	[142]
D	Raman	water-immersion lens	[143]
E	XRD	window-covered working electrode	[144]
F	XPS	backside window-free approach	[145]
G	XRD	window-covered working electrode	[146]
H	XRD/XAS	window-covered working electrode	[147]

cepts. One of these approaches is a reaction pool, as illustrated in Fig. 4.1B. The three electrodes and the electrolyte are sealed together by epoxy within Raman-inactive windows. The greatest disadvantages are the use of epoxy and electrolyte-contacting windows, which have to prove to be non-polluting, as well as the open question about the influence of evolving gasses and their removal from the system. A more reliable approach is shown in Fig. 4.1D. The objective is probing the working electrode surface through the counter electrode. The electrode-wetting is secured by the submersion into an electrolyte bath. However, this approach works best with a water-immersion lens, which was not available in this work. Furthermore, this approach is not applicable for X-ray based techniques.

Another technique for operando probing of fuel cells is shown in Fig. 4.1F. A fuel cell is probed on the working electrode backside by X-rays. Since this concept was developed for a fuel cell, the electrolyte in this concept is immobilized. Hence, electrolyte-handling may not be an issue for a fuel cell, but certainly could be for an electrolyzer cell, which is not operated in gas diffusion mode. Thus, the concept needs to be advanced.

In summary, in literature published setups usually display a thin electrolyte film concept for reflective radiation, electrolyte immersed reaction chambers for transmissive radiation and Raman spectroscopy, as well as an open concept from the backside of the working electrode. For the development of the own spectroelectrochemical setup, these concepts are taken as guidance. Nonetheless, especially the use of window materials is challenging. Within the self-developed setup, window materials, notably glass, are intended to be circumvented

to the greatest extent possible. The stability towards 11.6 M KOH at room temperature, and especially at elevated temperatures, the possible trapping of evolved gases, considerable challenges towards sealing, and measurement-interferences pose the objective to design a windowless spectroelectrochemical setup.

4.3 Approaches towards spectroelectrochemistry in alkaline electrolyte

Approach 1

The first approach aims to produce a three-electrode setup established on a windowless thin electrolyte film concept. Working and counter electrode are connected via a 2 mm diameter electrolyte channel, which is further in connection to the reference electrode and an inlet to replenish the electrolyte. The realization, which can be seen in Fig. 4.2, was conducted by two 1/16" PEEK T-fittings. The working electrode, which is a foil, openly presents a 5 mm · 5 mm surface, which can be probed with reflective X-rays, or with lasers perpendicularly for Raman spectroscopy. However, although an electrolyte film can be stabilized within stationary operation, a film of constant thickness could not be obtained with replenishing electrolyte. As electrolyte was consumed in the stationary approach, which caused fractions of the electrode to dry, replenishing was inevitable. Further, thin enough electrolyte films to avoid excessive X-ray absorption were another challenge, at least when a windowless approach is followed. For electrochemical measurements, the inconsistent wetting of the electrode's surface caused unstable measurements, which were further characterized by high series resistances in the k Ω scale. In short, this open concept approach was found to be impractical.

Approach 2

Since the fully open concept with a foil working electrode appeared problematic, an electrolyte immersed setup, which is illustrated in Fig. 4.3, was tried. Within this approach, which was also based on two T-fittings, working and counter electrode are wires, which are perspectivevely covered with electrocatalyst. The working electrode wire is additionally covered with PTFE outside the working electrode area, which ensures its consistency. Previously, a 2 mm diameter electrolyte channel displayed a series resistance in the k Ω scale.

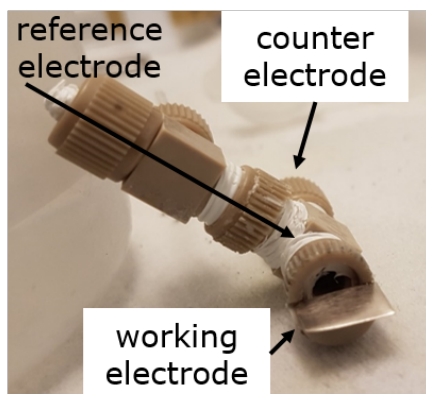


Fig. 4.2: The first approach towards spectroelectrochemistry with a 2 mm inner diameter PEEK T-fitting. The working electrode is a 5 mm by 5 mm platinum foil.

As a consequence, approach 2 was conducted with 4 mm diameter tubes. The transparent PFA material would allow for transmissive radiation. However, this approach changed from a desired open concept to a window-concept, which would interfere with the signal intensity and appear in the obtained measurements.

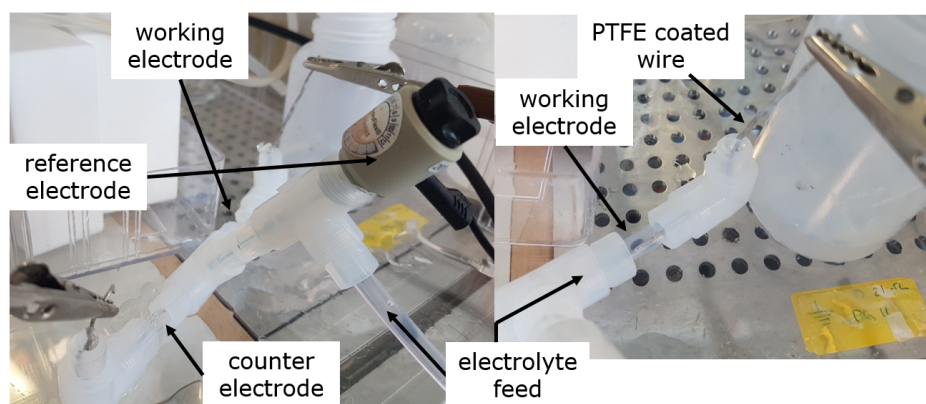


Fig. 4.3: The second approach towards spectroelectrochemistry with a 4 mm inner diameter PFA T-fitting and electrolyte flow. The working and counter electrodes are 1 mm round platinum wires.

From an electrochemical perspective, the electrolyte immersion resulted in stable measurements. Fig. 4.4 represents the electrochemical impedance spectroscopy at OCV and at -200 mV vs RHE (iR -uncorrected), and the resulting iR -compensated and uncompensated iV -curves at 20 mV/s. The EIS spectra display two semicircles, which can be ascribed to a transmission-line behavior (high frequency) and the electrode capacity (low frequency).

This assumption relies on the similarity of the high frequency arcs between OCV and overpotential, and the typical capacitive behavior of the second arc. A mass transport effect cannot be seen, and could further be excluded as a result of the constant electrolyte flow of this concept.

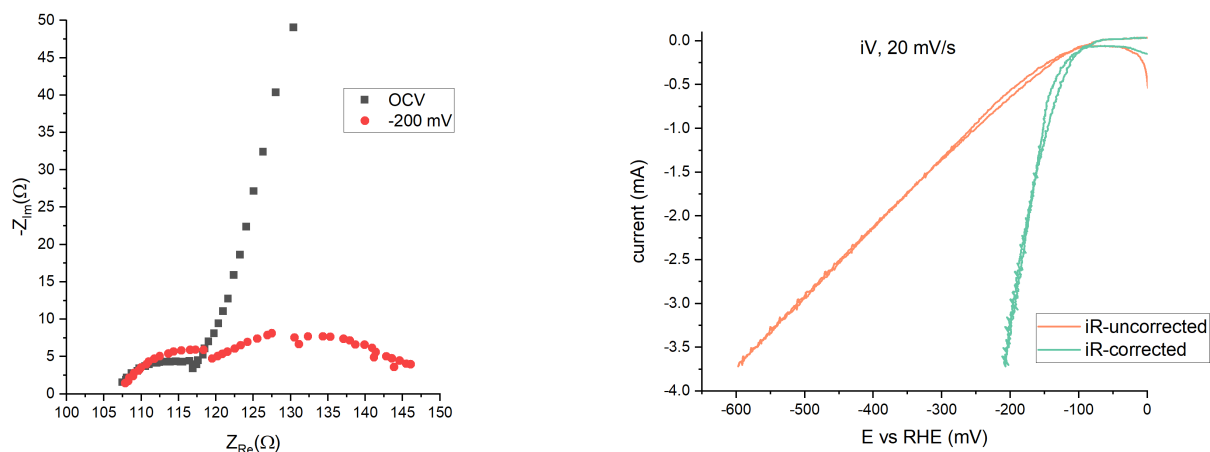


Fig. 4.4: Left: Electrochemical impedance spectra at OCV (20 kHz–10 Hz) and at 200 mV HER overpotential (20 kHz–0.8 Hz), iR -uncorrected, of a platinum wire ($A \approx 0.3 \text{ cm}^2$) used in approach 2. Right: iV -curve at 20 mV/s of a platinum wire used in approach 2, iR -uncorrected and corrected considering an $R_s \approx 105 \Omega$. Measurements at room temperature in 1 M KOH.

Although this approach seems to be successful at first glance, the high series resistance of $\approx 105 \Omega$, which is about $31 \Omega \text{ cm}^2$, is more than sixfold above the self-set target of $5 \Omega \text{ cm}^2$. In addition, the thickness of the 4 mm tube and the resulting amount of electrolyte may work with Raman spectroscopy, but X-ray based techniques would probably need the high energy source of a synchrotron. Therefore, this approach was not followed any further for the lab scale measurements.

Approach 3

The first two approaches revealed the practical disadvantages, but also advantages, of open and closed setups. Consequently, when combining the learning points of both, a third setup was designed.

The disadvantages of the open approach were the unreliability of the electrode wetting and the high series resistance. For the closed approach, it was the amount of electrolyte

covering the working electrode, the window-based approach and the high series resistance. Combining the advantages of both, with the thin film of electrolyte in the open setup and the constant electrochemical behavior in the closed setup, approach 3 was designed as illustrated in Fig. 4.5. In order to reduce the series resistance, the gap between working and counter electrode was reduced to the minimum possible. The reference electrode would be placed on the counter electrode side, yet still between both electrodes. Furthermore, the immersion into a bath allows to tune the optimal amount of electrolyte, at which the electrochemical measurements are stable and the loss of signal intensity in the spectroscopic measurements does not amplify.

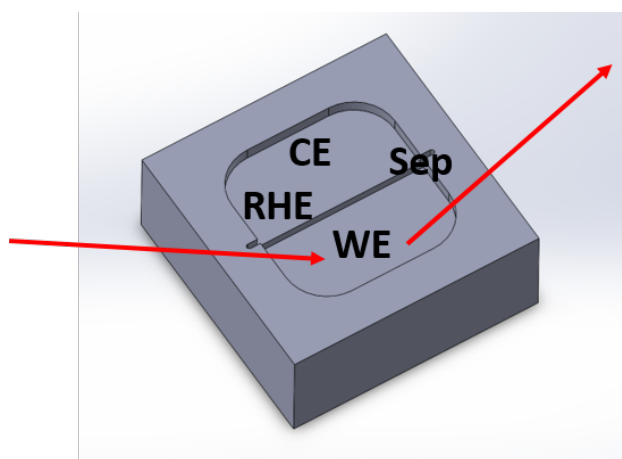


Fig. 4.5: The third approach towards spectroelectrochemistry in alkaline electrolyte. The arrows show the intended path for X-rays. With the intended placements of - WE: working electrode, CE: counter electrode, Sep: separator, RHE: RHE reference electrode.

However, this approach did not exceed the theoretical design stage, although the approach is promising towards solving the previous issues. Due to the fact that the working electrode would have to be of a certain size, a non-negligible potential-distribution alongside the working electrode cannot be excluded. Hence, measurements with X-ray based techniques would probe a larger area of the working electrode, which has an inconsistent and not well-defined electrode potential. Thus, the correlation between spectroscopic and electrochemical results cannot be granted. Nevertheless, this theoretical consideration led to the final approach, which is closer to Fig. 4.1F.

4.4 The inhouse developed, modular, spectroelectrochemical cell FeliS

Previously unsuccessful attempts to build a spectroelectrochemical cell led to the final working approach described in this section. The concept relies on the placement of the working and the counter electrode similar to a standard electrolyzer. Each electrode lies on a separator and the space between these contains an electrolyte chamber, which is connected to a reservoir via a Luggin capillary holding the reference electrode. By tilting the setup into a horizontal position, the working electrode can be probed spectroscopically from its backside.

This approach has several advantages. Due to the symmetrical build, a homogeneous lateral potential distribution over the working electrode is secured at any given current density. Additionally, the usage of two separators, with each electrode facing away from the electrolyte chamber, prevents gas crossover. Hence, side reactions on the working electrode as a result of an insufficient setup design are not expected. A schematic visualization of this concept, which was given the name FeliS, is represented in Fig. 4.6.

One of the greatest challenges of this concept is the principle that ensures the wetting of the working electrode. To enable a stable wetting film on the electrocatalyst of the working electrode, a constant supply of replenishing electrolyte must be present. FeliS relies on the capillary forces of the separator combined with the hydrostatic pressure of the electrolyte reservoir, whose liquid level is above the working electrode, to constantly wet the electrocatalyst. Subsequently, the sample preparation of the working electrode appears to be a crucial point. Working electrode samples are more reliable, if they are as thin as possible. The amount of necessary replenishing electrolyte increases with thickness and tortuosity of the working electrode.

An additional approach to ensure the wetting can be constructed by enabling a flowcell approach, in which electrolyte is pumped over the working electrode. Such an approach has, as a first attempt, not been followed within this work, but the description of the flowcell concept can be found in Chap. 4.5.1. Wetting might as well be ensured through a separator-free approach and an immersed electrode, which would be possible due to the use of a separator with the counter electrode. However, the needed flatness of the working electrode

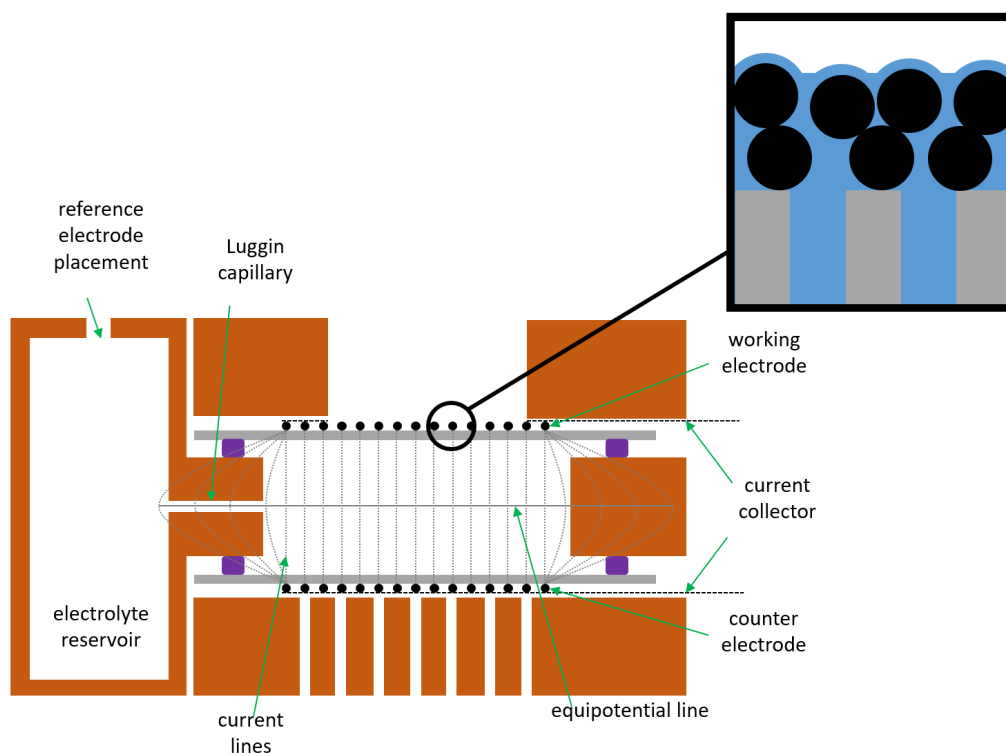


Fig. 4.6: The schematic cross-section of the spectroelectrochemical cell FeliS. In black: electrocatalyst, grey: separator, orange: cell house, purple: electrode sealings, blue: electrolyte. The magnification shows the working principle, which is based on capillary forces. For enhanced visibility, the cross-section is illustrated without electrolyte.

led to abandoning this way in favor of a rigid yttrium-stabilized zirconia (YSZ) separator. This separator has previously proven to work with gas diffusion electrodes [148, 149].

Another advantage of thin working electrodes, with a single electrocatalyst layer at best, is the prevention of a potential distribution across the thickness of the working electrode. The electrocatalyst's potential is probed and controlled from the frontside, which is facing the counter electrode, while the spectroscopic probing is done from the backside of the working electrode. Correspondingly, the working electrode sample must have a negligibly small potential distribution across its thickness, which assures the congruency between electrochemical and spectroscopic measurements.

Additional strengths of this concept stem from the sandwich-like system of FeliS. The working electrode lid is replaceable and adjustable, which allows to accommodate the necessities of different spectroscopic techniques, while the electrochemistry is unaffected.

CAD drawings of FeliS, including an aluminum heating stage, are illustrated in Fig. 4.7. Moreover, the gaseous void above the working electrode, which needs to be inertized to avoid air intake, grants the possibility to use encapsulating window materials, which are, in contrast to the literature setups in Chap. 4.2, not in electrolyte-contact. Electrolyte pollution can thereby be excluded. The non-contacting encapsulation further protects sensitive equipment from possible sprays and fumes from the cell. The materials used with this setup can either be PTFE, PEEK, or PFA for the housing and PTFE or EPDM for sealings. The aluminum heating stage is heated by four heating cartridges connected to a power supply and controlled with and a homemade PID-controller. Altogether, the setup allows measurements at elevated temperatures similar to the industrial application. Such a parallelism stands out in combining industrial applications to more fundamentally focused research.

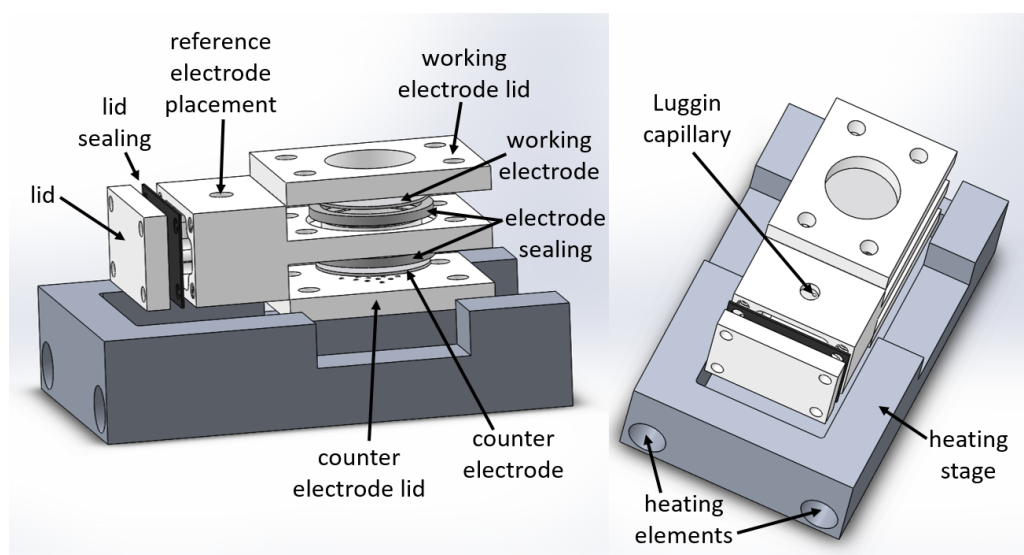


Fig. 4.7: Assembly of the spectroelectrochemical cell FeliS, made with the CAD software Solidworks. The illustration shows the general approach with a replaceable working electrode lid, which can be modified according to the requirements of specific spectroscopic techniques.

4.4.1 Electrochemical verification of FeliS with platinum

An electrochemical test of FeliS is deemed necessary to verify the application of the setup for electrochemical tests. Within this work, a platinum-paste painted YSZ separator, sintered

at 800 °C, with a platinum-mesh current collector was used as the working electrode for the verification test. The counter electrode and its current collector were made of nickel. A mini RHE, purchased from Gaskatel, served as the reference electrode. All measurements were conducted in 1 M KOH (degassed with nitrogen for 10 min) with a Gamry 3000 potentiostat.

Prior to designing and constructing working electrode lids for different spectroscopic techniques, a generic lid with a circular opening was used for the electrochemical test. To be able to inertize the gaseous void with nitrogen, parafilm provided an alternative for future window materials at this stage. The testing approach is visualized in Fig. 4.8A. To qualify the electrochemical behavior of FeliS, electrochemical impedance spectroscopy at 50 mV vs RHE (Fig. 4.8B), cyclic voltammetry (Fig. 4.8C), and an iV -curve (Fig. 4.8D) were performed under constant degassing of the electrolyte reservoir with nitrogen.

EIS resulted in a series resistance of $R_s = 1.087 \Omega$, which is equivalent to $3.261 \Omega\text{cm}^2$, and thus in accordance with the self-set target of $5 \Omega\text{cm}^2$ at maximum. The EIS spectrum indicates one semi-circle at high frequency together with an either capacitive or mass-transport limiting low frequency incline. As the measurement potential was in the underpotential region, the low frequency part is expected to result from the electrode's capacity and the high frequency part from a transmission-line behavior of the porous electrode structure. Overpotential EIS to confirm this hypothesis could not be performed.

As it can be seen in the iV -curve, the backscan causes hysteresis. Further electrochemical tests were not possible after the iV -curve, which could be correlated to a delamination of the platinum electrocatalyst from the separator, as observed after dismounting. Due to the evolution of hydrogen, the electrode was demolished. This observation adds to the above described challenges towards the sample production. The surface area in the iV -curve was corrected to the estimated ECSA from the H_{upd} -region between 50 – 500 mV vs RHE, obtained from the CV at 100 mV/s.

The CV further shows the characteristic hydrogen ad- and desorption peaks in the H_{upd} -region and the formation and reduction of platinum oxide at ≈ 800 mV vs RHE [150–152], which confirms the pollution-free approach of this setup. Nevertheless, the tilting of the CV towards more negative currents with decreasing electrode potential indicates that the degassing of the electrolyte and of the void above the working electrode was insufficient, which resulted in a side reaction on the working electrode through oxygen reduction. Hence,

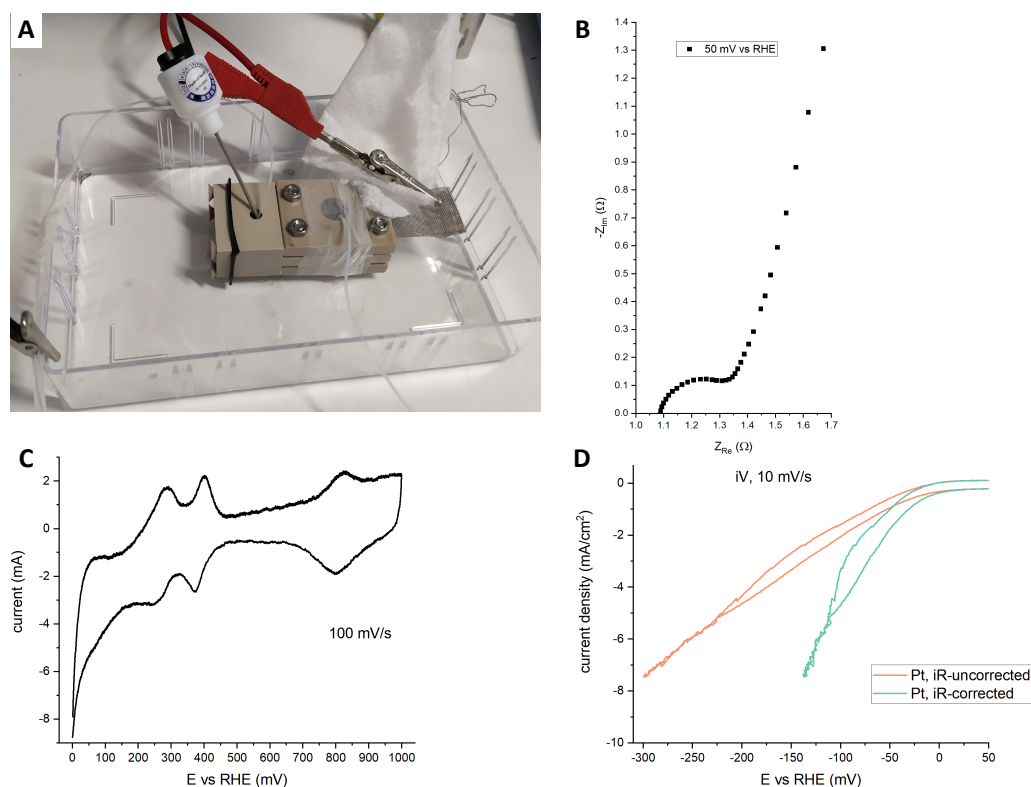


Fig. 4.8: **A:** The final spectroelectrochemical testing setup with a platinum electrode ($A_{geo} \approx 3 \text{ cm}^2$) and a platinum-mesh, fully covering the electrode backside, current collector. The void above the working electrode is covered with parafilm. The electrolyte, 1 M KOH, and the void between electrode and parafilm are degassed with nitrogen. **B:** Nyquist plot at 50 mV vs RHE (25 kHz – 10 Hz) of the platinum electrode. **C:** Sixth scan of cyclic voltammetry of the platinum electrode at 100 mV/s. Starting from 0 mV vs RHE to 1000 mV vs RHE, scanning back to 0 mV vs RHE. **D:** Resulting iV -curves at 10 mV/s in the HER region, correlated to the real Pt surface area estimated from the H_{upd} region ($A = 20.04 \text{ cm}^2$), iR -uncorrected and corrected considering an R_s of 1.087Ω .

longer degassing times, compared to the 10 min conducted here, and proper window materials over the working electrode will be key to avoid air intake.

In conclusion, the electrochemical testing of the setup FeliS with platinum as reference material revealed that electrochemical testing is indeed pollution-free. The matching of the characteristic underpotential CV of the platinum electrode with literature sources further confirms the undistorted, homogeneous potential distribution over the working electrode. However, the testing also indicated upcoming challenges towards the preparation and mechanical stability of working electrode samples.

4.4.2 FeliS in Raman configuration

Raman spectroscopy utilizes laser radiation perpendicularly to the surface of a sample. A working electrode lid that enables a perpendicular operation, while simultaneously degassing the void above the working electrode, is presented in this section.

These requirements demand an encapsulation with a Raman-inactive material. As commonly known [153], glass does not interfere with Raman spectroscopy. An uncoated 'N-BK7' glass window (12.5 mm diameter, 0.2 mm thickness) was purchased from Edmunds Optics. The working electrode lid was, as shown in Fig. 4.9, modified to host the window. While the electrode-touching bottom side of the working electrode lid remains at full diameter, the topside was reduced in size and includes an indent to hold the window in place. The 5 mm high gaseous void between working electrode and window can be degassed with a 1.2 mm PFA-tube mounted from the side of the lid.

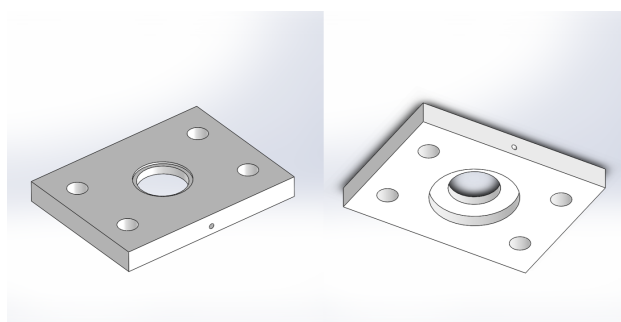


Fig. 4.9: Left: Top view with indentation for a quartz glass window and Right: Bottom view of the working electrode lid for the Raman configuration of FeliS. The hole from the side of the lid allows to inertize the gaseous void between working electrode and quartz window.

To evaluate the capability of FeliS for Raman spectroscopy, *in situ* measurements in dry and wet state were conducted. As working electrode, a hydrothermally synthesized [103] Ni₇Fe₃ LDH electrocatalyst was used. The hydrothermal synthesis was conducted at 120 °C for 12 h in a 100 mL PTFE-lined steel autoclave, with 40 mM urea (CAS 57-13-6, purity ≥ 99.5 %, Sigma Aldrich), 7 mM Ni(II)nitrate hexahydrate (CAS 13478-00-7, purity 99.999 %, Sigma Aldrich), 3 mM Fe(III)nitrate nonahydrate (CAS 7782-61-8, purity ≥ 98 %, Sigma Aldrich) and a $d = 3$ cm nickel-mesh substrate (10 μm spacing, 100 μm thick, 9.3 % open

area, purchased from Deze Products Lim.). After synthesis, the sample was washed three times in ethanol, dried in air and mounted with a nickel current collector in the setup FeliS.

Raman spectroscopy of the NiFe electrocatalyst was conducted with a Renishaw InVia spectrometer (calibrated on the 520.5 cm^{-1} peak of a monocrystalline silicon sample with a $\pm 0.5\text{ cm}^{-1}$ tolerance) with a 50x long distance objective (Olympus LMPlanFLN), as shown in Fig. 4.10. Firstly, the sample is probed as mounted in a dry state. Thereafter, the setup is filled with 11.6 M KOH and remeasured. Comparing both measurements intends to gain knowledge about the setup's behavior towards *in situ* measurements. As visible in Fig. 4.10, the as synthesized sample consists mainly of defective or disordered $\text{Ni}(\text{OH})_2$ and Fe-rich side phases [110]. After adding the electrolyte, some signal intensity was lost, which resulted in a multiplication of the 'wet'-measurements to compare the dry and the wet state appropriately. In addition to the signal-loss and the increased background, the signal from the Fe-rich side phase disappeared, which was confirmed by three measurements at different positions.

To understand the signal loss and the correlated background increase, Raman spectroscopy was conducted on the electrolyte. For comparison, the lowest and the highest electrolyte concentrations applied in this work, 1 M and 11.6 M KOH, were measured. The results, represented in Fig. 4.11, display a strong fluorescence background from $100\text{--}2400\text{ cm}^{-1}$ and KOH related peaks at $120, 280, 1642, 3280, 3418, 3610\text{ cm}^{-1}$. According to a published literature source [154], the peak at 3610 cm^{-1} can be associated to free hydroxide in the electrolyte, plus a broad water-related peak between $2400\text{--}3500\text{ cm}^{-1}$. Furthermore, the fluorescence signal increases with increasing electrolyte concentration.

Consequently, the observed loss of signal-intensity and increased background are a result of the high electrolyte concentration of 11.6 M KOH. Hence, this effect could be mitigated with less concentrated electrolytes, e.g. 1 M KOH, or through the application of surface-enhanced Raman spectroscopy (SERS) with e.g. Ag coated substrates.

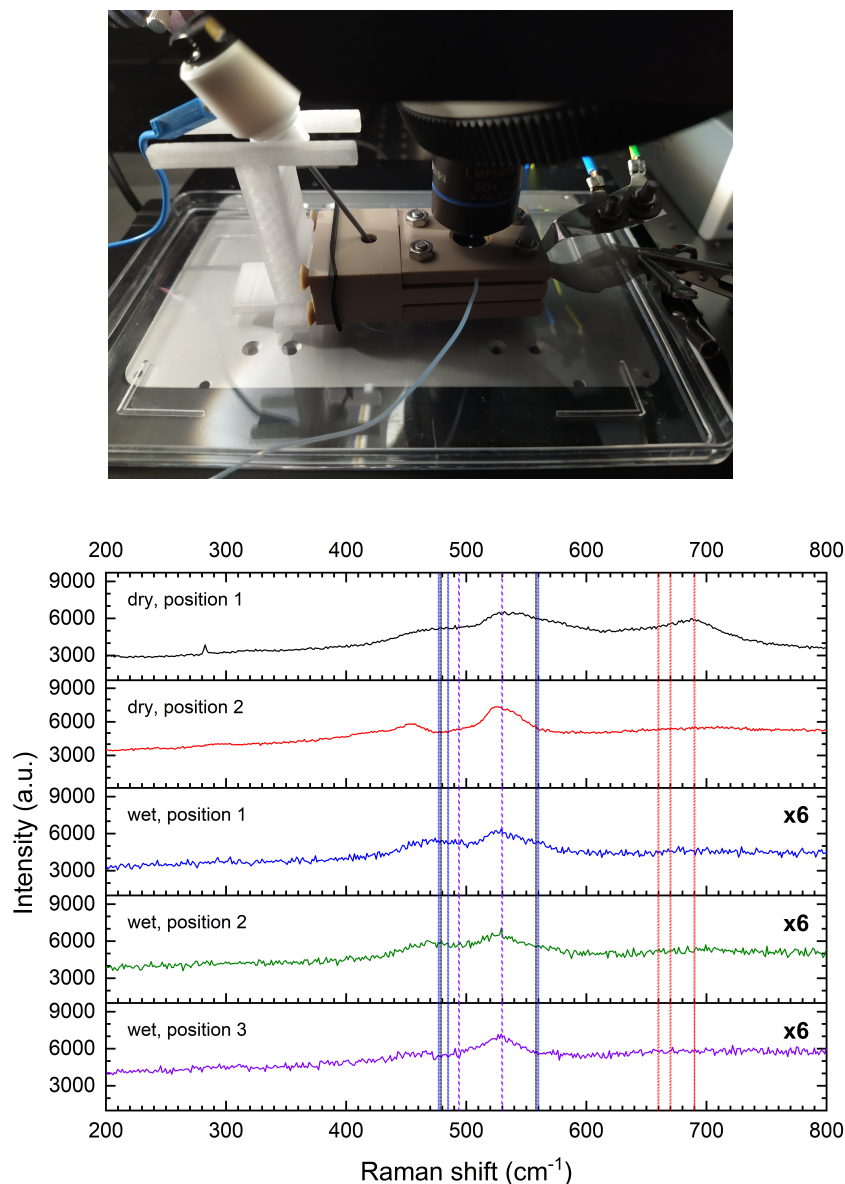


Fig. 4.10: Top: The operation of FeliS within the Renishaw InVia Raman spectrometer. Bottom: *In situ* measurement of a hydrothermally synthesized Ni_7Fe_3 LDH electrocatalyst, mounted in the spectroelectrochemical cell FeliS. The top two subfigures represent the dry state, the lower three subfigures after adding the 11.6 M KOH electrolyte. Note that the intensities of the wetted samples had to be six-fold increased, which is due to an intensity loss through the addition of the electrolyte. Black lines: $\alpha\text{-Ni(OH)}_2$, ($479, 558\text{ cm}^{-1}$); Blue lines: $\beta\text{-Ni(OH)}_2$, ($477, 485, 560\text{ cm}^{-1}$); Violet lines: defective or disordered Ni(OH)_2 , ($494, 530\text{ cm}^{-1}$); Red lines: $\text{Fe}_3\text{O}_4/\gamma\text{-Fe}_2\text{O}_3/\gamma\text{-FeOOH}$, ($670, 660, 690\text{ cm}^{-1}$). 532 nm laser (100 mW) at 10% intensity and a 50x long distance objective.

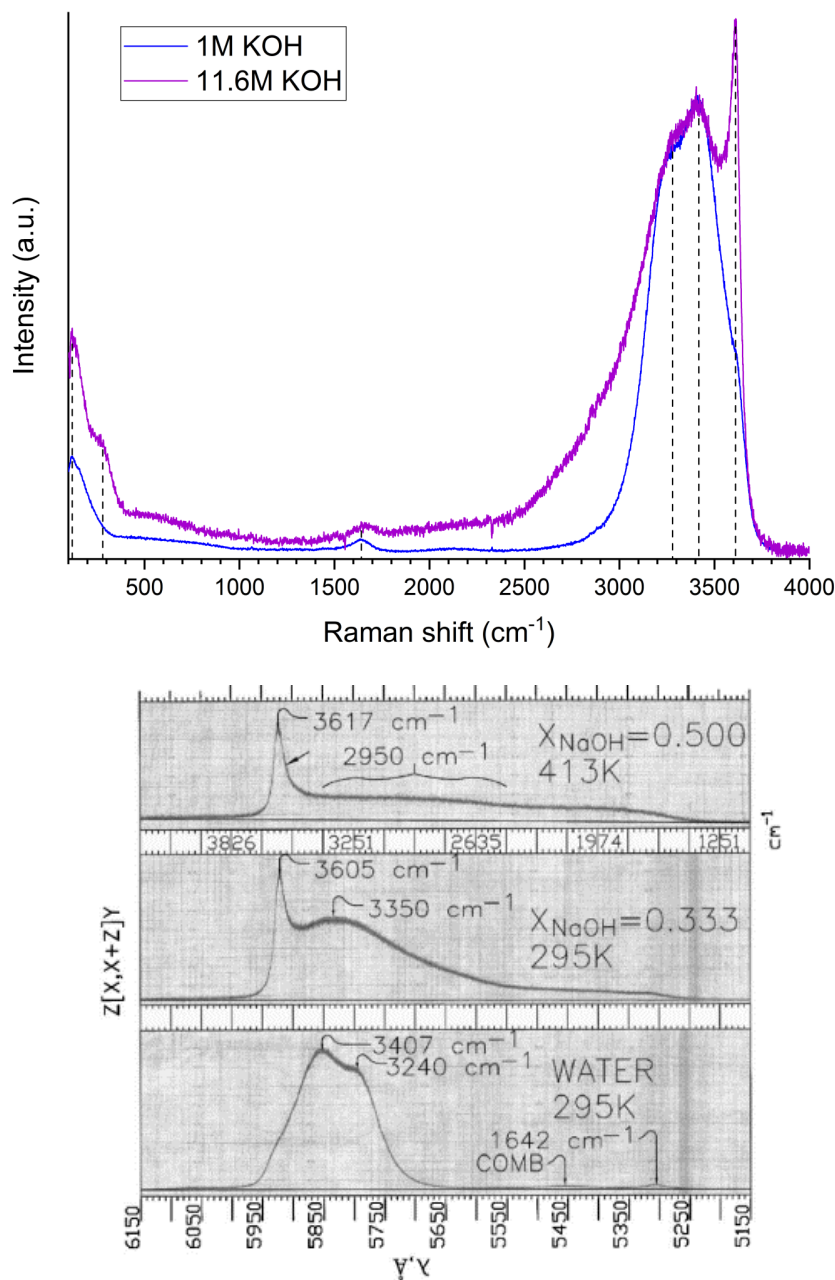


Fig. 4.11: Top: Raman measurement of 1 M and 11.6 M KOH electrolyte. Peaks at 120, 1642, 3280, 3418, 3610 cm^{-1} for both electrolytes. 11.6 M KOH has an additional peak at 280 cm^{-1} and a broader water peak at 2400 – 3700 cm^{-1} than 1 M KOH (2700–3700 cm^{-1}). Measurements made with a 532 nm laser (100 mW) at 10 % intensity and a 50x long distance objective, both spectra are normalized to another at the 3418 cm^{-1} peak to indicate the concentration-dependent fluorescence contributions. Bottom: Literature reference on the Raman measurements of water and 33.3 % NaOH at 295 K and of 50 % NaOH at 413 K, reproduced from [154]. Note that the literature source has a reversed abscissa orientation.

4.4.3 FeliS in X-ray configuration

X-ray based analysis techniques use a different approach compared to Raman, in which the angle, relative to the sample's surface, of the in- and outgoing radiation is varied throughout the course of the measurement. Therefore, the working electrode lid for the X-ray configuration of FeliS differs from the Raman configuration. As representative for the X-ray configuration, X-ray diffraction was performed. Although not limited to this technique, XRD was the only applied X-ray based technique within this work.

In addition to the difference of the path of radiation in comparison to Raman spectroscopy, the used glass window is neither XRD-inactive nor in correct size and shape for the X-ray configuration. As a result, the X-ray working electrode lid is designed based on an opening of 19 mm in diameter for the working electrode, and a carving in the path of the X-rays. This lid, illustrated in Fig. 4.12, leaves a 1.4 mm high residual within the X-ray path, which was necessary to preserve the mechanical stability of the lid. This allows for a trigonometrically calculated minimal X-ray angle of $\approx 8.4^\circ$, which would be sufficient for XRD measurements. As the gaseous void above the working electrode requires to be inertized, while not distorting the XRD measurements, a 'dome' was designed, which fits the working electrode lid. The round dome allows X-rays to always perpendicularly cross a sealing tape, which was chosen to be Kapton in this work. The X-ray inactive Kapton tape has shown to only marginally decrease the signal intensity, but without distorting the measurement itself.

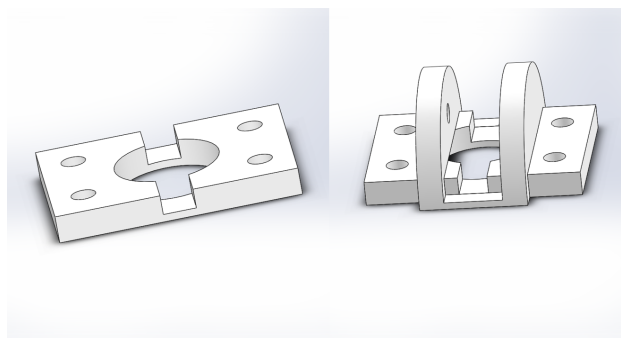


Fig. 4.12: Left: The first working electrode lid for the X-ray configuration of FeliS with carvings for the path of X-rays. Right: Placement of a dome above the X-ray working electrode lid. The semicircle allows X-rays to always perpendicularly cross a sealing Kapton-film.

The concept of this working electrode lid was evaluated by an operando XRD measurement with a Rigaku Smartlab diffractometer, shown in Fig. 4.13 (top). A nickel-YSZ gas diffusion electrode, which is usually used as the counter electrode, was used as the working electrode. The measurements between the dry and the wet state, as well as the wet state with and without the Kapton-film covered dome, did not indicate any difference besides marginal signal intensity decreases. A visualization was therefore omitted. The working electrode was then held at -400 mV vs RHE (*iR*-uncorrected) in 11.6 M KOH over ≈ 16 h. This approach intended to deliver answers about the open question of possible nickel hydride formation (see Chap. 2.4). However, two unexpected findings were made instead. Firstly, the XRD patterns did not indicate any difference between another, which resulted in a summation of all patterns gathered overnight, shown in Fig. 4.13 (bottom), to ensure a better signal-to-noise ratio. Despite this attempt, the pattern only displays phases associated with the PEEK holder, YSZ and metallic nickel; other forms of nickel cannot be found. Secondly, the background varied remarkably depending on the incidence angle of the X-ray source. In Bragg-Brentano geometry, the background intensity is expected to linearly increase with increasing incidence angle, as the X-ray aperture decreases on the sample while it captures an increasing amount of the substrate-depth. Within this measurement, the background decreased before it increased. In combination with the measured PEEK phases, the holder greatly influences low-angles up to $2\Theta \approx 35^\circ$.

As a result of these two unexpected findings, a new working electrode lid capable of GIXRD is needed, which does not affect the XRD measurements. The Bragg-Brentano approach appears to be too imprecise to study changes in this setup, whereas GIXRD grants a comparably higher near-surface sensitivity.

The problem associated with the low-angle influence stemmed from the residual 1.4 mm high path in the X-ray channel of the working electrode lid, which is inevitable to ensure mechanical stability. As a consequence, an 'out of the box thinking' was required to find a solution. In a second approach, in which the X-ray path should be unhindered by the working electrode lid, the height of the lid has to match with the working electrode. A matching between working electrode and lid height would be the only possibility to perform GIXRD at incidence angles as low as 0.5° . On the other hand, the mechanical integrity of the lid would be lost. Therefore, to combine the possibility of low-angle incidence angles

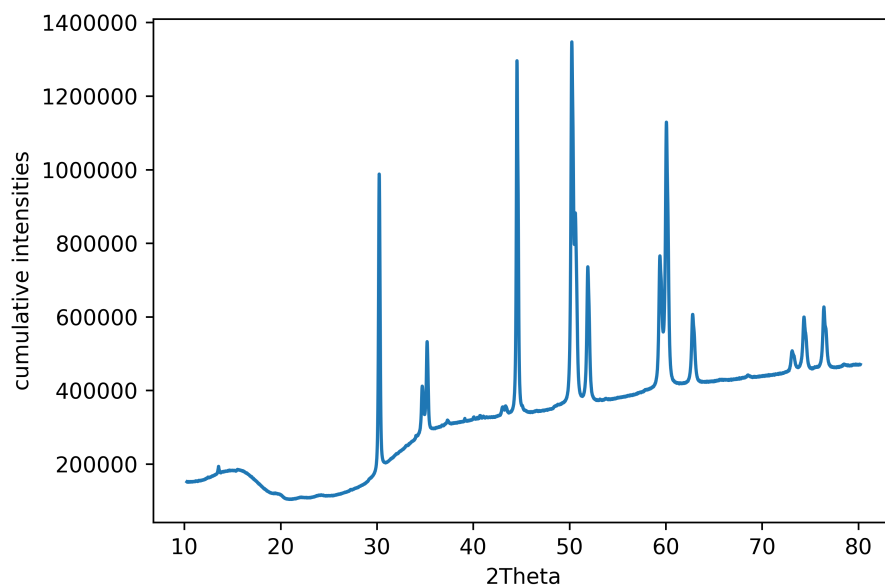
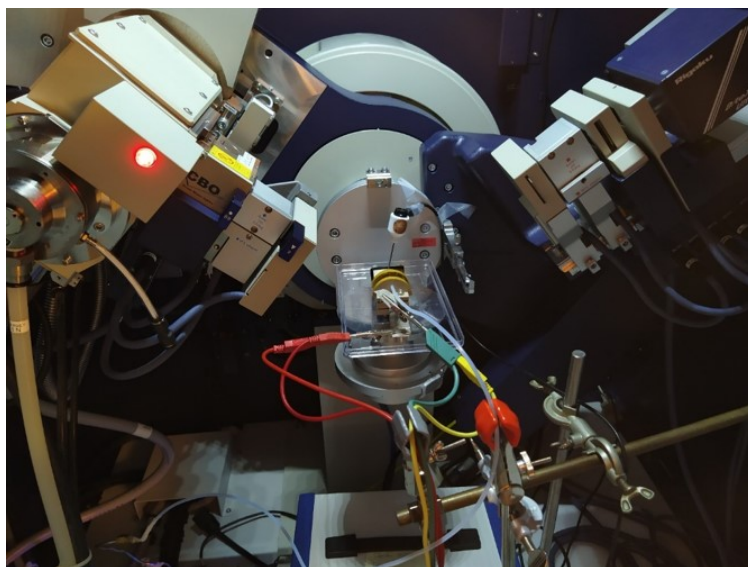


Fig. 4.13: Top: The operation of FeliS within the Rigaku Smartlab X-ray diffractometer. Bottom: X-ray diffraction pattern of a nickel-YSZ electrode during operando measurements in 11.6M KOH at room temperature with the first X-ray lid. The nickel electrode is held at HER overpotentials for 16 h over night. The measurement is influenced by the PEEK holder until $2\Theta \approx 35^\circ$, which results in lower incoming X-ray intensities at lower angles compared to higher angles. The pattern displays phases associated with PEEK, YSZ and nickel; changes associated with the overnight run could not be observed.

and mechanical integrity, the lid was designed with an outer laying bar, as illustrated in Fig. 4.14. The dome was changed accordingly by increasing its radius.

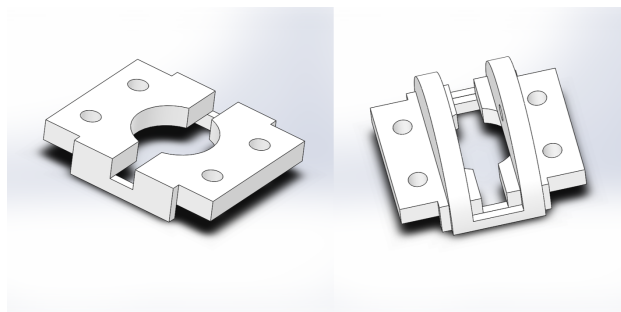


Fig. 4.14: Left: The second working electrode lid for the X-ray configuration of FeliS with carvings for the path of X-rays at all angles. Right: Placement of a dome above the second X-ray working electrode lid. The semicircle allows X-rays to always perpendicularly cross a sealing Kapton-film.

The second X-ray working electrode lid is manufactured to fit with the cell house, which reduces the possibility of misalignment through e.g. twisting of the working electrode lid. Furthermore, the excess material ensures that bending in the X-ray path is avoided. These two optimization steps from the first working electrode lid should avoid the influence of the PEEK holder on the X-ray measurements. A direct comparison between both X-ray working electrode lids is given in Fig. 4.15. The comparison undoubtedly displays the improvement from the first to the second lid. Besides the proper height alignment allowing for GIXRD, the second working electrode lid avoids bending of the X-ray channel through the outer laying bar, as bending of the first working electrode lid appears to be the cause of the low-angle influence observed in Fig. 4.13.

To assess the efficacy of the improvements, GIXRD was performed with the second X-ray working electrode lid and the associated second dome, as shown in Fig. 4.16A. The working electrode consisted of a silver-sputtered YSZ separator by plasma-coating. 100 μL of a solution of 10 mg/mL NiMoO_4 (from sol-gel-synthesis [155], see Chap. 5.1 for description) in isopropanol was drop-cast onto the silver-coated separator and reduced at 600 $^\circ\text{C}$ for 3 h in a safety-gas atmosphere (4 % H_2 / 96 % Ar). The measurements were conducted in a dry state, as the primary focus rests on the possibilities and limitations of GIXRD at varying incidence angles between 0.5 – 5 $^\circ$.

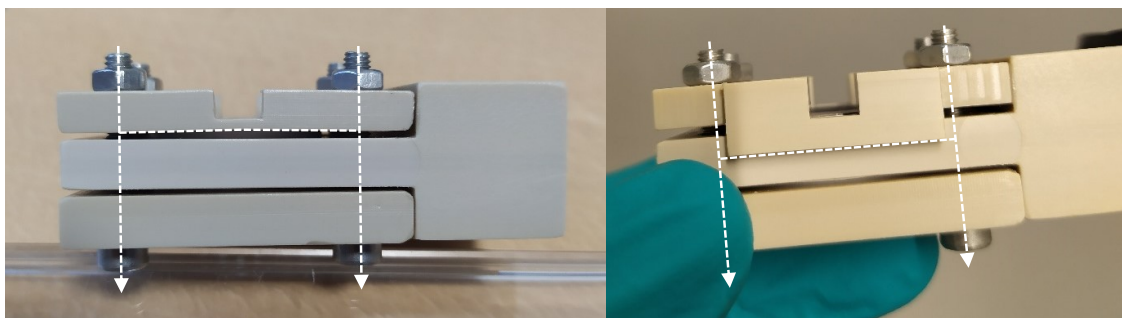


Fig. 4.15: Left: The first X-ray working electrode lid for the X-ray configuration of FeliS. The downwards forces of the screws cause a slight bending of the X-ray channel. Right: The second X-ray working electrode lid for the X-ray configuration of FeliS. The outer laying bars are resilient towards the bending, which keeps the X-ray channel straight. Furthermore, the height alignment of the working electrode lid with the sample allows to perform GIXRD.

As seen in the patterns in Fig. 4.16B and C, low-angle phases between $2\Theta \approx 18-21^\circ$ vary at incidence angles between $0.5-2.5^\circ$ in intensity and in position, while a phase around $2\Theta \approx 30^\circ$ constantly increases in intensity with increasing incidence angle and stabilizes in its position at an incidence angle of $\approx 1.5^\circ$.

The deviations between the patterns are explicitly pointed out in the comparison between the incidence angles 2° and 3° in Fig. 4.16D. The low-angle phases are associated with PEEK from the holder, while the other originates from the YSZ separator. The appearance and disappearance of the PEEK phase at the lowest incidence angles, while all phases position-stabilize at $\approx 1.5^\circ$, clearly indicates a lateral misalignment of the holder, which results in a tilted sample. Although the working electrode concept appears to work as intended, the alignment of the working electrode lid through the operator can introduce a slight lateral misalignment, which has a crucial impact at low incidence angles. However, the measurements at 3° and 5° display stable measurements, which noticeably proves that the concept itself performs well, if the working electrode is mounted perfectly flat. A possible solution for a better mounting concept, besides an increasingly experienced operator, will be given in Chap. 4.5.2.

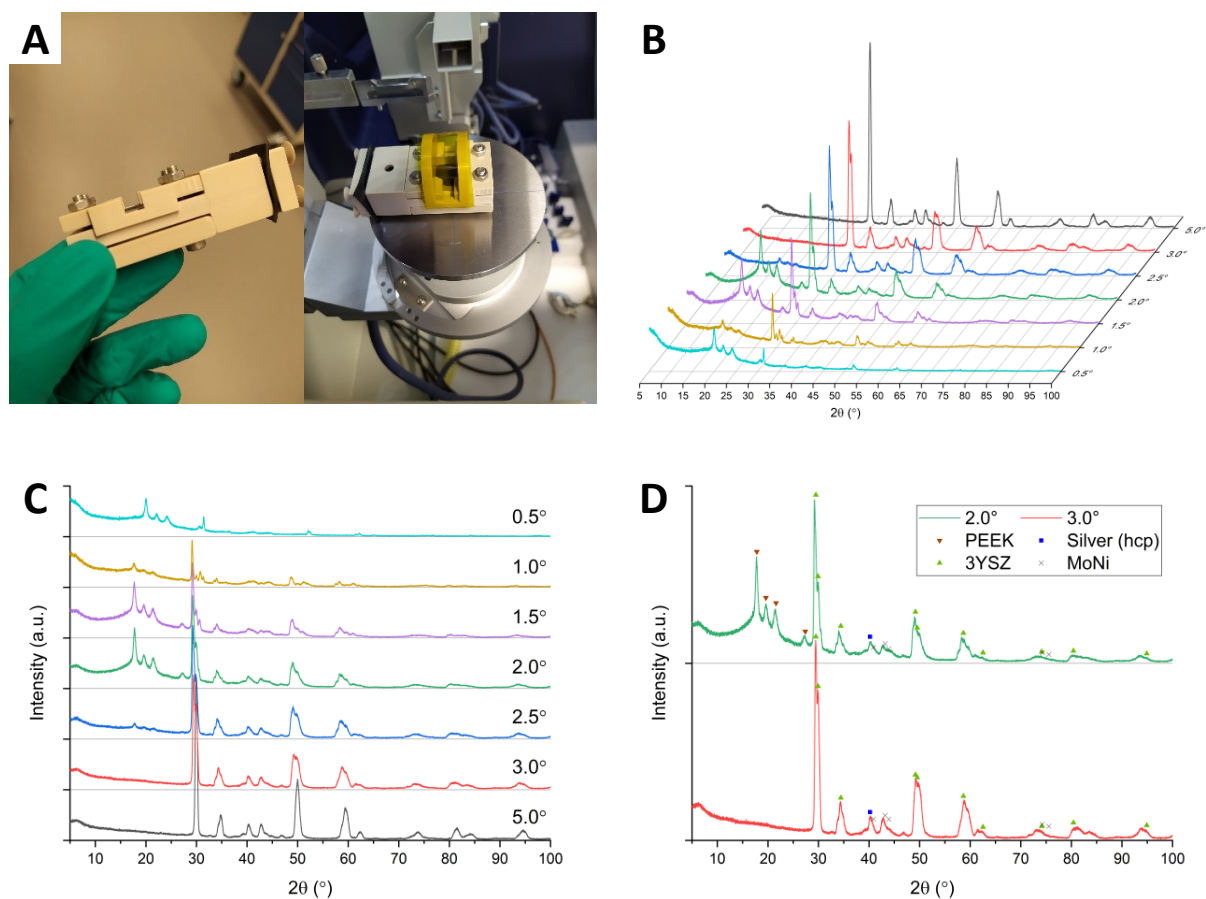


Fig. 4.16: GIXRD patterns of a plasma coated silver-YSZ electrode and at 600 °C thermochemically reduced NiMo solgel electrocatalyst with the second X-ray working electrode lid. The sample is mounted in the spectroelectrochemical cell FeliS with the second X-ray working electrode lid and the second dome in the Rigaku Smartlab X-ray diffractometer, as shown in **A**. **B**, **C**: 3D and 2D plotting of the patterns with varying incidence angles between 0.5 ° – 5.0 °. **D**: Comparison of the patterns at incidence angles 2.0 ° & 3.0 °, indicating the influence of the lateral holder misalignment on the measurement.

4.5 Conceptions for the prospective applications of FeliS

A major advantage of FeliS is its versatility, which allows modifications mainly through the working electrode lid. The modifiable working electrode lid enables the setup to accomplish changing demands to different approaches. For the prospective applications of the setup as a flowcell setup, or with a mounting tool, design concepts are reported in this section.

4.5.1 FeliS in a flowcell configuration

FeliS was constructed for stationary use, in which the wetting of the electrocatalyst is ensured by capillary forces. Considering the possibility of drying, especially over longer measurement times or at increased temperatures, which are possible with the homemade aluminum heating stage, a flowcell configuration can become necessary.

Within the frame of this work, the realization of this concept has not been pursued. However, with a few modifications, FeliS will also be capable of conducting spectroelectrochemical measurements with flowing electrolyte. One possibility is pumping electrolyte through the electrolyte chamber, such as shown in Fig. 4.17. This concept, named FeliS 2, can play a vital role when using a membrane with hydrophobic pores, which allows for gas permeation while inhibiting electrolyte diffusion. The electrocatalysts can then be immersed into the electrolyte, if the membrane does not interfere with the spectroscopic technique. This concept has recently been pursued in the department for the oxygen reduction reaction in acidic electrolyte.

A second approach in ensuring electrolyte flow is based on the original concept of the working electrode. Using the advantage of a modifiable working electrode lid, it can be modified to have an electrolyte-delivering capillary, which is connected to an electrolyte reservoir over a fitting and a tube. With this concept, the working electrode can be replenished with electrolyte in portions, or continuously with a closed liquid-circuit by an outlet tube. In both cases, a pump ensures the flow of the electrolyte. One possible approach to realize this concept with a 300 μm electrolyte film is illustrated in Fig. 4.18.

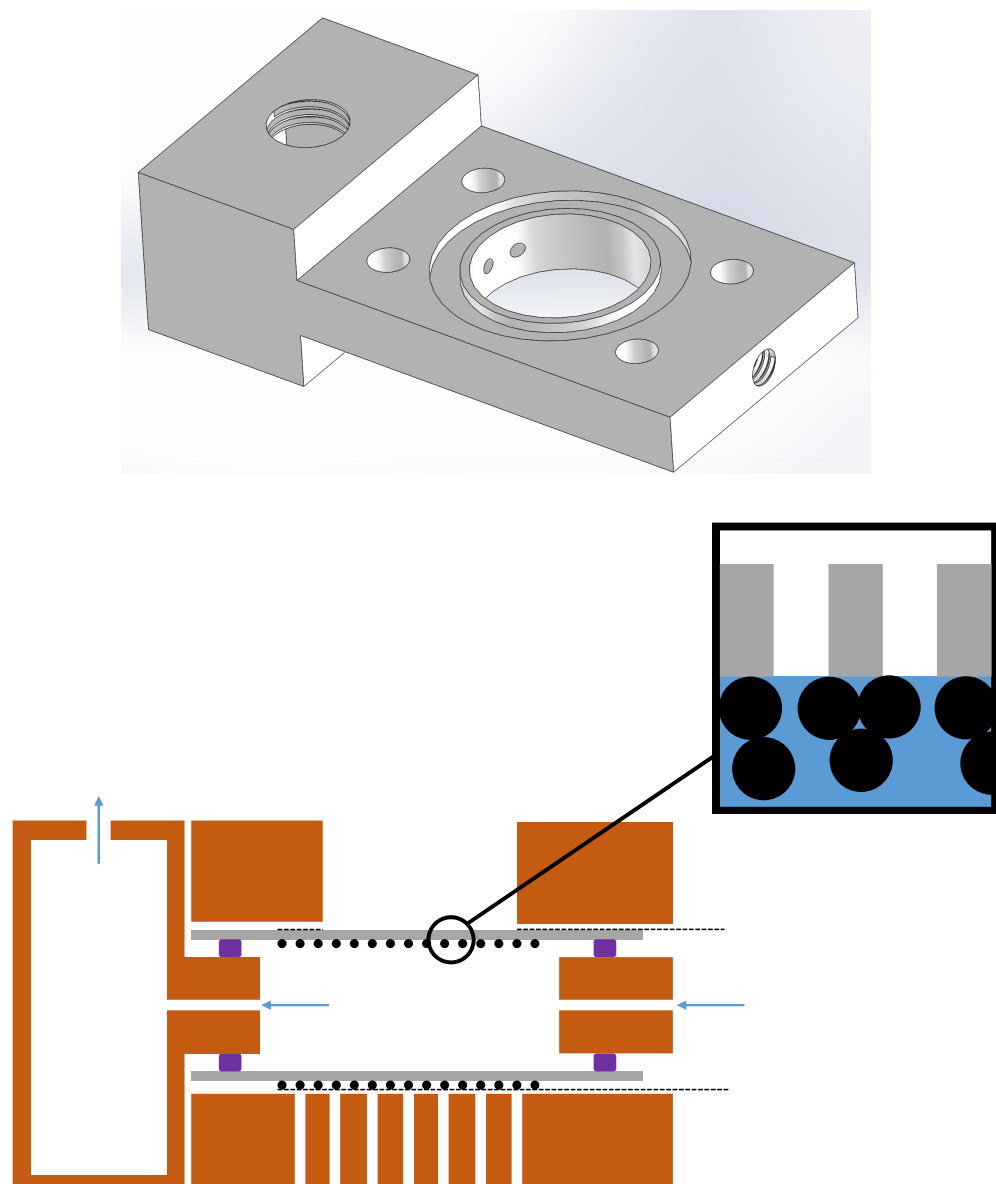


Fig. 4.17: FeliS in flowcell configuration. The concept is based on an inlet and an outlet tube fitted to the main body. Top: CAD drawings of FeliS 2 with flowing electrolyte through the main body. Bottom: Schematic cross-section of FeliS 2 showing the principle with hydrophobic pores allowing for the permeation of evolved gasses.

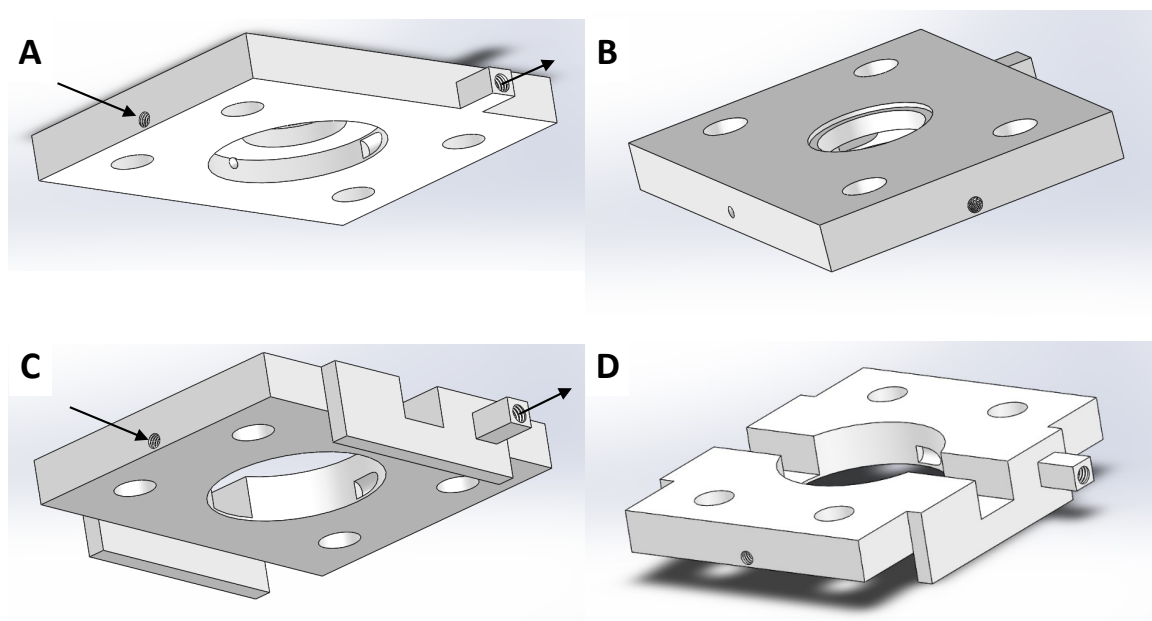


Fig. 4.18: FeliS in flowcell configuration. The concept is based on a 1.6 mm inlet and a 2.0 mm outlet tube, which ensures a 350/300 μm (with and without a 50 μm PTFE-sealing) electrolyte film on the working electrode. The thickness of the electrolyte film can be adjusted by milling down the distance between working electrode and inlet/outlet and by the choice of a PTFE-sealing with varying thickness. The outlet design allows to choose between a fitted outlet tube or simply dropping into a collecting beaker. **A, B:** Raman working electrode lid with threaded inlet and outlet for electrolyte flow. **C, D:** X-ray working electrode lid with threaded inlet and outlet for electrolyte flow. Inlet and outlet are 50 μm lower than the X-ray channel to avoid overflowing electrolyte.

4.5.2 Improving the assembly of FeliS with a mounting-tool

Using a rigid YSZ separator has proven to be a reliable solution to ensure a flat surface of the working electrode. However, the mounting by hand displayed irregularities in GIXRD. In order to eradicate tilting, a mounting-tool could be developed. The concept of such a tool could be based on e.g. the mass of a weight guided by a housing, which ensures an equal leveling of the working electrode, such as illustrated in Fig. 4.19.

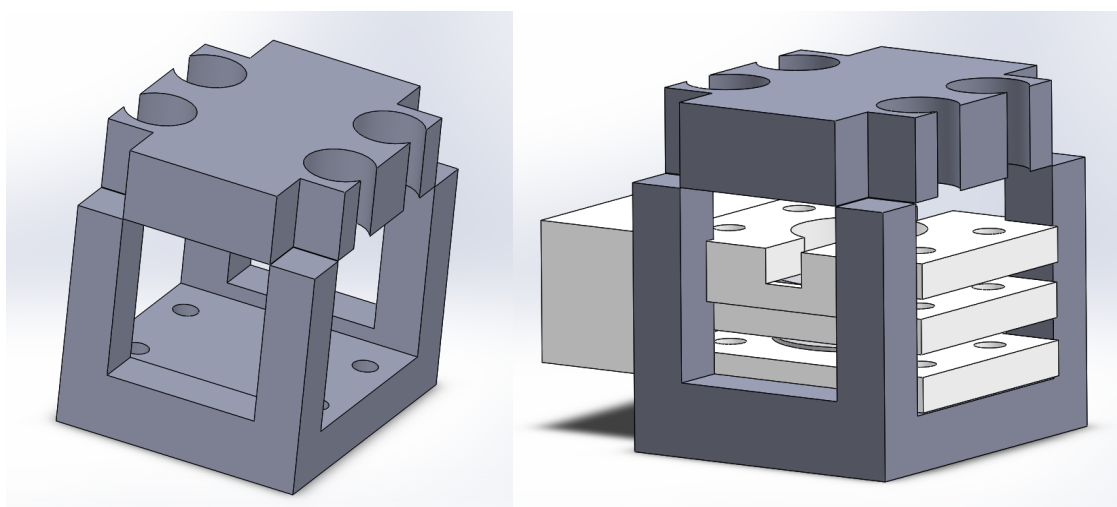


Fig. 4.19: Concept of a mounting-tool to ensure a flat working electrode of FeliS. The weight is uniformly distributed over the working electrode lid.

4.6 Conclusions on the spectroelectrochemical cell FeliS

The development of a novel spectroelectrochemical cell, named FeliS, followed the purpose to study water splitting electrocatalysts under operation in technologically relevant conditions.

FeliS has proven to work electrochemically. Furthermore, *in situ* measurements with Raman spectroscopy and X-ray diffraction displayed the possibility to measure in operating conditions. These measurements led to refinements for the design of the cell and the measured samples. For the Raman measurements, the results show that the electrolyte itself has an impact on the spectroelectrochemical measurements. An attempt to avoid this impact is based on a surface-enhanced Raman (SERS) approach, with a silver or gold substrate. For

the XRD measurements, the findings led to a working electrode lid proven to be capable of GIXRD, which was identified as the chosen approach with FeliS.

For both spectroelectrochemical approaches, Raman and XRD, the chosen approach is based on plasma-deposited silver, gold, or platinum electrodes. The YSZ based membranes are plasma coated, and the electrocatalysts are drop-cast onto this electrically conductive substrate. The plasma deposition has several advantages. Firstly, the YSZ membrane becomes conductive itself, without adding significant thickness to it. Thinner samples ensure the wetting of the electrocatalyst, as the risk for drying is minimized, and allow to neglect possible potential distributions across the electrode. Secondly, the deposition of silver nanoparticles gives the possibility for a SERS effect, which could help to circumvent electrolyte-fluorescence in Raman spectroscopy. Lastly, the omission of nickel substrates as conductive substrates grants the certainty that measurements can be correlated to the nickel-based electrocatalysts without possible substrate influences.

In conclusion, the work in this chapter eventually presents the functional spectroelectrochemical cell FeliS for Raman and X-ray based analysis techniques, which finds its application in Chap. 7. It displays further possibilities, such as a flowcell configuration or with XPS, which is beyond the application in this work. The greatest advantages of this cell are the versatility for different analysis techniques, through a modifiable working electrode lid, the possibility to heat with a homemade aluminum heating stage, and the resilience towards harsh measurement conditions, which is ensured by the use of high-grade PEEK and PTFE materials. In theory, this would allow for spectroelectrochemical measurements of up to 250 °C for electrolytes at any pH. However, this would certainly face practical safety and pressurizing limitations at temperatures above 100 °C.

Chapter 5

Influence of the electrochemical active surface area and partial oxidation of Ni and NiMo electrocatalysts

Nickel-molybdenum electrocatalysts were identified as highly active in the 1980s and early 1990s [81, 156, 157]. Thereafter, the focus on these electrocatalysts appears to have vanished, with only a few publications in the early 2000s (e.g. [38, 158]). Since the 2010s, the interest into these types of electrocatalyst has sparked, focusing primarily on fabrication procedures and characterizing the performance of the resulting electrocatalysts and electrodes [65, 68, 159, 160]. In parallel, studies on the mechanisms on nickel electrocatalysts [15, 33, 42, 57], as well as the effects of partially oxidized or oxide supported electrocatalysts [26, 47, 161–165], were targeted study lines.

However, at the time of the work presented in this chapter, a comprehensive and generalizing study outlining the intersections, agreements and disagreements between these study lines on kinetic performance descriptors on a similar and comparable baseline cannot be found. The literature studies focus on single study lines conducted in different electrolyte concentrations and with different considerations of the electrochemical active surface area (ECSA). While parts of the publications disregard the effects of surface roughness, a consensus on the procedure and validity of ECSA estimations is lacking among the studies including surface roughness considerations [34, 166, 167].

As a consequence of this gap in the literature, the first part of this chapter aims at

creating a validated estimation of the electrochemical surface area. Applying this method to define the surface roughness of electrocatalysts on the same baseline in the second part of the chapter, different nickel, nickel-molybdenum, oxide supported nickel-molybdenum and partially oxidized nickel electrocatalysts are compared to another. The figure of merit was chosen to be the overpotential at 10 mA/cm^2 (η_{10}), as it is a commonly denoted performance descriptor in the literature [8, 168].

5.1 Experimental details

5.1.1 Electrochemical characterization

The electrochemical tests were conducted with a Gamry Reference 3000 potentiostat. All tests were conducted galvanostatically or potentiostatically versus a commercial RHE, which was purchased from Gaskatel. The tests were conducted in a three-electrode-setup made of PTFE (FlexCell), purchased from Gaskatel and described in Chap. 3.7.1. Electrochemical impedance spectroscopy was conducted between 20 kHz and 700 mHz. Galvanostatic impedances were conducted with an amplitude equivalent to 7.5 % of the galvanostatic current, while potentiostatic impedance proceeded with a 10 mVrms amplitude. The measurements were conducted in pre-electrolyzed 11.6 M ($\sim 45 \text{ w\%}$) KOH and 1 M KOH to represent the industrial application in correlation to the predominant literature application at lower electrolyte concentration, and thereby covering the spectrum of relevance for the alkaline water electrolysis with regards to the electrolyte pH.

5.1.2 Electrocatalyst preparation

Electrocatalyst testing was conducted on dense samples. The purpose of this approach was to achieve homogeneous samples with well-defined electrochemical potentials in three-electrode measurements. Furthermore, the minimization of porosity down to the micro and nanoporosity of the electrocatalysts allows to exclude electrode effects, and thus allows to investigate intrinsic electrocatalytic properties.

Nickel-foil (125 μm thickness, $\geq 99.9 \%$, Sigma Aldrich) was either used as the substrate or the sample. Four types of nickel samples were investigated. Firstly, bare nickel-foil

was tested. Secondly, a commercial Ni catalyst (20 nm, 99.9 %, US Research Nanomaterials Inc) was drop-cast (1.3 & 2.6 mg/cm²) using isopropanol as solvent onto the foil. The sample was kept at 450 °C for 2 h under Ar-atmosphere to obtain a binder-free bond. Thirdly, a nickel-felt (110 μm thickness, Bekeart) was tested to achieve higher surface area measurements. Lastly, the felt was coated with Ni LDH using a hydrothermal synthesis [109, 111]. The felt was placed in a PTFE-coated autoclave with a water-based solution containing 40 mM urea (CAS 57-13-6, purity ≥ 99.5 %, Sigma Aldrich) and 10 mM Ni(NO₃)₂ · 6H₂O (CAS 13478-00-7, purity 99.999 %, Sigma Aldrich) and held at 120 °C for 12 h. The resulting sample was washed with ethanol, left to dry in ambient air and reduced at 450 °C with safety-gas (4 % H₂ / 96 % Ar) for 2 h.

In addition to plain Ni samples, four different types of NiMo samples were investigated. With a view on the technical application, three promising synthesis routes to achieve high surface area NiMo electrocatalysts had been identified and were provided by the "BEEST" project team. These methods include a hydrothermal synthesis [64], a solgel synthesis [155], and a coprecipitation synthesis [65], as described in the following.

For the hydrothermal synthesis, two solutions of 800 mM Ni(NO₃)₂ · 6H₂O (CAS 13478-00-7, 99.999 %, Sigma Aldrich) and of 200 mM (NH₄)₆Mo₇O₂₄ · 4H₂O (CAS 12054-85-2, pharm., Sigma Aldrich) were added equally (v/v) to an autoclave. The synthesis was conducted at 150 °C for 6 h. The resulting catalyst precursor was separated from the solution by centrifuging and cleaning with ethanol. For the solgel synthesis, 3 g ethyl cellulose was sprinkled slowly under continuous stirring into deionized water at 50 °C. 17.7 g of (NH₄)₆Mo₇O₂₄ · 4H₂O (see above) and 29.1 g of Ni(NO₃)₂ · 6H₂O (see above), and 10 g citric acid (CAS 77-92-9, 99 %, Sigma Aldrich) were each dissolved separately in 50 mL water. These three solutions were slowly added under stirring to the ethyl cellulose solution to form sol. Slow heating to 90 °C resulted in a wet gel, which was dried at 105 °C for 1 h. The dried powder was finally calcined at 650 °C for 2 h in ambient air to form the precursor. The precursors of the hydrothermal and solgel synthesis showed NiMoO₄ (solgel synthesis) and a mixture of NiMoO₄ and different types of molybdenum oxides (hydrothermal synthesis) in powder X-ray diffraction, as illustrated in Fig. 5.1. For the coprecipitation synthesis, 1.512 g of Ni(NO₃)₂ · 6H₂O (see above) and 0.600 g of (NH₄)₆Mo₇O₂₄ · 4H₂O (see above) were added to 5 mL of water. 2 mL of ammonium hydroxide solution (CAS 1336-21-6, 28 %,

Sigma Aldrich) was added to the solution. This solution was added at once into 45 mL of diethylene glycol (CAS 111-46-6, 99 %, Sigma Aldrich), and then heated to 110 °C. The resulting suspension was centrifuged while still being hot. The obtained solid fraction was washed with water and sonicated once. This procedure was repeated with acetone as solvent. The final solid was added to a crystallization dish and wetted with methanol. After several hours of crystallization at 60 °C, a green solid formed.

All three precursors were drop-cast onto nickel-foils with isopropanol as solvent. To produce fully covered, homogeneous electrocatalyst surfaces, several iterative approaches resulted in different mass loadings of 190 $\mu\text{g}/\text{cm}^2$ (hydrothermal), 380 $\mu\text{g}/\text{cm}^2$ (solgel), and 755 $\mu\text{g}/\text{cm}^2$ (coprecipitation). Five samples of each type were placed in a gradient furnace, which was heated to 400, 500, 600, 700 and 800 °C under Ar-atmosphere and then switched to safety-gas (4 % H₂ / 96 % Ar). The reduction of these 15 samples was conducted for 3 h and allows to produce binder-free samples, which furthermore resemble the industrial application with nickel-based substrates. The varying reduction temperature further results, according to the literature [71, 160, 169], in the formation of molybdenum oxide (Mo_aO_b) supported Ni_xMo_y and fully reduced Ni_xMo_y electrocatalysts.

The fourth type of NiMo samples (including one Ni sample) was obtained through electrodeposition with a modified procedure of the steps conducted elsewhere [68]. Silver foil was used as the substrate with deposition solutions containing varying amounts (5, 4.5, 4, 3.5 mM) of NiSO₄ · 7H₂O (CAS 10101-98-1, 99.999 %, Sigma Aldrich), and (0, 0.5, 1.0, 1.5 mM) of (NH₄)₆Mo₇O₂₄ · 4H₂O (see above), and 285 mM NaCl (CAS 7647-14-5, ≥ 99.0 %, Sigma Aldrich), and 16 mM (CAS 18996-35-5, ≥ 99.5 %, Sigma Aldrich), which were regulated to pH 10 with an ammonium hydroxide solution (see above). The deposition was carried out at 40 °C and 20 mA/cm² for 20 min. EDS results in Mo-contents (calculated as Mo in NiMo) of 0 %, 12 %, 24 %, and 32 %.

5.2 Electrochemical impedance studies in the HER overpotential region

In this chapter, EIS studies were conducted in the HER overpotential region to study the kinetics of Ni and NiMo electrocatalysts. A primary focus was placed on the analysis of the

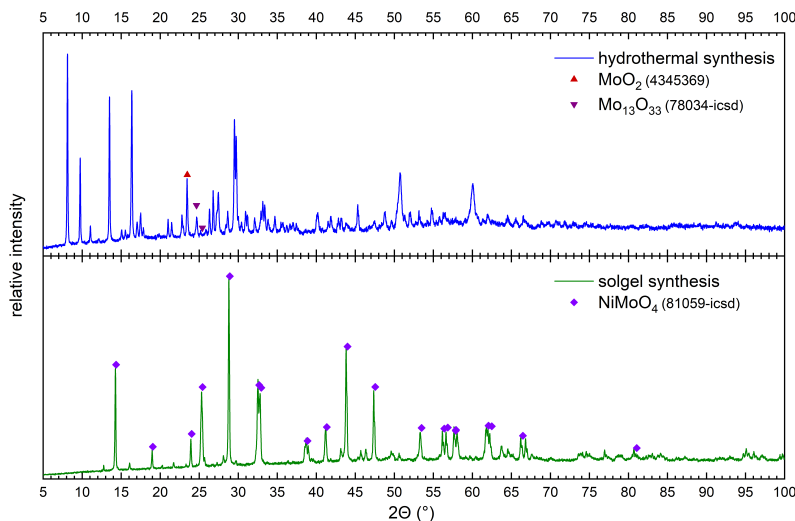


Fig. 5.1: Powder X-ray diffraction of the precursors by hydrothermal and solgel synthesis. Measurements made with a Rigaku Miniflex.

double layer. The assessment of the double layer capacitance, which is assumed to represent the electrochemically active surface area (ECSA), should serve as marking point to obtain intrinsic electrocatalytic properties. Normalizing the kinetics to the ECSA would allow to compare electrocatalysts on a common baseline.

5.2.1 Modeling with a simple R(RQ) equivalent circuit

As the first approach towards modeling of the electrochemical impedance, a simple $R_s(R_{ct}Q_1)$ electric equivalent circuit, see Fig. 5.2, was applied to fit the electrocatalyst contributions in the HER overpotential region. The fitting model consists of an electrolyte describing series resistance R_s , an electrocatalyst describing charge transfer resistance R_{ct} , and a constant-phase element equivalent to the double layer capacitance of the electrode reaction Q_1 . The obtained double layer capacitances from galvanostatic impedance at varying current densities in 11.6 M KOH for the NiMo electrocatalyst series, produced through hydrothermal and through solgel synthesis, are illustrated with respect to the measurement overpotential in Fig. 5.3. For comparison, the figure includes the results from potentiostatic EIS on a Ni foil in 1 and 11.6 M KOH.

Despite the difference of the obtained double layer capacitance by a factor of up to

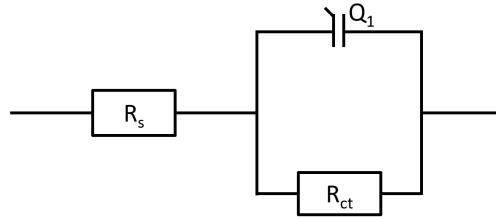


Fig. 5.2: The R(RQ) electric equivalent circuit for electrocatalyst modeling.

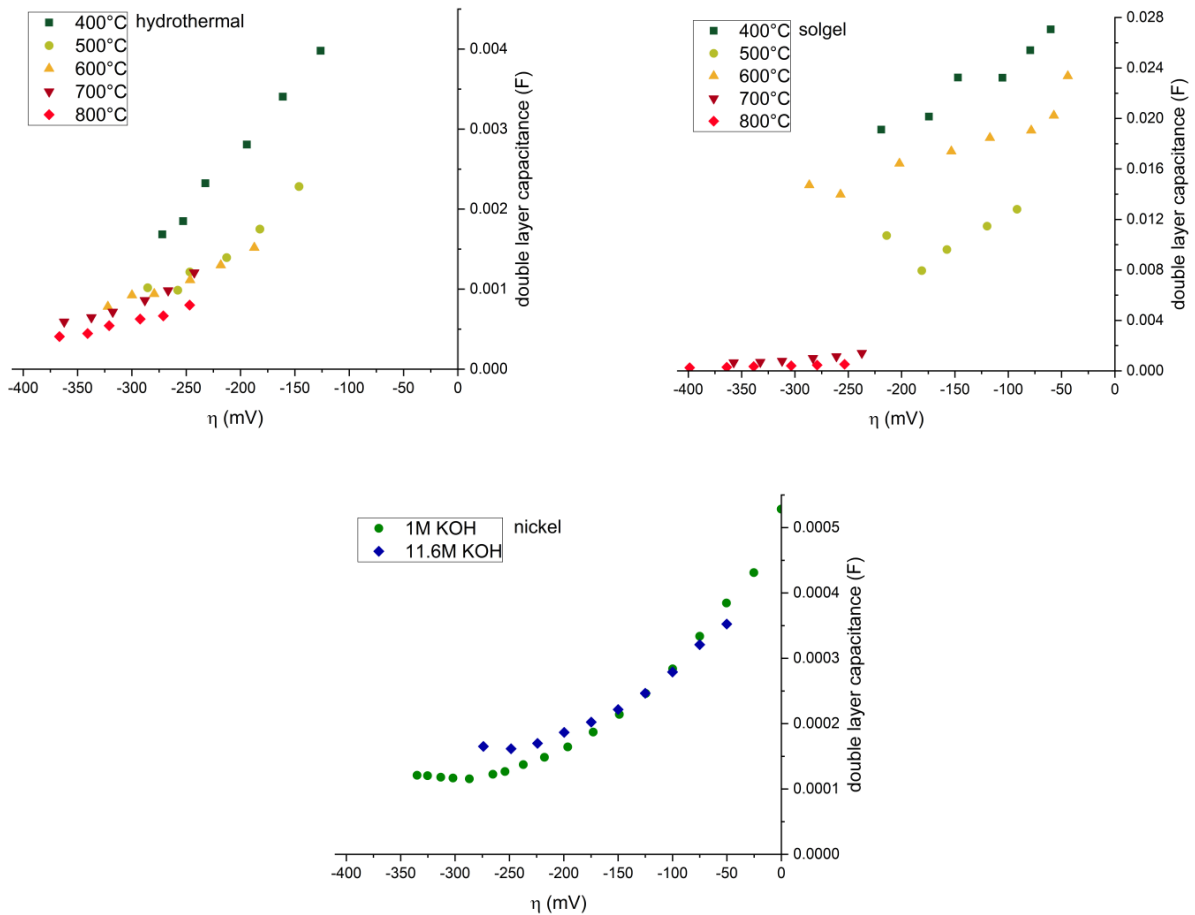


Fig. 5.3: Correlation of the double layer capacitance, obtained from an R(RQ) fitting, to the HER overpotential at room temperature in 45 w% KOH. Top left: Nickel-molybdenum electrocatalysts produced through hydrothermal synthesis and reduced at different temperatures, with a mass loading of $190 \mu\text{g}/\text{cm}^2$. Top right: Nickel-molybdenum electrocatalysts produced through solgel synthesis and reduced at different temperatures, with a mass loading of $380 \mu\text{g}/\text{cm}^2$. Bottom: Nickel-foil, substrate material of the samples above, tested in 1 M and 11.6 M (~ 45 w%) KOH. Note that the ordinate changes between the plots.

≈ 280 between the measured samples, which is a direct effect of the different loadings of the electrocatalysts, a relative trend for all samples is visible. In spite of the difference, all measurements appear to have an overpotential-dependent decrease of the double layer capacitance by a factor of up to ≈ 5 between lowest and highest overpotential. Although a decrease of the ECSA, and thus the double layer capacitance, could be considerable through an increasing amount of trapped hydrogen with increasing current density, the deviation is too high to result from surface blocking alone. In order to investigate possible overpotential-depending effects, the impedance analyses of two representative samples, hydrothermal 400 °C and solgel 700 °C, were extended with DRT analyses. DRT was applied to understand if several processes are distinguishable with regards to the overpotential. The DRT extended impedance spectra are displayed in Fig. 5.4 and 5.5, respectively.

Remarkably, DRT does not show any distinguishable processes besides a single process. The process increases in summit frequency, while it simultaneously decreases in amplitude with increasing current density and overpotential. Hence, the origin of only one visible process, while the obtained double layer capacitance varies by a factor exceeding possible experimental deviations in a simple R(RQ)-fitting, is likely to be correlated to an underlying secondary process on the same timescale as the faradaic hydrogen evolution.

Two possible processes may be describing the underlying effect. Hydrogen adsorption and Mo-leaching might be causing a non-faradaic pseudocapacitive contribution. This contribution is modeled together with the double layer capacitance in the R(RQ)-fitting, which would overestimate the double layer capacitance. The difference between these two considerable contributions can be deduced as follows. Mo-leaching is a redox process, which occurs, according to the literature [73, 76], at potentials > -150 mV vs HER equilibrium potential. It is further not necessarily correlated to the hydrogen evolution reaction rate. Hydrogen adsorption, on the other hand, can occur between a potential of 0 to -300 mV vs HER equilibrium potential [63, 170]. This process is further directly linked to the hydrogen evolution kinetics, where the pseudocapacitance is a function of the RDS. It is thus a process occurring on the identical timescale as the hydrogen evolution. Therefore, the observed pseudocapacitance contributions to the double layer capacitance may be attributed to the effect of overpotentially deposited hydrogen H_{opd} . The adsorption process occurs simultaneously with the HER. On the other hand, the possibility of Mo-leaching with hydrogen

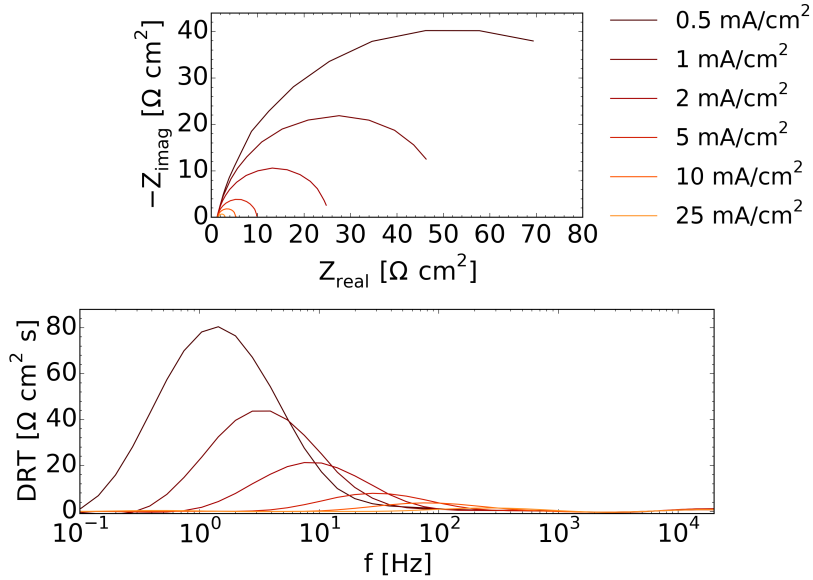


Fig. 5.4: Results from electrochemical impedance spectroscopy of the hydrothermal 400 °C electrocatalyst. Top: Nyquist plots. Bottom: DRT plots. Results from galvanostatic EIS measurements at 0.5, 1, 2, 5, 10, and 25 mA/cm²_{geometric} in 45 w% KOH.

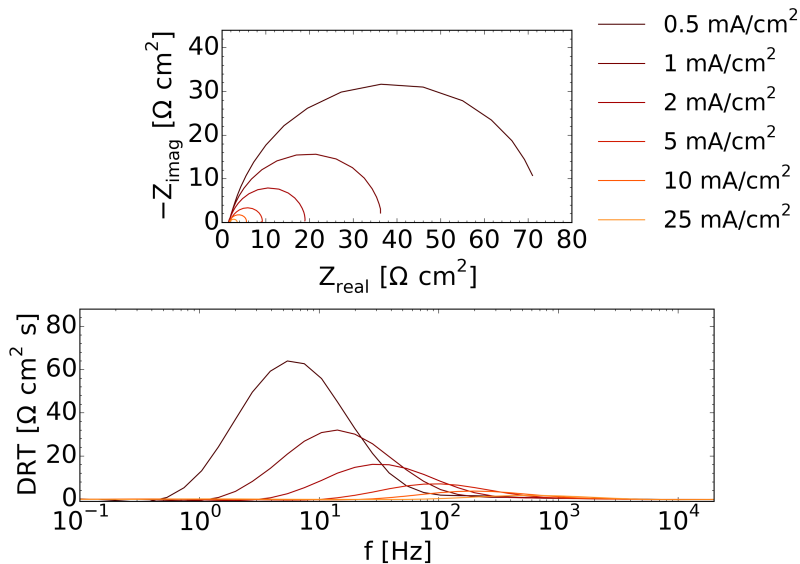


Fig. 5.5: Results from electrochemical impedance spectroscopy of the sol-gel 700 °C electrocatalyst. Top: Nyquist plots. Bottom: DRT plots. Results from galvanostatic EIS measurements at 0.5, 1, 2, 5, 10, and 25 mA/cm²_{geometric} in 45 w% KOH.

evolution [69] (Eq. (2.23)) cannot be ruled out at this point. As a process causing pseudocapacitance occurs either way, a new impedance modeling is necessary, which considers this parallel occurring process.

5.2.2 Kramers-Kronig tests

As the overpotential-dependent double layer capacitance variations may be explained by a pseudocapacitance, it is of particular interest to understand if the observed effect indeed originates from an electrode process, such as hydrogen adsorption or from Mo-leaching, or from a measurement inaccuracy.

Consequently, Kramers-Kronig (KK) analyses were conducted to exclude that measurement artifacts cause the observed correlation between the obtained double layer capacitance by an R(RQ)-fitting and the overpotential. The KK-analyses of the aforementioned selected electrocatalysts, hydrothermal 400 °C and solgel 700 °C, are representatively visualized in Fig. 5.6. Apparently, the impedance measurements have an increasing error with lowering measurement frequencies. The higher current density impedance spectra, 5, 10 and 25 mA/cm², approach a stable residual error at around 3% for frequencies below 20 Hz in both cases. The lower current density spectra reach errors above 5% with the 0.5 mA/cm² spectra not reaching a stable value despite the high residual error above 20%. These errors are easily explainable by measurement noise at these low frequencies, where gas evolution, mass transport and instrument noise can result in varying measurement results over the longer measurement time at low frequencies.

Notably, in comparison with Fig. 5.4 and 5.5, the low frequency noise of the low current density spectra overlap with the DRT-calculated impedance maxima. Hence, the obtained double layer capacitances with these spectra inherit a noteworthy error, which may cause a several-fold difference between all obtained double layer capacitance values. However, the by KK-tests evaluated errors do not reflect this deviation. Therefore, albeit lower current density spectra can be considered erroneous, the remarkable deviation cannot stem from errors alone, which points towards electrode processes causing a pseudocapacitive contribution.

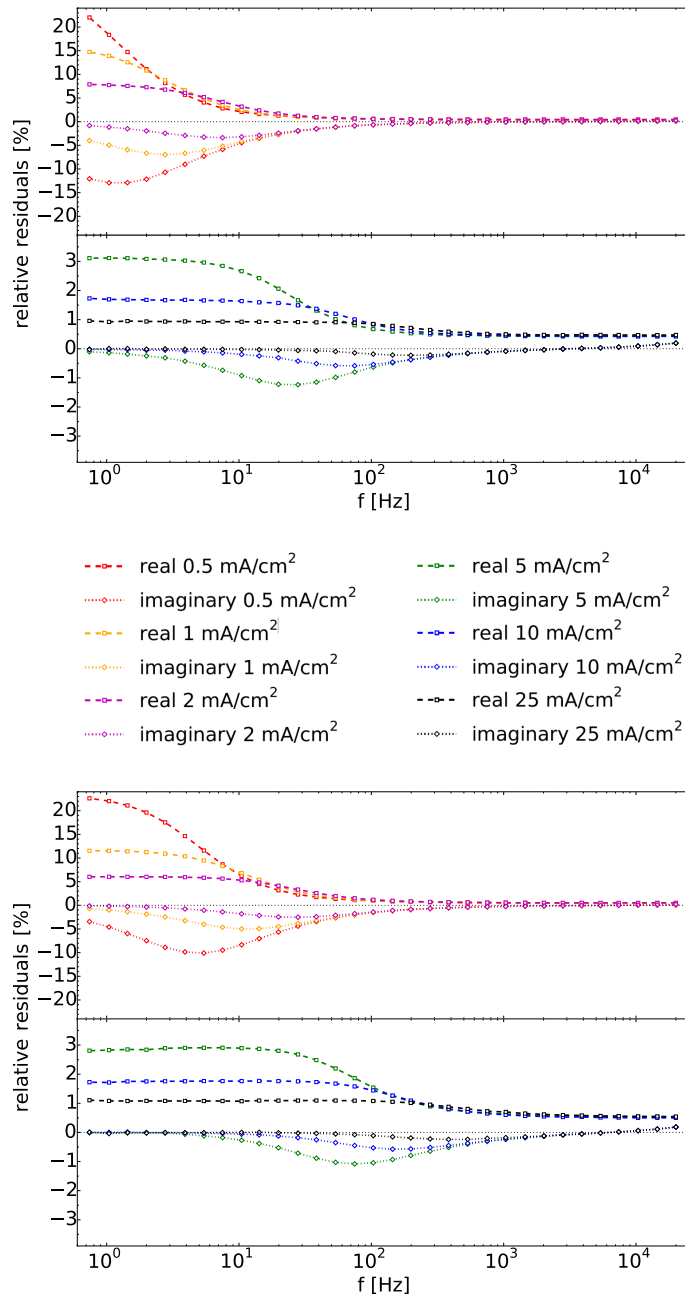


Fig. 5.6: Kramers-Kronig tests of the hydrothermal 400 °C (top) and of the sol-gel 700 °C (bottom) electrocatalyst. Results from galvanostatic EIS measurements at 0.5, 1, 2, 5, 10, and 25 mA/cm²_{geometric} in 45 w% KOH. For enhanced visibility, results from 0.5, 1, and 2 mA/cm²_{geometric} (top of the subplot) and from 5, 10, and 25 mA/cm²_{geometric} (bottom of the subplot) are plotted with different ordinate-scaling.

5.2.3 Advanced impedance modeling with Armstrong's electric circuit

As shown in the previous sections, a simple R(RQ)-fitting does not describe the HER electrocatalyst testings accurately. DRT analyses guide to a process occurring on the same timescale as the HER, which is supposedly the hydrogen adsorption pseudocapacitance effect [63, 170, 171]. According to published work [35, 38, 158], NiMo electrocatalysts can be described with Armstrong's electric circuit $R_s(C_1(R_{ct}(R_p Q_2)))$, illustrated in Fig. 5.7.

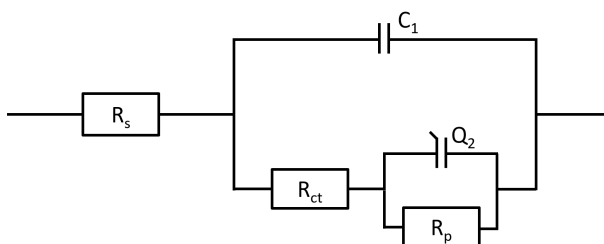


Fig. 5.7: Armstrong's electric circuit. A simple $R_s(R_{ct}C_1)$ electrocatalyst equivalent circuit is extended by a pseudocapacitive process $R_p Q_2$, which occurs in parallel to the double layer capacitance as described by C_1 .

Armstrong's electric circuit extends a simple $R_s(R_{ct}C_1)$ electrocatalyst modeling (R_s : series resistance, R_{ct} : charge transfer resistance, and C_1 : capacitor equivalent to the electrode's double layer capacitance) by a $R_p Q_2$ element, which describes the pseudocapacitance effect (R_p : resistance of the pseudo-process and Q_2 : CPE describing the pseudocapacitance). For the fitting of this model, the origin of the pseudocapacitance is not of relevance. The double layer capacitance during the HER, which is taken for the electrochemical surface area estimation, can be obtained either way. Hence, the model is suitable for the hydrogen adsorption phenomena as well as the molybdenum redox activity, if only one of these occurs without the other. In relation to Fig. 5.3, the double layer capacitance obtained through the R(RQ)-fitting and through Armstrong's electric circuit are demonstrated in relation to the overpotential for the representative samples in Fig. 5.8.

From Fig. 5.8, it becomes apparent that the R(RQ)-fitting indeed overestimates the double layer capacitance at lower overpotentials. The more complex Armstrong model leads to more coherent results over the entire HER overpotential spectrum. However, fitting two processes occurring on similar timescales makes distinguishable differences challenging. The

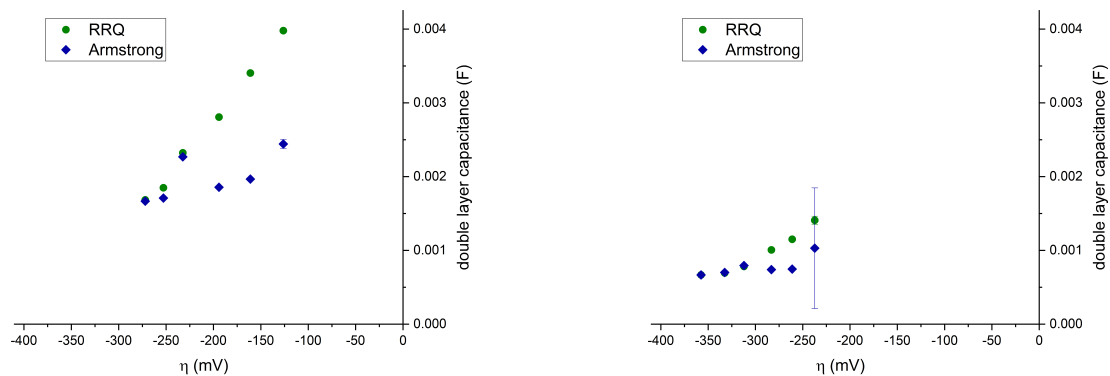


Fig. 5.8: Correlation of the double layer capacitance obtained from two different fitting models to the HER overpotential. The fitting models are R(RQ) (green) and Armstrong’s electric circuit $R_s(C_1(R_{ct}(R_p Q_2)))$ (blue). Measurements from the electrocatalyst hydrothermal 400 °C (left) and solgel 700 °C (right), with a mass loading of 190 and 380 $\mu\text{g}/\text{cm}^2$, respectively, on nickel-foil substrate. Measurements at room temperature in 45 w% KOH.

fitted value at the highest overpotential shows that both fitting models turn to unity in this point. This is in agreement with a pseudocapacitive effect, which becomes negligible at high overpotentials, and thus becomes negligible in the fitting process and in the associated fitting uncertainty.

In conclusion, the R(RQ)-fitting describes the double layer capacitance as good as Armstrong’s electric circuit at overpotentials higher than 250–300 mV. Therefore, impedance fittings at high overpotentials with a simple R(RQ)-fitting lead to a reliable estimate of the double layer capacitance, while Armstrong’s electric circuit can be applied at all overpotentials. The residual deviations are estimated to stem from measurement noise at low current densities. A further change of the fitting model was left out, as the complexity of several processes occurring on the same timescale does not necessarily increase the accuracy of the fitted data. Furthermore, the origin of two pseudocapacitive processes is not proven. Additionally, an R(RQ)-fitting at high overpotentials and a fitting with Armstrong’s electric circuit appear to sufficiently describe the processes, which leads to coherent double layer capacity estimates. The different overpotential limits, where R(RQ)-fitting and Armstrong’s electric circuit turn to unity, can be considered as a direct result of different rate-determining steps, ultimately affecting the pseudocapacitance by hydrogen adsorption. These different RDS might result from different apparent active species in the various electrocatalysts.

5.3 Electrochemical active surface area

The approach to model the double layer capacitance from impedance aims to evaluate the electrochemically active surface area (ECSA). As this approach is debated within the literature [34, 166, 167], this chapter precedes to compare different methods to evaluate surface area estimates. Besides impedance modeling, non-faradaic cyclic voltammetry and the formation of a monolayer of α -Ni(OH)₂ are compared to another.

5.3.1 Correlating the electrochemical active surface area obtained by EIS, the formation of alpha nickel hydroxide and non-faradaic cyclic voltammetry

The method based on impedance spectroscopy led to the conclusion that double layer estimates from EIS appear to deliver fair values, when the HER overpotential is either sufficiently high, regardless of the more complex fitting model, or a more complex fitting model with Armstrong's electric circuit is applied.

Two further methods to obtain surface area estimates proceed by cyclic voltammetry. In general, non-faradaic cyclic voltammetry at different scan rates leads to the double layer capacitance [11]. This approach hence is compared to the modeled double layer capacitance from EIS, as similar results would support the previously obtained results from EIS. Another method to estimate the ECSA in nickel electrodes is the transition of Ni⁰ → Ni²⁺. Through voltammetric measurements, the formation of a monolayer of α -Ni(OH)₂ can be used for an estimation of the ECSA. The charge of the oxidation peak at $E_{\text{peak}} \approx 350$ mV vs RHE in a potential window of 0 – 500 mV vs RHE is equal to the ECSA with a charge density of 514 $\mu\text{C}/\text{cm}^2$ [18, 43]. This method is not directly applicable for nickel-molybdenum electrodes, as it would exclude the possibility of molybdenum being part of the ECSA. However, it can be taken into consideration for nickel electrocatalysts, which show a similar behavior as the nickel-molybdenum electrocatalysts in the impedance studies. The similarity of the impedance studies allows for a conclusion by analogy between nickel and nickel-molybdenum electrocatalysts.

To define the non-faradaic region, Fig. 5.9 represents five cyclic voltammograms between –200 and 500 mV vs RHE at a scan rate of 50 mV/s on the sample NiMo solgel

600 °C. The CVs show two redox processes occurring at $\approx 150/ - 75$ mV vs RHE (red marking) and at $\approx 350/0$ mV vs RHE (green marking). The non-faradaic area was defined to be 50 – 100 mV vs RHE (blue marking). In this area, CVs at scan rates from 500 mV/s down to 5 mV/s were conducted to obtain the double layer charging currents, as illustrated in Fig. 5.10. For each scan rate, the third cycle is displayed. From the charging currents over the scan rates, a linear fitting results in the double layer capacitance of $(14.98 \pm 0.22) \cdot 10^{-3}$ F ($r^2 = 0.985$), after excluding the scan rates 5, 10 & 20 mV/s.

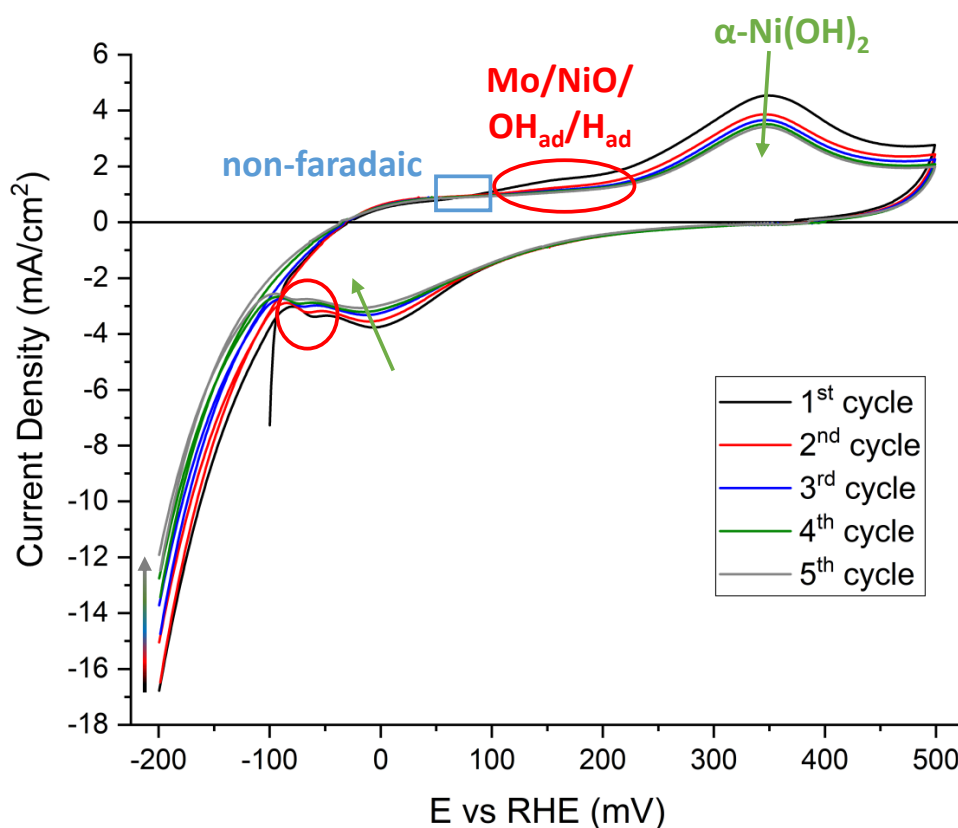


Fig. 5.9: Cyclic voltammograms of the NiMo solgel 600 °C electrocatalyst between $-200 - +500$ mV vs RHE, starting at -100 mV vs RHE, at 50 mV/s in 45 w% KOH. The voltammograms indicate the altering oxidation and reduction of α -Ni(OH)₂ around 350 mV and 0 mV vs RHE, respectively. It is following another redox-process occurring between 150 mV (oxidation) and -75 mV (reduction) vs RHE, which could be the leaching and redeposition of Mo, or the oxidation and reduction of NiO, or hydroxide or hydrogen ad/desorption. The non-faradaic region was chosen to be between 50 mV and 100 mV vs RHE for following measurements.

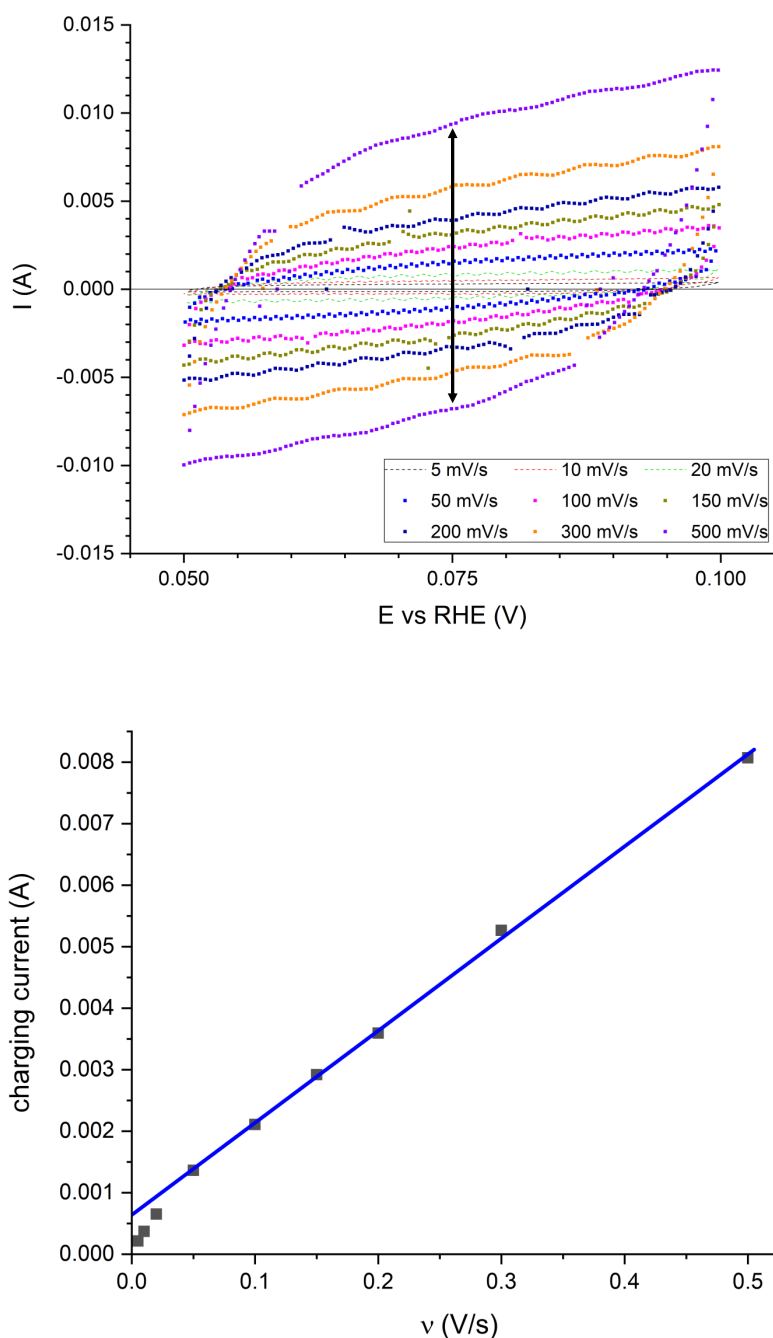


Fig. 5.10: Top: 3rd cycle of cyclic voltammograms in the non-faradaic region of the sol-gel 600°C electrocatalyst at scan rates between 500 and 5 mV/s in 45 w% KOH. Bottom: The charging currents at 75 mV vs RHE (see top of the figure) are plotted vs the scan rate. The double layer charge is obtained by a linear fit (blue line), excluding the scan rates below 50 mV/s. Geometric surface area of 3.14 cm^2 . Fitting result: $(14.98 \pm 0.22) \cdot 10^{-3}\text{ F}$.

In relation to the double layer capacitance obtained through non-faradaic cyclic voltammetry (CV-DL), the modeled capacitances from an R(RQ) and an Armstrong-fitting are illustrated with regards to the HER overpotential in Fig. 5.11. As the result from non-faradaic CV is considered to be the most reliable, it was set as the reference point 1.0 in the figure. Both fitting routines follow the previously observed overpotential-dependent effects. At HER overpotentials higher than 200 mV, both fitting routines turn to unity. Furthermore, they turn to unity with the value obtained from non-faradaic CV, when the associated errors are considered. In case of the Armstrong-fitting, the modeled double layer capacitance represents the non-faradaic double layer capacitance within $\pm 10\%$ for all measurements, except for 0.5 mA/cm^2 .

The observed deviations between CV-DL and Armstrong-fitting could result from either an erroneous fitting-model or from measurement noise. Thus, Fig. 5.12 represents the comparison of the impedance plots from the sample NiMo solgel 600°C with the results from KK tests. As the summit frequency of the measurements at $0.5, 1$ & 2 mA/cm^2 exhibit relative errors between $3 - 6\%$ for the imaginary and $5 - 8.5\%$ for the real impedance, the differences, especially of the measurement at 0.5 mA/cm^2 , can be correlated to measurement noise. Hence, impedance measurements modeled with an Armstrong-fitting indeed result in coherent and valid estimations of the double layer capacitance. Consequently, surface area estimates from overpotential EIS can be made.

The surface area estimate of the NiMo solgel 600°C sample from $\alpha\text{-Ni(OH)}_2$, calculated as Ni, is between $\approx 10 - 15$ times lower than the values obtained by EIS and CV-DL. The double layer was estimated to scale with the ECSA by $40 \mu\text{F/cm}^2$ [8]. This difference can be explained by the presence of Mo in the catalyst. Either the Mo takes part in the ECSA and is not considered in the ECSA estimation of $\alpha\text{-Ni(OH)}_2$, or Mo alters the active Ni site, without taking place in the ECSA, to the extent that the active Ni site does not form the $\alpha\text{-Ni(OH)}_2$ phase.

The cyclic voltammograms in the HER underpotential region are detrimental to the NiMo solgel 600°C electrocatalyst. The decrease of both redox processes with cycling is associated with a decrease of the current achieved at -200 mV vs RHE. To rule out that this deterioration had a substantial destructive effect on the electrocatalyst, Fig. 5.13 shows the backscans of iR -corrected iV -curves at 5 mV/s after the CVs. The underpotential ex-

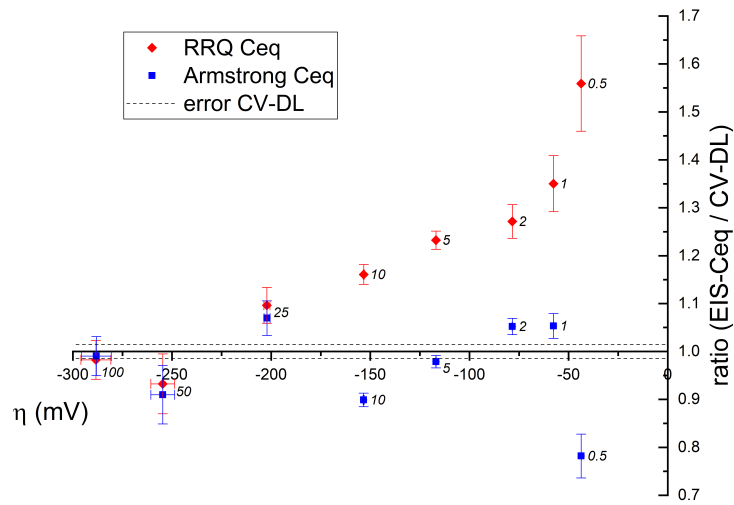


Fig. 5.11: Relative ratio between the double layer capacitance obtained by galvanostatic EIS, through an R(RQ) (legend: RRQ Ceq) and an Armstrong (legend: Armstrong Ceq) fitting, in relation to the double layer capacitance from the non-faradaic region (legend: CV-DL) of the solgel 600 °C electrocatalyst. The value of 1.0 represents the double layer capacitance from the non-faradaic region (Fig. 5.10); the dashed lines are the error bars of the capacitance from CV-DL. Measurements at 1, 2, 5, 10, 25, 50 and 100 mA/cm² (indicated in the figure) at room temperature in 45 w% KOH.

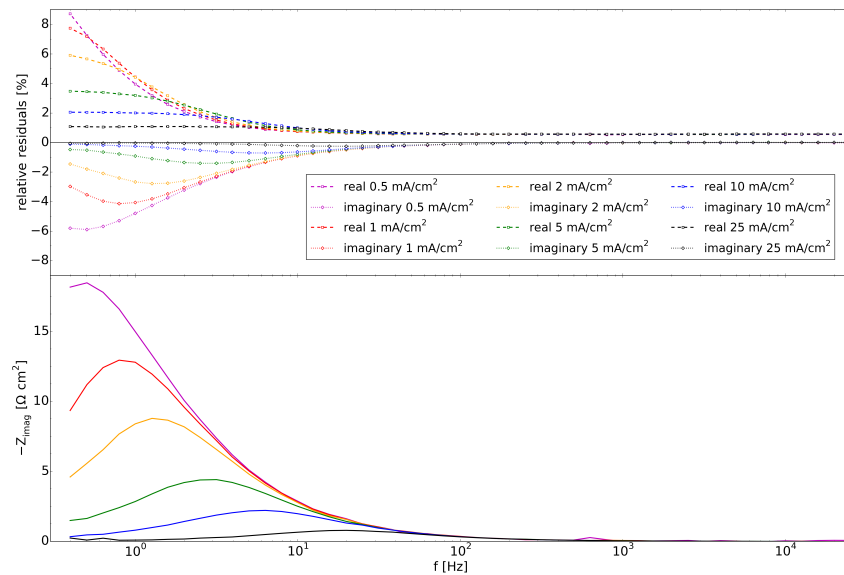


Fig. 5.12: Evaluation of the quality of the results from Fig. 5.11. Top: KK tests. Bottom: $-Z_{Im}$ over f . The 0.5 mA/cm² measurement represents the data point with the lowest overpotential in Fig. 5.11; 1, 2, 5, 10, 25 mA/cm² accordingly with increasing overpotential. For enhanced visibility, 50 and 100 mA/cm² are spared from this plot.

posure did cause an increase of the HER overpotential of ≈ 20 mV at 100 mA, while EIS at 10 mA/cm² did not show a deviation of the double layer capacitance. Therefore, a modification of the electrocatalyst caused a minor loss of intrinsic electrocatalytic activity, while no electrocatalyst was lost. This effect may further explain the $\pm 10\%$ deviation between EIS and CV-DL.

Surface area estimates through the formation of a monolayer of α -Ni(OH)₂ by cyclic voltammetry were described previously to deliver reasonable estimates on plain nickel electrodes [18, 43]. Since such a procedure is to this date not established for nickel-molybdenum electrodes, a conclusion by analogy was made. Earlier in this chapter, it was shown that overpotential EIS does result in the approximation of the double layer capacitance by comparing the EIS results to non-faradaic CV. In the following, a similar comparison is repeated with a plain nickel foil. However, the reference point 1.0 is set to the surface area estimate from the formation of a monolayer of α -Ni(OH)₂. Furthermore, the surface area estimate from the double layer capacitance was chosen to be at 40 μ F/cm² [8]. The results of this comparison, for both fitting models and for 1 and 11.6 M KOH, are represented in Fig. 5.14.

The comparison indicates that the surface area estimates from EIS, with an R(RQ)-fitting, coincide at overpotentials greater than 200 mV with the surface area estimate from the α -Ni(OH)₂ method. A similar result can be obtained for the Armstrong-fitting, while this model allows for a comparison at lower overpotentials than the R(RQ)-fitting. The deviations at low HER overpotentials may, similar to previous results, stem from measurement noise. Therefore, surface area estimates by EIS are an applicable method for Ni electrocatalysts, as the method delivers comparable results to the widely accepted α -Ni(OH)₂ method, when the modeled double layer capacitance is not influenced by noise or side processes. Additionally, it is further possible to argue that the ECSA estimation of NiMo electrocatalysts by EIS is an applicable method, as the EIS results on these electrocatalysts allow to obtain the double layer capacitance. The double layer capacitance, with a value of 40 μ F/cm² [8], reflects similar surface area estimates in Ni electrodes in comparison to the α -Ni(OH)₂ method. The *in situ* EIS method further bears the advantage that ECSA estimations can be made during operation, without introducing further chemicals or by changing the electrocatalyst's potential to possibly degrading HER-underpotential conditions.

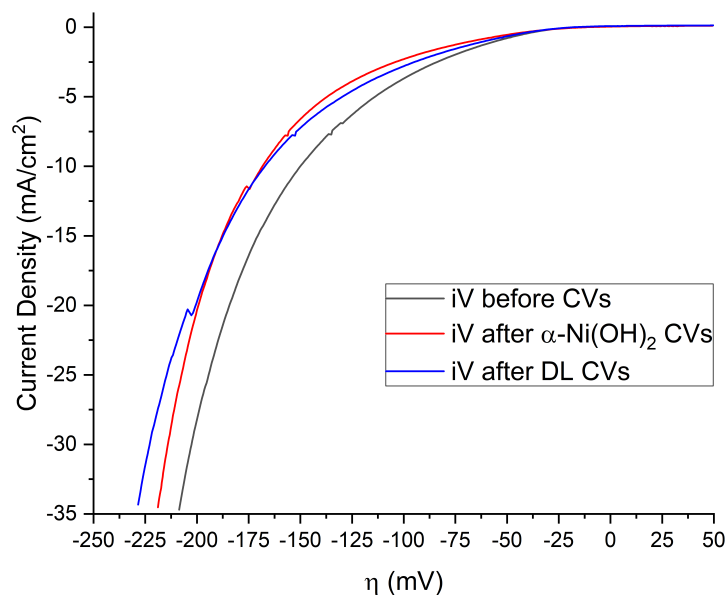


Fig. 5.13: Influence of the cyclic voltammograms on the kinetics of the NiMo solgel 600 °C electrocatalyst in 45 w% KOH. Results from iV -curves at 5 mV/s, corrected for the series resistance. The ECSA, derived from overpotential impedance at $10 \text{ mA/cm}^2_{\text{geometric}}$, did not show a significant difference between the three measurements before cyclic voltammetry, after $\alpha\text{-Ni(OH)}_2$ CV or after double layer CV.

5.3.2 Interdependency between electrochemical active surface area, partial oxidation and kinetics

The origin of the high activity of nickel-molybdenum electrocatalysts for the alkaline HER is debated in the literature. It is elusive whether the origin of the high performance is due to an intrinsic effect, if it is due to high surface areas in nickel-molybdenum electrocatalysts, or if nickel is the active site with a different chemical state than in plain nickel electrocatalysts. To address this question, the *in situ* electrochemical impedance method to derive the electrochemical active surface area was first validated in correlation to the more established methods in the literature of non-faradaic cyclic voltammetry and the formation of alpha nickel hydroxide. In this section, the ECSA will be correlated to the performance of a variety of Ni and NiMo electrocatalysts.

In order to shed light on the question of the importance of the ECSA in these electrocatalysts, the iR -corrected overpotentials measured at a geometric current density of

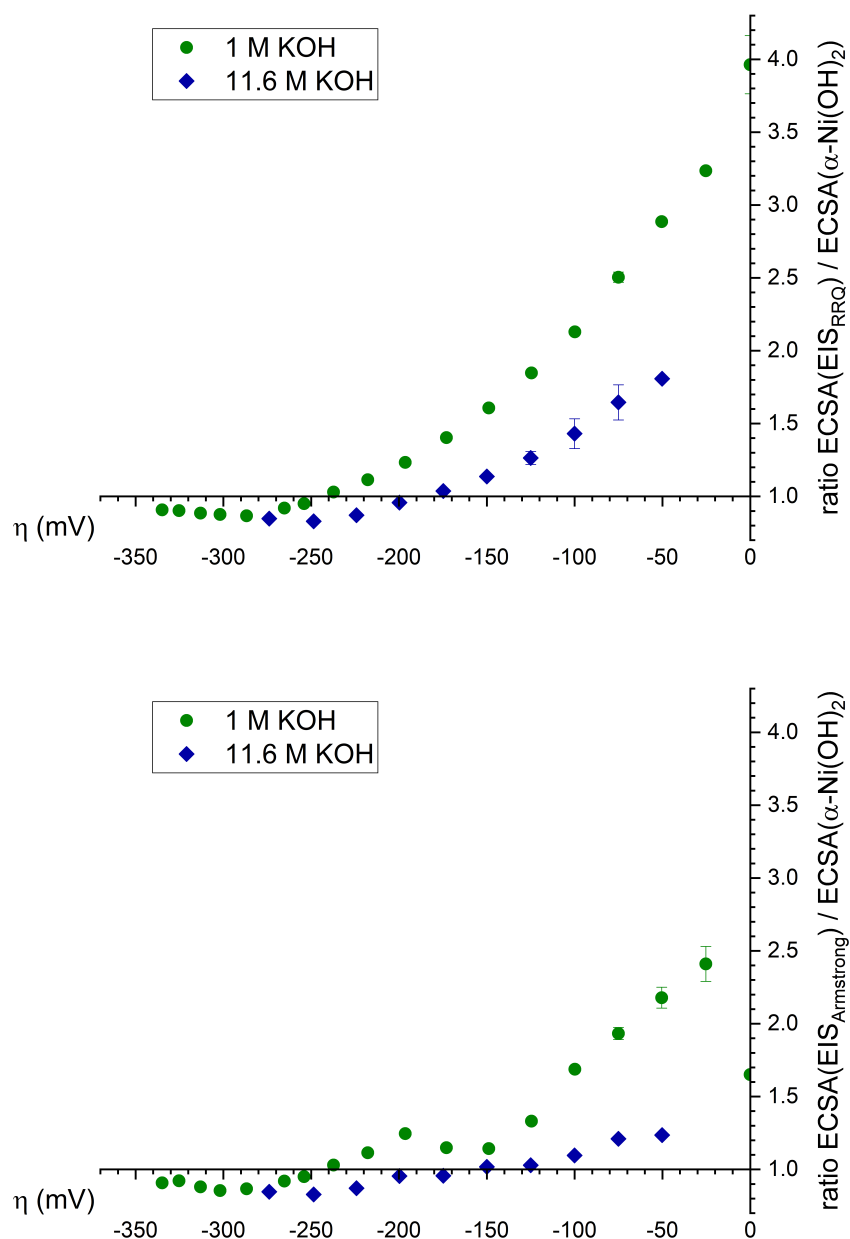


Fig. 5.14: Correlation between surface area estimates on a nickel foil in 1 M and 11.6 M (~ 45 w%) KOH. Ratio between the estimate obtained from potentiostatic EIS to the estimate by the formation of a monolayer of α -Ni(OH)₂, with respect to the HER overpotential. Results from an R(RQ)-fitting (top), and from an Armstrong-fitting (bottom). The ECSA value for the double layer obtained by EIS is $40 \mu\text{F}/\text{cm}^2$, the ECSA value for the formation of α -Ni(OH)₂ is $514 \mu\text{C}/\text{cm}^2$. Measurements at room temperature.

10 mA/cm² after 5 min were related to the surface roughness factor. The surface roughness R_f is the ratio between the estimated ECSA and the geometric surface area (3.14 cm²) of the sample, following Eq. (5.1). The ECSA estimation was made, based on Chap. 5.3.1, by electrochemical impedance spectroscopy at 10 mA/cm² with an Armstrong fitting and a value of 40 μF/cm².

$$R_f = \frac{A_{ECSA}}{A_{geometric}} \quad (5.1)$$

The resulting values shown in Fig. 5.15 are given as a semi-logarithmic dependence of the performance at 10 mA/cm²_{geometric} of a variety of Ni and NiMo electrocatalysts in 11.6 M KOH. The expected correlation of an electrocatalyst, whose intrinsic kinetics remain identical, is a linear decrease with surface roughness in this semi-logarithmic correlation. It is noteworthy mentioning that the variety of these electrocatalysts, as mentioned in Chap. 5.1, consists of different alloys and oxides. The measured samples are tabulated in Tab. 5.1. Ni samples, which have identical numbers in the figure, are the same sample. The sample was measured in its as received state first. For the second measurement, it was exposed through one voltammogram up to 1 V vs RHE at 50 mV/s to obtain a partially oxidized surface [42, 45]. According to the literature, partially oxidized Ni electrocatalysts appear to have a superior performance compared to plain Ni or NiO [47, 161, 172], see also Chap. 2.4.

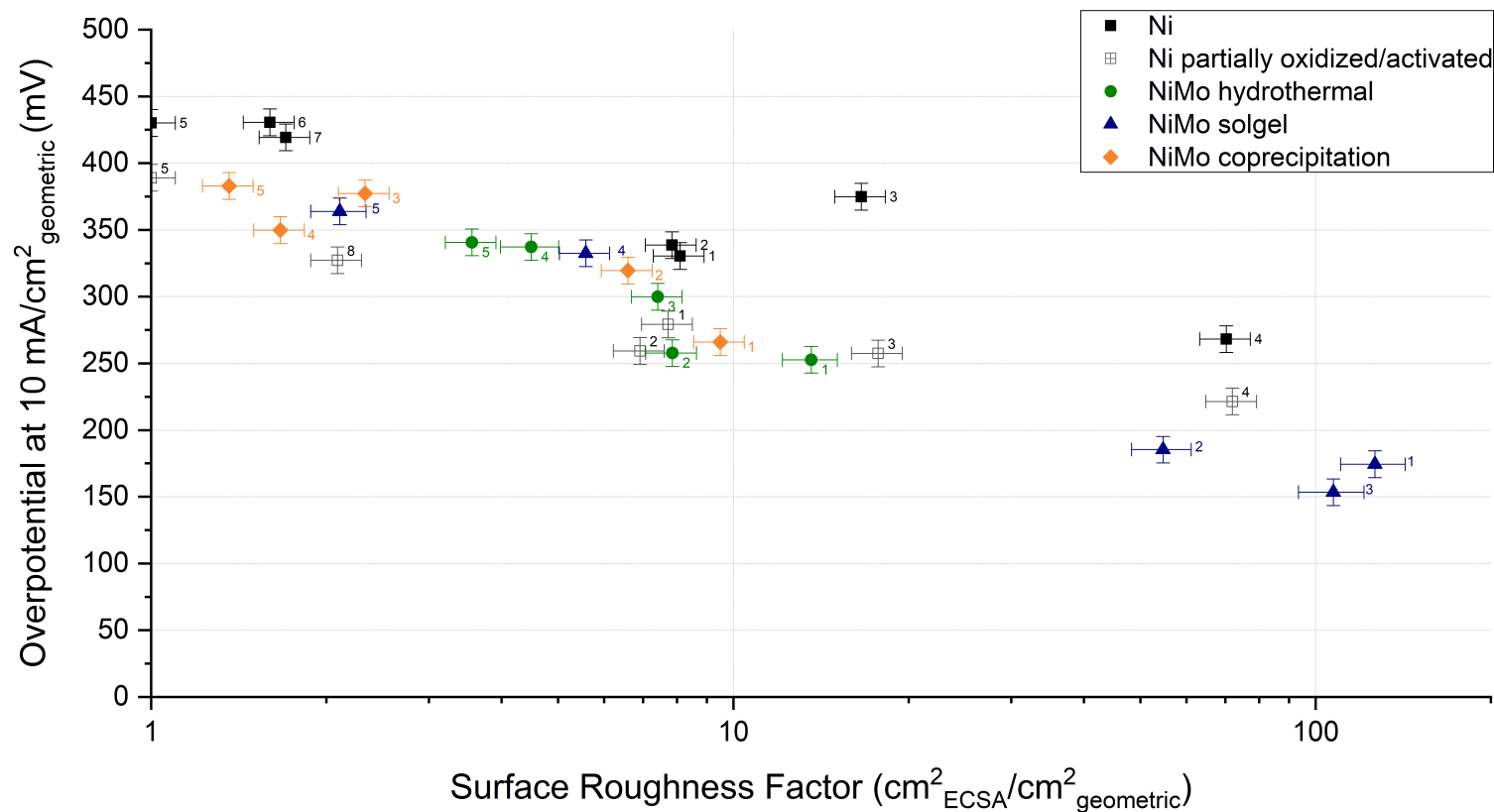


Fig. 5.15: The geometric performance at 10 mA/cm² after 5 min chronopotentiometry of a variety of nickel, partially oxidized/activated nickel and nickel-molybdenum electrocatalysts in correlation to the surface roughness factor. Ni and Ni partially oxidized/activated samples with similar numbers are the same sample. The Ni sample was subjected to 1 V vs RHE by cyclic voltammetry at 50 mV/s to obtain the partial oxidation. The surface roughness is calculated through the ratio between ECSA, derived from EIS at 10 mA/cm²_{geometric} with an Armstrong-fitting, and the geometric surface area of 3.14 cm². Measurements at room temperature in 45 w% KOH. See Tab. 5.1 for sample description.

Tab. 5.1: Electrocatalyst samples and substrates (written as electrocatalyst / substrate), as presented in Fig. 5.15.

No.	Ni	NiMo hydrothermal	NiMo solgel	NiMo coprecipitation
1	Ni-felt	reduced at 400 °C / Ni-foil	reduced at 400 °C / Ni-foil	reduced at 400 °C / Ni-foil
2	Ni LDH reduced at 450 °C / Ni-felt	reduced at 500 °C / Ni-foil	reduced at 500 °C / Ni-foil	reduced at 500 °C / Ni-foil
3	sintered US nano Ni 1.3 mg · cm ⁻² / Ni-foil	reduced at 600 °C / Ni-foil	reduced at 600 °C / Ni-foil	reduced at 600 °C / Ni-foil
4	sintered US nano Ni 2.6 mg · cm ⁻² / Ni-foil	reduced at 700 °C / Ni-foil	reduced at 700 °C / Ni-foil	reduced at 700 °C / Ni-foil
5	polished Ni-foil	reduced at 800 °C / Ni-foil	reduced at 800 °C / Ni-foil	reduced at 800 °C / Ni-foil
6	ethanol cleaned Ni-foil			
7	ethanol cleaned Ni-foil			
8	chemically and electrochemically activated Ni-foil			

In comparing different types of electrocatalysts on the same baseline, two main trends can be differentiated from Fig. 5.15. The plain Ni electrocatalysts apparently seem to reveal a trend with surface roughness, which is less pronounced than all other electrocatalysts. The scattering of the plain Ni-trend could result from the history-dependence of Ni electrocatalysts described previously in Chap. 2.4. For the second trend, which includes all types of NiMo electrocatalysts, without a differentiation of the presence or absence of molybdenum oxide, the scattering of the data at $R_f \approx 7 - 8$ could either relate to an effect or measurement artifact. From these results alone, a deviation from the overarching trend of all types of NiMo electrocatalysts cannot be concluded. Most importantly, the partially oxidized Ni electrocatalysts display an intrinsic electrochemical activation with, for instance, a decrease of the overpotential by more than 100 mV at consistent surface roughness for sample 3 (sintered US nano Ni). The activation of partially oxidized Ni electrocatalysts is, following publications, expected. Rather unexpected is the overlap of the partially oxidized Ni electrocatalysts with the trend of the NiMo electrocatalysts.

The overlap of activated Ni samples with the oxide supported and alloyed NiMo samples is a consequential result in the understandings of Ni and NiMo electrocatalysts. It can be hypothesized that Ni, in a specific chemical state, is the active site in all of these Ni and NiMo electrocatalysts. This chemical state can either be achieved through a partially oxidized Ni surface, or through the presence of Mo. The oxide support, despite reports claiming otherwise in publications concerning other types of electrocatalysts [26, 162], primarily has an effect on the apparent geometric performance enhancement through a high electrochemical surface area. Although it cannot be ruled out at this stage, the presence of oxides in NiMo electrocatalysts does not appear to increase the intrinsic electrocatalytic performance, but rather increases the amount of highly active Ni sites.

As these measurements were all conducted in 11.6 M KOH, and the comparison to 1 M KOH is of interest, measurements on further Ni and on electrodeposited NiMo samples were added to the figure. In short, a significant deviation between the results in both electrolyte concentrations outside the previously described scatter could not be observed. Furthermore, the comparison in this figure was extended with results from the literature. In the previous sections, the comparability of ECSA estimations through non-faradaic CV, overpotential EIS and the formation of α -Ni(OH)₂ (only for plain Ni electrocatalysts) was

shown. Since the electrolyte concentration further does not appear to have a major impact, it is possible to compare literature results irrespective of the electrolyte concentration, when the ECSA estimations match the procedure of this chapter. Consequently, literature results considering the ECSA through these methods were included. For a part of these literature results, the estimation of the ECSA was recalculated to match with the, in this work verified, assumption of $40 \mu\text{F}/\text{cm}^2$ for the equivalence between double layer capacitance and ECSA.

Admittedly, results from the literature obtained in different setups under different measurement conditions and with different ECSA estimations certainly face measurement-related deviations. However, the comparison of the samples from this work requires a context to a greater amount of data. This is especially the case for the correlation to data from previous literature findings on the effects of partial oxidation, as Fig. 5.15 reveals that this effect is a crucial key point in the intersection between Ni and NiMo electrocatalysts. Hence, Fig. 5.16 includes the performance data obtained from different literature sources, which are tabularized in Tab. 5.2, 5.3, 5.4, and 5.5. The tables also include the procedures for how the ECSA and η_{10} were obtained. When the overpotential at $10 \text{ mA}/\text{cm}^2$ was obtained through a Tafel analysis (galv.: galvanostatic Tafel analysis; pot.: potentiostatic or potentiodynamic Tafel analysis), η_{10} was calculated from the published Tafel parameters. The figure additionally includes platinum measurements as reference to show the intrinsic difference to this benchmarking electrocatalyst.

At first glance, the necessity of a comprehensive study including lower surface roughness (< 100) samples is underlined by this comparison. A dominant challenge from literature values can be attributed to the predominantly followed goal of creating high surface area electrocatalysts, which increases the difficulty of comparing intrinsic properties. The samples of this work cover the range between a surface roughness of 1–100. Thereby, an overarching comparison between all data points may be made, as the figure includes the entire range between a surface roughness of 1 and an overpotential in close proximity to zero. Furthermore, the literature and self-obtained data overlap in terms of the surface roughness, which allows to claim comparability of such. As the previously found trends of plain Ni electrocatalysts and of NiMo and activated Ni electrocatalysts could be problematic to observe among these 88 data points, Fig. 5.17 divides Fig. 5.16 into the trend-correlated data.

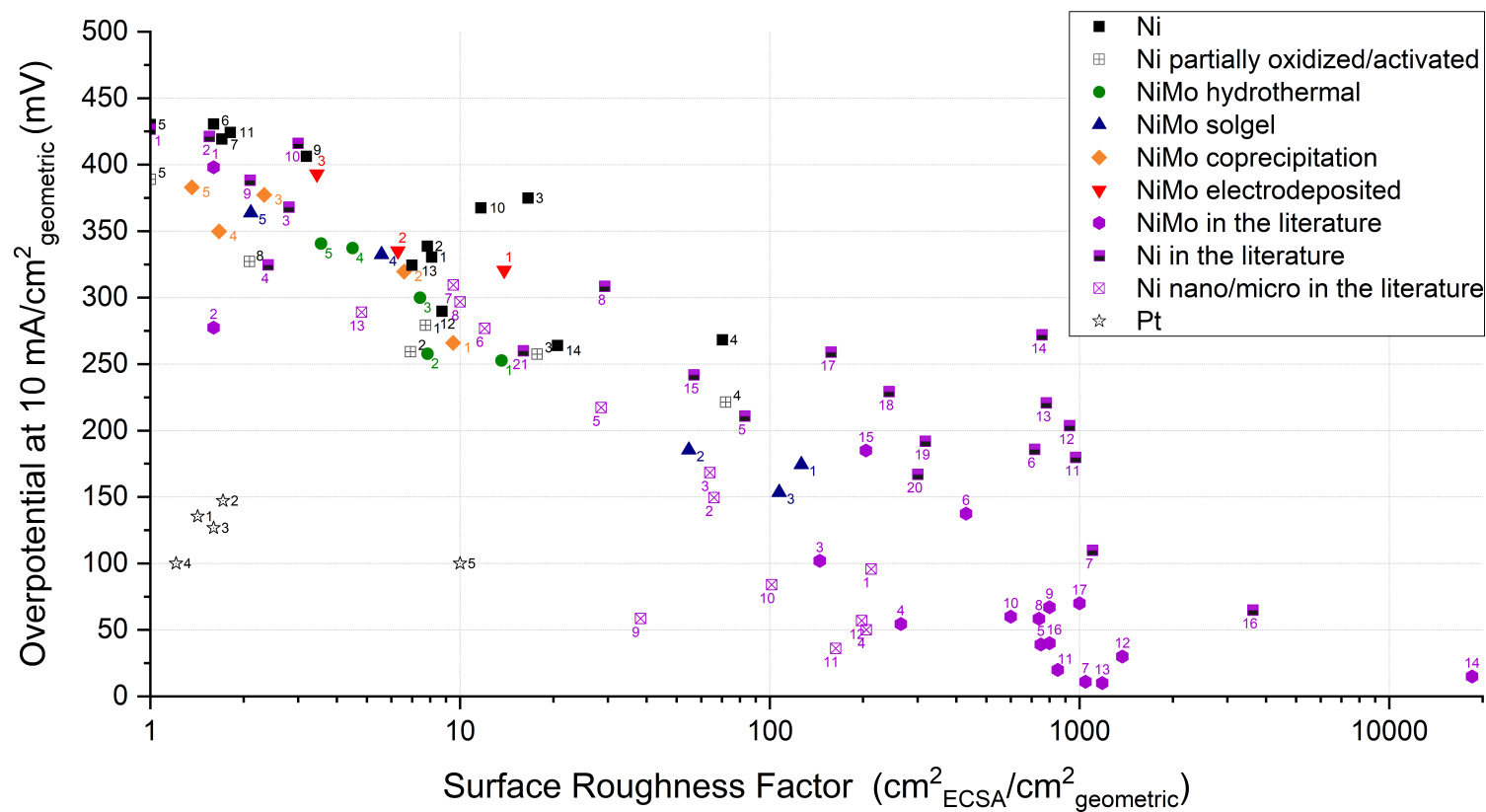


Fig. 5.16: Repetition of Fig. 5.15, with additional nickel samples, samples made by electrodeposition and a variety of nickel and nickel-molybdenum samples from the literature. Platinum samples, which display significantly higher intrinsic activity, are shown for reference. See Tab. 5.2, 5.3, 5.4 and 5.5 for sample descriptions. Note that the abscissa has changed by a factor of 100 for the integration of higher surface roughness samples from the literature.

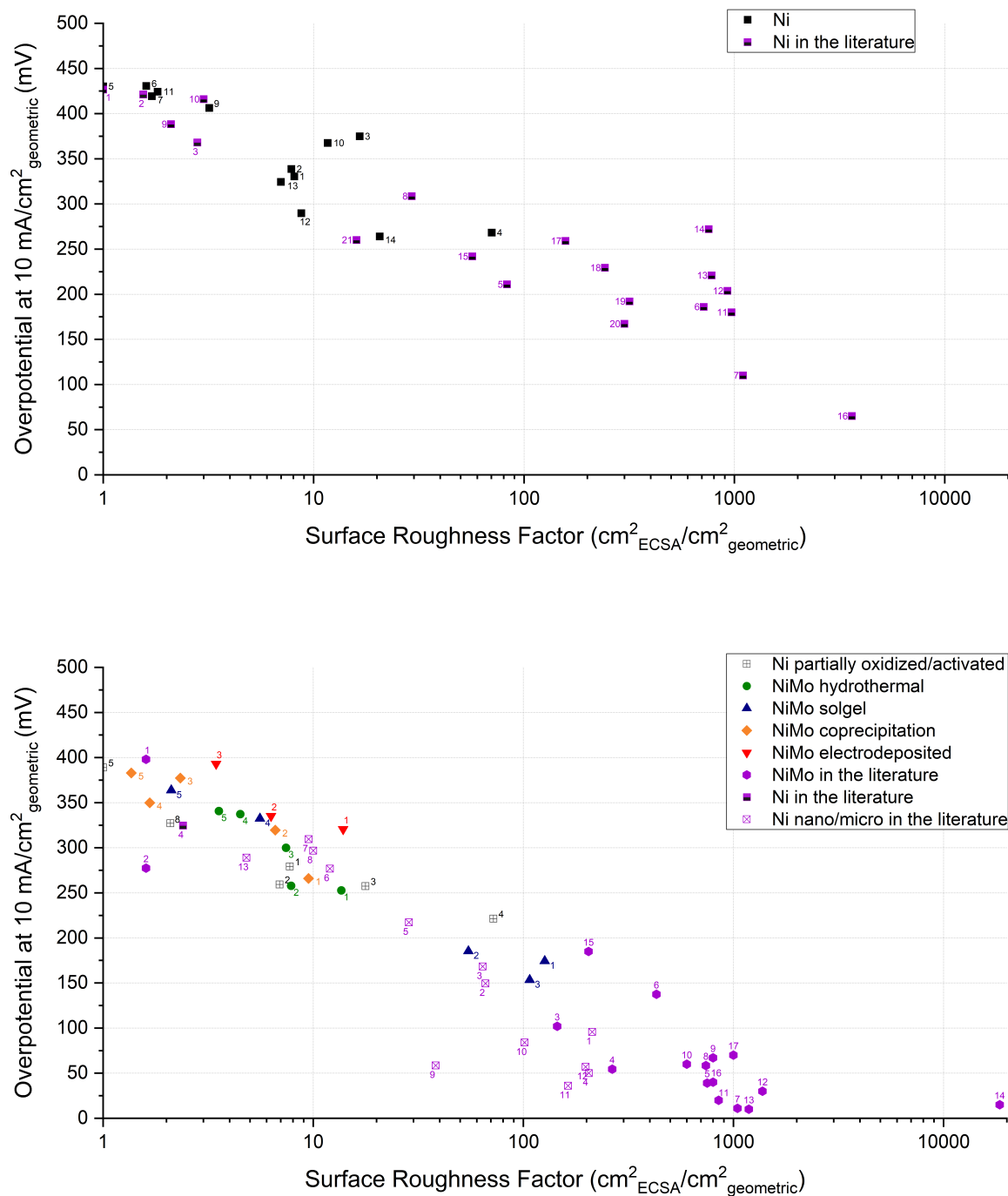


Fig. 5.17: Repetition of Fig. 5.16, divided into nickel (top) and nickel-molybdenum plus active nickel (bottom) electrocatalysts.

Tab. 5.2: Additional Ni (top), NiMo electrodeposited (middle) and NiMo in the literature (bottom) samples presented in Fig. 5.16.

No.	electrolyte	sample	ECSA evaluation	η_{10} evaluation	source
9	1 M KOH	Ni-foil	overpotential EIS	galvanostatically	this work
10	1 M KOH	electrodeposited	overpotential EIS	galvanostatically	this work
11	1 M KOH	Ni-foil	overpotential EIS	galvanostatically	this work
12	1 M KOH	Ni LDH reduced 450 °C / Ni-felt	overpotential EIS	galvanostatically	this work
13	1 M KOH	Ni-felt	overpotential EIS	galvanostatically	this work
14	1 M KOH	sintered US nano Ni 1.3 mg · cm ⁻² / Ni-foil	overpotential EIS	galvanostatically	this work
1	1 M KOH	Ni + Mo 12 % Mo	overpotential EIS	galvanostatically	this work
2	1 M KOH	Ni + Mo 24 % Mo	overpotential EIS	galvanostatically	this work
3	1 M KOH	Ni + Mo 32 % Mo	overpotential EIS	galvanostatically	this work
1	1 M KOH	Ni ₂ Mo	non-faradaic CV	<i>iV</i> -curve 10 mV/s	[173]
2	1 M NaOH	NiMo	overpotential EIS	pot. Tafel-analysis	[38]
3	5 M KOH	Ni + Mo 28 %Mo	overpotential EIS	galv. Tafel analysis	[67]
4	5 M KOH	Ni + Mo 36 %Mo	overpotential EIS	galv. Tafel analysis	[67]
5	5 M KOH	Ni + Mo 46 %Mo	overpotential EIS	galv. Tafel analysis	[67]
6	30 % KOH	NiMo	overpotential EIS	pot. Tafel analysis	[35]
7	30 % KOH	NiMo	overpotential EIS	pot. Tafel analysis	[35]
8	1 M KOH	MoO ₂ – Ni	non-faradaic CV	<i>iV</i> -curve 2 mV/s	[74]
9	6 M KOH	<i>in situ</i> added Na ₂ MoO ₄	overpotential EIS	pot. Tafel analysis	[159]

Tab. 5.3: NiMo in the literature (top, continued) and Ni in the literature (bottom) samples presented in Fig. 5.16.

No.	electrolyte	sample	ECSA evaluation	η_{10} evaluation	source
10	1 M KOH	Ni ₃ Mo/Ni ₄ Mo/MoO _{3-x}	non-faradaic CV	<i>iV</i> -curve 5 mV/s	[71]
11	1 M KOH	Ni ₄ Mo/MoO _{3-x}	non-faradaic CV	<i>iV</i> -curve 5 mV/s	[71]
12	1 M KOH	Ni ₁₀ Mo/MoO _{3-x}	non-faradaic CV	<i>iV</i> -curve 5 mV/s	[71]
13	1 M NaOH	NiMo	non-faradaic CV	galvanostatically	[68]
14	1 M KOH	Ni ₄ Mo	non-faradaic CV	<i>iV</i> -curve 1 mV/s	[64]
15	1 M KOH	Ni _{0.9} Mo _{0.1}	overpotential EIS	<i>iV</i> -curve 5 mV/s	[62]
16	1 M NaOH	NiMo	non-faradaic CV	galvanostatically	[8]
17	1 M NaOH	NiMo	non-faradaic CV	galvanostatically	[8]
1	0.5 M NaOH	Ni-foil	α -Ni(OH) ₂	galv. Tafel analysis	[43]
2	1 M NaOH	-	overpotential EIS	pot. Tafel analysis	[38]
3	0.1 M NaOH	Ni-rod	α -Ni(OH) ₂	pot. Tafel analysis	[45]
4	0.1 M NaOH	Ni-rod	α -Ni(OH) ₂	pot. Tafel analysis	[45]
5	5 M KOH	electrodeposited	overpotential EIS	galv. Tafel analysis	[67]
6	30 % KOH	electrodeposited	overpotential EIS	pot. Tafel analysis	[35]
7	4 M NaOH	electrodeposited	α -Ni(OH) ₂	galv. Tafel analysis	[174]
8	30 % KOH	electrodeposited	overpotential EIS	pot. Tafel analysis	[36]
9	0.5 M KOH	Ni-rod	α -Ni(OH) ₂	pot. Tafel analysis	[46]
10	0.5 M KOH	chemically etched Ni-rod	α -Ni(OH) ₂	pot. Tafel analysis	[46]

Tab. 5.4: Ni in the literature (top, continued) and Ni nano/micro in the literature (bottom) samples presented in Fig. 5.16.

No.	electrolyte	sample	ECSA evaluation	η_{10} evaluation	source
11	1 M KOH	Ni/NiO 12.5 nm on CNT	non-faradaic CV	pot. Tafel analysis	[165]
12	1 M KOH	Ni/NiO 12.5 nm on CNT	non-faradaic CV	pot. Tafel analysis	[165]
13	1 M KOH	Ni/NiO 12.5 nm on CNT	non-faradaic CV	pot. Tafel analysis	[165]
14	1 M KOH	Ni/NiO 12.5 nm on CNT	non-faradaic CV	pot. Tafel analysis	[165]
15	5 M KOH	electrodeposited	α -Ni(OH) ₂	pot. Tafel analysis	[30]
16	0.5 M NaOH	electrodeposited	α -Ni(OH) ₂	pot. Tafel analysis	[175]
17	8 M KOH	Ni-foam	non-faradaic CV	pot. Tafel analysis	[176]
18	8 M KOH	Ni-foam	non-faradaic CV	pot. Tafel analysis	[176]
19	8 M KOH	Ni-foam	non-faradaic CV	pot. Tafel analysis	[176]
20	30 % KOH	electrodeposited	overpotential EIS	pot. Tafel analysis	[177]
21	1 M NaOH	electrodeposited	non-faradaic CV	galvanostatically	[8]
1	1 M KOH	KBr 22 nm	overpotential EIS	pot. Tafel analysis	[53]
2	1 M KOH	PVP 27 nm	overpotential EIS	pot. Tafel analysis	[53]
3	1 M KOH	NaBH ₄ free 52 nm	overpotential EIS	pot. Tafel analysis	[53]
4	1 M KOH	polyol 5 nm	overpotential EIS	pot. Tafel analysis	[53]
5	1 M KOH	commercial 1.15 μ m	overpotential EIS	pot. Tafel analysis	[53]
6	1 M KOH	commercial milled 37 μ m	overpotential EIS	pot. Tafel analysis	[53]
7	1 M KOH	commercial milled 73 μ m	overpotential EIS	pot. Tafel analysis	[53]

Tab. 5.5: Ni nano/micro in the literature (top, continued) and Pt (bottom) samples presented in Fig. 5.16.

No.	electrolyte	sample	ECSA evaluation	η_{10} evaluation	source
8	1 M KOH	commercial milled 38 μm	overpotential EIS	pot. Tafel analysis	[53]
9	1 M KOH	electrodeposited 8.7 nm	non-faradaic CV	pot. Tafel analysis	[168]
10	1 M NaOH	Ni-rGO _{0.5}	non-faradaic CV	<i>iV</i> -curve 10 mV/s	[178]
11	1 M NaOH	Ni-rGO _{1.0}	non-faradaic CV	<i>iV</i> -curve 10 mV/s	[178]
12	1 M NaOH	Ni-rGO _{2.0}	non-faradaic CV	<i>iV</i> -curve 10 mV/s	[178]
13	1 M KOH	Ni/PVP-rGO (20)	α -Ni(OH) ₂	<i>iV</i> -curve 5 mV/s	[179]
1	1 M KOH	foil/polycrystalline	H _{upd}	galvanostatically	this work
2	1 M KOH	foil/polycrystalline	H _{upd}	galvanostatically	this work
3	0.1 M NaOH	disc/polycrystalline	H _{upd}	pot. Tafel analysis	[180]
4	0.1 M NaOH	foil/polycrystalline	H _{upd}	pot. Tafel analysis	[139]
5	1 M NaOH	disc/polycrystalline	non-faradaic CV	galvanostatically	[8]

In accordance with the previous observations on the dependence of the overpotential at 10 mA/cm^2 with the surface roughness in 11.6 M KOH, the overview with self-measured data in 1 and 11.6 M KOH and literature data in 0.1 M KOH – 8 M KOH confirms that two trends exist. Plain nickel electrocatalysts apparently scale less with increasing surface roughness than NiMo and activated Ni electrocatalysts, and further display higher overpotentials at similar surface roughness. Most importantly, some plain nickel electrocatalysts deviate from this behavior and intersect with the NiMo/active Ni trend. The first exemption, which is also visually deducted from the other nickel data, present "Ni nano/micro in the literature". The description was chosen, as these electrocatalysts are taken from studies investigating nano- and micron-sized electrocatalysts, which are not supported on nickel substrates. Hence, they resemble surface specific electrocatalysts in contrast to bulk nickel electrocatalysts denoted under "Ni in the literature". Another observation of importance are the values 3 and 4 of "Ni in the literature". These are taken from the study by Oshchepkov et al. [45], which was previously taken as guidance for the partial oxidation of a choice of nickel samples tabularized in Tab. 5.1. Similar to the self-obtained observations, the partial oxidation decreases the overpotential by $\approx 44 \text{ mV}$ without significantly influencing the surface roughness ($R_f = 2.8 \rightarrow R_f = 2.4$). Moreover, this intrinsic electrocatalytic activation overlaps with the NiMo/active Ni trend, as it does with the self-obtained data of partially oxidized Ni samples.

In summary, alloyed NiMo electrocatalysts, oxide supported NiMo electrocatalysts, activated Ni electrocatalysts, and surface specific Ni electrocatalysts display an overlapping scaling of the overpotential at 10 mA/cm^2 with surface roughness, irrespective of the electrolyte concentration. In addition, plain/bulk Ni electrocatalysts also display a trend, which, however, differs from the NiMo/active Ni trend. Therefore, it is possible to hypothesize that the high performance of NiMo electrocatalysts stems from a highly active nickel site, which is presented in a favorable chemical oxidation state for the HER. This hypothesis is backed by the similar performance of highly active nickel electrocatalysts. The observed scatter among the nickel and the NiMo/active Ni data can be attributed to the collection of different sources working with different setups, using different electrolytes, and applying varying methods to deduct η_{10} and the ECSA. Besides, the comparison of the overpotential with surface roughness assumes a Tafel-like scaling of the overpotential with surface roughness.

Hence, the validity of this approach is given, if not more than one Tafel-slope per observed trend exists. Additionally, the predominant deviations from the trends can be detected at overpotentials < 120 mV, at which the legitimacy of a Tafel-slope is not given [11].

5.3.3 Statistical evaluation of the importance of the electrochemical surface area

In spite of the spread of the data, two main trends were observed. To qualify this observation, the fitting of the observed trends in the following include statistical considerations.

The fittings of the Ni and the NiMo/active Ni trends follow a semi-logarithmic, linear correlation according to Eq. (5.2). The slope describes the decrease of the overpotential at 10 mA/cm^2 per decade of surface roughness and is thus not to be mistaken with a Tafel-slope, which results from the linearization of the Butler-Volmer equation (see Chap. 2.1). The intercept describes the intrinsic overpotential at surface roughness 1.

$$\eta_{10} = \text{slope} \cdot \log(R_f) + \text{intercept} \quad (5.2)$$

Since a scatter was observed, the fitting is accompanied by considering a Student-t normal distribution of the data with a 95 % confidence interval. Implementing a confidence interval to the fitting routine aims at assessing the statistical significance of the previously described trends.

The results of the semi-logarithmic fitting and the statistical considerations are illustrated in Fig. 5.18 and tabularized in Tab. 5.6. Following these results, the Ni trend and the NiMo/active Ni trend disperse by 28.8 mV/dec for the slope and 39.6 mV for the intercept. Moreover, the 95 % confidence intervals overlap only marginally. As a consequence, the previously described trends display statistically significant deviations. Accordingly, the hypothesis describing a certain chemical state of Ni in NiMo and Ni electrocatalysts as the active site of these is further supported by statistical considerations.

Nevertheless, the above made considerations and calculations are based on the, formerly verified, assumption that the double layer capacitance and the ECSA are equal by a value of $40 \mu\text{F/cm}^2$. On the one hand, this estimation finds further support from the litera-

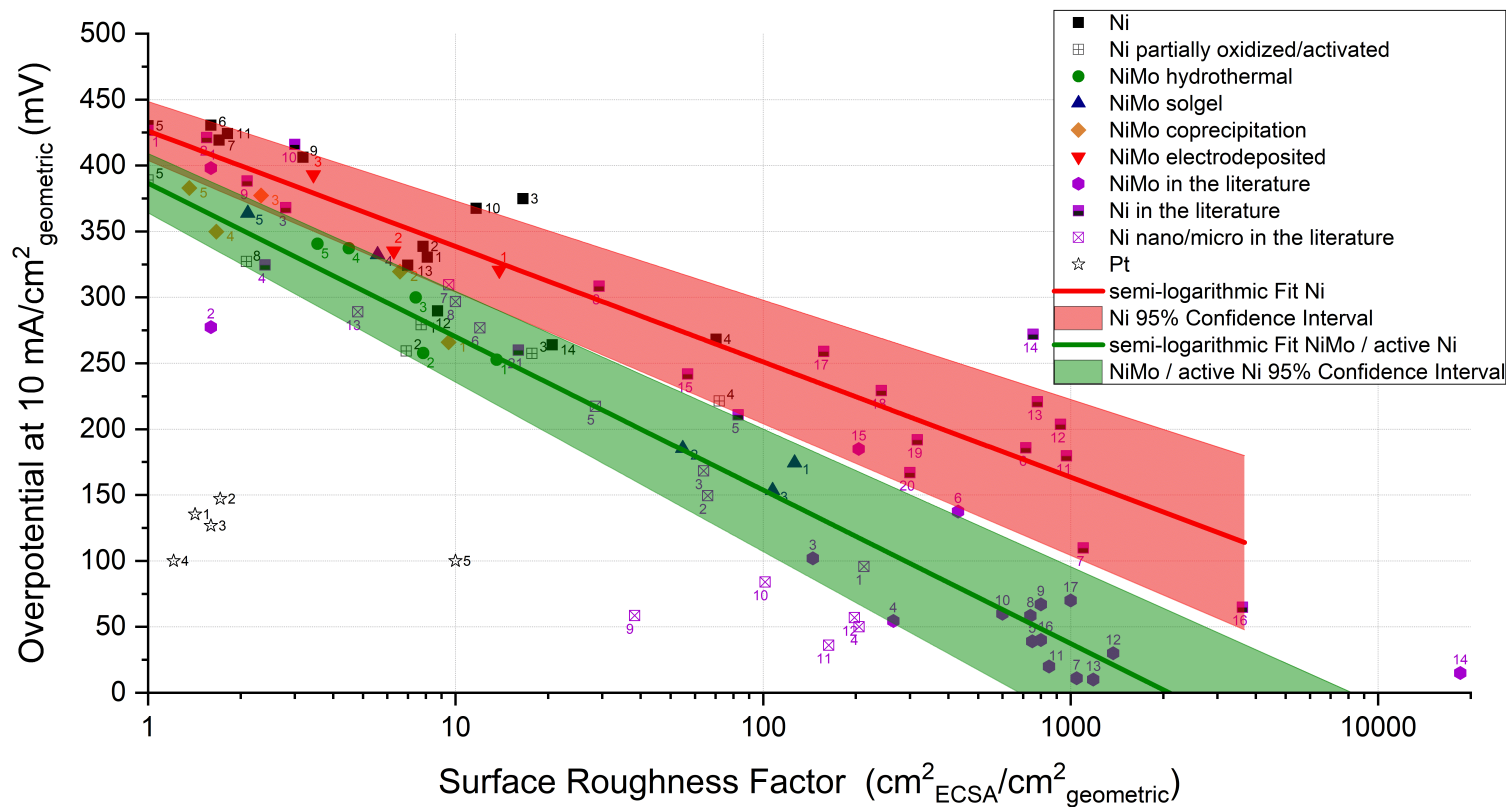


Fig. 5.18: Repetition of Fig. 5.16, including the semi-logarithmic fittings and corresponding Student-t (95%) statistical evaluations of the nickel (see Fig. 5.17 (top)) and the nickel-molybdenum plus active nickel (see Fig. 5.17 (bottom)) electrocatalysts. All surface area estimates based on double layer capacitance are made with a value of 40 $\mu\text{F}/\text{cm}^2$.

Tab. 5.6: Fitting and Student-t (95 %) statistical parameters for Ni and NiMo / active Ni from Fig. 5.18. Based on the fitting equation $\eta_{10,\text{geometric}} = \text{slope} \cdot \log(\text{Surface Roughness Factor}) + \text{intercept}$. The same parameters including only the samples from this work in 11.6 M KOH (see Fig. 5.15) are shown for comparison. All surface area estimates from the double layer capacitance considered a value of $40 \mu\text{F}/\text{cm}^2$.

Parameter	Unit	Ni	(11.6 M)	NiMo/ active Ni	(11.6 M)
fitted slope	mV/dec	-87.6	-86.2	-116.4	-108.2
95 % lower limit		-99.8	-127.5	-128.4	-124.3
95 % upper limit		-75.3	-44.9	-104.4	-92.0
standard error		6.0	16.1	6.0	7.7
fitted intercept	mV	426.2	435.6	386.6	388.2
95 % lower limit		403.9	395.4	364.1	370.8
95 % upper limit		448.5	475.8	409.1	405.5
standard error		11.0	15.6	11.2	8.3
root mean square		0.873	0.852	0.878	0.912
fitted points		33	7	55	21

ture [8, 62]. In addition, others report a similar observation of the overpotentially-dependent double layer capacitance obtained with EIS, which equals the actual double layer capacitance with Armstrong's electric circuit [15, 36, 181, 182]. On the other hand, these authors consider a value of $20 \mu\text{F}/\text{cm}^2$. It is therefore considerable that a part of the observed scatter might be attributed to the different experimental conditions and pretreatments of the electrocatalysts, which would require considering different values depending on the nature of the electrocatalyst's surface.

Consequently, the aforementioned fitting routine including a 95 % Student-t normal distribution is repeated in Fig. 5.19 and Tab. 5.7 considering a value of $20 \mu\text{F}/\text{cm}^2$ for all ECSA estimations obtained through the double layer capacitance. The estimations based on the formation of $\alpha\text{-Ni}(\text{OH})_2$ remain unchanged. Although Chap. 5.3.1 contradicts this approach, a comparison to the literature applying this value plays an important role in understanding the significance of the Ni and NiMo/active Ni trends.

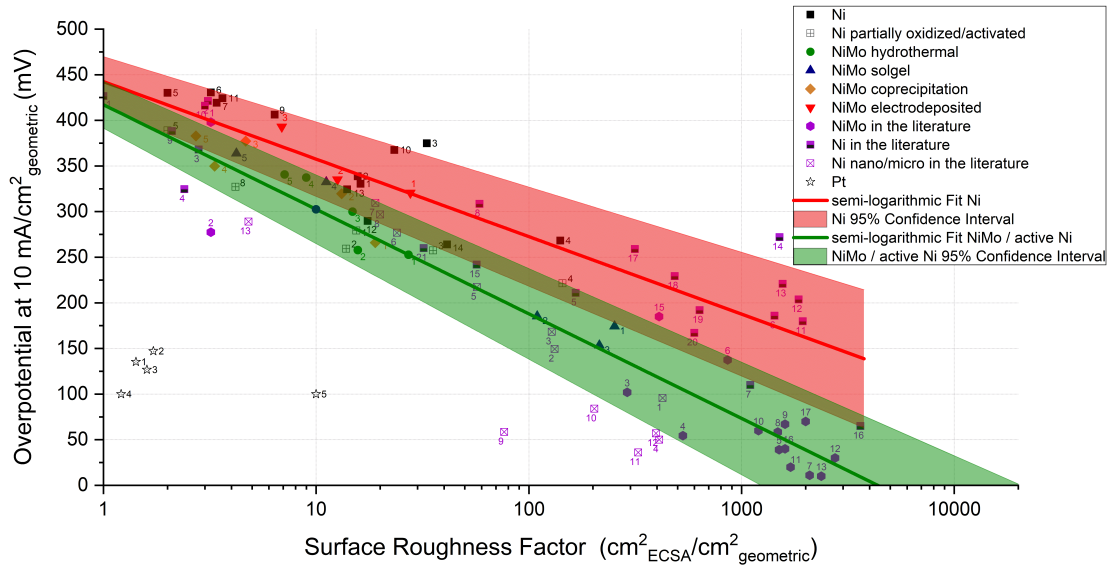


Fig. 5.19: Repetition of Fig. 5.18 considering surface area estimates from double layer capacitance with a value of $20 \mu\text{F}/\text{cm}^2$. The corresponding fitting and Student-t (95 %) statistical parameters are summarized in Tab. 5.7.

Tab. 5.7: Fitting and Student-t (95 %) statistical parameters for Ni and NiMo / active Ni from Fig. 5.19. Based on the fitting equation $\eta_{10,\text{geometric}} = \text{slope} \cdot \log(\text{Surface Roughness Factor}) + \text{intercept}$. All surface area estimates from the double layer capacitance considered a value of $20 \mu\text{F}/\text{cm}^2$.

Parameter	Unit	Ni	NiMo/ active Ni
fitted slope		-84.9	-114.6
95 % lower limit	mV/dec	-98.4	-126.6
95 % upper limit		-71.4	-102.6
standard error		6.6	6.0
fitted intercept		442.5	417.1
95 % lower limit	mV	415.1	391.5
95 % upper limit		469.8	442.8
standard error		13.4	12.8
root mean square		0.842	0.874
fitted points		33	55

Changing the value for surface area estimates has not changed the overarching trends. This could rather be expected, as only 9 out of 88 data points, equaling 10.3% of the data, were assessed through the unchanged α -Ni(OH)₂ method. Thereby, the correlations predominantly experience a near-parallel shift. Nevertheless, the Ni and the NiMo/active trends overlap to a greater extent than previously, especially nearby $R_f = 1$. In lieu of changing the hypothesis on highly active Ni sites in NiMo and activated Ni electrocatalysts, the overlap is an artificial result from changing the value unspecifically. As a result, future work has to include further studies clarifying which value can be ascribed to the electrocatalysts. Based on the findings of this work, $40 \mu\text{F}/\text{cm}^2$ has proven to be valid for Ni electrocatalysts, and concluded by analogy to be for NiMo electrocatalysts.

In any case, a deviation between Ni and NiMo/active Ni electrocatalysts in the factor decreasing η_{10} with the surface roughness stands out. Hence, an intrinsic difference between these two types, with a greater intrinsic performance for the latter, cannot be denied according to the study presented here. Moreover, the hypothesis generalizes into a relatively rough categorization of electrocatalyst types. It is conceivable that electrocatalysts have falsely been assigned to a trend. The resolution can only come from further studies investigating the hypothesis, e.g. through spectroelectrochemical XPS.

5.4 Conclusions and discussions on performance descriptors for Ni and NiMo electrocatalysts

Two main conclusions can be drawn from the results of this chapter. Firstly, following the purpose of assessing the ECSA resulted in an agreement between the electrochemical double layer approach, with a value equaling double layer capacitance and ECSA by $40 \mu\text{F}/\text{cm}^2$, and the formation of a monolayer α -Ni(OH)₂ in Ni electrocatalysts. Impedance studies on Ni_xMo_y, oxide supported Ni_xMo_y, and Ni electrocatalysts in the HER overpotential indicate that the double layer capacitance can be assessed with Armstrong's electric circuit. This observation has previously been made elsewhere as well [15, 36, 181, 182]. However, the different value of $20 \mu\text{F}/\text{cm}^2$ from these literature sources raises the question of the precise value, as others [8, 62] also apply $40 \mu\text{F}/\text{cm}^2$. Hence, further studies including more

techniques are required to understand the correlation between the electrocatalyst's surface state and the value of the double layer capacitance.

For instance, other techniques to estimate the ECSA such as the hexaamineruthenium (+II/+III) redox couple [34] should be applied in combination with BET for comparison to the above described methods. It should be noted that techniques to estimate the ECSA at the $\text{Ni}^{2+} \rightleftharpoons \text{Ni}^{3+}$ transition [73, 167] were excluded in the considerations of this work. The pretreatment-dependence of Ni electrocatalysts (see Chap. 2.4) would cause an irreversible change of the HER kinetics. Therefore, this type of ECSA estimation would only be applicable as a one-time measurement at the end. Non-destructive techniques, as the *in situ* EIS approach, are accordingly favorable. In addition, the validity of the congruence of the ECSA between the $\text{Ni}^0/\text{Ni}^{2+}$ redox couple in the HER and the $\text{Ni}^{2+}/\text{Ni}^{3+}$ redox couple in the OER region can be questioned.

Secondly, the identical correlation of the Ni_xMo_y , oxide supported Ni_xMo_y , and activated Ni electrocatalysts with the surface roughness leads to the assumption that Ni is the active site in all of these electrocatalysts. As bulk Ni follows a different trend with an intrinsic inferiority to the first mentioned trend, it can be hypothesized that the active Ni site is presented in a favorable chemical oxidation state in the high-performing electrocatalysts. This hypothesis could be made despite the open question of the value of 20 or 40 $\mu\text{F}/\text{cm}^2$, as the observed scattering of the data within the trends are preponderantly covered in 95 % Student-t confidence intervals that are significantly different between the trends.

Furthermore, the collection of this data measured from different scientific groups in several non-standardized fashions, in addition to the relatively rough categorizations of electrocatalysts, can sufficiently describe the scatter. In default of more standardized and comprehensive data from the literature, the estimated correlations are to date the best possible practice for a comparison of the results of multiple scientific groups with the here presented approach. As a consequence, future work can be compared more easily if a standardization of the testing conditions and testing parameters is implemented. As such, data from different scientific groups can be compared more easily by measuring η_{10} galvanostatically over the course of 5 min, the ECSA through EIS and non-faradaic cyclic voltammetry as verification, and in correlation to the semi-logarithmic fittings made in this work (Chap. 5.3.3).

If additionally aspects of the chemical state of Ni, e.g. by spectroelectrochemical

XPS, are correlated to the observed semi-logarithmic trends, the origin of the high performance of Ni_xMo_y , oxide supported Ni_xMo_y , and activated Ni electrocatalysts can finally be concluded. At this stage, it is possible to claim that reports denying an intrinsic effect of Mo in Ni_xMo_y [73] contradict the findings of this work. An agreement can be found in Ni as the active site, as well as a predominant performance achievement through high surface areas. Nevertheless, the comprehensive overview of 35 literature sources plus this work displays an intrinsic superiority of NiMo to bulk Ni electrocatalysts. The hypothesis that the active Ni site is in a favorable chemical oxidation state is supported by the findings of Wang et al. [165] and Kabir et al. [75]. Accompanied by DFT, Wang et al. identify Ni^0 as the promoter of the HER. Kabir et al. conclude, based on *in situ* XPS, that Mo does not take part in the adsorption of hydrogen. The active site is Ni, whose electronic properties are affected by the presence of Mo and therefore lowering the binding energy of H_{ad} on Ni.

In conclusion, the hypothesis in this work of a highly active Ni site in Ni_xMo_y , which is in a favorable chemical oxidation state due to the presence of Mo, adds to the findings from the literature with a broad data basis considered in this work. This includes the findings about partially oxidized Ni electrocatalysts [47, 161, 163], which show, following the presented study in this chapter, a congruent trend to Ni_xMo_y electrocatalysts. Thus, future work should address the role of the oxidation state of Ni in these electrocatalysts, which perspectively should occur with spectroelectrochemical XPS.

Chapter 6

Stability testing of NiMo and NiFe LDH electrocatalysts

The literature contains a vast choice of non-noble electrocatalysts for the alkaline water electrolysis. The focus of the majority of these publications is set on either developing and synthesizing new, promising compositions and structures, or in understanding the origin of their high performance. These studies are undoubtedly important for the technical application as well. However, the literature-studies mostly don't consider technical relevant conditions. High pH electrolytes and elevated temperatures, such as 30 w% KOH and 80 °C, are not sufficiently represented for these promising electrocatalysts in the literature. Moreover, it is important to investigate the stability of these promisingly high-performing electrocatalysts at these conditions over extended periods of time.

In a technical application, the electrocatalysts are exposed to strong potential-changes between the maximum operation point and the shutdown of the electrolyzer over the course of several years, or even decades. A benefit of high-performing non-noble over noble-metal electrocatalysts for a commercial electrolyzer would only exist if the high performance persists within the entire technological operation window and time. First studies about the stability of nickel-molybdenum and raney-nickel electrodes, at technical relevant conditions, were conducted by Brown et al. [81] and Divisek et al. [183] in the 1980s.

To be able to answer the necessary question about the stability and durability of highly performing nickel-molybdenum and nickel-iron electrocatalyst, this chapter will test these electrocatalysts in technological relevant conditions of 30 w% KOH (pre-electrolyzed) and 80 °C in a zero-gap alkaline water electrolyzer with a Zirfon separator. Accelerated

degradation tests and an approximately 15 days lasting long-term test, including dynamic load changes resembling intermittent operation, are conducted to simulate the technical operation.

The combination of accelerated degradation tests and a long-term test intends to reflect the years-long application of a commercial electrolyzer as the best compromise between the need for long-term testing and the practicability in this work. The lab scale setup, with an electrode area of 10 cm^2 , is described in Chap. 3.7.2. As a convention in this work, the two-electrode system will be named after the electrocatalysts, starting with the cathode-catalyst, and followed by the support. For instance, *NiMo/felt vs Ni-felt* describes a cell with a nickel-molybdenum catalyst on the cathode with a felt support, and a nickel catalyst on the anode. In case of nickel as a catalyst, the electrode was an uncoated support.

6.1 Experimental details

6.1.1 Sample preparation

The electrode supports in a technical electrolyzer are usually fully coated with the electrocatalyst. In this work, the stability behavior of the electrocatalyst is studied over a rather short period of time, when compared to the technical application. In other words, small changes to the electrocatalyst occurring over time might not be remarked, when the electrode has a similar high catalyst-loading as in the technical electrolyzer. Lowering the loadings, in which the supports are not fully covered by the electrocatalysts, has two causes.

Firstly, a slowly occurring effect, such as continuous dissolution of the catalyst, as reported for e.g. nickel-molybdenum [73, 78], becomes more apparent at low loadings. The loss of the catalyst has a greater impact on the electrode performance, within the same time-frame, when the initial loading is smaller. Secondly, the single electrocatalyst experiences a higher stress, as the local current density and thus the local overpotential is higher than at normal loadings. Both effects are unfavorable for a commercial application.

However, for the purpose of this work, both causes are advantageous. They reduce the amount of time needed to evaluate smaller effects. Furthermore, exceeded local current densities and overpotentials, when compared to technical electrodes, allow to draw conclusions beyond the actual operational window. Moreover, an electrocatalyst, showing tolerance

towards exceeded stress over the course of about two weeks, may be stable at a standard stress over several years of operation.

All electrodes were produced with either a perforated plate (PP) (by Veco B.V.), or a felt (felt) (by Bekeart) support. Both supports are made of nickel. Prior to the coating process, all supports were cut to a round shape with a diameter of $d \approx 36$ mm ($\sim A = 10$ cm²), sonicated for 5 min in 10 % HCl, and subsequently washed with water and ethanol.

For the nickel-molybdenum (NiMo) electrodes, two methods were applied to coat the supports. For the PP-supported electrodes, an ink of 20 mg NiMoO₄ (from sol-gel-synthesis [155], see 5.1) and 8 mL Isopropanol (CAS 67-63-0, analytical grade, $\geq 99.9\%$, Merck Millipore) was freshly prepared for each electrode under 5 min of sonication. The ink was sprayed with an airgun onto the support, giving a catalyst-coating of ≈ 2 mg/cm². For the felt-supported electrodes, a 10 mg/450 μ L ink was drop-cast in portions of 50 μ L over different parts of the support (≈ 1 mg/cm²). After a drying process at room temperature, the electrodes are transferred to a quartz-tube, heated to 600 °C (10 °C/min) in an Ar-atmosphere, and finally reduced for 3 h in a safety-gas atmosphere (4 % H₂ / 96 % Ar). The cooling-down process was conducted under safety-gas atmosphere. The electrodes were removed from the tube and stored until further use.

For the nickel-iron LDH (NiFe LDH) electrocatalysts, a hydrothermal synthesis procedure [109, 111] was used to coat both supports. The cleaned support and a solution of 30 mM urea (CAS 57-13-6, purity $\geq 99.5\%$, Sigma Aldrich), 20 mM trisodium citrate (CAS 6132-04-3, purity $\geq 99.0\%$, Sigma Aldrich), 10 mM Ni(II)nitrate hexahydrate (CAS 13478-00-7, purity 99.999 %, Sigma Aldrich), and 3.5 mM Fe(III)nitrate nonahydrate (CAS 7782-61-8, purity $\geq 98\%$, Sigma Aldrich), were transferred into a 25 mL PTFE-lined autoclave. The autoclave was closed and heated to 120 °C. The LDH synthesis was conducted for 18 h, before the autoclave was allowed to cool down to room temperature naturally. The electrodes were removed from the reaction solution and washed three times with ethanol. After drying at room temperature, the electrodes were stored until further use. For a technical electrolyzer, the support would previously be coated with nickel to enhance the surface area and consequently the catalyst-loading, as the catalyst grows directly on the support's surface.

6.1.2 Effects of polarization and potential-distribution

During alkaline water electrolysis, hydroxide-anions are constantly produced on the cathode and consumed on the anode side. The migration of the hydroxide-anions, on the other hand, give rise to a concentration gradient within the electrolysis cell, which is known as the pH-gradient [184, 185]. The gradient has a direct influence on single-electrode measurements, if the chosen reference electrode is pH-sensitive. In this work, RHEs were used as reference electrodes. The reference electrode potential of an RHE is, by definition, the equilibrium potential of the HER at the given pH and temperature. It is therefore depending on the local pH.

Another effect coming into play during alkaline water electrolysis is the potential-distribution across the electrolyzer [186]. With increasing current density, the galvanipotential changes over the electrodes, as well as over the electrolyte and the separator. The change of the galvanipotential is linear in an ideal case. However, it is further possible that the potential-distribution is non-linear and asymmetric. The distribution is a direct cause of the chosen electrodes, the electrocatalysts, the separator, the electrolyte, the current density, and the electrochemical reactions.

A validated estimate about how the pH-gradient and the potential-distribution develops would require modeling supported studies, which are outside the scope of this work. However, the knowledge about these effects is essential when measuring single-electrode potentials with pH-sensitive reference electrodes, especially when the reference electrodes are placed behind the electrodes. A schematic illustration of these effects is given in Fig. 6.1.

An idealized scenario, shown in the top part of the figure, might in an approximation describe the situation close to the equilibrium potential. The potential-gradients across the electrodes are negligible, and the pH does not change over the electrolyzer. In this case, both pH-sensitive reference electrodes would remain at the same reference electrode potential. Furthermore, both reference electrodes would measure the same single-electrode potentials due to the absence of a potential-distribution over the electrodes. With increasing current density, the development of the potential-distribution, the pH-gradient, and the series resistance will result in different single-electrode potential measurements. In such a case, as shown in the bottom of the figure (note that the illustration is only schematic; it shows different, not necessarily correlated, possible cases), the pH-gradient causes a bias between

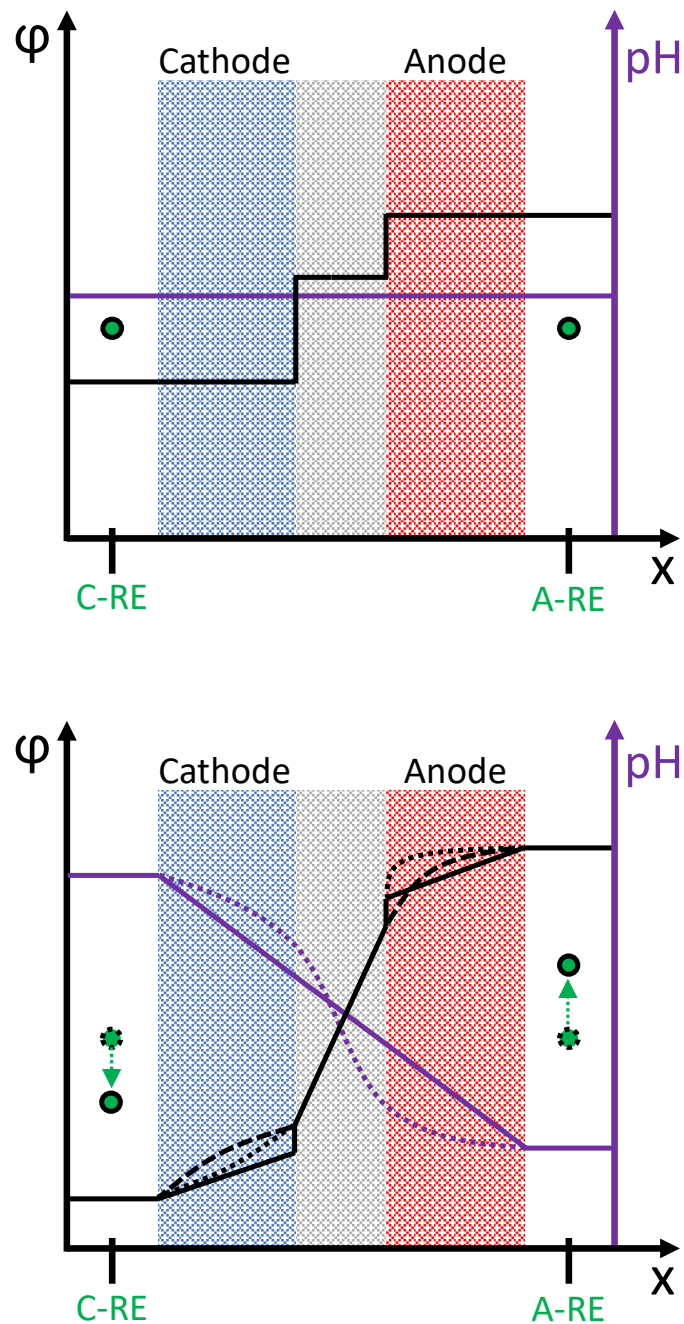


Fig. 6.1: Schematic evolution of the galvanic-potential and the pH over a zero-gap water electrolyzer, including a pH-sensitive reference electrode behind the cathode (C-RE) and behind the anode (A-RE). Top: Idealized version without the influence of current, in which both reference electrodes are at the same pH and thus identical reference potential, which results in similar electrode potential measurements. Bottom: Different possible scenarios to illustrate the potential distribution over an electrolyzer during electrolysis. The electrolysis induced pH-gradient and the potential distribution and resistance contributions cause an essential difference in the electrode potential measurements between the reference electrodes.

the reference electrode potentials. Additionally, the potential-gradients over the electrodes result in two different electrode potentials (front- and backside) that are measured from the reference electrodes. As aforementioned, these effects may be calculated by kinetic modeling. In this work, the effects were considered in a practical approach, by considering the bias between the reference electrodes in single-electrode potential measurements.

6.1.3 Single electrode kinetics by electrochemical impedance spectroscopy

Zero-gap setups involve a challenge in evaluating single electrode kinetics. As the electrodes are directly pressed onto the separator, it is difficult to place a third electrode as a reference electrode between anode and cathode. The setup at DTU utilizes two reference electrodes, which are placed behind the anode and the cathode. Since this approach is vulnerable towards the effects of potential-distribution and pH gradients, electrochemical impedance spectroscopy was conducted to qualify measurements at low current densities.

In the following section, electrochemical impedance studies of the cells *Ni-PP vs NiFe LDH/PP* and *NiMo/PP vs NiFe LDH/PP*¹ are presented as representative examples. EIS was conducted with a Biologic VSP-300 potentiostat.

Impedance was conducted between anode and cathode as working and counter electrodes (alternating). All impedances were operated galvanostatically with a 5 % amplitude of the applied current between 100 kHz and 50 mHz. In order to deconvolute the two-electrode impedance between anode and cathode (full cell EIS; anode WE vs cathode RE), single-electrode impedance studies with changing reference electrodes (anode WE vs anode-RHE RE, anode WE vs cathode-RHE RE, cathode WE vs cathode-RHE RE) followed the full cell EIS at the same current density. A comparison between these measurements at the same operating point, but with changing reference electrodes, allows to deduct the frequency-response of the single electrodes through plots of $-Z_{Im}$ over f . The comparison thereby eliminates the influence of the respective counter electrode, which is present in the full cell

¹The cell *NiMo/PP vs NiFe LDH/PP* is only represented for the impedance studies in this chapter. Due to software issues in this test, the data after the impedance studies, which occurred first, is lost to a great fraction.

EIS. Thereafter, the full cell EIS can be deconvoluted into the anode and cathode contributions by the dissimilar frequency-dependencies of the single electrodes.

As the measurements versus the reference electrodes behind the anode and cathode have to be reliable, the effects of a pH-gradient and potential-distribution, as well as noise through gas evolution, have to be limited to a minimum. Hence, the here presented measurements were conducted at a current density of 1 mA/cm^2 ; measurements at a current density of 10 mA/cm^2 were already challenging to analyze due to the noise-level in single-electrode impedances, and further did not show any different trends from the lower current density measurements. Furthermore, the quality of single-electrode impedances cannot be quantified without additional verifying tests including a reference electrode placed between anode and cathode. Therefore, it is generally most reasonable to analyze zero-gap alkaline electrolyzers by full cell impedance, with the knowledge about the dissimilar frequency-dependence to split the full cell EIS into the single electrode contributions.

The impedance spectra of the *Ni-PP vs NiFe LDH/PP* and *NiMo/PP vs NiFe LDH/PP* cells are shown in Fig. 6.2 and 6.3, respectively. In case of the first cell, the full cell EIS is compared to the single electrode impedance of the anode, with changing reference electrodes. In case of the second cell, the full cell EIS is correlated to both single electrode impedances, conducted versus the reference electrodes behind the respective electrodes.

Comparing the impedances with different placements of reference electrodes in Fig. 6.2, the Nyquist plots reveal two unfinished semi-circles for the anode, which appear to be of similar shape. However, the measurement with the reference electrode behind the cathode indicates a higher series resistance contribution. This effect can be explained by the resistance contributions from the cathode and the separator, which are absent in the measurement with the reference electrode behind the anode. The series resistance contributions of this measurement, on the other hand, do not only appear to be lower than from the cathode-RHE measurement, but also lower than the contribution in the full cell EIS and, moreover, negative.

Such results from single electrode measurements, with reference electrodes behind the electrodes, do not appear to be an artifact, but rather be a proof of the influence of the potential-distribution in an electrolyzer. For the measurement with the reference behind

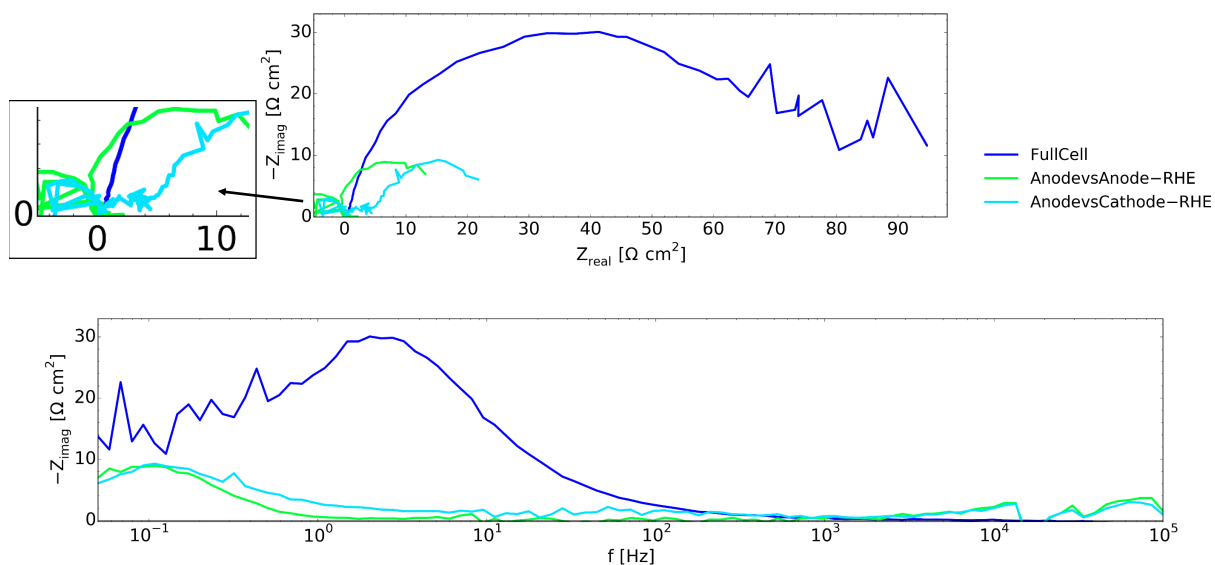


Fig. 6.2: Electrochemical impedance at 1 mA/cm^2 and 80°C on the *Ni-PP vs NiFe LDH/PP* cell of the full cell, anode WE vs anode-RHE RE and anode WE vs cathode-RHE RE. Top: Nyquist plots. Bottom: $-Z_{Im}$ over f .

the counter electrode, the electrode overpotential will be overestimated by the contributions from the counter electrode and the separator, which further explains the origin of the higher series resistance in the single electrode impedance compared with the full cell EIS in Fig. 6.2. The measurement with the reference behind the working electrode will underestimate the overpotential due to the potential-distribution over the working electrode. This is indicative by the negative series resistance in the single electrode impedance.

On the contrary, the $-Z_{Im}$ over f plots of Fig. 6.2 indicate no difference of the frequency-dependence of the anode, regardless of the placement of the reference electrode. It shows that, upon evaluating the frequency-dependence of a single electrode, the choice of the reference electrode placement does not impact the findings. It appears that the anode contribution is represented by a low frequency response at about 100 mHz, following a higher frequency response in the full cell EIS, which is likely due to the cathode contribution.

To further assess the validity of the frequency response of the single electrodes, the single electrode impedance results from the *NiMo/PP vs NiFe LDH/PP* cell are compared to the full cell EIS in Fig. 6.3. Since the reference electrode placement does not impact the frequency response, either single electrodes are measured with the reference electrode behind

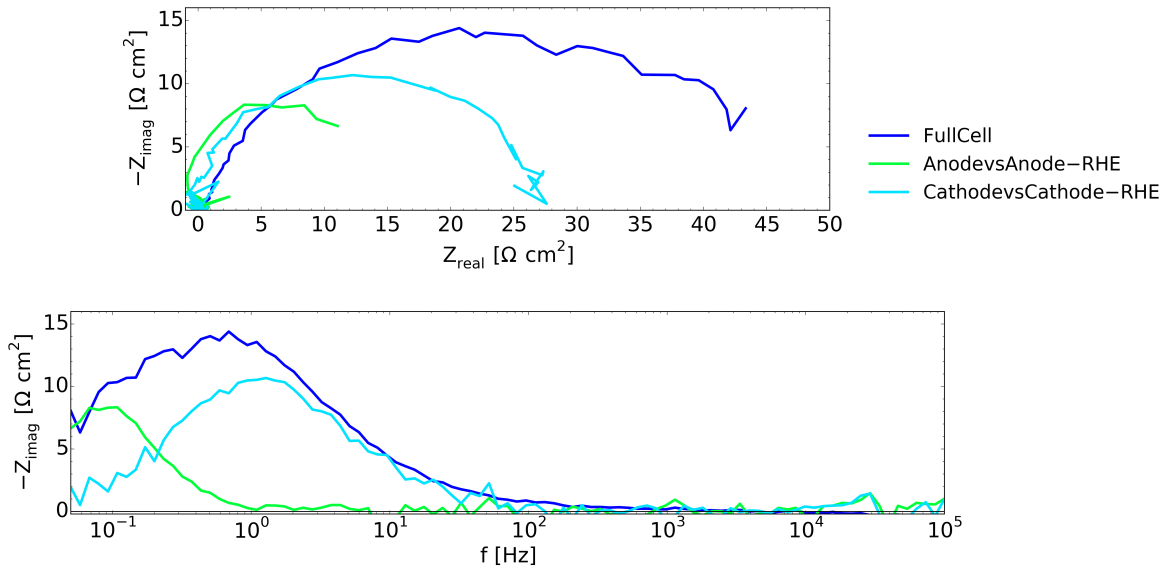


Fig. 6.3: Electrochemical impedance at 1 mA/cm^2 and 80°C on the *NiMo/PP vs NiFe LDH/PP* cell of the full cell, anode WE vs anode-RHE RE and cathode WE vs cathode-RHE RE. Top: Nyquist plots. Bottom: $-Z_{Im}$ over f .

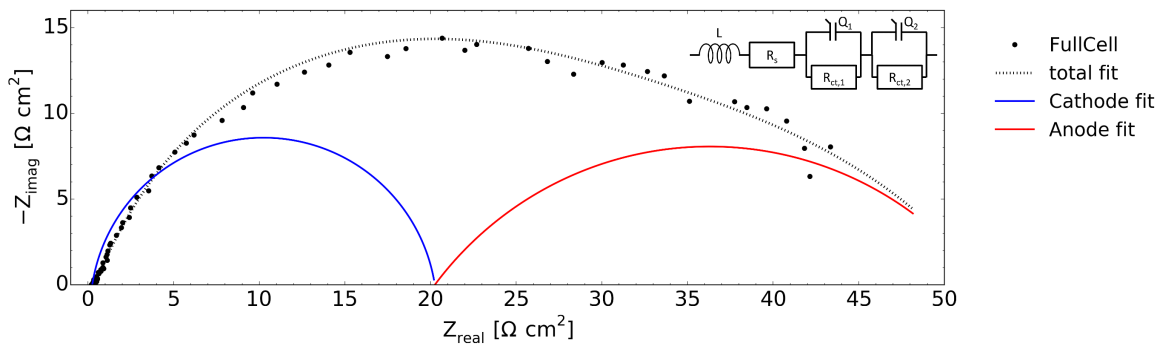


Fig. 6.4: Fitting of the full cell electrochemical impedance at 1 mA/cm^2 and 80°C of the *NiMo/PP vs NiFe LDH/PP* cell with a LR(RQ)(RQ) fitting. The total impedance fitting is shown together with the fitted contributions from cathode and anode.

the respective electrode. In either case, similar effects on the series resistance contributions, as seen in the *Ni-PP vs NiFe LDH/PP* cell, are visible for the cathode and the anode in the Nyquist plots, which further proves the influence of the potential-distribution. In addition, the $-Z_{Im}$ over f plots clearly indicate what was assumed in the *Ni-PP vs NiFe LDH/PP* cell beforehand; the cathode is characterized by a higher frequency response (≈ 1 Hz) than the anode (≈ 100 mHz). Both single electrode impedances match up with the full cell impedance.

Accordingly, the full cell EIS can be analyzed by two main processes, each described by an RQ circuit, in which the higher frequency part represents the cathode and the lower frequency part the anode. As an example, the fitting of the *NiMo/PP vs NiFe LDH/PP* full cell EIS, considering the cell inductance, the series resistance, and two electrode describing RQ elements, is represented with an LR(RQ)(RQ) fitting in Fig. 6.4. The full cell fitting divides into two semi-circles, in which the first one describes the cathode and the second one the anode.

Nonetheless, such fitting results are depending on the quality of the full cell EIS. Although the fitting of the full cell EIS is successful in this case, it may not be on cells in which the dissimilarity of the frequency dependence from both electrodes is less than one order of magnitude, as it is in this example. Additionally, as visible for the anode contribution, the semi-circle of this electrode is yet to be fulfilled. If the impedance spectra are not satisfactorily describing both electrode contributions, the fitting might confuse the single electrode contributions and misinterpret them. Therefore, it is mandatory to critically assess the quality of the impedance spectra before one concludes on the fitting results. In this example, the imaginary part of the impedance at the lowest frequency, which should be close to zero to fully represent the electrode contributions, is about one third of the maximum. Therefore, an adequate amount of data is present to model the electrode contributions in this example.

6.1.4 Single electrode kinetics by reference electrode measurements

Obtaining a greater depth of detail by measuring single electrode kinetics of a zero-gap electrolyzer is undoubtedly crucial, if one is interested in the kinetics and the stability of the electrocatalysts. Besides the approach with electrochemical impedance spectroscopy, see Chap. 6.1.3, this section will focus on the electrode potentials obtained from the measure-

ments with the reference electrodes behind the electrodes. The single-electrode potentials result from two measurement points in a polarization curve, obtained through galvanostatic steps for 60 s. A prescan ($1-1000 \text{ mA/cm}^2$) and a backscan ($1000-1 \text{ mA/cm}^2$) are averaged and the error bars are, accordingly, from the bias between both measured values.

For the analysis of the electrocatalyst kinetics, it is important to define the kinetic segment of the cells. The kinetic segment is defined at low current densities, until the cell becomes mixed controlled with ohmic contributions. For example, the polarization curves of the cells *Ni-PP vs Ni-PP*, *Ni-PP vs NiFe LDH/PP*, and *NiMo/PP vs Ni-PP*, from $0-100 \text{ mA/cm}^2$, are presented in Fig. 6.5. In all three cases, the cells are mostly kinetically controlled up to $\approx 5 \text{ mA/cm}^2$. After a transition zone, the cells are mostly ohmic controlled at current densities higher than 20 mA/cm^2 . As a result, the kinetic segment was defined for current densities between $1-20 \text{ mA/cm}^2$.

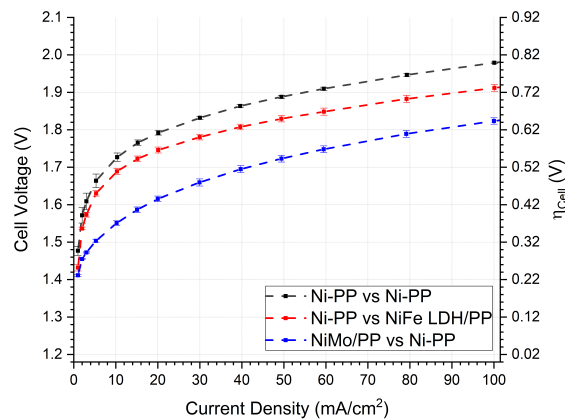


Fig. 6.5: Polarization curves of the *Ni-PP vs Ni-PP*, the *Ni-PP vs NiFe LDH/PP*, and the *NiMo/PP vs Ni-PP* cell at 80°C in 30 w\% KOH . A transition from kinetically to ohmic controlled cell voltage is visible between $5-20 \text{ mA/cm}^2$. As the cell is mostly ohmic controlled at current densities higher than 20 mA/cm^2 , the focus of the electrocatalyst kinetics is made at current densities below this value.

Setting the focus on the kinetic segment, Fig. 6.6 (left) shows the cell performance for the three exploratory cells. The plots were not corrected for the series resistance. Electrochemical impedance spectroscopy has repeatedly shown that the cells have an unchanged series resistance at about $300 \text{ m}\Omega\text{cm}^2$, which is expected for a Zirfon separator at a diam-

eter of 10 cm^2 in this setup [140]. A series resistance of $300\text{ m}\Omega\text{cm}^2$ results in a correction between 0.3 mV at 1 mA/cm^2 and 6 mV at 20 mA/cm^2 . This correction would be within the error bars. Hence, it was decided to present iR -uncorrected results only to guarantee an undistorted overview about the results.

Single-electrode potential measurements are carried out during the polarization curves versus both reference electrodes. As described before, the measurement with the reference electrode behind the electrode will, with increasing current density, underestimate the actual electrode overpotential. The opposite reference electrode will accordingly overestimate it. For the evaluation of the single-electrode potentials throughout this work, the reference potential measurements with the reference electrodes behind the respective electrodes were chosen. This approach appears more sensitive, as the measurement versus the opposite reference electrode has a greater influence from potential-distribution, pH-gradient, noise, which results from gas evolution, and from the counter electrode. In order to address the ambiguity of this approach, the single-electrode potentials will be given with an asymmetric error. The more positive error, with regards to the overpotential, will remain from the dual measurement versus the reference electrode behind the electrode. For the more negative error, which results in a higher overpotential, the average of both measurements versus the opposite reference electrode was chosen. Admitting that this error greatly overestimates it, it is not possible that the actual overpotential is higher than this value. Therefore, the represented data and errors must include the actual single-electrode potential.

An illustration to validate this approach is given in Fig. 6.6 (right). If the approach to deduct single-electrode potentials holds true, the summation of both electrode overpotentials and the series resistance have to match with the cell voltage. The cell voltage is directly measured by the setup and is a set cell characteristic, which is not doubted. As mentioned before, the series resistance may be neglected in the kinetic segment. So, Fig. 6.6 (left) was extended with the summation of the single-electrode overpotentials, obtained from the reference electrodes behind the respective electrodes, in the right part of the figure (dotted lines). The colored shapes represent the errors from this approach, which, as described previously, result from the measurements of the electrode-potentials versus both of the reference electrodes.

It is apparent that the approach indeed underestimates the single electrode over-

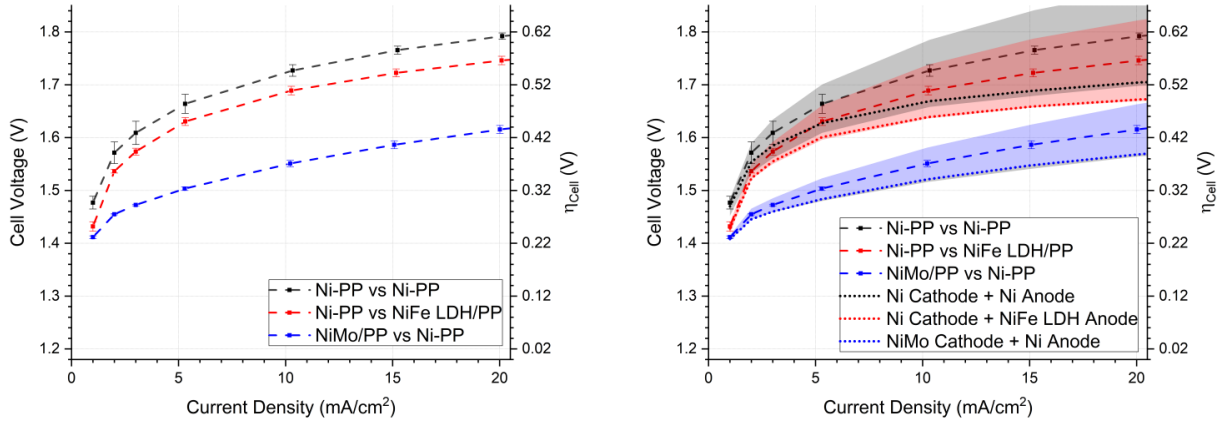


Fig. 6.6: Left: Repetition of Fig. 6.5, focused on the kinetic segment up to 20 mA/cm^2 . Right: Additional plotting of the summation of the single electrode overpotentials (dotted lines) and the respective errors (shades). The deviation between the cell voltage and the summed single electrode overpotentials of the three cells is $4\text{--}7 \text{ mV}$ at 1 mA/cm^2 , $20\text{--}36 \text{ mV}$ at 5 mA/cm^2 , $30\text{--}58 \text{ mV}$ at 10 mA/cm^2 and $48\text{--}87 \text{ mV}$ at 20 mA/cm^2 .

potentials, when the errors are neglected. However, this is not the case for lower current densities. Furthermore, the summation does match up with the measured cell voltages when considering the errors. It is therefore possible to declare the approach as valid.

The accuracy of this approach can be evaluated by the deviation between the summation of the overpotentials and the cell voltage. The deviation between the cell voltage and the summed single electrode overpotentials of the three cells is $4\text{--}7 \text{ mV}$ at 1 mA/cm^2 , $20\text{--}36 \text{ mV}$ at 5 mA/cm^2 , $30\text{--}58 \text{ mV}$ at 10 mA/cm^2 and $48\text{--}87 \text{ mV}$ at 20 mA/cm^2 . The deviations result from both electrodes, and thereby do not represent a deviation of the single electrode, which is certainly lower. Without further studies, including kinetic modeling and a reference electrode between anode and cathode, it is not possible to quantify how much lower the deviation of a single electrode is.

Lower current density single electrode overpotential measurements at $1\text{--}5 \text{ A/cm}^2$ are, in summation, in close proximity to the cell voltage. The measurement at 10 mA/cm^2 comes out to be in a transition zone, in which the deviation becomes significantly higher than the error of the cell voltage. It shall be noted that, due to the exceptional high positive error resulting from the measurements versus the opposite reference electrodes, which was considered twice in the summation of both overpotentials, the error with increasing current

density might be too pessimistic. This error has anyways been taken into account, as it is the maximum possible error. This allows for a critical assessment of the approach to obtain single-electrode potentials.

Based on these findings, most of the discussion about the single electrode potentials will be made at the lowest current densities within this work. As the value of 10 mA/cm^2 represents an important benchmark in the literature [8], it will further be considered at different stages.

6.2 Cell performance in zero-gap configuration

One important parameter before evaluating the stability and durability of electrocatalysts is to ensure that conclusions about such can be drawn. Especially in case of a low electrocatalyst-coverage, as in this work, it's mandatory to conclude that the electrocatalyst is driving the reaction. A comparably simple way, which is anyways necessary to evaluate a possible degradation, is the comparison of the electrochemical performance of coated and uncoated electrodes. This section is divided into two parts. It will present the results from the initial electrochemical tests of the cells *Ni-PP vs Ni-PP*, *Ni-PP vs NiFe LDH/PP*, and *NiMo/PP vs Ni/PP* (Fig. 6.7), which were used for the accelerated degradation tests, and the results of the cells *Ni-felt vs Ni-felt*, and *NiMo/felt vs NiFe LDH/felt* (Fig. 6.8), which are compared for the purpose of the long-term test.

In all illustrations about cell performances in the following, a figure with four subfigures will be shown. The top left subfigure shows the full cell performance of a polarization curve from $1 - 1000 \text{ mA/cm}^2$, with a limiting cell voltage of 2.6 V . The polarization curve is a result of a pre- and backscan, with a measurement time of $2 \cdot 60 \text{ s}$ at each current density. The top right figure zooms onto the kinetic segment of the cell, which was defined up to 20 mA/cm^2 (see Chap. 6.1.4). In the bottom, the single-electrode measurements, obtained as described previously in Chap. 6.1.4, of the cathode (left) and of the anode (right) are presented. In all cases, a correction for the series resistance was spared. The focus of this work remains on the kinetic segment, in which the series resistance contributions are negligible. To be able to compare to series resistance free values, it shall be noted that EIS

showed a non-diverting trend of the series resistance at about $300 \text{ m}\Omega\text{cm}^2$ for all presented cells, which results in an additional 6 mV of polarization at $20 \text{ mA}/\text{cm}^2$.

For the PP-supported cells, Fig. 6.7 illustrates their performance. It is apparent that, on a full cell level, the coating of the substrate in both cases, in which electrocatalyst was applied, had a positive impact on the cell performance. For the *NiMo/PP vs Ni-PP* cell, it is undoubtedly the result of the cathode performance, which is responsible for the performance increase. Considering the errors, the cathode performance at $10 \text{ mA}/\text{cm}^2$ increases by more than 100 mV compared to the uncoated nickel support. For the NiFe LDH coating, it is not apparent that the improvement in the cell kinetics results from an improved anode coating, or from a slightly improved cathode. However, when comparing the performance at $1 \text{ mA}/\text{cm}^2$, both, anode and cathode, show an improvement compared to uncoated electrodes, which exceeds the errors. It is therefore most reasonable to assume that both electrodes contribute to an improvement, and a comparison at higher current densities bears challenges due to the measurement ambiguity and the corresponding errors. In any case, it can be concluded that, for both cells with catalyst-coating, the electrocatalyst is indeed present and, at least in case of the kinetic segment, driving the reaction.

A similar picture can be drawn from the felt-supported cells, as shown in Fig. 6.8. For these two cells, it is apparent that both coated electrodes have a sufficient catalyst-coating, which drives the reaction in the kinetic segment. However, the NiFe LDH anode appears to have a higher onset-potential and thus reduced performance at the lowest current densities than the uncoated electrode. This effect may have several causes.

Firstly, the measurement accuracy at these low current densities could cause this difference. Secondly, it could be possible that the catalyst-coating was not as successful. However, the low overpotential of $\approx 245 \text{ mV}$ at $10 \text{ mA}/\text{cm}^2$ and the low increase of the overpotential from $\approx 195 \text{ mV}$ at $1 \text{ mA}/\text{cm}^2$ opposes this possibility. The uncoated electrode experienced a twice as high increase of the overpotential in the same window. Thirdly, it cannot be excluded that impurity-uptake has a non-negligible impact on the uncoated nickel electrodes. Impurities, especially iron [21, 59, 92, 118, 187], can explain the effect sufficiently. Since the setup is used for a variety of electrodes, it cannot be, despite the efforts of pre-electrolyzing the electrolyte and cleaning the system after each test, excluded that impurities are present.

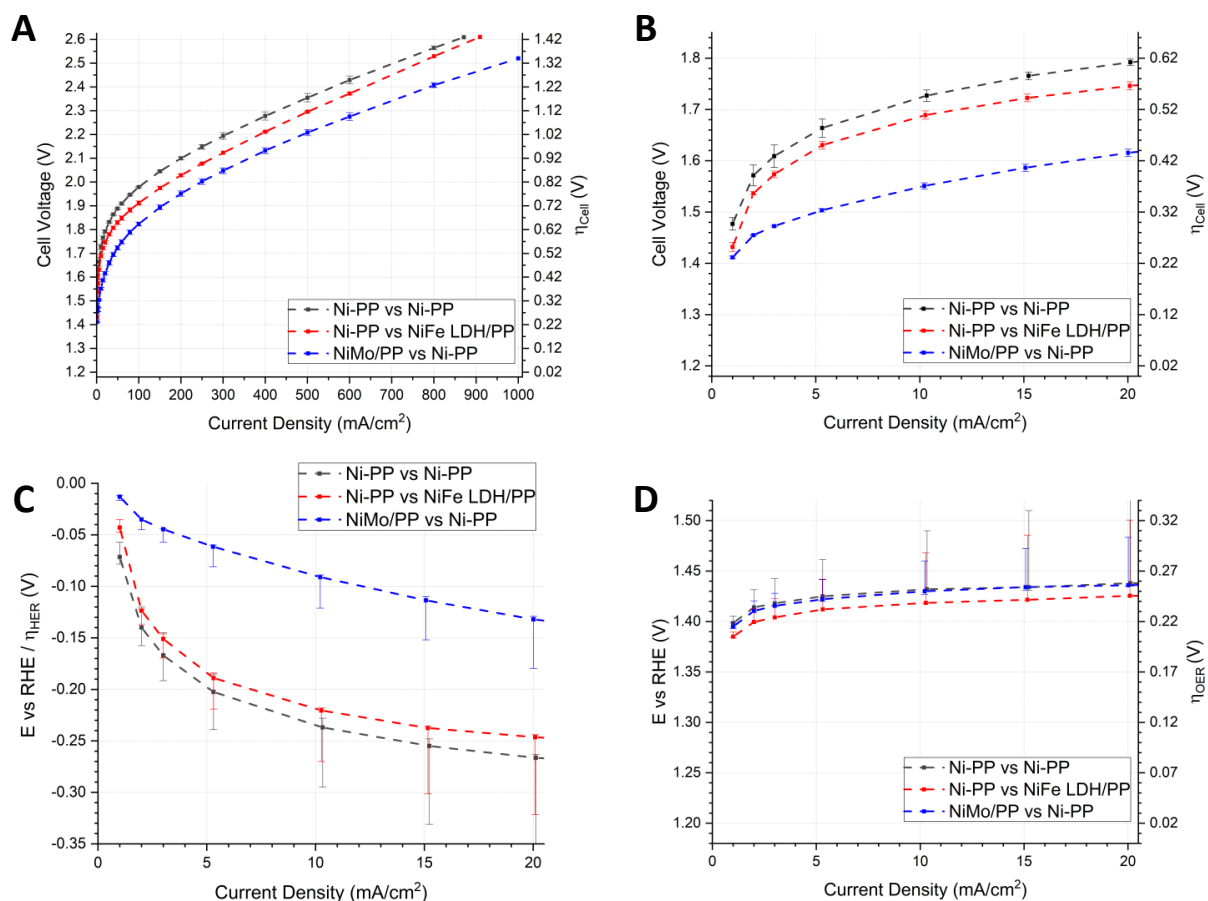


Fig. 6.7: Polarization curves of electrodes with perforated plate-support at 80 °C in 30 w% KOH. **A:** Cell voltage and respective overpotential. **B:** Focused view on the kinetic segment. **C:** Cathode potential vs RHE in the kinetic segment. **D:** Anode potential vs RHE and respective overpotential in the kinetic segment.

In conclusion, the measurements allow to claim that the electrode manufacturing was successful, to the degree that electrocatalyst stability and durability tests are feasible despite the low catalyst-loading. Furthermore, interfering artifacts can be correlated to the measurement errors and the presence of impurities.

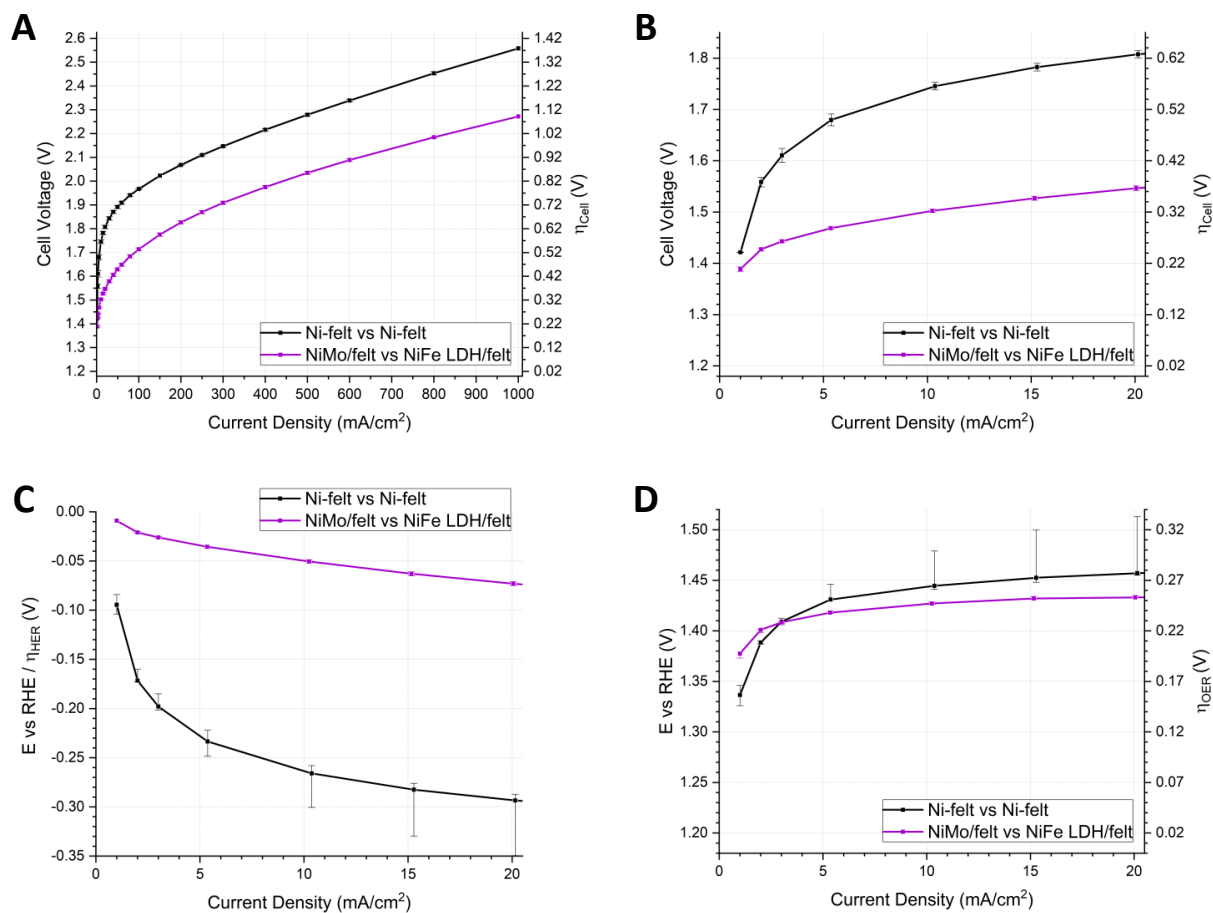


Fig. 6.8: Polarization curves of electrodes with felt-support at 80 °C in 30 w% KOH. **A:** Cell voltage and respective overpotential. **B:** Focused view on the kinetic segment. **C:** Cathode potential vs RHE in the kinetic segment. **D:** Anode potential vs RHE and respective overpotential in the kinetic segment.

6.3 Voltammetry and open-circuit as tools for accelerated degradation studies

Reliable statements towards the stability of electrocatalysts, which have to ensure a decade-long high performance, are challenging without respective long-term testing. An attempt to shed light on the important long-term stability of electrocatalysts, within comparably short measurement times and the frame of a laboratory setup, is an accelerated degradation study.

An accelerated degradation test allows to estimate whether the tested electrocatalyst may suffer from severe degradation over time. The focus of these studies lays on the upper and the lower operational point of an electrode in a commercial setup.

Procedure

One approach to simulate the dynamic operation of an electrode in a commercial setup, within a short time-frame, is voltammetry. The cell is exposed to a dynamically changing cell voltage from below the equilibrium voltage to the highest operational voltage. In this work, the cells were cycled 20 times between a cell voltage of 1.0 – 2.5 V² at a sweep rate of 50 mV/s. In addition, the cells are held at OCV over night to simulate a shut-down of the commercial setup. In both cases, polarization curves and EIS were conducted before and after the accelerated tests. The accelerated degradation tests were conducted on the PP-supported cells *Ni-PP vs Ni-PP*, *Ni-PP vs NiFe LDH/PP*, and *NiMo/PP vs Ni-PP*, at a temperature of 80 °C.

6.3.1 Cyclic voltammetry on perforated plate supported electrodes

The cyclic voltammograms of the cells *Ni-PP vs Ni-PP*, *Ni-PP vs NiFe LDH/PP*, and *NiMo/PP vs Ni-PP* are presented in Fig. 6.9, 6.10, and 6.11, respectively. The focus was placed on the region of up to 50 mA/cm², as firstly redox-processes are visible in this part of the tests, and secondly it reflects the kinetic segment. On behalf of completeness, the figures represent the full measurement in a small window.

²The upper point was limited by the VSP-300 (with 20 A booster) potentiostat, while other measurements with the DC supply allowed limits of 2.6 V. As the aim for an efficient alkaline electrolysis system is to remain at a cell voltage below 2.0 V, the difference can be considered negligible, as both upper limits are well above this target.

For the *Ni-PP vs Ni-PP* cell (Fig. 6.9) an increase of the current density at cell voltages above 1.7 V is visible from the first to the 10th cycle, whereafter it remains stagnant. This behavior is in line with the stagnation of two oxidation peaks at ≈ 1.2 and ≈ 1.55 V, which experience a negative shift in the peak potential and a decrease within the first ten cycles. Since a corresponding reductive process is only visible in the first cycle, it can be concluded that the cycling of the cell voltage results in a continuous, yet equilibrating, oxidation of one of the electrodes. This can be explained by the formation of a nickel oxyhydroxide/oxide phase on the anode, which could further take up iron-traces. Otherwise, the formation of nickel hydroxide on the cathode could occur as well. Most importantly, a degradation of the cell is not visible. In fact, the cell displays some activation.

For the *Ni-PP vs NiFe LDH/PP* cell (Fig. 6.10) a deviation from the initial voltammogram to a decreasing performance is visible with increasing cycles. For instance, a continuing decrease of the current density at 1.7 V from ≈ 28 mA/cm² to ≈ 12 mA/cm² from the first to the 20th cycle indicates an ongoing degradation of the electrocatalyst. Furthermore, an initial oxidation process, occurring at ≈ 1.45 V, is invisible in the following cycles. The absence in further cycles, while the *Ni-PP vs Ni-PP* cell does not implicate such an absence, leads to the assumption that the as synthesized electrocatalyst layer experiences an initial oxidation. The oxidation, which may or may not be partial, indicates an *in situ* modification of the surface. It does, contrarily, not allow to conclude on a degradation process. However, the accelerated degradation does show a decrease in performance with cycling, which could be due to the applied high overpotentials on the anode at high cell voltages. The voltammograms further indicate a decrease in the slope at cell voltages higher than 2.15 V in the first cycle, which can be associated to a, during CVs remaining, further oxidation of the anode electrocatalyst above this cell voltage, as this process is absent in the pure nickel cell. The performance decrease might further be due to the exposition to underpotential conditions after oxygen evolution, or due to both; high overpotentials and underpotentials. As the cathode was a nickel electrode as in the *Ni-PP vs Ni-PP* cell, it seems to be only remotely possible that the observed degradation in the *Ni-PP vs NiFe LDH/PP* cell, which is not present in the all nickel cell, results from anything else other than the anode.

For the *NiMo/PP vs Ni-PP* cell (Fig. 6.11) the progression of the voltammograms match with the results from the *Ni-PP vs NiFe LDH/PP* cell. An initial high performance

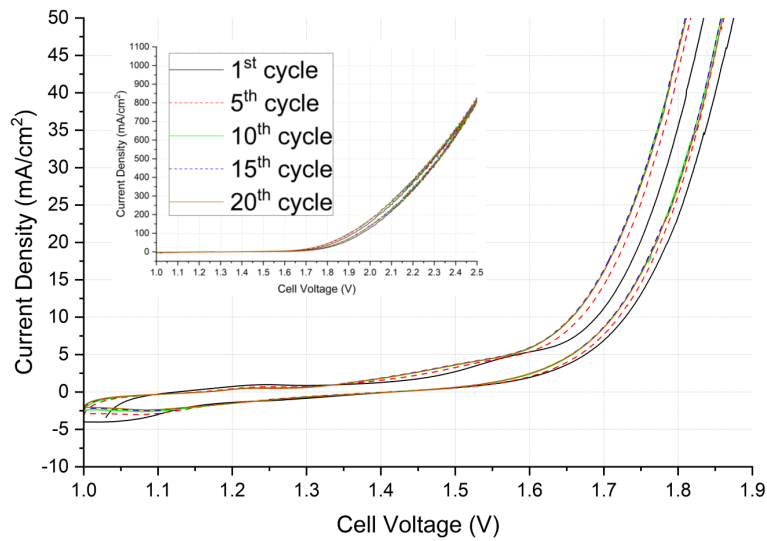


Fig. 6.9: Cyclic voltammograms of the *Ni-PP vs Ni-PP* cell at 50 mV/s and 80 °C in 30 w% KOH, not corrected for the series resistance. Shown are the 1st, 5th, 10th, 15th, and 20th cycle; the smaller figure shows the full range from 1.0 – 2.5 V, the other zooms on the region up to 50 mA/cm².

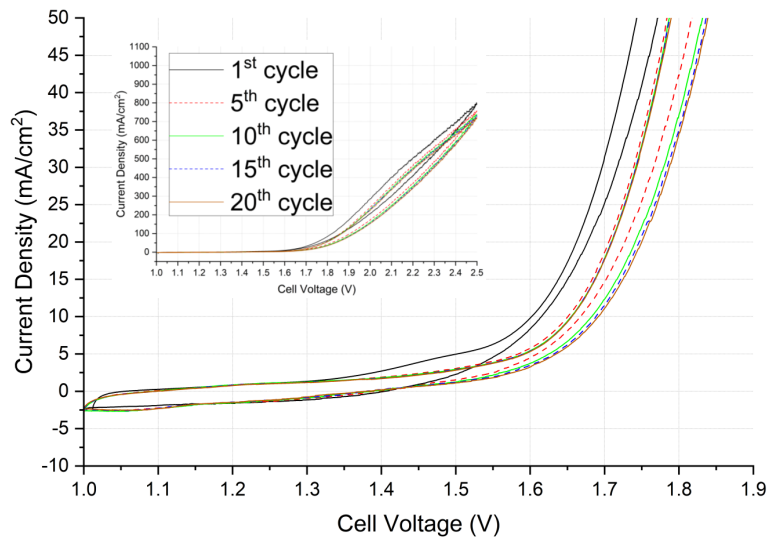


Fig. 6.10: Cyclic voltammograms of the *Ni-PP vs NiFe LDH/PP* cell at 50 mV/s and 80 °C in 30 w% KOH, not corrected for the series resistance. Shown are the 1st, 5th, 10th, 15th, and 20th cycle; the smaller figure shows the full range from 1.0–2.5 V, the other zooms on the region up to 50 mA/cm².

decreases with cycling. However, two oxidation peaks at ≈ 1.22 V and ≈ 1.45 V are visible, which decrease with cycling and stagnate after the 10th cycle. While the lower oxidation peak does not remarkably change in the peak potential, the higher oxidation peak experiences a positive shift. The reductive peak at ≈ 1.0 V corresponds well with the higher oxidation peak. While it appears to be obvious to associate this redox-couple with the $\text{Ni}^{2+}/\text{Ni}^{3+}$ redox couple in the nickel anode, the direction of the shift in the peak-potential, the peak-potential position, and the current at the peak-potential of the oxidation peak at ≈ 1.45 V differ from the peak at ≈ 1.55 V in the *Ni-PP vs Ni-PP* cell. If these redox-processes were only to be associated with the nickel anode, all three aforementioned parameters should be similar for both cells, as both used a nickel anode. Hence, it is reasonable to think that an altering process occurs on the cathode simultaneously, which ultimately causes the ongoing performance decrease in the *NiMo/PP vs Ni-PP* cell with cycling.

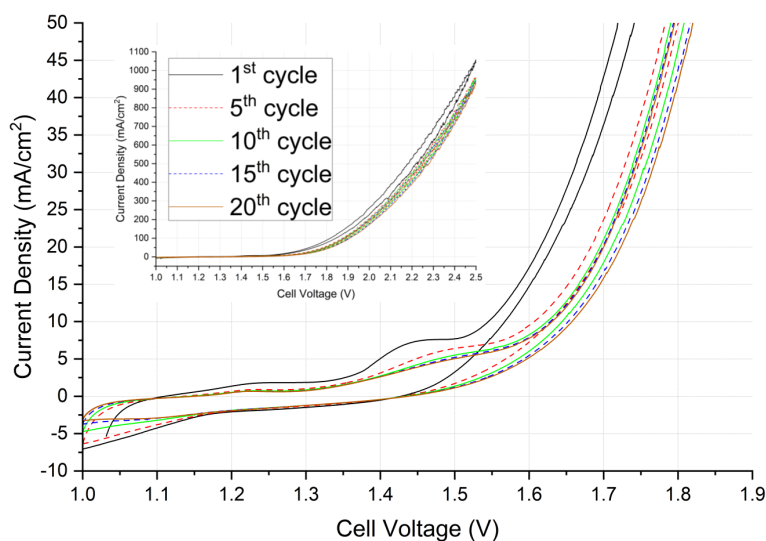


Fig. 6.11: Cyclic voltammograms of the *NiMo/PP vs Ni-PP* cell at 50 mV/s and 80 °C in 30 w% KOH, not corrected for the series resistance. Shown are the 1st, 5th, 10th, 15th, and 20th cycle; the smaller figure shows the full range from 1.0 – 2.5 V, the other zooms on the region up to 50 mA/cm².

In order to draw further conclusions of the observed processes in cyclic voltammetry, it is essential to know the single-electrode potentials during the voltammograms, especially in the region close to the equilibrium cell voltage. As such, Fig. 6.12 illustrates the averaged

single electrode potentials measured during the 20 voltammograms on the *Ni-PP vs NiFe LDH/PP* cell close to the equilibrium potential. Furthermore, the illustration shows the measurements versus both reference electrodes and their bias, which allows to show the quality of the single electrode potentials with respect to the cell voltage. A bias close to zero verifies the assumption that the effects of potential-distribution, a pH-gradient, and the series resistance are negligible. The measured values did vary unremarkably little between the cycles, which results in an invisible error bar.

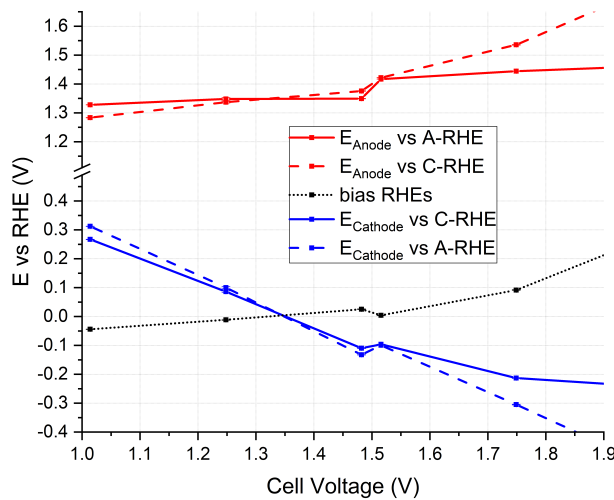


Fig. 6.12: Single electrode potentials vs both reference electrodes, and their bias, during cyclic voltammetry on the *Ni-PP vs NiFe LDH/PP* cell, see Fig. 6.10. Lines as guidelines to the eye between measurements.

The anode is subjected to about 1.3 V vs RHE at a cell voltage of 1.0 V. The cathode, correspondingly, is subjected to a potential of up to 0.3 V vs RHE. The bias between the measurements of the single electrode potentials with both reference electrodes is close to zero, more specifically less than $|50|$ mV up to a cell voltage of ≈ 1.65 V. Depending on the cycle number, this corresponds to $6 - 18$ mA/cm² in Fig. 6.10. This further shows the quality of the single electrode potential measurements close to the equilibrium cell voltage.

Furthermore, the exposure of the cathode to underpotential conditions is an important detail, as the voltammograms hint towards a degradation process of the NiMo cathode after the first cycle. As the cell experiences a reversed current at these underpotential conditions,

an oxidation process on the cathode, such as hydrogen or catalyst oxidation, must occur. Hence, the degradation is likely to result from underpotential conditions on the reverse scan.

6.3.2 Open-circuit voltage simulating the shutdown response

The second accelerated degradation test was the exposure to the OCV. After a polarization curve, the cells were shut down and held at 80 °C with circulating electrolyte between 13.5–15.5 h overnight. During this process, the cell voltage and the single electrode potentials were recorded. As the OCV is free of influences of a potential-distribution, a pH-gradient and the series resistance, a bias between the reference electrodes was not measured. The results of the evolution of the three parameters are shown for the *Ni-PP vs Ni-PP*, *Ni-PP vs NiFe LDH/PP*, and *NiMo/PP vs Ni-PP* cells in Fig. 6.13.

In all three cases, the cell voltage decreases continuously within the first two hours. The decrease is highest within the first 30 min. The anode electrode potential follows the trend of the cell voltage, while it remains at 0.6–0.7 V vs RHE in the time-frame of 30 min to two hours. The cathode experiences a potential of up to 0.1–0.2 V vs RHE within the first 30 min, and almost linearly increases thereafter. All three profiles resemble the discharge cycle of a battery.

The resemblance is further the explanation for the evolution of the single electrode potentials and the cell voltage over time. The electrolyte reservoirs separate the gaseous electrolysis products, hydrogen and oxygen, from the electrolyte. However, both gases dissolve and saturate the electrolyte over time. This saturation remains until the current is cut and causes the cells to reverse the hydrogen and oxygen evolution to the hydrogen oxidation and oxygen reduction reactions. Furthermore, the electrodes inherit a charge of ad- and absorbed species from electrolysis. By reversing the potential, the electrodes discharge. The electrolyzer cell then behaves like a fuel cell. After the dissolved gases and the ad- and absorbed species are consumed, the cell voltage drops to zero. The cathode and the anode then experience an OCV of ≈ 0.95 V vs RHE.

This discharge-process, which has a remarkable similarity to a deep discharge-process of a battery, thereby exposes the electrocatalyst not just to underpotential conditions, but also to the reverse electrochemical reactions. Hence, it is important to address both cases, when the stability of electrocatalysts is evaluated.

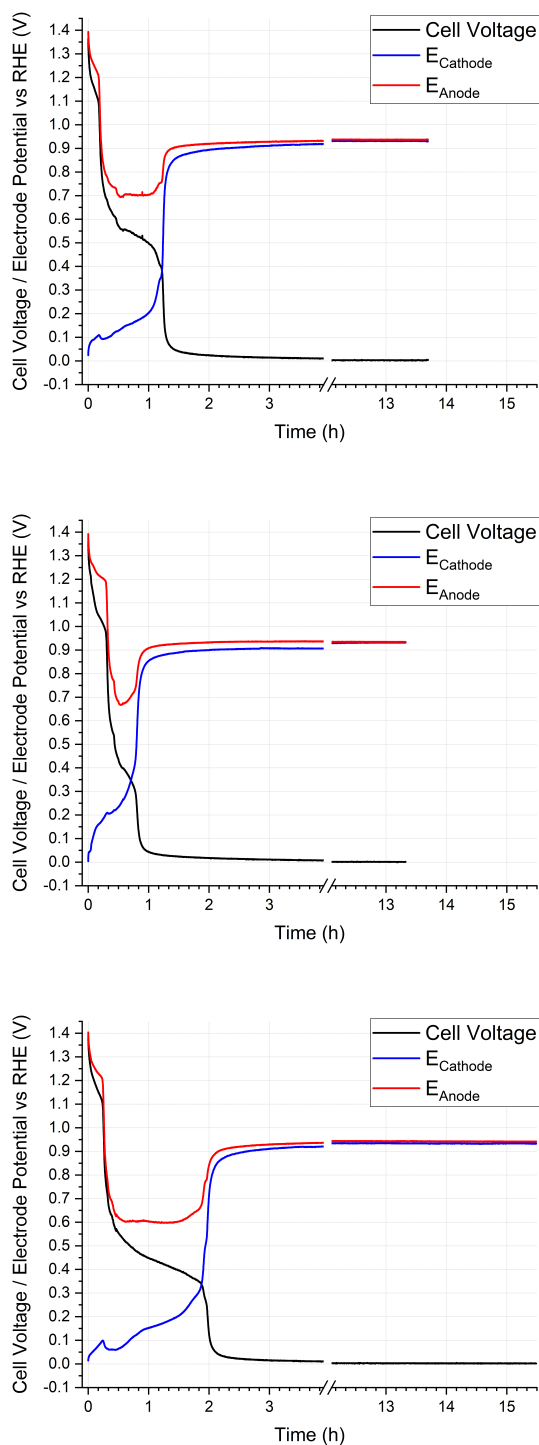


Fig. 6.13: Evolution of the cell voltage, the cathode and the anode electrode potential vs RHE at open-circuit voltage. Time since shut-down, which occurred immediately after a polarization curve. Top: *Ni-PP vs Ni-PP* cell. Middle: *Ni-PP vs NiFe LDH/PP* cell. Bottom: *NiMo/PP vs Ni-PP* cell. Measurements at 80 °C in 30 w% KOH.

6.3.3 Influence of cyclic voltammetry and open-circuit voltage on the cell and electrode kinetics

The accelerated degradation tests by CV and by OCV indicate degradation processes. In order to enlighten their effects, this chapter will compare the performance of the cells before (see Chap. 6.2) and after accelerated degradation. For each cell, the results from the polarization curve and the following electrochemical impedance spectroscopy at 1 mA/cm^2 are shown together. The EIS-fitting with an LR(RQ)(RQ) equivalent circuit allows to calculate an equivalent capacity, as non-blocking electrode, for each of the electrodes. With an equivalent value of $40 \mu\text{F/cm}^2$ for a metallic surface [8] and $60 \mu\text{F/cm}^2$ for an oxide surface [188] for cathode and anode, respectively, it is possible to further give an estimate about the surface roughness. However, it was shown in Chap. 5 that these estimates are not accurate at low overpotentials for the hydrogen evolution reaction. Minor changes in the estimated roughness may not explain a change to it but to the reaction mechanism. A different reaction mechanism affects a pseudocapacitive contribution, which is inherited in the fitted double layer capacitance. In either case, an alteration of the electrocatalyst's surface occurs. Therefore, these estimations are explicitly reported in parentheses, as they can be seen as guidelines, but not absolute values.

For the *Ni-PP vs Ni-PP* cell, Fig. 6.14 shows the results from the polarization curve, Fig. 6.15 the spectra and Fig. 6.16 the fitting of the electrochemical impedance spectroscopy. The summarized results from both are given in Tab. 6.1.

As visible by the polarization curves, the all nickel cell does suffer from a slight degradation through CVs. The degradation appears to be associated with a change in the anode performance. This is in line with the fitting results from EIS. The cathode appears to improve by 27% with respect to the charge transfer resistance. An increase of the equivalent capacity of the cathode by 61% further indicates an improvement in of its kinetic performance. The slight improvement can be associated with a partial oxidation of the surface [42, 48]. However, the performance increase is rather small, and further becomes a slight decrease with increasing current density according to the polarization curves. The deviation, on the contrary, is marginal and within the associated errors. Hence, the cathode performance can be considered as kinetically unaffected, although surface alterations occur.

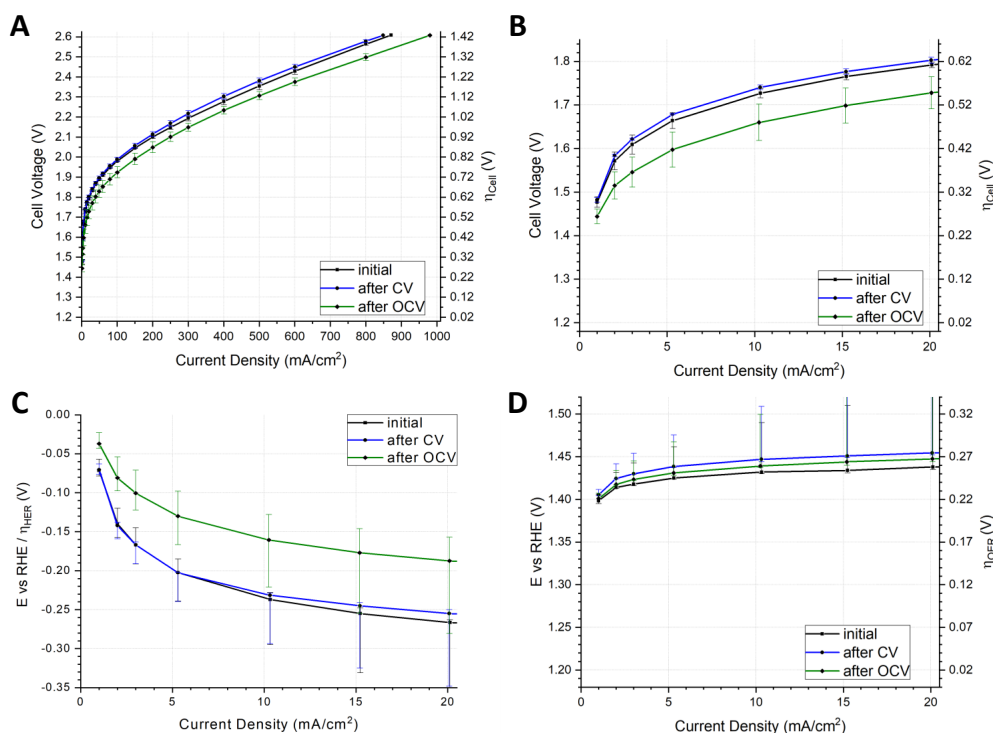


Fig. 6.14: Influence of cyclic voltammetry and open-circuit on the kinetics of the *Ni-PP vs Ni-PP* cell at 80 °C in 30 w% KOH. **A:** Polarization curve of the cell. **B:** The kinetic segment of the cell polarization curve. **C:** Kinetics of the cathode. **D:** Kinetics of the anode.

Tab. 6.1: Kinetics of the *Ni-PP vs Ni-PP* cell at 1 mA/cm², before and after accelerated degradation. Charge transfer resistances and equivalent capacitances as fitting results from EIS with an LR(RQ)(RQ) equivalent circuit. *: erroneous.

Parameter	Unit	initial	after CV	after OCV
Cell Voltage	V	1.477 ± 0.012	1.482 ± 0.005	1.444 ± 0.017
Cathode potential vs RHE	V	-0.072 +0.015/ - 0.007	-0.071 +0.008/ - 0.006	-0.037 +0.014/ - 0.006
Cathode R_{ct}	Ωcm^2	57.5	41.9	20.8
Cathode C_{eq} (Roughness)	$\mu\text{F}/\text{cm}^2$ cm^2/cm^2	566.75 (14.2)	914.17 (22.9)	64.33 (1.6)
Anode potential vs RHE	V	1.399 +0.007/ - 0.004	1.406 +0.006/ - 0.002	1.401 +0.006/ - 0.000
Anode R_{ct}	Ωcm^2	61.8	70.3	26.7*
Anode C_{eq} (Roughness)	$\mu\text{F}/\text{cm}^2$ cm^2/cm^2	167.78 (2.8)	197.34 (3.3)	58499.70* (975.0)*

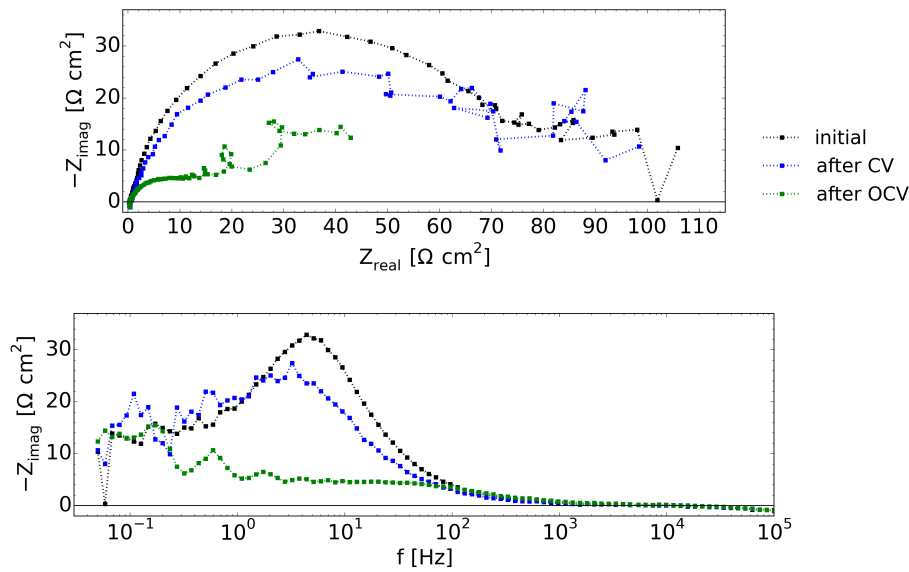


Fig. 6.15: Electrochemical impedance spectra of the *Ni-PP vs Ni-PP* cell at 1 mA/cm^2 and 80°C in 30 w\% KOH , before and after accelerated degradation. Top: Nyquist plots. Bottom: $-Z_{Im}$ over f .

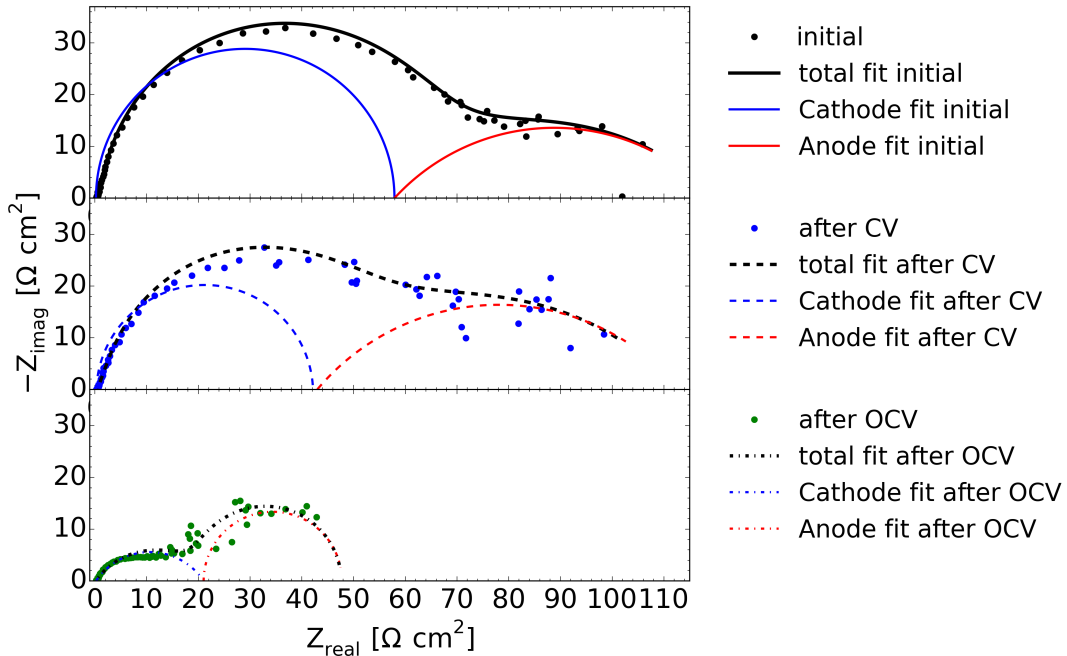


Fig. 6.16: Fitting results of the electrochemical impedance of the *Ni-PP vs Ni-PP* cell at 1 mA/cm^2 and 80°C in 30 w\% KOH with an $\text{LR}(\text{RQ})(\text{RQ})$ equivalent circuit. Top: Before accelerated degradation. Middle: After cyclic voltammetry. Bottom: After OCV.

The anode decreases in performance after CVs, as visible by the 18 % increase of the charge transfer resistance. The performance decay can be associated with the formation of higher oxidation states, as, for instance, with the formation of a Ni⁴⁺ containing phase [96], which thickens at potentials above 1.56 [91]–1.59 V [96] vs RHE. With a cell voltage of 2.5 V as the upper limit of the cyclic voltammograms, it is very likely that these anode potentials are exceeded. The phase forming above these potentials is not conclusively studied in the literature [96], but it is often referred to the formation of γ -NiOOH by overcharging [14, 21, 95]. The formation of a higher oxidation state in the anode is further backed by the equivalent capacity, which increases by 18 % compared to the initial value. This increase in equivalent capacity, while the performance decreases, therefore may not be related to an increase of the surface area, but to the formation of a higher oxidation state.

After OCV, the all nickel cell appears to improve in performance, also in comparison to the initial performance. The polarization curve results clearly show that this improvement must result from the cathode, while the anode improves closely to its initial performance. The fitting of the impedance has to be seen with caution. The fitting results of the equivalent capacities appear unrealistic, which is a cause of the impedance quality. While the previous impedances showed a distinct cathode peak in the $-Z_{Im}$ over f plots, the impedance after OCV shows a shift towards low frequencies, at which the noise level is higher. The interference of the cathode with the noise level and the possible overlap with the anode does not allow to draw precise results from the fitting. However, the shift of the cathode towards lower frequencies is equivalent to an increase of the electrode's capacity. The equation to calculate the capacity from impedance, see Eq. 3.10, is inverse proportional to the frequency. A decrease in the frequency response thereby corresponds to an increase in the capacity. Together with an improvement of the overpotential at 1 mA/cm², even after considering the possible errors, the cathode undoubtedly increases in performance after OCV.

This effect can be explained by the partial oxidation of the cathode's surface [42, 48]. Following Fig. 2.9, the exposure of the cathode to 0.3 V vs RHE on the reverse scan of the cyclic voltammetry has a small effect on the cathode performance. During OCV, the cathode experiences a potential of 0.95 V vs RHE. At this potential, the partial oxidation of the nickel surface has a major impact on the kinetic performance for the HER. According to Liang et al. [42], as shown in Fig. 2.9, a partial oxidation at 1 V vs RHE results in a

performance increase by a factor of ≈ 5 of the measured current compared to pure nickel. Although the presence of iron traces cannot be ruled out, the overall response of the cathode to the accelerated degradation tests can be explained by the partial oxidation of nickel.

The nickel anode, considering the errors, shows the same performance after OCV, compared to the initial value. The higher oxidation state, which was presumably formed during cyclic voltammetry, was rejuvenated at underpotential conditions. The rejuvenating effect, which is described in the literature [91, 189], further confirms the presence of higher oxidation states at high overpotentials. In addition, the nickel anode, when operated in an overpotential window below the (reversible) formation of the higher oxidation state, may show a stable high-performance.

For the *Ni-PP vs NiFe LDH/PP* cell, Fig. 6.17 shows the results from the polarization curve, Fig. 6.18 the spectra and Fig. 6.19 the fitting of the electrochemical impedance spectroscopy. The summarized results from both are given in Tab. 6.2.

The cathode of this cell was again a nickel electrode. It should therefore show a similar response as the cathode from the all nickel cell. After CV, however, the cathode shows a slight decrease in performance with regards to the charge transfer resistance. On the other hand, the marginal decrease with current density is similar. Furthermore, the increase of the equivalent capacity follows the trend from the previous nickel cathode. Hence, the slight differences may result from statistical deviations. After OCV, this nickel cathode shows a performance increase as well, just as the previous nickel cathode. In comparison to the initial value, a decrease of the charge transfer resistance by 49% and an increase of the equivalent capacity by 16% indicate a performance gain. The impedance after OCV of this cell, in contrast to the all nickel cell, was of high quality enough for a fitting. The results from both cells together confirm the improvement of a nickel cathode after accelerated degradation.

Albeit traces of iron, especially in the *Ni-PP vs NiFe LDH/PP* cell, cannot be excluded, the nickel-cathode improvement can be ascribed to the, in the literature described [42, 48], intrinsic effect of partial oxidation. The performance increase could further be explained by an increase of the surface roughness, which is also associated by an increase of the equivalent capacity. However, due to the knowledge from the literature, the obtained results from Chap. 5, and the decrease of the charge transfer resistances, surface roughening is the less plausible cause in comparison to an intrinsic origin.

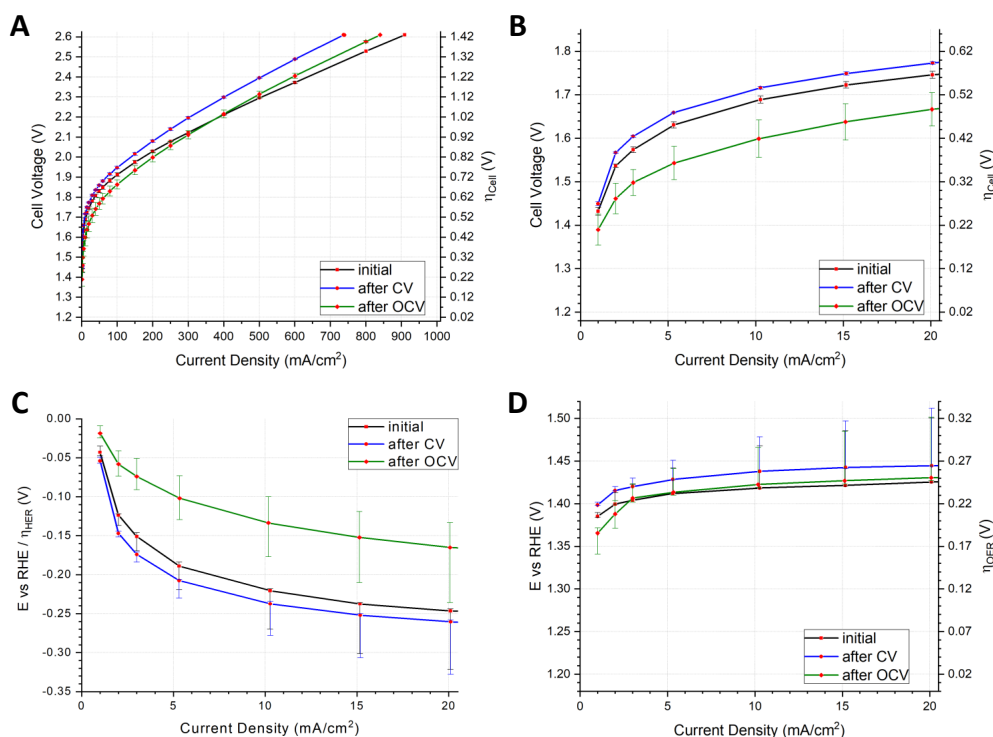


Fig. 6.17: Influence of cyclic voltammetry and open-circuit on the kinetics of the *Ni-PP vs NiFe LDH/PP* cell at 80 °C in 30 w% KOH. **A:** Polarization curve of the cell. **B:** The kinetic segment of the cell polarization curve. **C:** Kinetics of the cathode. **D:** Kinetics of the anode.

Tab. 6.2: Kinetics of the *Ni-PP vs NiFe LDH/PP* cell at 1 mA/cm², before and after accelerated degradation. Charge transfer resistances and equivalent capacitances as fitting results from EIS with an LR(RQ)(RQ) equivalent circuit.

Parameter	Unit	initial	after CV	after OCV
Cell Voltage	V	1.432 ± 0.009	1.450 ± 0.005	1.390 ± 0.036
Cathode potential vs RHE	V	-0.043 +0.008/ - 0.005	-0.054 +0.005/ - 0.003	-0.019 +0.010/ - 0.006
Cathode R_{ct}	Ωcm^2	51.5	55.9	26.3
Cathode C_{eq} (Roughness)	$\mu\text{F}/\text{cm}^2$ cm^2/cm^2	1060.95 (26.5)	1128.01 (28.2)	1227.75 (30.7)
Anode potential vs RHE	V	1.385 +0.005/ - 0.001	1.399 +0.003/ - 0.001	1.366 +0.006/ - 0.025
Anode R_{ct}	Ωcm^2	64.2	67.2	54.4
Anode C_{eq} (Roughness)	$\mu\text{F}/\text{cm}^2$ cm^2/cm^2	341.09 (5.7)	490.62 (8.2)	864.86 (14.4)

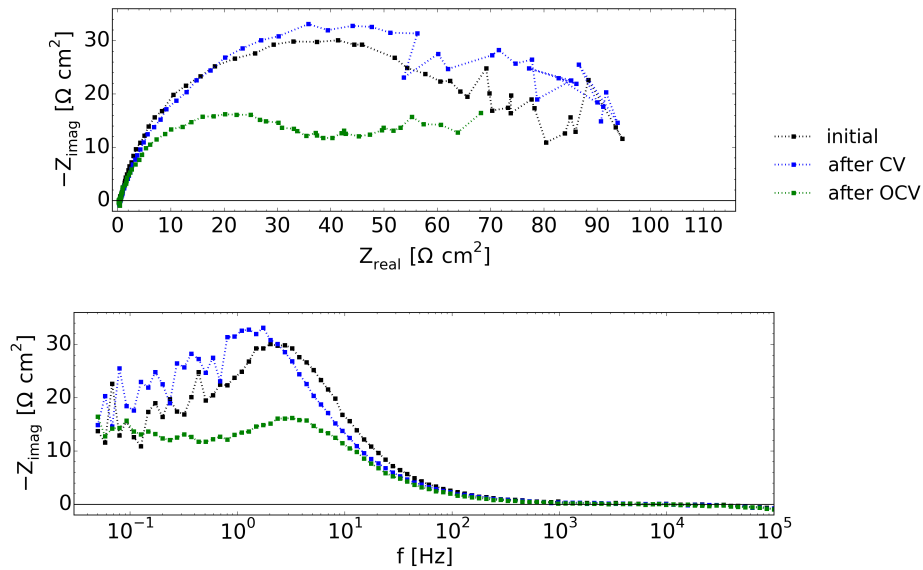


Fig. 6.18: Electrochemical impedance spectra of the *Ni-PP vs NiFe LDH/PP* cell at 1 mA/cm^2 and 80°C in 30 w\% KOH , before and after accelerated degradation. Top: Nyquist plots. Bottom: $-Z_{Im}$ over f .

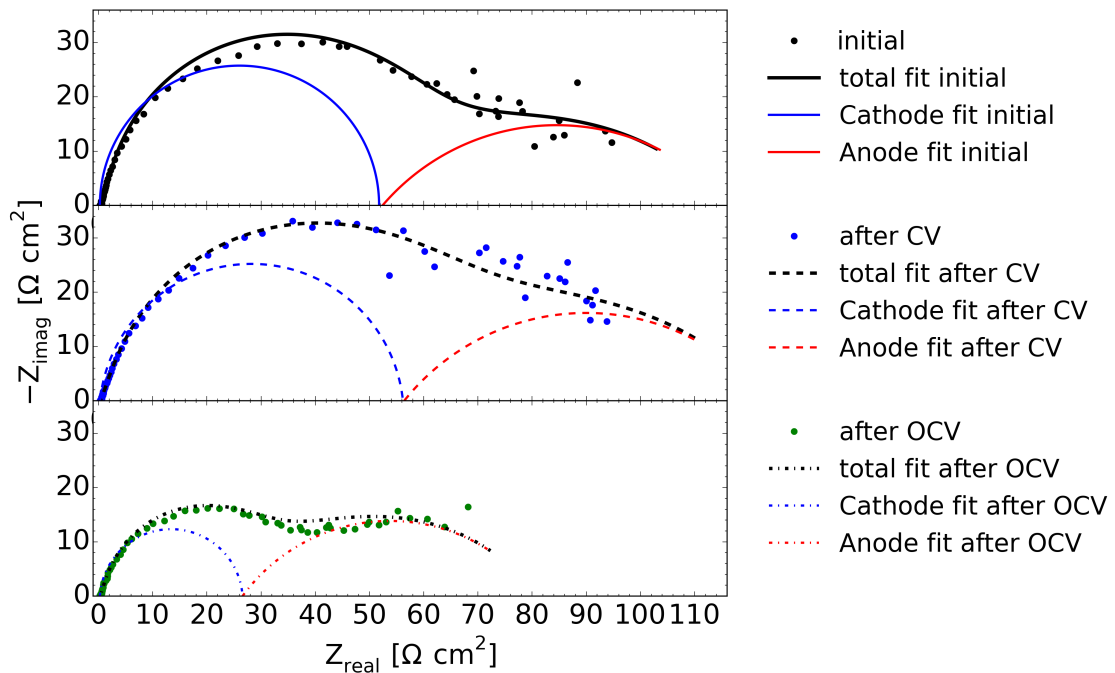


Fig. 6.19: Fitting results of the electrochemical impedance of the *Ni-PP vs NiFe LDH/PP* cell at 1 mA/cm^2 and 80°C in 30 w\% KOH with an LR(RQ)(RQ) equivalent circuit. Top: Before accelerated degradation. Middle: After cyclic voltammetry. Bottom: After OCV.

In terms of the NiFe LDH anode, the general trend is similar to the nickel anode. A slight decrease from the initial performance to the performance after CV is visible. The increase of the charge transfer resistance by 5% is accompanied with an increase of the overpotential by 14 mV, which is greater than the margin of error. An additional increase of the equivalent capacity by 44% relates to the formation of higher oxidation states during CV. The results from EIS are taken as a qualitative rather than as a quantitative guidance for the anode of this cell. Its impedance response is at low frequencies, at which noise is interfering. Quantitative differences, such as the 5% different charge transfer resistance, are therefore not definite differences. However, the performance decay with current density in the polarization curve complies with these EIS fitting results. Thereby, a performance decay alike the nickel anode is seen in the NiFe LDH anode after CV.

After OCV, the NiFe LDH anode improves in performance. Compared to the initial performance, the exposure to 0.95 V vs RHE leads to a by 15% improved charge transfer resistance. The overpotential at 1 mA/cm² improves by 19 mV, but further shows no deviation to the initial performance with increasing current density. As the equivalent capacity increases by 154%, a significant alteration of the surface must occur at OCV conditions. This deviation, although associated with errors through the impedance quality and fitting, is too high to describe surface roughening alone. In fact, an oxidation of the surface, ultimately changing the reaction mechanism and thereby adsorbents, is the most plausible explanation.

The surface oxidation would also explain the, to the initial polarization curve, identical performance with increasing current density. Oxidizing the catalyst's surface will decrease its intrinsic catalytic performance. In parallel, the oxidation increases the surface roughness. Both responses together clarify, why the polarization curve reveals no kinetic improvement, while the equivalent capacity increases; the decrease of the catalytic performance is counter-balanced by the extended amount of active sites. However, an intrinsic catalytic performance loss is controversial to a decrease of the charge transfer resistance. This may be explained by an over-proportional increase of active sites. An increase of the exchange current density, with respect to the geometric surface area, overall improves the electrode's charge transfer resistance, while the intrinsic, single site, exchange current density decreases. An intrinsic decay is backed by the fact that, albeit the margins of error, the increase of the overpotential between 1 – 10 mA/cm² from the initial value of ≈ 34 mV increases to ≈ 57 mV after

OCV. Based on these results, it is conceivable that the NiFe LDH anode suffered from severe degradation in these tests. In contrast, the possible degradation does not appear to severely affect the anode's kinetic performance.

For the *NiMo/PP vs Ni-PP* cell, Fig. 6.20 shows the results from the polarization curve, Fig. 6.21 the spectra and Fig. 6.22 the fitting of the electrochemical impedance spectroscopy. The summarized results from both are given in Tab. 6.3.

The nickel anode of this cell shows a similar trend as the nickel anode from the all nickel cell from the polarization curve. The differences that appear in the EIS measurements can be explained with the quality of the impedance, which result in fitting differences. Most important is the focus on the cathode of this cell. The cathode suffers from the accelerated degradation test by CV. The charge transfer resistance increased by 245 %, the overpotential at 1 mA/cm² increases by 11 mV, along with a 53 % decrease in the equivalent capacity. The performance loss after CV can thereby easily be explained by a loss of electrocatalyst. The significant decrease in the equivalent capacity is a clear indicator that roughly half of the electrocatalyst is lost after CV, which ultimately increases the charge transfer resistance and thereby the overpotential.

A similar effect occurred during OCV, but to an even higher degree. The equivalent capacity decreases by 92 % in comparison to the initial value. The charge transfer resistance increases by 323 % accordingly. These changes are easily visible in the impedance spectra as well. In the $-Z_{Im}$ over f plots, the cathode peak changes to higher frequencies with the accelerated degradation tests. Correspondingly, the charge transfer resistance clearly increases according to the impedance fittings. The performance of the degraded NiMo cathode, after OCV, reaches a value of $-0.152 + 0.031 / -0.045$ V at 10 mA/cm². The initial nickel values of the other cells, with $-0.220 + 0.003 / -0.050$ V and $-0.237 + 0.009 / -0.058$ V (*Ni-PP vs Ni-PP* and *Ni-PP vs NiFe LDH/PP* cells, respectively) are lower, which would lead to the assumption, that the NiMo electrocatalyst did not fully degrade. However, the equivalent capacity of the NiMo coated cathode is close to a nickel cathode after OCV. Furthermore, the nickel cathodes after OCV with $-0.134 + 0.034 / -0.044$ V and $-0.161 + 0.033 / -0.061$ V reach the same performance as the degraded NiMo coated cathode. It is obvious that the NiMo electrocatalyst has thereby fully degraded to the nickel substrate after OCV, and already degraded partially during the CV.

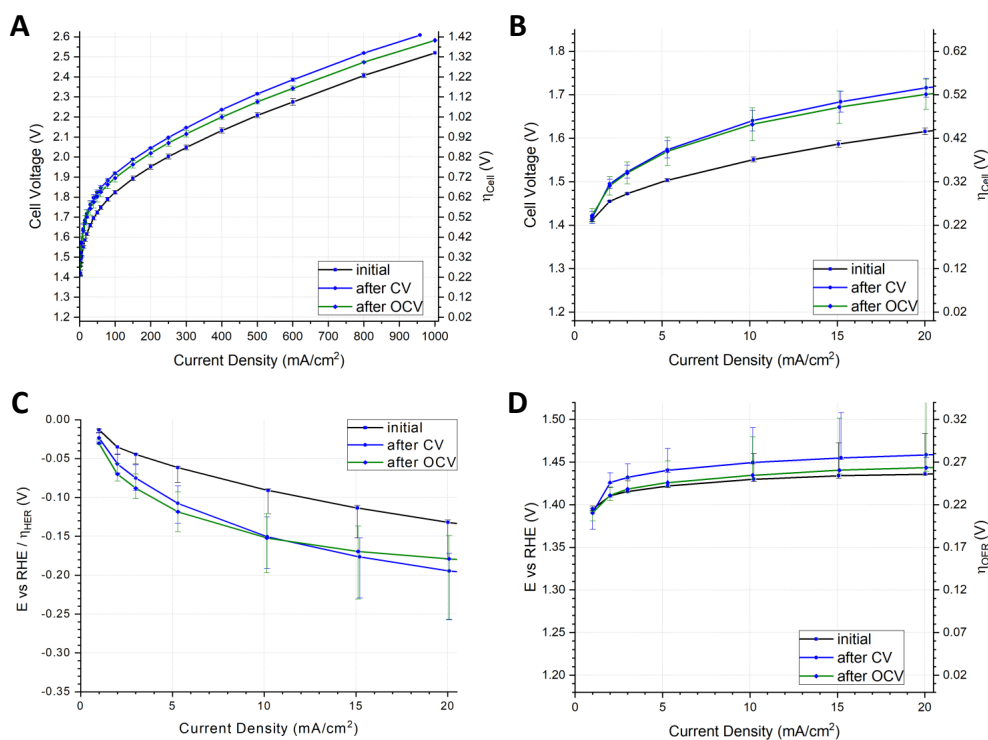


Fig. 6.20: Influence of cyclic voltammetry and open-circuit on the kinetics of the *NiMo/PP vs Ni-PP* cell at 80 °C in 30 w% KOH. **A:** Polarization curve of the cell. **B:** The kinetic segment of the cell polarization curve. **C:** Kinetics of the cathode. **D:** Kinetics of the anode.

Tab. 6.3: Kinetics of the *NiMo/PP vs Ni-PP* cell at 1 mA/cm², before and after accelerated degradation. Charge transfer resistances and equivalent capacitances as fitting results from EIS with an LR(RQ)(RQ) equivalent circuit.

Parameter	Unit	initial	after CV	after OCV
Cell Voltage	V	1.412 ± 0.003	1.418 ± 0.014	1.423 ± 0.016
Cathode potential vs RHE	V	-0.013 +0.001/ - 0.004	-0.024 +0.007/ - 0.005	-0.031 +0.005/ - 0.001
Cathode R_{ct}	Ωcm^2	8.2	28.3	34.7
Cathode C_{eq} (Roughness)	$\mu\text{F}/\text{cm}^2$ cm^2/cm^2	11077.63 (276.9)	5223.09 (130.6)	837.94 (20.9)
Anode potential vs RHE	V	1.395 +0.004/ - 0.002	1.391 +0.005/ - 0.020	1.391 +0.001/ - 0.010
Anode R_{ct}	Ωcm^2	51.7	52.3	60.6
Anode C_{eq} (Roughness)	$\mu\text{F}/\text{cm}^2$ cm^2/cm^2	723.29 (12.1)	751.52 (12.5)	295.74 (4.9)

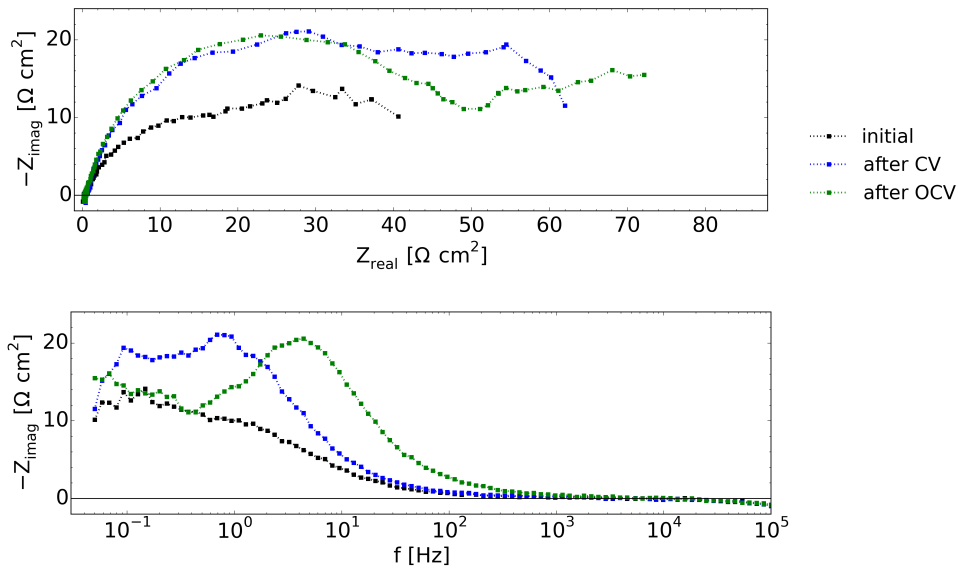


Fig. 6.21: Electrochemical impedance spectra of the *NiMo/PP vs Ni-PP* cell at 1 mA/cm^2 and 80°C in 30 w\% KOH , before and after accelerated degradation. Top: Nyquist plots. Bottom: $-Z_{Im}$ over f .

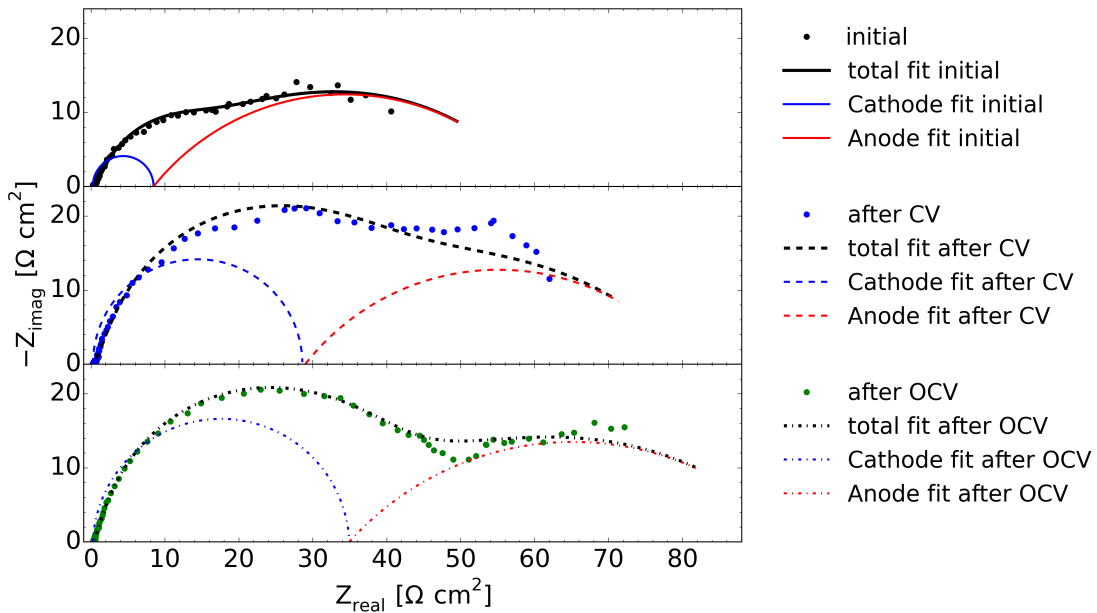


Fig. 6.22: Fitting results of the electrochemical impedance of the *NiMo/PP vs Ni-PP* cell at 1 mA/cm^2 and 80°C in 30 w\% KOH with an LR(RQ)(RQ) equivalent circuit. Top: Before accelerated degradation. Middle: After cyclic voltammetry. Bottom: After OCV.

6.3.4 Pre- and post-mortem characterization of electrodes from accelerated degradation testing

Scanning electron microscopy (SEM) was conducted before and after the accelerated degradation tests on the NiMo and NiFe LDH coated electrodes, illustrated in Fig. 6.23 and Fig. 6.24, respectively. The figures are segmented, with the left images being from the pristine electrode and the right images being from the degraded electrode. Images of the as well characterized nickel counter electrodes are spared. SEM was accompanied by electron dispersive spectroscopy (EDS), analyzed with the software Bruker Esprit 2.1. The EDS results are summarized in 6.4 and Tab. 6.5, respectively. The EDS results of the as tested electrodes include potassium, which results from residual electrolyte.

The as synthesized NiMo coated electrode (Fig. 6.23A,C) has a low coverage of electrocatalyst. EDS 1 and EDS 2 directly measured the electrocatalyst. The comparison between the two reveals the limitations of EDS, as both have a significant difference in molybdenum content between another, although the same electrocatalyst is measured. The difference clearly results from the different amounts of measured electrocatalyst. While the actual electrocatalyst, according to EDS 1, is closer to a molybdenum content of 30.6%, EDS 2 and the broad average of EDS 3 only measure 2.3% and 3.7%, respectively. This effect is important to consider when comparing possibly degraded electrodes, as the interaction volume of SEM has a crucial impact.

The degraded electrode (Fig. 6.23B,D) shown here is the result of investigating the electrode's surface for an extended time of about 5 min. The low initial electrocatalyst coverage of the as synthesized electrode requires that a greater area of the sample is investigated, before any form of electrocatalyst loss can be concluded. In this case, EDS 5 did find a small amount of molybdenum containing electrocatalyst. On the other hand, as seen by the broad average of EDS 4, a large part of the electrode's surface is almost molybdenum free, compared to the initial state. While trace amounts of molybdenum are found on the nickel counter electrode, SEM/EDS indicate that the electrocatalyst mostly vanished into the electrolyte.

However, some electrocatalyst remained, but experienced structural changes. Small, spherical parts, together with needle-like parts, are left. Comparing EDS 2 and EDS 5, both of which representing a low coverage of electrocatalyst, have a similar nickel to molybdenum

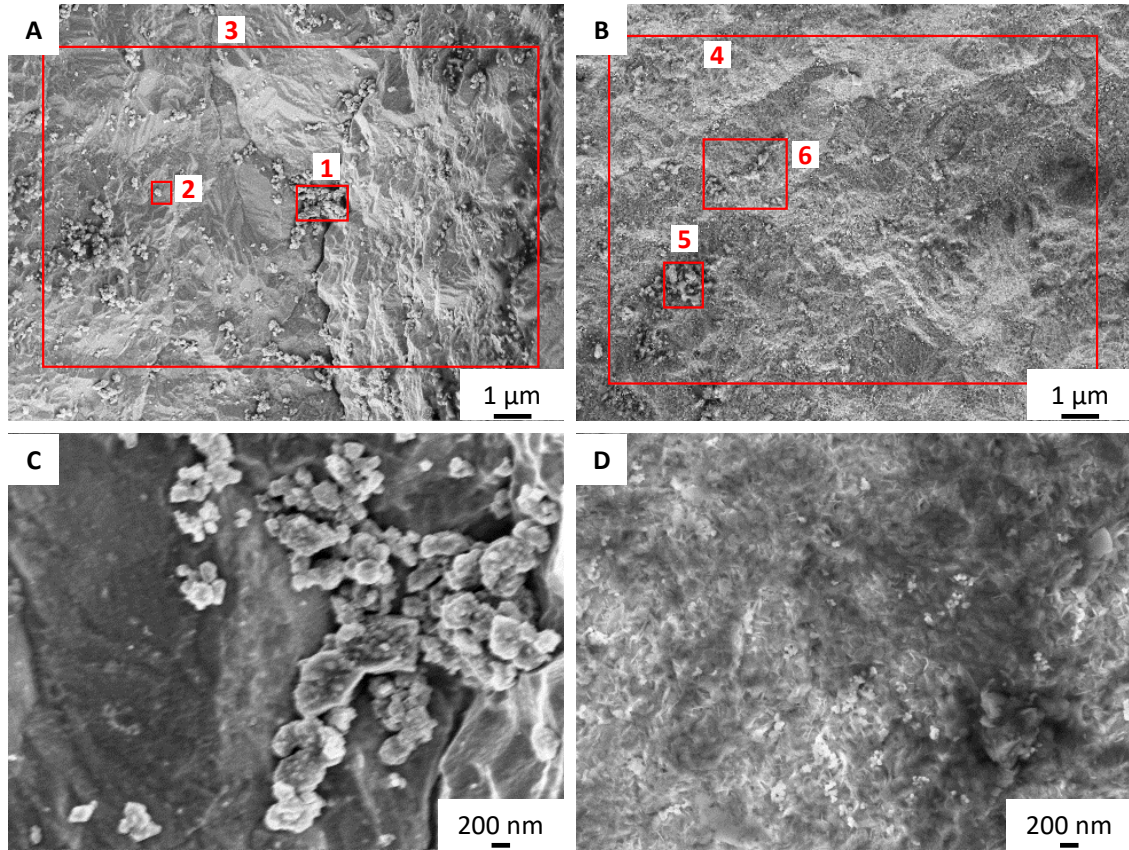


Fig. 6.23: SEM images of the cathode of the *NiMo/PP vs Ni-PP* cell. **A, C:** Pristine cathode. **B, D:** Tested cathode. In red marked boxes represent the EDS measurement areas, whose results are summarized in Tab. 6.4.

Tab. 6.4: EDS results from the pristine and aged cathode of the *NiMo/PP vs Ni-PP* cell shown in Fig. 6.23, as well as the tested anode. Elemental compositions are given as atomic-%.

Sample	Box	Ni	Mo	O	K	Mo/NiMo
as synth.	1	39.2 ± 5.9	17.3 ± 1.8	43.4 ± 2.1	–	30.6
	2	90.7 ± 11.0	2.2 ± 0.3	7.2 ± 0.4	–	2.3
	3	84.3 ± 10.7	3.2 ± 0.4	12.5 ± 0.7	–	3.7
cathode	4	60.5 ± 11.8	0.3 ± 0.1	39.2 ± 2.5	0.0 ± 0.0	0.5
	5	29.1 ± 7.6	0.6 ± 0.2	69.9 ± 5.1	0.4 ± 0.1	2.1
	6	57.4 ± 11.8	0.3 ± 0.1	42.0 ± 2.8	0.3 ± 0.1	0.5
anode	7	66.6 ± 13.9	0.2 ± 0.1	31.3 ± 2.2	1.9 ± 0.3	0.3
	8	63.6 ± 11.1	0.4 ± 0.1	34.4 ± 2.0	1.6 ± 0.2	0.6

ratio. On the contrary, the EDS of the degraded electrode shows an almost ten times increase of oxygen. The electrocatalyst, which is left, hence experienced significant oxidation during accelerated degradation. Both, electrocatalyst loss and oxidation, explain the decreasing kinetics of the NiMo cathode.

A similar picture from the as synthesized to the degraded electrode can be seen in the NiFe LDH anode, although the as synthesized NiFe LDH electrode reveals a high coverage of a platelet-like LDH electrocatalyst.

To get an average iron-content of the electrocatalyst-coating, EDS 1 measured a broad area to an iron-content of 19.2 % in NiFe, after neglecting other elements, in the as synthesized sample (Fig. 6.24A,C). The targeted iron-content of this synthesis was 20 %. Since the substrate of this sample, which is made from nickel, influences the EDS, an admitting too low iron content will be gathered. Despite the shortcoming of this approach, EDS is an important point of reference for the comparison of electrodes. EDS 2 and EDS 3 were chosen to distinguish between the two distinct, visible phases. While the platelet-like phase, as in EDS 3, is the targeted structure, slightly more iron and oxygen-rich sphericals are seen on top of the platelet-structure. Since these sphericals appear on top of the platelets, it is not possible, with EDS, to distinguish the composition between these two parts. The upper layer will be influenced by the lower layer in EDS, while the lower layer will be more influenced by the nickel support. It is more likely that both have a similar composition, with the upper part having less influence of the nickel substrate.

In comparison to the as synthesized NiFe LDH, the degraded electrode (Fig. 6.24B,D) appears to have lost a great fraction of the coating. Furthermore, the coating left appears to have fully phase-changed. This is supported by the EDS measurements, which do not show that any iron left. These findings have to be taken cautiously, as EDS is not a surface sensitive technique. A possible presence of surface or near-surface iron cannot be determined.

However, it is apparent that the bulk of the electrocatalyst has degraded. This is in line with Andronescu et al. [130], who found that NiFe LDH phase-changes to β -Ni(OH)₂ after 60 h without polarization in 30 w% KOH at 80 °C. This leads to the conclusion that the observed electrochemical degradation of the NiFe LDH results from a decimated electrocatalyst.

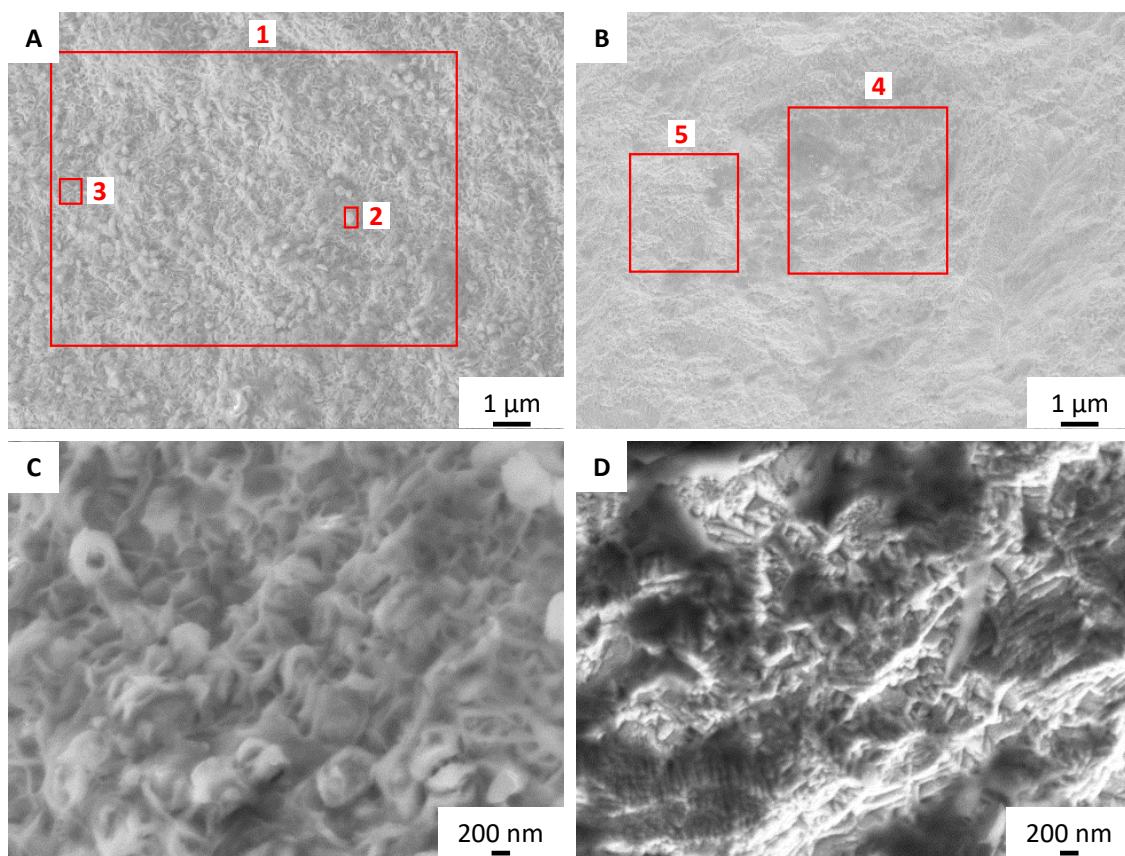


Fig. 6.24: SEM images of the anode of the *Ni-PP vs NiFe LDH/PP* cell. **A, C:** Pristine anode. **B, D:** Tested anode. In red marked boxes represent the EDS measurement areas, whose results are summarized in Tab. 6.5.

Tab. 6.5: EDS results from the pristine and aged anode of the *Ni-PP vs NiFe LDH/PP* cell shown in Fig. 6.24, as well as the tested cathode. Elemental compositions are given as atomic-%.

Sample	Box	Ni	Fe	O	K	Fe/NiFe
as synth.	1	24.3 ± 7.3	5.8 ± 2.2	69.9 ± 5.7	–	19.2
	2	18.0 ± 5.9	7.3 ± 2.8	74.6 ± 6.4	–	28.9
	3	29.9 ± 7.9	5.6 ± 1.9	64.5 ± 4.8	–	15.9
anode	4	62.1 ± 14.8	0.0 ± 0.0	31.4 ± 2.6	6.5 ± 0.9	0.0
	5	72.7 ± 13.7	0.0 ± 0.0	23.4 ± 1.6	3.9 ± 0.5	0.0
cathode	6	35.9 ± 6.3	0.1 ± 0.1	53.5 ± 2.8	10.5 ± 0.9	0.4
	7	27.3 ± 5.5	0.0 ± 0.0	54.1 ± 3.1	18.6 ± 1.6	0.0

6.3.5 Results from accelerated degradation testing

Cyclic voltammetry and open-circuit were applied to study the degradation processes in a NiMo and a NiFe LDH electrocatalyst in comparison to nickel.

By the results from CV, the NiMo electrocatalyst displayed degradation. Following the redox behavior of this cell compared to an all nickel cell, the degradation most likely, but not fully conclusively, occurred in the HER underpotential region. At underpotential conditions of up to 0.3 V vs RHE, following Fig. 6.12, the NiMo cathode irrecoverably degrades. Although it is possible that this degradation process starts already before this potential, the CVs do not allow to conclude at which potential this is exactly the case. The temporal evolution of the cathode electrode potential during OCV might lead to the assumption that this process does not start before 0.1 – 0.2 V vs RHE, albeit this does not grant any certainty.

However, this HER underpotential exposure, which appears to cause the electrocatalyst to degrade and reverse the reaction to the hydrogen oxidation reaction, is certainly negative towards the catalyst's stability. With further exposure to the OCV, causing hydrogen oxidation and eventually a potential of 0.95 V vs RHE, the electrocatalyst practically fully destructs. This is backed by the kinetic results and SEM/EDS. The NiMo cathode after OCV kinetically behaves like the bare nickel support after exposure to OCV. It might be considered that these destructive processes are a result of multiple mechanisms. However, it cannot be distinguished if the underpotential region is split into several degradation mechanisms, or if the seen degradation is a result of the exposure time at above a certain underpotential threshold potential. In any case, underpotential and hydrogen oxidation conditions at potentials higher than 0.3 V vs RHE end in a kinetically unrecoverable degradation.

The NiFe LDH electrocatalyst experiences, following the results from CV, an *in situ* modification within the first cycle. Following the EIS supported kinetic results, the electrocatalyst experiences degradation during CV. Since the electrode does not experience potentials below 1.3 V vs RHE, it is most reasonable to assume that the degradation occurs at high overpotentials. This assumption is supported by the change of the slope in the CV at higher cell voltages, which indicates the formation of higher oxidation states, such as Ni⁴⁺ in γ -NiOOH. The threshold for this higher oxidation state can, on the other hand, not be determined. Due to the high cell voltage, a reliable single electrode potential cannot be mea-

sured in this setup. At OCV, the NiFe LDH electrocatalyst experiences oxygen reduction and OER underpotential conditions down to 0.6 V vs RHE. As the electrode experiences 0.95 V vs RHE in the following, a kinetic recovery from the high oxidation state takes place. However, as seen by SEM/EDS, the NiFe LDH electrocatalyst oxidizes to a mainly nickel based oxide, hydroxide, or oxyhydroxide. The bulk of the tested electrocatalyst is, in contrast to the pristine electrocatalyst, free of iron according to EDS. While it remains elusive, due to the measurements depth of EDS, if iron is still present in the surface, it is apparent that the electrocatalyst undergoes severe structural changes. Nonetheless, these structural changes do not appear to critically affect the kinetic performance of the electrocatalyst.

A graphical summary of the aforementioned findings, with respect to the potential vs RHE on the kinetic performance of the NiMo and the NiFe LDH electrocatalysts, is illustrated in Fig. 6.25.

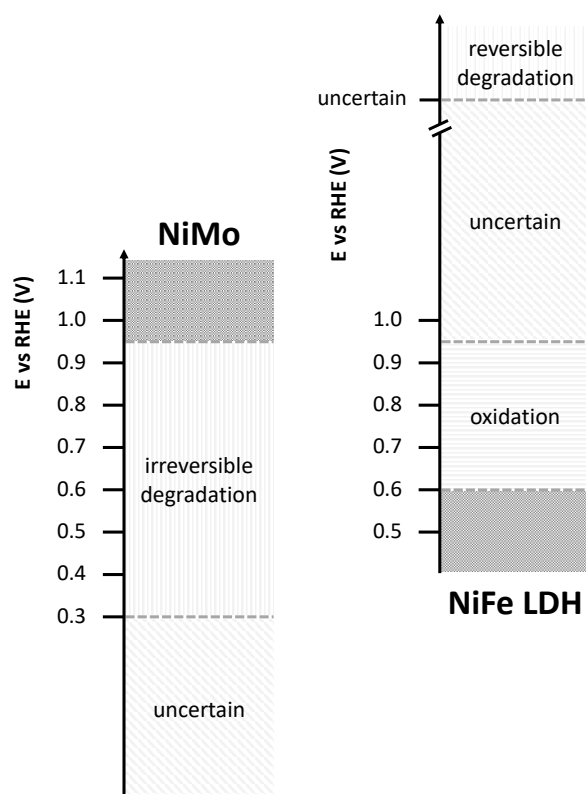


Fig. 6.25: Results from accelerated degradation testing about the operational domains of a NiMo HER electrocatalyst (left) and a NiFe LDH OER electrocatalyst (right), with respect to the influence of the electrode potential vs RHE on the kinetic performance. Results at 80 °C in 30 w% KOH.

6.4 Dynamic long-term operation simulating the industrial application under fluctuating energy supply

A second attempt to address the long-term reliability of the NiMo and the NiFe LDH electrocatalysts was conducted by a 15 days long test under dynamically changing loads. The dynamic changes are supposed to resemble the industrial operation following the intermittent energy supply of renewable energies. As seen previously, underpotential and OCV conditions cause the electrocatalysts to degrade. Therefore, the long-term test was conducted under varying but uninterrupted polarization. The current density was varied between $1 - 1000 \text{ mA/cm}^2$. After ≈ 1 day and before the test-end, a shutdown under a protective cell polarization of 1.2 V resembles the shutdown of an industrial electrolyzer, as e.g. during shortages in the energy-supply. Due to the polarization just above the equilibrium cell voltage, the single electrodes are not expected to experience decimating underpotential conditions.

As the testing over a longer period of time consumes a non-negligible amount of water, the cell was replenished with Milli-Q water at different stages during the 15 days long test. The amount of added water was calculated according to Faraday's law (Eq. (2.12)).

An initial EIS measurement at 1 mA/cm^2 and a polarization curve were conducted first. In the following, the time at the start of the polarization curve is marked as "0 h", which relates to a fictive start of the long-term test right after the EIS measurement. The heating up process of about 1 h, which occurred at 100 mA/cm^2 , is exempted.

Within the first 4 h of the long-term test, a conditioning step at 100 mA/cm^2 was followed by a 500 mA/cm^2 step. The data recording between ≈ 6 h and 18 h failed due to a software issue, while the cell remained at 500 mA/cm^2 . In the following and during the first 5 days of the test, the cell conditions were varied the most.

After 5 days, the cell was held at 100 mA/cm^2 for about 2.5 days. This procedure repeated in the period between 12 days and 14.75 days. Both are the result of the need for a proper water management, which is conducted manually, but not over the course of a weekend. Hence, a lower current density and accordingly lower water consumption was chosen. The total amount of electrolyte in this test summed up to 400 mL, equally divided between anode and cathode. To ensure a proper water management, the replenishing was

conducted at the very latest when 40 mL of water ($\sim 10\%$ of the electrolyte) had to be added. However, especially after higher loads, water was added twice on a day.

In between these two low demand periods, the cell was held at 500 and 1000 mA/cm² for an extended amount of time. The 1000 mA/cm² measurement was limited to just about one working day to ensure the proper water management. At different stages during the long-term test, a total of 12 polarization curves, including the initial test, were conducted to assess the stability of the electrocatalysts. At the end of the test, another EIS measurement was conducted for comparison to the initial one.

6.4.1 Dynamic operation over 357 h on felt supported electrodes

The aforementioned dynamic operation of the long-term test is analyzed with a time resolved observation of the cell voltage. Including a visualization of the changes in the current density, Fig. 6.26 represents the whole long-term test. The blue annotations indicate when the cell was replenished with water. Sharp vertical lines, which are especially visible in the current density part of the figure, indicate when a polarization curve was conducted. The relatively short time-frame of 43 min, in comparison to the 15 days of the test, appear as a vertical line, although the current density during a polarization curve is varied from 1 – 1000 – 1 mA/cm².

Albeit the dynamic changes between low and high current densities, including a simulated shutdown under protective polarization, the first 5 days did not show any apparent degradation. Fig. 6.27 repeats the previous figure, but with the focus on the more static parts. Including the first 8 h of the test, which can be considered as the conditioning step, the static parts after the densely changing first 5 days are shown. For a better understanding of the evolution of the cell voltage, the two 100 mA/cm² steps from 118 – 186 h and from 287 – 354 h each only show the start and the end of the respective step.

In total, the cell was held at 1.2 V in two steps for 3.5 h, at 1 mA/cm² in a single step for 3 h, at 100 mA/cm² in nine steps for 149.5 h, at 500 mA/cm² in nine steps for 178.7 h, and at 1000 mA/cm² in four steps for 13.6 h. This sums up to an overall load of 117.90 Ah/cm² for the galvanostatic steps. Including the 12 polarization curves with overall 1.65 Ah/cm², the cell experienced a total load of 119.55 Ah/cm². In comparison to a commercial electrolyzer, with an estimated operation of 8000 h/a at averaged 400 mA/cm², this test reflects about 3.7% of the annual industrial operation.

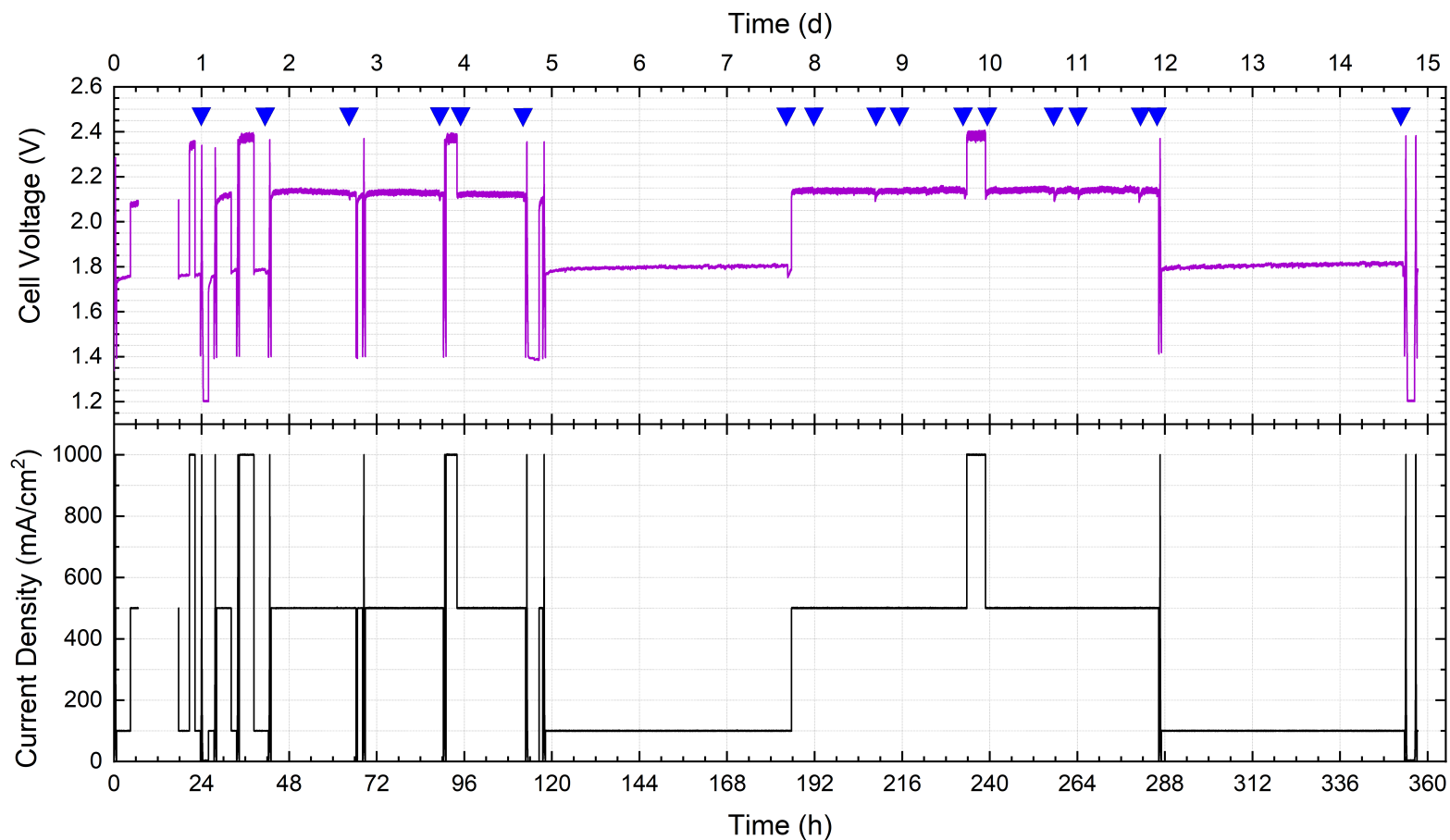


Fig. 6.26: Dynamic operation of the *NiMo/felt vs NiFe LDH/felt* cell at 80 °C in 30 w% KOH. The current density (lower part of the figure) is varied between 1–1000 mA/cm². The cell voltage (upper part of the figure) is monitored accordingly. The blue annotations mark the addition of water. Vertical lines in the current density part are polarization curves (see results in Fig. 6.28 and 6.31); the comparably short time-frame of 43 min appears as a vertical line, albeit the current density is varied.

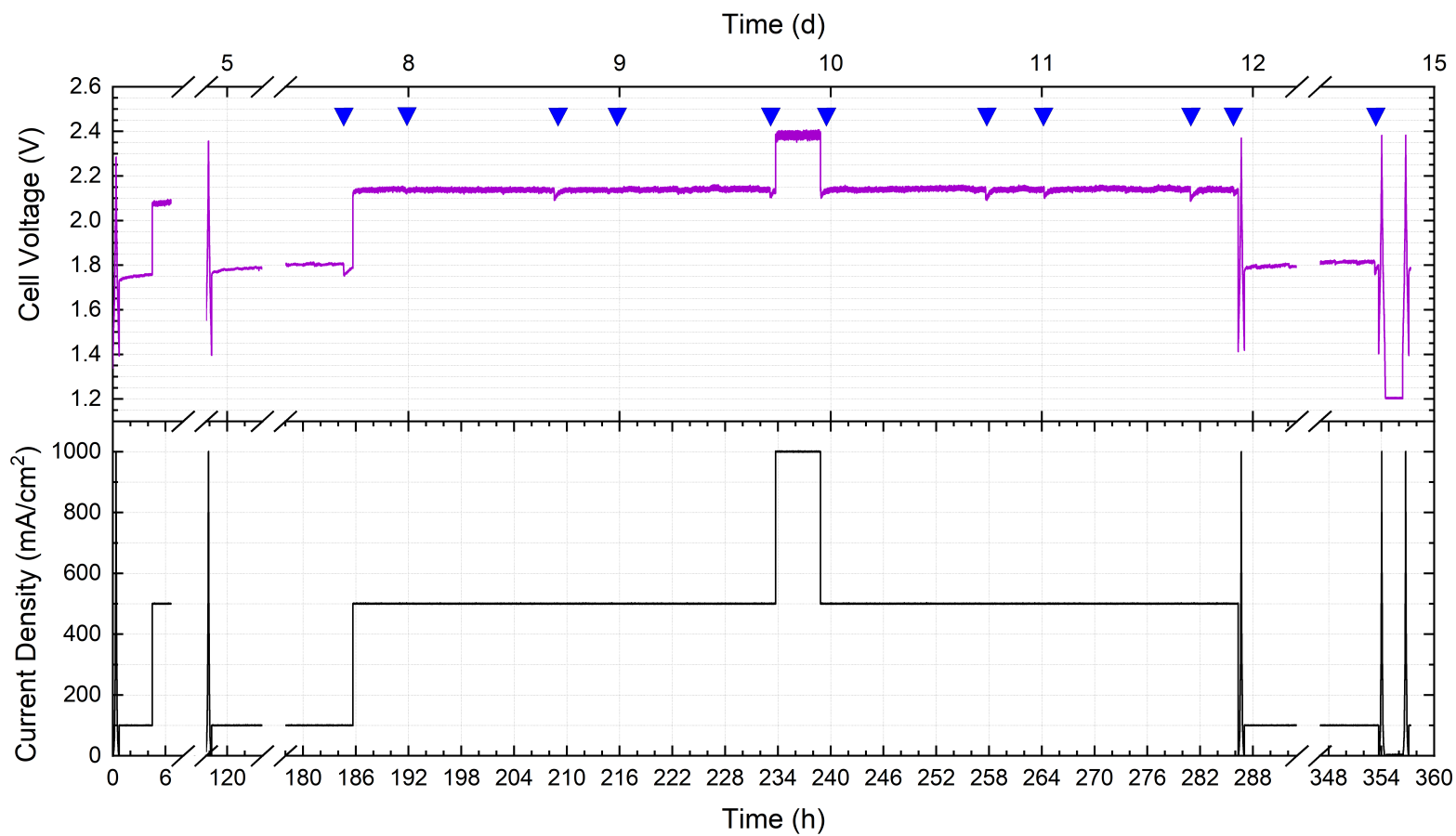


Fig. 6.27: Repetition of Fig. 6.26, with cut-outs between 8 h – 118 h, 124 h – 178 h and 293 h – 347 h. The blue annotations mark the addition of water. Vertical lines in the current density part are polarization curves (see results in Fig. 6.28 and 6.31); the comparably short time-frame of 43 min appears as a vertical line, albeit the current density is varied.

Within the first 4 h of the test, the cell voltage increases linearly at 100 mA/cm^2 from $\approx 1.73 \text{ V}$ to $\approx 1.76 \text{ V}$. After a period of 13.5 h at 500 mA/cm^2 , in which the data recording mainly failed, another 3 h long period at 100 mA/cm^2 shows a stable cell voltage at $\approx 1.76 \text{ V}$. Therefore, the first 4 – 18 h can be seen as a conditioning step. As a result of the data recording failure, it is elusive whether the conditioning step finishes at 100 mA/cm^2 after 4 h, or if the consecutive 500 mA/cm^2 step has a further influence. Nevertheless, it is apparent that an initial alteration of at least one of the electrocatalysts must occur. On the other hand, such an initial conditioning step does not have an overall negative impact on the cell, as the loss of the performance remains low and does not proceed. This is further visible in the cell voltage after a high-stress phase at 1000 mA/cm^2 between 20.5 h and 22 h of operation. The cell voltage at 100 mA/cm^2 prevails at $\approx 1.76 \text{ V}$ despite the preceding high current density step.

With further dynamic operation, including a protected shutdown after 24 h of operation, the cell does not display any apparent degradation. In fact, between 44 h and 66 h of operation, at which the cell was static at 500 mA/cm^2 , the cell voltage drops from $\approx 2.14 \text{ V}$ to $\approx 2.12 \text{ V}$. As this can be seen as a further confirmation that, besides the initial conditioning step, no apparent degradation occurs during the first days of dynamic operation, the spotlight is set on a comparison after ≈ 5 days of operation to the initial and conditioned values after about 1 day of operation.

After 118.5 h of operation, the cell voltage at 100 mA/cm^2 with $\approx 1.77 \text{ V}$ is just marginally higher than the conditioned cell voltage of $\approx 1.76 \text{ V}$ after about 1 day of operation. Although this might be correlated to a constant degradation process, the view on the whole 100 mA/cm^2 step between 118 h and 185.5 h of operation leads to another hypothesis for the slightly increasing cell voltage. Over the course of 66.5 h at this current density, the cell voltage linearly increases from $\approx 1.77 \text{ V}$ to $\approx 1.80 \text{ V}$. However, after adding water at 184.5 h of operation, the cell voltage drops immediately to $\approx 1.76 \text{ V}$, before it stabilizes at around $\approx 1.78 \text{ V}$. A similar behavior can be seen at every other following water replenishing step. The cell voltage drops immediately with the addition of water, and recovers to a slightly lower value than before the addition.

This effect might be due to the temperature difference of about $60 \text{ }^\circ\text{C}$ between electrolyte and added water. However, it is plausible that the effect is a cause of the electrolyte

concentration within the cell. During electrolysis without continuous water management, the concentration in the cell increases and hence, exceeds the maximum conductivity concentration. The increasing electrolyte concentration is further promoted on the cathode side through the electrolysis induced pH-gradient. After addition of water, the locally lowering concentration increases the conductivity of the electrolyte primarily in the cathode, as water is added to the cathode electrolyte circuit. After a short period of time, the concentration equilibrates between cathode and anode, but follows the electrolysis induced pH-gradient. Overall, the addition of water decreases the electrolyte concentration to the initial value of 30 w% KOH, but the pH-gradient causes local differences. As a result, the immediate decrease of the cell voltage is followed by an increase, but to lower values than before the addition of water.

Subsequently, increasing cell voltages cannot be associated to a degradation process with certainty, but may be a result of concentration effects within the cell. The drop in cell voltage of ≈ 0.04 V at 184.5 h of operation guides to the assumption that a deviation of the cell voltage below this threshold is likely due to concentration effects, and not due to degradation. Although this explanation may fit the conditioning period at the beginning of the test as well, concentration induced effects are more likely to occur over time. Thus, the initial increase of the cell voltage by ≈ 0.03 V within the first 4 h of operation is still considered to be a conditioning step.

After 186 h of operation, the cell is operated at 500 mA/cm^2 until 286 h of operation, including a 1000 mA/cm^2 step between 233.5 h and 239.5 h of operation. During this 100 h long high-stress period, the cell voltage at 500 mA/cm^2 does not degrade and remains stable at ≈ 2.13 – 2.14 V. In comparison to the cell voltage of ≈ 2.12 V after 32 h of operation, which is the first steady operation at 500 mA/cm^2 after the conditioning step, the cell degrades by less than 0.02 V, which can be ascribed to concentration effects. Compared to the initial value of 2.09 V at 6 h of operation, it can be concluded that the first 500 mA/cm^2 step contributed to the cell conditioning. Despite these variations, a degradation of the cell performance cannot be observed. This is further supported by the 100 mA/cm^2 step in the following, between 288 – 353.5 h of operation. The starting cell voltage of this step with ≈ 1.79 V is identical to the ending value, after water was added. The cell hence is mostly influenced by concentration effects, but not by apparent degradation processes.

In order to validate the assumption that the cell is mainly influenced by concentration effects, a 2 h long protected shutdown was conducted after 354.5 h of operation. As water was added just prior to this step, and further a pH-gradient will dismantle due to the lack of a current, the protected shutdown is expected to exclude concentration effects in the following. Therefore, subsequent measurements should, free of concentration effects, reveal possible impacts by degradation processes. The cell voltage of ≈ 1.78 V at 100 mA/cm^2 following the protected shutdown hence underlines that previously observed performance decreases are indeed due to concentration effects. Furthermore, in comparison to the conditioned cell voltage of 1.76 V, a maximum degradation of 0.02 V at 100 mA/cm^2 within 339 h of dynamic operation can be deducted. The first 18 h, in which conditioning takes place, are deducted in this reflection. This degradation equals $59.0 \mu\text{V/h}$ at 100 mA/cm^2 for this specific dynamic operation.

Nonetheless, the observed degradation during this test is a result of the quickly changing conditions. It is possible that a more statically operated cell shows a similar decay over a much longer operation period than the assessed 15 days. Furthermore, an extrapolation from this test to a decade-long operation cannot be conducted from these results. The observed degradation may, due to measurement and experimental accuracy, especially in the electrolyte handling, deviate over longer times from the deducted $59 \mu\text{V/h}$ at 100 mA/cm^2 . Since these 15 days reflect about 4 % of a year, and hence only 4 ‰ of a decade (or 3.7 %/ 3.7 ‰ considering operational loads, see above), only inaccurate assumptions may be drawn over the course of a technological operation. In fact, the observed 0.02 V at 100 mA/cm^2 decay may decrease or remain at this level with further operation.

In any case, the studied electrocatalysts show remarkable stability over the course of 15 days after an initial conditioning step. This promising result, consequently, makes further investigations necessary. At the same time, their stability makes these non-precious metal electrocatalysts conceivable candidates for the technical operation. Although especially the recent literature does not address stability remarks under technological relevant conditions sufficiently, the results of this work do not raise any serious doubts about their applicability in technological electrolyzers at this stage.

6.4.2 Results from polarization curves and electrochemical impedance spectroscopy of the 357 h test

To further understand possible degradation processes, 12 polarization curves were conducted at different stages during the long-term test. In many cases, the cell was replenished with water prior to the polarization curve. If water was added prior to a polarization curve, at least 30 min were passed before the polarization curve was obtained. The measure to start a polarization curve, which was a stable cell voltage for a minimum of 5 min, should ensure that the electrolyte is equilibrated prior to the measurement.

However, it is challenging to plot all 12 polarization curves together, and still be able to deduct deviations. As a result, Fig. 6.28 reflects the 5 most important polarization curves. Besides the initial polarization curve, the after conditioning curve at 23 h 41 min will be a second point of reference. The following three polarization curves are after the highly dynamic operation (117 h 30 min), after the more static operation (353 h 40 min), and at the end (356 h 24 min). Each time stamp remarks the start of the polarization curve, of which each is measured over the course of 43 min.

For better comparison, Tab. 6.6 represents the measured values of the initial test, the lowest kinetic performance after 353 h 40 min, which was shown to be influenced by concentration effects, and at the end. In addition, Fig. 6.29 and 6.30 illustrate the electrochemical impedance spectroscopy at 1 mA/cm^2 and their fitting at the start and at the end of the 15 days long test, respectively.

The results from the polarization curves, with respect to the cell voltage, follow the same trend as seen in the previous section. With focus on the kinetic segment, an initial performance decays by $\approx 0.02 \text{ V}$ at 10 mA/cm^2 to the conditioned performance after 23 h 41 min. Thereafter, a stagnation of the cell performance is visible, but ending with a visible decay after 353 h 40 min. However, as discussed previously, this further decay is associated with concentration effects. A further proof is the performance at the end. Following the protected shutdown, which dismantled the concentration effects, the cell performance after 356 h 24 min at 10 mA/cm^2 is identical to the conditioned value.

Besides the evolution of the cell performance, a view on the single electrodes allows to associate the overall cell response to the single electrodes and, furthermore, to the single electrocatalysts.

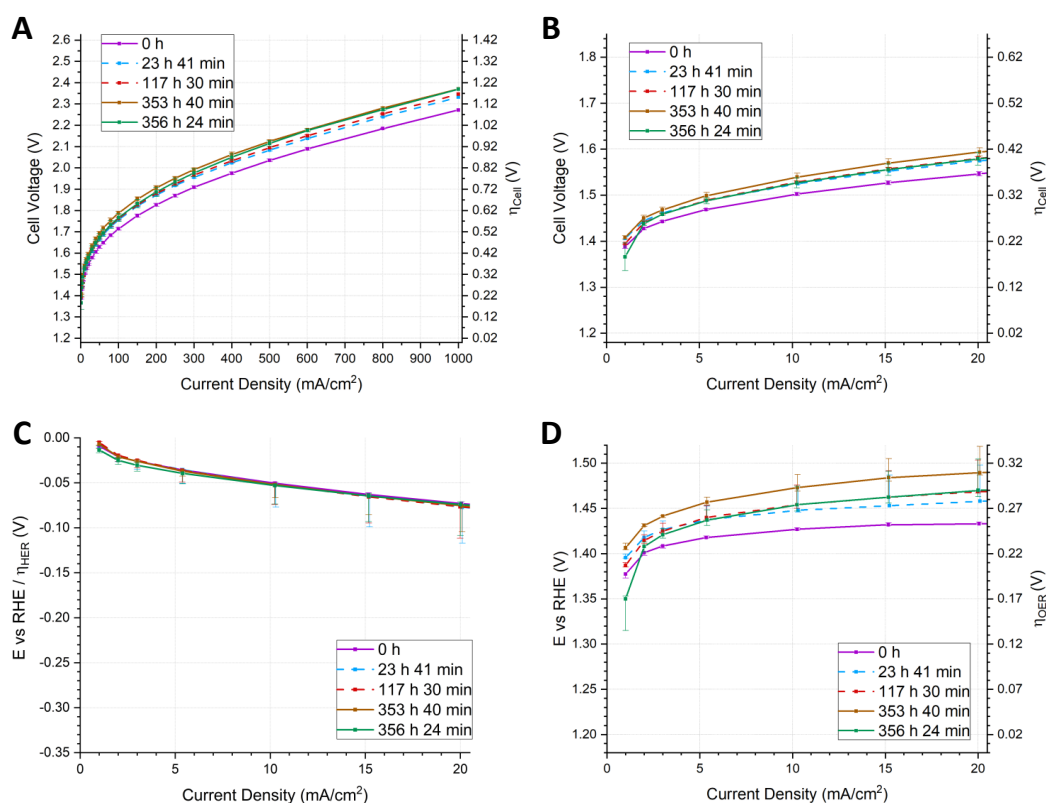


Fig. 6.28: Polarization curve results from the long-term test on the *NiMo/felt vs NiFe LDH/felt* cell at 80 °C in 30 w% KOH, in accordance with Fig. 6.26 and 6.31. **A:** Polarization curves from 1–1000 mA/cm². **B:** Focus on the kinetic segment up to 20 mA/cm². **C:** Cathode electrode potential in the kinetic segment. **D:** Anode electrode potential in the kinetic segment.

Tab. 6.6: Kinetics of the *NiMo/felt vs NiFe LDH/felt* cell at 1 mA/cm² (top) and 10 mA/cm² (bottom) at 80 °C in 30 w% KOH. Results from 0 h (beginning), 353 h 40 min (lowest kinetic performance), and 356 h 24 min (ending).

	Parameter	Unit	0 h	353 h 40 min	356 h 24 min
1 mA/cm ²	Cell Voltage	V	1.389 ± 0.005	1.409 ± 0.004	1.366 ± 0.030
	Cathode potential vs RHE	V	-0.009	-0.007	-0.014
	Anode potential vs RHE	V	+0.000/ - 0.000	+0.000/ - 0.005	+0.005/ - 0.003
10 mA/cm ²	Cell Voltage	V	1.503 ± 0.004	1.540 ± 0.009	1.527 ± 0.011
	Cathode potential vs RHE	V	-0.051	-0.052	-0.053
	Anode potential vs RHE	V	1.427	1.473	1.454
			+0.002/ - 0.001	+0.015/ - 0.004	+0.021/ - 0.007

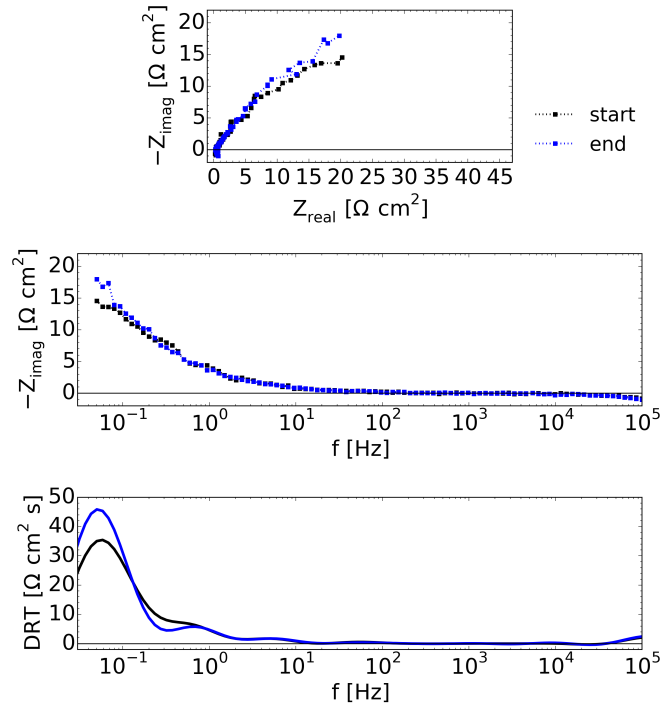


Fig. 6.29: Electrochemical impedance spectroscopy at the start and at the end of the long-term test on the *NiMo/felt vs NiFe LDH/felt* cell at 80°C in 30 w% KOH. Top: Nyquist plots. Middle: $-Z_{Im}$ over f . Bottom: DRT plots. Due to the quality of the spectra, it is questionable if two main processes indeed occur at ≈ 800 and ≈ 50 mHz, as indicated by DRT.

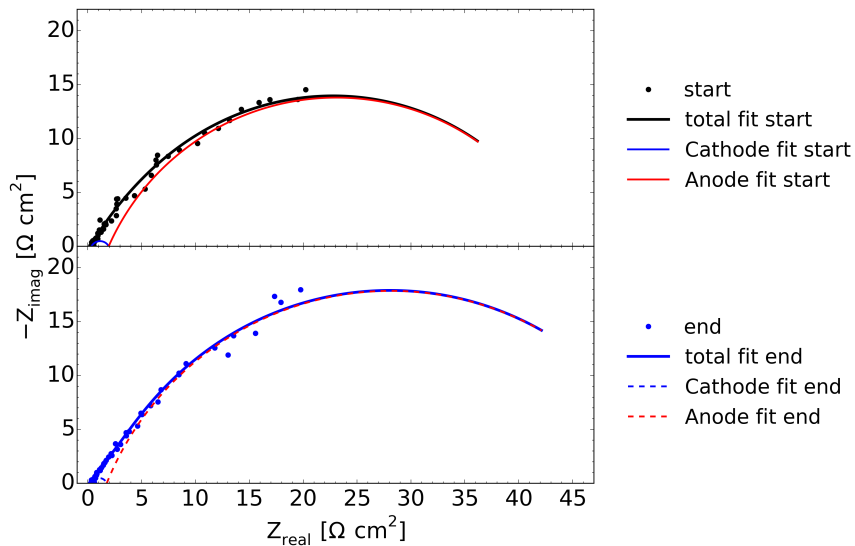


Fig. 6.30: Fitting of the electrochemical impedance spectroscopy at the beginning (top) and at the end (bottom) of the long-term test on the *NiMo/felt vs NiFe LDH/felt* cell at 80°C in 30 w% KOH. LR(RQ)(RQ) equivalent circuit.

While the cathode performs remarkably similar, when considering the associated errors, within the kinetic segment, the anode displays a trend that strongly follows the behavior of the cell voltage. After an initial conditioning step, the anode remains at ≈ 1.45 V vs RHE at 10 mA/cm^2 , with the lowest performance at ≈ 1.47 V vs RHE after 353 h 40 min. Alike the cell voltage, the anode performance regains the performance after conditioning when a protective shutdown is performed. In comparison of both single electrodes, the probable conclusion is that the anode is the main responsible part for both, conditioning and concentration influences on the cell voltage.

A further insight should have been gathered by EIS. However, as already seen in the EIS measurement, the peak of the imaginary impedance is not measured at low frequencies. Although DRT was conducted to conclude at which peak frequencies the cathode and anode processes occur, the EIS measurement does not contain enough information for this conclusion. This is mainly seen in the fact that the lowest frequency peak in DRT is directly at the measurement end of the impedance. Hence, the shown fitting is, as a result of insufficient data, not representative of the whole cell. This is further seen in the fitting results as presented in Tab. 6.7. The surface roughness factors close to one for both electrodes are, considering the high surface areas of the substrates alone already, unrealistic.

Tab. 6.7: Kinetics of the *NiMo/felt vs NiFe LDH/felt* cell at 1 mA/cm^2 and 80°C in 30 w% KOH. Results from electrochemical impedance spectroscopy at the start and at the end of the test. Charge transfer resistances and equivalent capacities (surface roughness factor 40 and $60 \mu\text{F/cm}^2$ for cathode and anode, respectively), calculated as non-blocking electrodes, as fitting results with an LR(RQ)(RQ) equivalent circuit. Note that the fitting is considered erroneous.

Parameter	Unit	start	end
Cathode R_{ct}	Ωcm^2	1.597	1.387
Cathode C_{eq} (Roughness)	$\mu\text{F/cm}^2$ cm^2/cm^2	124.59 (3.1)	52.97 (1.3)
Anode R_{ct}	Ωcm^2	42.24	52.78
Anode C_{eq} (Roughness)	$\mu\text{F/cm}^2$ cm^2/cm^2	91.73 (1.5)	102.12 (1.7)

However, although EIS does not allow to obtain quantitative results in this measurement, it contains crucial qualitative information. Following the $-Z_{Im}$ over f plot, the cell behaves remarkably identical at the start and at the end of the test until about 90 mHz. The behavior at lower frequencies can be associated to either noise, or to a slight performance decrease. This finding is complementary to the polarization curve results. While the cathode, which would be represented at higher frequencies, remains stable over the course of the test, degradation can mainly be ascribed to the anode, which would be represented at lower frequencies than the cathode.

To further prove the assumption that mainly the anode is affected during the long-term test, Fig. 6.31 shows the results from all 12 polarization curves. The results from the polarization curves at 1 and 10 mA/cm² are shown (top and bottom of the figure, respectively) with respect to the measurement time. Similar to Fig. 6.26, the figure also indicates when water was added.

The cell voltage and the anode electrode potential develop in parallel, while the cathode electrode potential appears to remain stable. At both current densities, the anode electrode potential and the cell voltage increase by about ≈ 0.02 V from the initial to the conditioned value. Thereafter, the anode electrode potential varies by several millivolts over the course of the test, while the cathode electrode potential only displays insignificant variations. Accordingly, the previously seen concentration effect on the cell performance results mainly from the anode. Since the OER proceeds via hydroxide-anions, the concentration effect affects the OER performance directly. At the end of the test, after the protective shutdown, the anode electrode potential at 10 mA/cm² reaches the value of the conditioned state.

Particular attention should be set on the fact that the anode potential increases by almost 0.03 V at the end compared to the initial performance at 1 mA/cm². Even though this may be associated with a measurement error, it is conceivable that the anode underwent a surface modification. As a result of the modification, the onset potential may have decreased, while the associated current-overpotential correlation increased, ultimately ending with a similar performance at 10 mA/cm². Correspondingly, the assumption, which associates a slight increase in the first day of operation to a conditioning step, can be linked to a modification of the anode. The cathode, on the other hand, appears to be mainly unaffected.

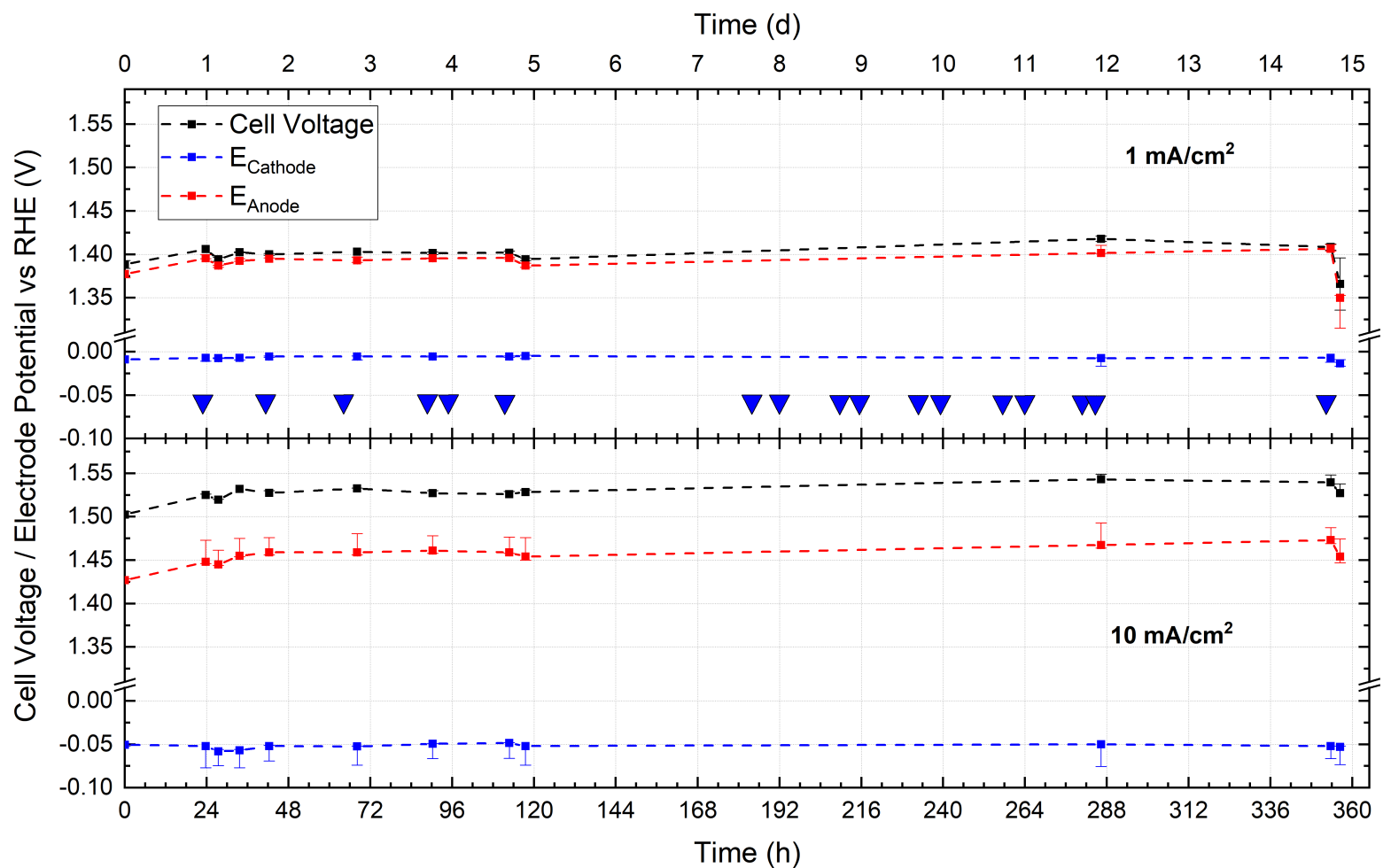


Fig. 6.31: Cell voltage, cathode electrode potential and anode electrode potential at 1 mA/cm^2 (top) and at 10 mA/cm^2 (bottom). Results from polarization curves obtained from the long-term test on the *NiMo/felt vs NiFe LDH/felt* cell at 80°C in 30 w\% KOH , in accordance with Fig. 6.26 and 6.28. The blue annotations mark the addition of water. Dashed lines are guidelines to the eye between measurements.

6.4.3 Pre- and post-mortem characterization of electrodes from long-term dynamic operation

Illustrated in Fig. 6.32, SEM, coupled with EDS, which is summarized in Tab. 6.8, was conducted before and after the long-term test. The as synthesized NiMo cathode is represented in the left part of the figure, and the cathode after 15 days long-term testing accordingly in the right part of the figure. The as synthesized and as tested NiFe LDH anode is similarly represented in Fig. 6.33, with the EDS results in Tab. 6.9.

For the NiMo cathode, the images of the as synthesized sample (Fig. 6.32A,C,E) show the desired low electrocatalyst coverage of the substrate. EDS results of this electrode display only low molybdenum contents. However, this has to be associated to the measurement depth of EDS. The nickel substrate will contribute to large parts to the EDS measurements, which will greatly underestimate the electrocatalyst's molybdenum content. Most importantly, EDS does indicate a measurable molybdenum content. Hence, the electrocatalyst-substrate-ratio in the EDS measurements is high enough to measure sufficient amounts of electrocatalyst. This allows to compare if the long-term test affected the electrocatalyst. The micron-sized sphericals on the substrate, see e.g. EDS 3, are nickel and oxygen rich. These parts are not from the electrocatalyst, but rather are original parts of the nickel substrate.

The NiMo cathode does not appear to be suffering from degradation ((Fig. 6.32B,D,F). In fact, the by EDS measured molybdenum content is higher than in the as synthesized sample. This can be associated with the greater amount of particles on the substrate, which change the electrocatalyst-substrate-ratio towards the electrocatalyst. Ultimately, more electrocatalyst will be measured by EDS. Although the increased amount of particles in the tested sample may origin in synthesis irregularities, it can be associated to iron- and potassium-deposition. Considering that the NiMo electrocatalyst did not degrade, as the electrochemical results do not indicate the opposite, the amount of deposited iron implies that the counter electrode, the NiFe LDH anode, must have suffered from severe iron-depletion.

The as synthesized NiFe LDH anode (Fig. 6.33A,C,E) displays two different electrocatalyst-layers on the substrate. A nano-sized platelet-like layer appears as the first layer on the substrate. The low iron content, as seen in EDS 3, reveals that the first LDH

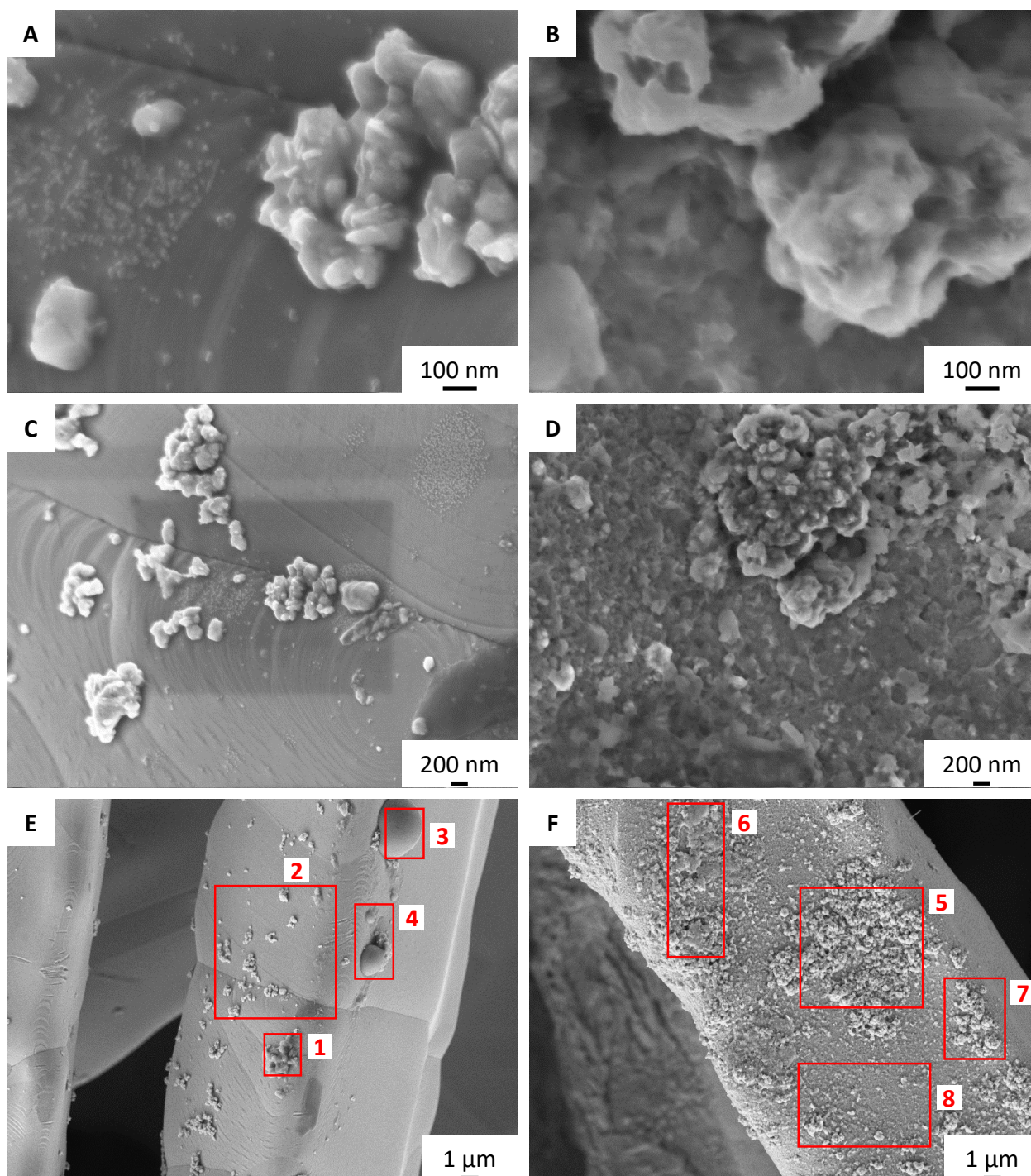


Fig. 6.32: SEM images of the cathode of the *NiMo/felt vs NiFe LDH/felt* cell. **A, C, E:** NiMo as synthesized. **B, D, F:** Cathode after 15 days operation. In red marked boxes represent the EDS measurement areas, whose results are summarized in Tab. 6.8.

Tab. 6.8: EDS results from the cathode of the *NiMo/felt vs NiFe LDH/felt* cell shown in Fig. 6.32. Elemental compositions are given as atomic-%.

Sample	Box	Ni	Mo (Mo/NiMo)	Fe	O	K
NiMo as synth.	1	28.3 ± 10.6	0.6 ± 0.3 (2.1)	–	71.0 ± 7.5	–
	2	82.2 ± 12.5	1.8 ± 0.3 (2.1)	–	16.0 ± 1.0	–
	3	20.9 ± 6.6	0.0 ± 0.0 (0.0)	–	79.1 ± 6.6	–
	4	54.2 ± 10.8	0.6 ± 0.2 (1.2)	–	45.2 ± 2.9	–
cathode	5	28.6 ± 5.1	5.0 ± 0.7 (14.8)	4.5 ± 1.1	55.3 ± 2.9	6.7 ± 0.6
	6	24.9 ± 4.4	3.9 ± 0.5 (13.6)	3.9 ± 1.0	60.4 ± 3.0	6.8 ± 0.6
	7	35.3 ± 5.8	4.3 ± 0.6 (10.8)	6.1 ± 1.4	47.7 ± 2.4	6.7 ± 0.6
	8	38.8 ± 6.0	3.6 ± 0.5 (8.4)	7.4 ± 1.5	42.6 ± 2.1	7.6 ± 0.6

electrocatalyst layer must be comparably thin. The intended 20% iron content in this layer may be greatly underestimated by the influence of the nickel substrate. The second layer on top consists of coagulated nano-sized platelets, which results in micron-sized particles. As indicative by EDS 2, this layer is comparably thick, as the iron content is close to the intended value. In an average over both layers, EDS 1 amounts about 15% of iron, when iron and nickel are considered only.

Albeit both layers each appear to be homogeneous, and a third layer is absent, a future alteration of the synthesis condition, such as different precursor concentrations or synthesis time, may be considered. The desired first layer is certainly affected by the coagulated top layer. However, the aim in this test is not to test the best performing electrode, but to understand the degradation behavior. Hence, the artificially decreased amount of active sites is favorable to increase the stress on the electrocatalyst during testing.

After the long-term test, the anode's surface alters exceptionally. As it was indicative by the electrochemical results before, SEM (Fig. 6.33B,D,F) confirms that the electroca-

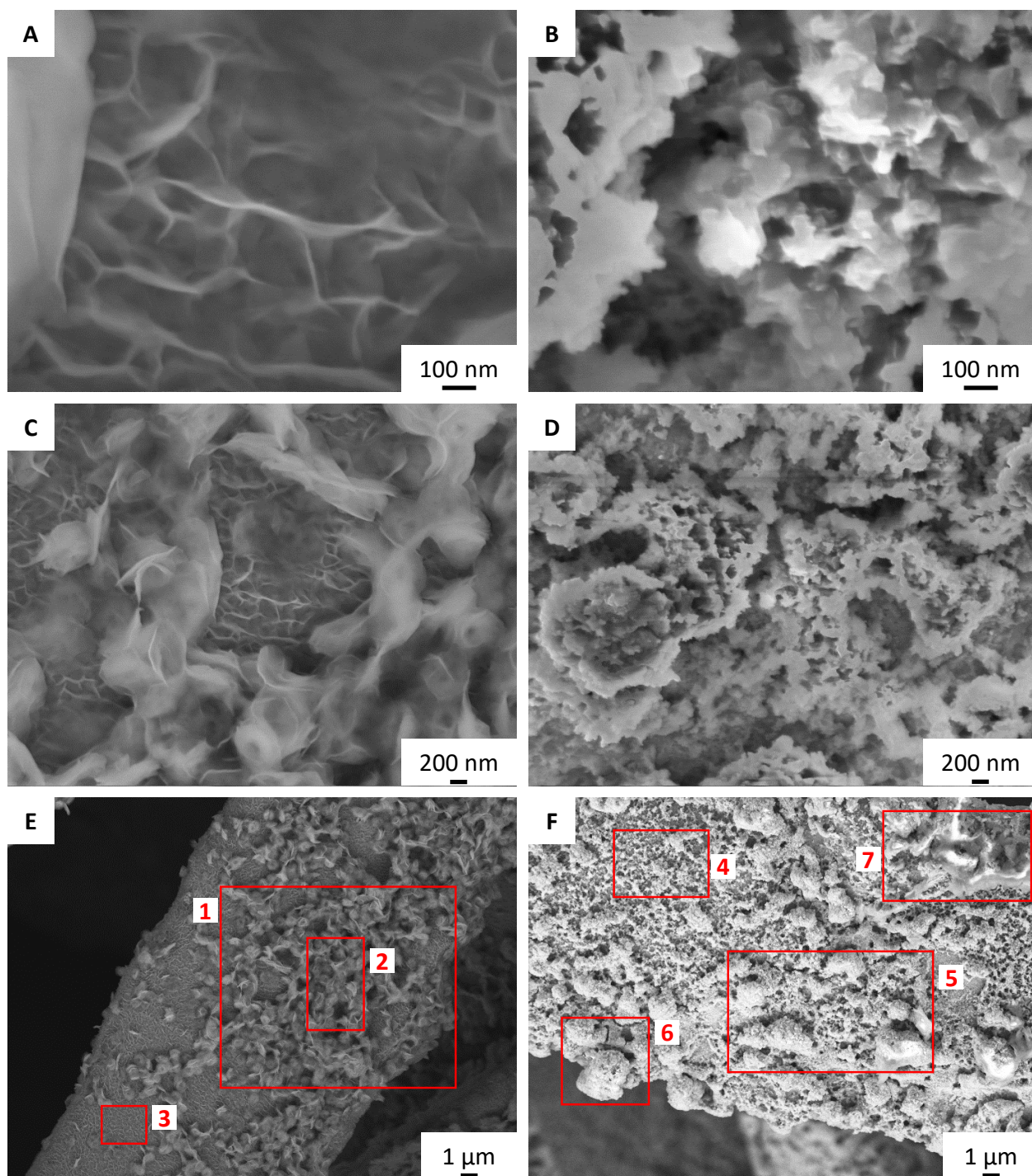


Fig. 6.33: SEM images of the anode of the *NiMo/felt vs NiFe LDH/felt* cell. **A, C, E:** NiFe LDH as synthesized. **B, D, F:** Anode after 15 days operation. In red marked boxes represent the EDS measurement areas, whose results are summarized in Tab. 6.9.

Tab. 6.9: EDS results from the anode of the *NiMo/felt vs NiFe LDH/felt* cell shown in Fig. 6.33. Elemental compositions are given as atomic-%.

Sample	Box	Ni	Mo	Fe (Fe/NiFe)	O	K
NiFe LDH as synth.	1	25.1 ± 7.4	–	4.5 ± 1.9 (15.3)	70.4 ± 5.7	–
	2	20.7 ± 6.4	–	5.2 ± 2.1 (20.2)	74.1 ± 6.1	–
	3	44.3 ± 10.0	–	1.8 ± 0.8 (3.9)	53.9 ± 3.7	–
anode	4	23.0 ± 3.8	0.0 ± 0.0	0.0 ± 0.0 (0.0)	66.5 ± 3.0	10.5 ± 0.8
	5	18.6 ± 3.3	0.0 ± 0.0	0.1 ± 0.1 (0.3)	71.1 ± 3.3	10.3 ± 0.8
	6	17.0 ± 2.9	0.0 ± 0.1	0.2 ± 0.2 (1.3)	72.2 ± 3.2	10.6 ± 0.8
	7	19.6 ± 7.4	0.0 ± 0.0	0.0 ± 0.0 (0.0)	72.3 ± 7.4	8.1 ± 1.5

talyst underwent severe changes during the course of 15 days of testing, although the anode never experienced OER underpotential conditions. Especially seen in the highest magnification, the first layer of the as synthesized layer has sintered from a platelet-like into a cauliflower-like shape. The previously coagulated second layer has further sintered, as e.g. visible by EDS 6. It shall be noted that, despite the small sample area of these images in comparison to the 10 cm² in the cell, an identical picture of the anode’s condition after testing was gathered at different parts of the SEM/EDS sample.

EDS 4 was chosen to represent an area which consists mainly of the first layer, while EDS 6 and EDS 7 both more represent the second layer. EDS 5 was taken as an average over both. The decision was based on EDS 1, 2, and 3, to be able to compare the different layers between the as synthesized and the as tested sample. As visible in the EDS results, the anode suffered from severe iron-depletion during the test. In particular, EDS 7, which is likely to be less influenced by the nickel substrate and thus measuring mainly the electrocatalyst, cannot determine any iron. In the other three measurements, iron was only detected within the margins of error. Therefore, it can be concluded that at least the bulk of the electrocatalyst depleted iron, which then deposited on the cathode.

Nonetheless, EDS alone does not allow to conclude if iron is still present within the surface or the subsurface. EDS does, on the other hand, lead to the conclusion that the electrocatalyst phase-changed from NiFe LDH to a nickel based oxide, oxyhydroxide, hydroxide, or a mixture of these. The phase-change, however, does not appear to have a significant impact on the anode's performance after a conditioning step. As such, the observed electrochemical conditioning step can be confirmed to result from an anode alteration.

As a consequence, XRD and XPS were conducted on the as synthesized and as tested NiFe LDH anode, as shown in Fig. 6.34. The XRD patterns are, despite the GIXRD approach, strongly impacted by the nickel-felt. In fact, no LDH related peaks can be observed in the pristine sample, which is likely due to the low loading and the background of the substrate. In the tested sample, peaks at $2\Theta = 11.2^\circ$ and $2\Theta = 22.4^\circ$ display the (003) and (006) planes of carbonate-intercalated LDH [190], respectively. Hence, the previous assumption of a phase-change is thereby disproven. In fact, the results from XRD confirm that the electrocatalyst coagulates, as the electrocatalyst can be measured with XRD indicating the increased amount of it, but remains in a form of a nickel-based LDH. XPS indicates that iron is present in the surface of the pristine as well as of the tested sample. The quantification of the spectra was conducted with the software CasaXPS and a Shirley model. Due to the overlap of the LMM Auger peak of nickel with the 2p peak of iron [116], the results are based on the Fe 3p and the Ni 3p peaks. The pristine NiFe LDH electrocatalysts has a nominal iron-content of 9.9% and the tested of 14.4%. Consequentially, the electrocatalyst does experience iron-depletion in the bulk, as assessed through EDS. The surface, however, preserves iron. Presumably, the iron content in the surface is at a dynamic equilibrium with dissolved iron-cations in the electrolyte.

The cathode and the anode never experienced potentials higher than 0.06 V vs RHE or lower than 1.23 V vs RHE, respectively. These electrode potentials were measured during the protective shutdown. As a consequence, the alteration of the anode surface is not correlated to any underpotential conditions, as it was observed in Chap. 6.3.2. In addition, a blackening of the electrolyte on the cathode side after about 11 d 22 h of operation was observed. Since both electrolyte circuits are connected through the separator and after the electrolyte reservoirs, the blackening can be associated with the iron-depletion from the anode. The iron-based oxides, oxyhydroxides, or hydroxides migrate due to the charge-

differences from the anode towards the cathode, eventually depositing on it. To ensure that the electrocatalysts are not affected by the full test shutdown after 15 days, the cell was cooled down to 25 °C at 1 mA/cm². Additionally, the electric connections were cut immediately after setting the cell current to zero, which ensures that discharging is physically inhibited. As a result, the here observed changes in the NiFe LDH anode can be correlated to the long-term test itself, and not to the test-end.

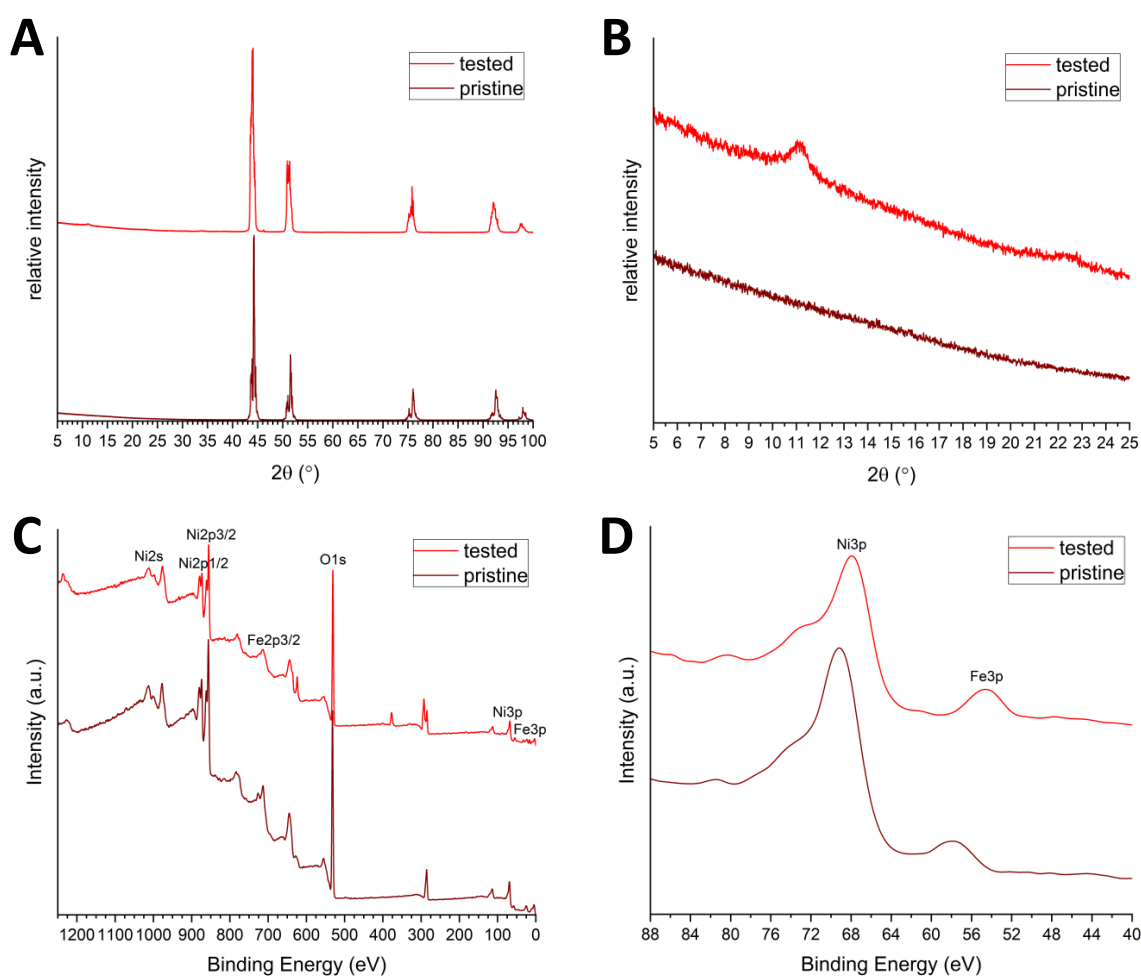


Fig. 6.34: XRD patterns and XPS spectra of the pristine and 357 h tested NiFe LDH anode. **A, B:** GIXRD patterns at an incidence angle of 5°, including the focus on the characteristic area of LDH. **C, D:** XPS survey scan and focus on the Ni3p and Fe3p peaks. Measurements made with a Rigaku Smartlab diffractometer with a Cu K α X-ray source and a ThermoFisher Escalab 250 Xi with an Al K α X-ray source.

6.5 Conclusions and discussions on the operational domains of NiMo and NiFe LDH electrocatalysts

The NiMo electrocatalyst degrades when it experiences underpotential conditions. As by the results from the accelerated degradation tests, the process occurs at potentials around 0.1 – 0.3 V vs RHE, which increases the electrocatalyst’s charge transfer resistance by 245 % and decreases the equivalent capacity by 53 % at 1 mA/cm². Moreover, the NiMo electrocatalyst oxidizes and eventually vanishes in a great fraction from the substrate at higher potentials. The similar kinetic performance after OCV at 0.95 V vs RHE in comparison to the uncoated nickel substrates clearly indicates the destruction of the electrocatalyst.

On the one hand, these results may question the applicability of the NiMo electrocatalyst. On the other hand, the 15 days long-term test displays high stability, although the cathode is subjected to dynamically changing potentials. The difference between the accelerated and the long-term tests is the potential window; the long-term test did not expose the cathode to potentials higher than 0.06 V vs RHE. With support from the SEM/EDS results, a deterioration of the NiMo electrocatalyst is absent in this case. Thus, this electrocatalyst is stable at potentials below 0.06 V vs RHE.

Another important observation is the stable performance of the NiMo electrocatalyst over time. As found elsewhere [59, 187], a pure nickel electrode experiences significant deactivation during extended electrolysis times at industrial relevant conditions of 8 M KOH and 70 °C. In detail, a nickel electrocatalyst increased the HER overpotential at 100 mA/cm² within the first \approx 48 h of electrolysis by 0.38 V. The nickel deactivation is correlated to the hydrogen-permeation through the bulk of the metal electrode, which influences its structure. Ultimately, the authors connect the deactivation with the formation of nickel hydride, which is also reported by others [56, 57, 191]. However, it is debated under which conditions bulk and surface/subsurface nickel hydrides can form [58]. Most importantly, the here assessed NiMo electrocatalyst does not experience a similar deactivation process.

These observations are well in agreement with the literature. Although more recent literature questions the stability of NiMo electrocatalysts [73, 78], they agree quite well with the here presented findings. In both published works, concerns about the stability of NiMo

electrocatalysts result from HER underpotential conditions. The concerns mainly arise from potentials at 0.0 – 0.4 V vs RHE, which is alike the findings of this work.

Furthermore, the findings of this work are well in agreement with Brown et al. [81] and Divisek et al. [183]. Brown et al. conducted a > 10000 h test on a NiMo electrocatalyst with a molybdenum content of 40 % in nickel-molybdenum. With an electrolyte concentration of 30 % KOH at 70 °C, the test resembles the industrial conditions well. During the course of the test, the cell was constantly held at 500 mA/cm² and the NiMo cathode did not deteriorate. Despite the stability during continuous operation, potential interruptions resulted in increased overpotentials. Based on cyclic voltammograms with hydrogen fluxed electrolyte, the authors declare oxidation of the electrocatalyst at potentials higher than 0.12 V vs RHE. A similar conclusion was made by Divisek et al. During prolonged operation in 10 M KOH at 100 °C, a NiMo electrocatalyst, with 33 % of molybdenum, displays stable operation during continuous operation. After interrupted operation, and at potentiostatic operation more positive than 0.155 V vs RHE, the NiMo electrocatalyst displays apparent irreversible degradation.

In comparison to the literature, the observations of this work solidify the understandings about the operational windows of NiMo electrocatalysts. In fact, the electrocatalyst in this work, which is a nickel-molybdenum electrocatalyst consisting nominally of 50 % molybdenum, displays an identical behavior towards underpotential degradation as seen by Brown et al. and Divisek et al. In this work, the underpotential oxidation is expected to be between 0.1–0.3 V vs RHE, while only the upper potential can be confirmed at this stage. In any case, all three works investigated a different nickel-molybdenum electrocatalyst, covering a range of 33 – 50 % of molybdenum. According to the literature background, see Chap. 2.5, the consortium of all three works covers the most important nickel-molybdenum electrocatalysts.

Since the electrocatalysts differ, but the conclusions of the underpotential oxidation are similar, which are further backed by the findings from Schalenbach et al. [73] and Davydova et al. [78], it may be generalized that the irreversible underpotential degradation of nickel-molybdenum electrocatalysts is uniform across the nickel-molybdenum electrocatalyst-platform. Admitting that this work only studied one electrocatalyst, the combination of this work with four literature sources, which covers a total of nine different NiMo electrocatalysts, justifies this hypothesis.

The NiFe LDH electrocatalyst displayed vulnerability towards the whole relevant potential window. As seen during the accelerated degradation studies, a modification of the electrocatalyst, which is supposedly the formation of higher oxidation states, causes a performance decrease. Although certainty about the exact electrochemical potential, at which the higher oxidation states form, does not exist at this point, hypothetically overcharging to γ -NiOOH is suspected to reason the performance change. The hypothesis is based on the fact that the equivalent capacity at 1 mA/cm^2 increases by 44 %, associated with a parallel decrease in performance by 14 mV. Furthermore, this explanation follows the observations made for plain nickel anodes, as described by the Bode diagram [14, 21, 91, 95, 96]. Despite the ambiguity of its origin, the combination of the EIS results, polarization curve results and the CVs does not cast any doubt on a high overpotential electrocatalyst decay.

On the other hand, OCV has shown that the initial performance can be regained at unpolarized underpotential conditions. Hence, the increasing overpotential is not correlated to a destructive, but a reversible degradation effect. Notwithstanding the OCV correlated relaxation, the NiFe LDH does experience significant surface alterations in these conditions. Besides a 154 % increase of the equivalent capacity, the results from the polarization curve reveal an intrinsic aggravation. Therefore, the similar performance, in comparison to the performance before accelerated degradation, cannot be correlated to a reversibility of the electrocatalyst, but to an alteration that counterbalances intrinsic aggravation with enhanced active sites. As proven by SEM/EDS, the electrocatalyst alteration does take place, including the leaching of iron.

The in SEM/EDS confirmed surface alteration may have already resulted previously from the cyclic voltammograms, which indicated an electrocatalyst modification within the first cycle. Hence, the correlation between surface alterations, iron leaching and specific conditions cannot be drawn at this stage. By contrast, it is demonstrated elsewhere that the LDH structure collapses in similar electrolyte and temperature conditions even without an applied potential [130]. As a consequence, the long-term test ensured that the NiFe LDH anode was never unpolarized. In particular, the anode has never been exposed to potentials below 1.23 V vs RHE.

During the long-term test, the NiFe LDH electrocatalyst again displayed an initial modification, which was considered as a conditioning step. This conditioning step, which

took place within the first day of the test and increased the OER overpotential at 10 mA/cm^2 by $\approx 0.02 \text{ V}$, is congruent with the observations made by cyclic voltammetry. Thus, *in situ* restructuring of the bulk NiFe LDH OER electrocatalyst may be inevitable at these conditions. This effect has previously been proposed by Diongi and Strasser already [28]. Their review concludes that structural transformations through anodic polarization and OER conditions unquestionably materialize, which is accomplished by the need for spectroelectrochemical measurements investigating these effects.

After the conditioning step, the transformed NiFe LDH electrocatalyst displayed remarkable stability. The observations made around alternating overpotentials could be associated to the hydroxide-concentration dependence of the electrocatalyst, which was pronounced due to the water management of the setup. With the support of SEM/EDS, the electrocatalyst modification is correlated to a morphological change from a platelet-like to a cauliflower-like electrocatalyst. Concordant with the SEM/EDS results after accelerated degradation, the NiFe LDH electrocatalyst leached iron. While iron is still present in the surface and subsurface according to XPS, the bulk depletion results in free particles, which were visible by the eye in the electrolyte circuit after about 11 d 22 h of operation. These particles eventually deposited on the cathode without interfering its performance.

Concluding on the behavior of the NiFe LDH electrocatalyst, a stable operation window between 1.23 V vs RHE and the upper, yet still not certain, potential forming higher oxidation states can be defined. However, the structural transformation and iron-depletion, which could cause issues such as clogging and corrosion of the periphery in a full-size technical setup, are more cautiously to be described as pseudostability.

The effect of iron depletion has previously been described by Etzi Coller Pascuzzi et al. [131]. The authors electrochemically conditioned electrodeposited NiFe LDH electrocatalysts (with 26 – 30 % Fe) at 100 mA/cm^2 for 1 h. The conditioning was carried out at room temperature and $75 \text{ }^\circ\text{C}$ in 1, 5, and 10 M KOH, which allows to draw a good comparison to this work with $80 \text{ }^\circ\text{C}$ in 30 w% ($\sim 7 \text{ M}$) KOH. As demonstrated by XPS and EDS in the work of Etzi Coller Pascuzzi et al., the electrocatalyst films leach with increasing electrolyte concentration, while the leaching is much more pronounced with temperature. In detail, the electrocatalyst film subjected to 10 M KOH and $75 \text{ }^\circ\text{C}$ appears to have been massively destructed. Furthermore, the leaching of iron was substantially higher than of nickel.

Hence, the observed leaching of iron in this work over the course of 15 days in 30 w% KOH at 80 °C is well in agreement with the literature. Moreover, the instability of iron raises the question, to which degree it is dispensable. As often discussed in the literature [28, 92, 93, 99, 118, 119], a high performing nickel OER electrocatalyst requires iron. In addition, XPS confirms that iron is preserved after 15 days in the surface of the anode. As a consequence, the process of iron-depletion must be studied to find an optimal point between the benefits of iron and the disadvantage of electrocatalyst corrosion.

The findings of this work about the stability aspects affecting the kinetics of a NiMo and a NiFe LDH electrocatalyst, under technical relevant conditions, are graphically summarized in Fig. 6.35.

For future works, optimizations of both electrocatalysts are required to ensure a stable technical operation. For NiMo HER electrocatalysts, the vulnerability to underpotential conditions must be addressed. Although a shutdown under a protective polarization can be one approach to protect the electrocatalyst from degradation, it is essential that the electrocatalyst can endure pure OCV conditions without full degradation. Albeit the OCV-tolerance may not necessarily need to be longer than a few hours, a technical operation without a full power-cut, e.g. due to maintenance, cell-replacement or grid-failures, is unrealistic. Hence, coming studies should optimize the electrocatalyst focusing on its underpotential tolerance.

In a first step, the exact degradation processes in the underpotential region need to be understood well. If the degradation mechanisms are known, alterations of the electrocatalyst synthesis or further manufacturing steps shall be conducted to circumvent the degradation processes. Conceivable further manufacturing steps could be the coating of the as synthesized NiMo electrode with other metals, as the literature presents remarkable tolerance towards deactivation for e.g. different nickel-iron [59] or nickelvanadium [60] compositions. Furthermore, the results from the accelerated degradation tests on nickel cathodes showed tolerance to, and even improvement by, underpotential conditions. It may therefore be a considerable approach to coat nickel-molybdenum electrocatalysts with nickel.

A nickel-coating of the nickel-molybdenum electrode would resemble a raney-nickel type electrode, as the nickel-molybdenum synthesis creates high surface area electrodes. On the other hand, this method could possibly result in similar deactivation processes as in pure nickel electrodes. As a result, it would be necessary to shed light on the dependence

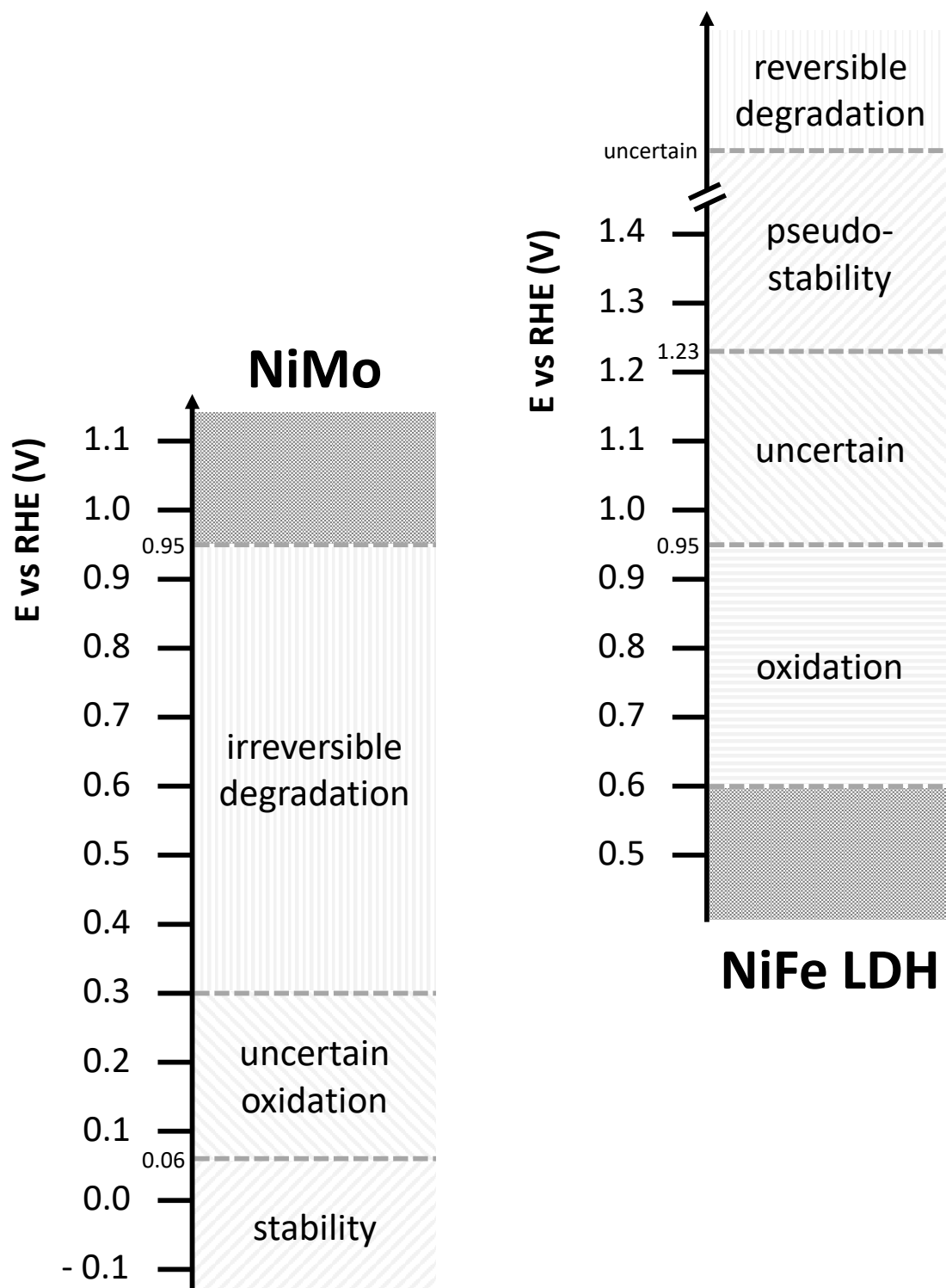


Fig. 6.35: Conclusions about the operational domains of a NiMo HER electrocatalyst (left) and a NiFe LDH OER electrocatalyst (right), with respect to the influence of the electrode potential vs RHE on the kinetic performance. Results at 80 °C in 30 w% KOH.

between the nickel surface layers, the electrode bulk and the different deactivation processes. The aforementioned influence of hydrogen dissolution and hydride formation of nickel as electrocatalyst, which were proposed by Conway and Jerkiewicz [192] to catalytically poison the electrocatalyst by promoting hydrogen sorption into the host metal, may be one concern with this approach. Furthermore, other literature sources indicate the importance of material strain [53, 54] and the oxidation state of nickel [15, 42, 45, 57, 165, 193]. Therefore, a nickel-coating, which covers and thus protects the nickel-molybdenum, might cause further issues. A conceivable working hypothesis could be an optimal coating-thickness, obtained by e.g. electroless or electrodeposition, which is at balance between the need for a coating and the negative impacts of bulk nickel. Another possibility could be the implementation of core-shell type electrocatalysts through the addition of surface-dissolved molybdenum.

For NiFe LDH electrocatalysts, it may be challenged if the applied hydrothermal synthesis is, from an application point of view, superior to a nickel-iron-alloy or iron-doped nickel electrode. A structural collapse seen in the bulk LDH electrocatalyst at OCV, which appears to have only marginal impacts on the kinetic performance, allows to hypothesize that a nickel-iron electrode may show similar performance after *in situ* oxidation. This hypothesis has yet to be supported by further tests. However, if the kinetics and the stability are similar to the hydrothermally prepared NiFe LDH electrocatalyst, more synthesis routes become available. For instance, dip-coating or spray-coating nickel and iron oxides followed by thermochemical reduction are highly controllable methods. With similar kinetics and stability, the *in situ* oxidation would produce a kinetically active oxide, oxyhydroxide or oxide film on the surface, with a highly conductive nickel-iron substrate.

To proceed this path, it is necessary to firstly understand the exact corrosion mechanisms of bulk NiFe LDH at 80 °C in 30 w% KOH, including potential changes below and above the OER equilibrium potential. It is mandatory to investigate the process of iron-depletion at higher temperatures and electrolyte concentrations, in order to understand the maximum possible use of this beneficial secondary element. In a second step, these processes should be correlated to the *in situ* oxidation processes of nickel-iron electrodes. If both are identical, ultimately resulting in similar kinetics and a similar prolonged stability, the superiority of bulk NiFe LDH over nickel-iron electrodes can be questioned. The suggested pathway to focus on an *in situ* formed electrocatalyst is supported by the studies from Tro-

tochaud et al. [122], who have demonstrated that a thin film of as prepared $\text{Ni}_{0.9}\text{Fe}_{0.1}\text{O}_x$ is highly active. They suggest that the reason for the high activity originates from an *in situ* transformation into the LDH structure, which is proposed for all of their investigated nickel containing films.

Another possible path to investigate LDH OER electrocatalysts for the technical operation are single-layer NiFe LDH electrocatalysts. As shown by Chen et al. [114], and in accordance with the findings of this work, bulk LDH was found to deteriorate over the course of 20 h in 1 M KOH at 500 mA/cm^2 and 80°C . The authors conclude that the observed deactivation of their catalyst was due to the small interlayer spacing of the LDH, which slows down the diffusion of the OH^- proton acceptor. As a result, the electrocatalyst dissolves. This result can be associated with the conditioning step observed in this work, at which the anode appeared to increase in overpotential, but remained stable thereafter. A solution to stabilize the electrocatalyst was given by Chen et al. in exfoliating the bulk LDH to atomically thin nanosheets. Single-layer LDH would not hinder the diffusion of the proton acceptor, which was shown to give a stable performance over 20 h at the same conditions as the bulk LDH. Besides exfoliation, a second approach to obtain single-layer LDH could be realized with a surface sensitive synthesis, such as published by Liu et al. [132]. This method is mentioned here, as the authors present remarkable stability of their electrode over the course of $> 1000 \text{ h}$ at 1000 mA/cm^2 in 10 M KOH and presumably room temperature. To obtain such a stable electrode, the authors corroded iron substrates in nickel-containing solutions. Likewise, nickel-iron or iron coated nickel electrodes, as for instance by the above described coating-thermochemical dual step process, should be corroded by similar corrosion solutions as Liu et al., with the goal to obtain stable single-layer NiFe LDH electrocatalysts.

Although the investigated NiMo and NiFe LDH electrocatalysts displayed some apparent degradation, the results of this work are promising and guiding towards optimizations. The investigated electrocatalysts may not be stable over the full technical operational window. However, severe degradation during continuous dynamic operation was not observed. Furthermore, the results of this work form the foundation for future investigations on the degradation processes, which can then be circumvented through optimization steps, of which several possible approaches are proposed within this chapter.

Chapter 7

Spectroelectrochemical Raman and X-ray diffraction studies of NiMo and NiFe LDH electrocatalysts

Studies considering stability aspects and the nature of high-performing electrocatalysts are crucial for their technical application. This is particularly true for spectroelectrochemical studies, as understandings on the stability and reaction mechanisms during operation aid in designing optimal electrocatalysts, which should perspectively demonstrate a resilient high performance over a decade. The following chapter presents such spectroelectrochemical studies based on the findings from Chap. 5 and 6, utilizing the spectroelectrochemical setup FeliS described in Chap. 4.

Starting from the findings of the previous chapters, the active site in NiMo electrocatalysts stands out to be Ni. In addition, the stability of these types of electrocatalysts is given under HER conditions, while the exposure to HER underpotential conditions is detrimental to the kinetics. Following these observations, this chapter studies the effects of the HER underpotential exposure on the HER kinetics of a NiMo electrocatalyst by combining the previous results with spectroelectrochemical Raman. Furthermore, the kinetics of a NiFe LDH electrocatalyst turn out to be affected by OER conditions. Even though OER underpotential conditions do not show adverse effects on the kinetics of this electrocatalyst, this chapter investigates the stability of a NiFe LDH electrocatalyst over the potential range of interest for the technical application by spectroelectrochemical X-ray diffraction.

7.1 Experimental details

Spectroelectrochemical samples are based on the rigid 3YSZ separator used previously in Chap. 4. Electrocatalysts are drop-cast onto this separator to produce binder-free samples. Since the separator itself is an electric insulator, it was plasma coated with a sputter coater Quorum 150T ES (with Ar 99.999%). For Raman samples, a surface enhancing effect can be achieved through a silver coating. For this, a current of 20 mA was used to coat the separator for 60 s, which was measured by the plasma-coater to result in a 17 nm thick film. To evaluate the coating, the inplane resistance over 1.5 cm was measured and resulted in 9 Ω . For samples investigating the OER, which was done with spectroelectrochemical XRD, the stability of silver in alkaline solutions is not sufficient [76]. Gold has further been excluded following the potential-pH diagram and a recent publication due to stability concerns at oxygen evolving conditions [76, 194]. For these samples, the substrates are coated with platinum with a current of 20 mA for 60 s, which resulted in an inplane resistance over 1.5 cm of 500 Ω . Hence, a second coating with 80 mA for 30 s was added, which resulted in a total film-thickness of 27 nm and an inplane resistance over 1.5 cm of 45 Ω .

Raman spectroscopy was conducted with a Renishaw InVia spectrometer, calibrated on the 520.5 cm^{-1} peak ($\pm 0.5 \text{ cm}^{-1}$ tolerance) of a monocrystalline silicon sample, with a 50x long distance objective (Olympus LMPlanFLN). Electrochemical measurements were conducted in 1 M KOH (pre-electrolyzed) with a Gamry Reference 600 potentiostat at room temperature. Raman spectra (100–2000 cm^{-1}) took roughly 5 min. X-ray diffraction studies were realized in a Rigaku Smartlab X-ray diffractometer with a Cu $K\alpha$ X-ray source and a d/tex detector. For a sufficient signal-to-noise ratio, an XRD measurement ($2\Theta = 8 - 80^\circ$) took roughly 25 min, with two different settings for the X-ray intensity at $2\Theta = 8 - 25^\circ$ and $2\Theta = 25 - 80^\circ$. For the electrochemical tests in this setting, a Biologic SP-200 with a low current probe was applied. The XRD tests were conducted in 30 % KOH (pre-electrolyzed) between room temperature and 85 $^\circ\text{C}$. All results are presented versus RHE reference electrode. Potentiostatic impedance was conducted with a 10 mVrms amplitude.

For the NiMo electrocatalyst, a solgel precursor, as described in Chap. 5.1.2, was reduced in a ceramic boat at 600 $^\circ\text{C}$ for 3 h in safety-gas. 20 mg of the reduced powder were added to 500 μL of isopropanol and sonicated for 30 min. 50 μL of this ink were drop-cast onto the center of a silver-coated separator and left to dry at room temperature, resulting

in a coverage of 2 mg electrocatalyst. As this procedure differs slightly from the approach in Chap. 5 and 6, where the precursor was reduced on a nickel substrate, Fig. 7.1 compares the GIXRD of the sample from Chap. 5 with the Powder XRD from this chapter. Powder and solid sample both display Ni_4Mo and molybdenum oxide phases. However, the differences mainly stem from two causes. Firstly, the GIXRD measurement suppresses the peaks of the electrocatalyst at e.g. $2\Theta \approx 41^\circ$ and $2\Theta \approx 65^\circ$ and distorts the peak positions, as the sample is not perfectly flat. Secondly, the greatest difference between both samples can be found in the peak at $2\Theta \approx 25^\circ$, which indicates molybdenum oxide. As both samples were reduced in the same sequence, it is conceivable that the molybdenum oxide in the powder sample is amorphous. The nickel substrate provides a center for the anisotropic growth of molybdenum oxide, which is not existing in the substrate-free reduction. In spite of these differences, the comparability of the electrochemical results can be assumed. The differences are explainable and both samples were reduced in the same reduction sequence. Furthermore, Raman spectroscopy confirms the comparability of these two samples at a later stage of this chapter.

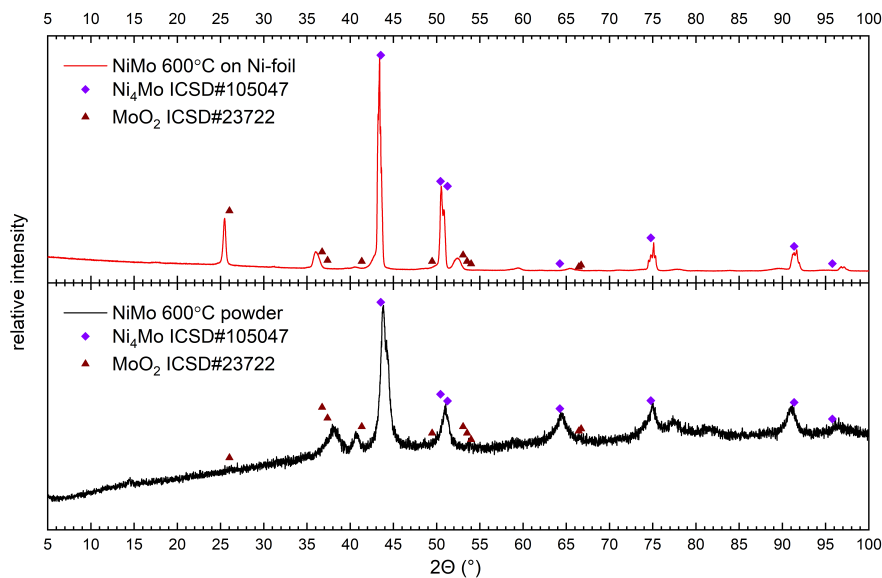


Fig. 7.1: Grazing incidence at 5° incidence angle (top) and Powder X-ray diffraction (bottom) of the solgel precursor reduced at 600°C . The samples differ by the presence of a Ni-foil as substrate (top) and substrate-free reduction (bottom). Both samples were reduced in parallel in the same oven.

For the NiFe electrocatalyst, the synthesis described in Chap. 6.1.1 was repeated without a nickel substrate in the autoclave. The resulting suspension was centrifuged for 5 min in a Thermofischer SL 16 centrifuge at 5000 1/min, the liquid part was decanted and the powder was washed with water. After a second centrifugation and decanting step, the powder was washed with ethanol and centrifuged for a third time. The liquid was decanted and the powder was transferred into a vial through the addition of fresh ethanol, which resulted in an ink containing 58 mg/mL Ni₈Fe₂ LDH electrocatalyst. This ink was sonicated for 30 min and drop-cast onto a platinum-coated substrate. Drop-casting was conducted in several portions, including drying steps at room temperature between portions, until a total amount of 172 μ L resulted in a coverage of 10 mg NiFe LDH electrocatalyst.

7.2 NiMo in the cathode operational window

The NiMo electrocatalyst solgel 600 °C from Chap. 5 was previously tested in parts in the HER underpotential region in 11.6 M KOH. In the first part of this section, the measurements between -200 to $+500$ mV vs RHE with 50 mV/s are reiterated in Fig. 7.2A (range 1). Furthermore, Fig. 7.2B displays a second sequence of cyclic voltammograms conducted on this sample. For this sequence, the potential was swept between -200 to $+1000$ mV vs RHE (range 2) with 50 mV/s. Hence, the cyclic voltammograms cover the entire range of interest according to the results of Chap. 6 for the NiMo HER electrocatalyst. In the second part of this section, the extended results from this sample are supported by spectroelectrochemical Raman at relevant potentials.

7.2.1 Results from cyclic voltammetry

The CVs in Fig. 7.2 show three different oxidation peaks and two reduction peaks. In range 1, an oxidation peak O1 at ≈ 150 mV vs RHE corresponds to a reduction peak R1 at ≈ -75 mV vs RHE. Additionally, an oxidation peak O2 at ≈ 350 mV vs RHE corresponds to a reduction peak R2 at ≈ 0 mV vs RHE. In range 2, an oxidation peak O3 at ≈ 785 mV vs RHE does not indicate a corresponding reduction peak. Furthermore, the reduction peaks R1 and R2 are absent on the backscan. On the second cycle, peak O2 is the only remaining peak identifiable, although at lower intensity than in CVs limited

to a maximum potential of 500 mV vs RHE. In addition, the achieved current density at -200 mV vs RHE constantly reduces, with 11.9 mA/cm^2 for CVs limited to range 1, and down to 4.6 mA/cm^2 after the second cycle of range 2. The irreversible electrochemical oxidation at O3 occurs with a charge of 295.9 mC. In combination with the vanishing of the other peaks, the decrease of the current density at -200 mV vs RHE, and the absence of the O3 peak in further cycles, it indicates a destruction of the electrocatalyst. Different to Chap. 5, the redox processes are not assigned to possible electrochemical reactions. In Chap. 7.2.2, spectroelectrochemical Raman at the potentials indicated by the arrows in Fig. 7.2B was applied to assess the associated electrochemical reactions.

Beforehand, the impacts of the exposure to range 1 and range 2 on the HER kinetics of the NiMo electrocatalyst were investigated through iV -curves, EIS at $10 \text{ mA/cm}^2_{\text{geometric}}$, and *ex situ* pre- and post-mortem SEM. The iV -curves, as shown in Fig. 7.3A, indicate a marginal decrease of the HER kinetics after exposure to range 1. The achieved current density of 28.4 mA/cm^2 at -200 mV vs RHE before exposure to HER underpotential conditions reduces to 19.8 mA/cm^2 after range 1. After range 2, it reduces with 1.4 mA/cm^2 to 4.9% of the initial value before CVs. The results from EIS, as tabularized in Tab. 7.1, do not display noticeable differences between the initial measurement and after range 1. The surface roughness with $R_f = 138.4\text{-}141.0$, assessed from the double layer capacity at a summit frequency of $\omega = 5.9\text{-}6.4$ Hz, remains within a stable area. However, the results after range 2 confirm the detrimental effect on the electrocatalyst, as the surface roughness reduces to 4.2% of the surface roughness before CVs, which is further supported by the increase of the summit frequency to $\omega = 180.2$ Hz.

Supplementary, the SEM micrographs indicate the vanishing of the electrocatalyst in Fig. 7.3C and D, leaving the nickel substrate as the electrocatalyst. Importantly, the normalization of the current to the ECSA in Fig. 7.3B leaves a contrary overview. The intrinsic kinetics of the NiMo electrocatalyst decrease after range 1, but regain values obtained before HER underpotential exposure after undergoing range 2. As the electrocatalyst is lost, the Ni-substrate and the NiMo electrocatalyst display similar intrinsic HER kinetics according to this comparison. This observation supports the hypothesis from Chap. 5 that Ni is the active site in NiMo electrocatalysts.

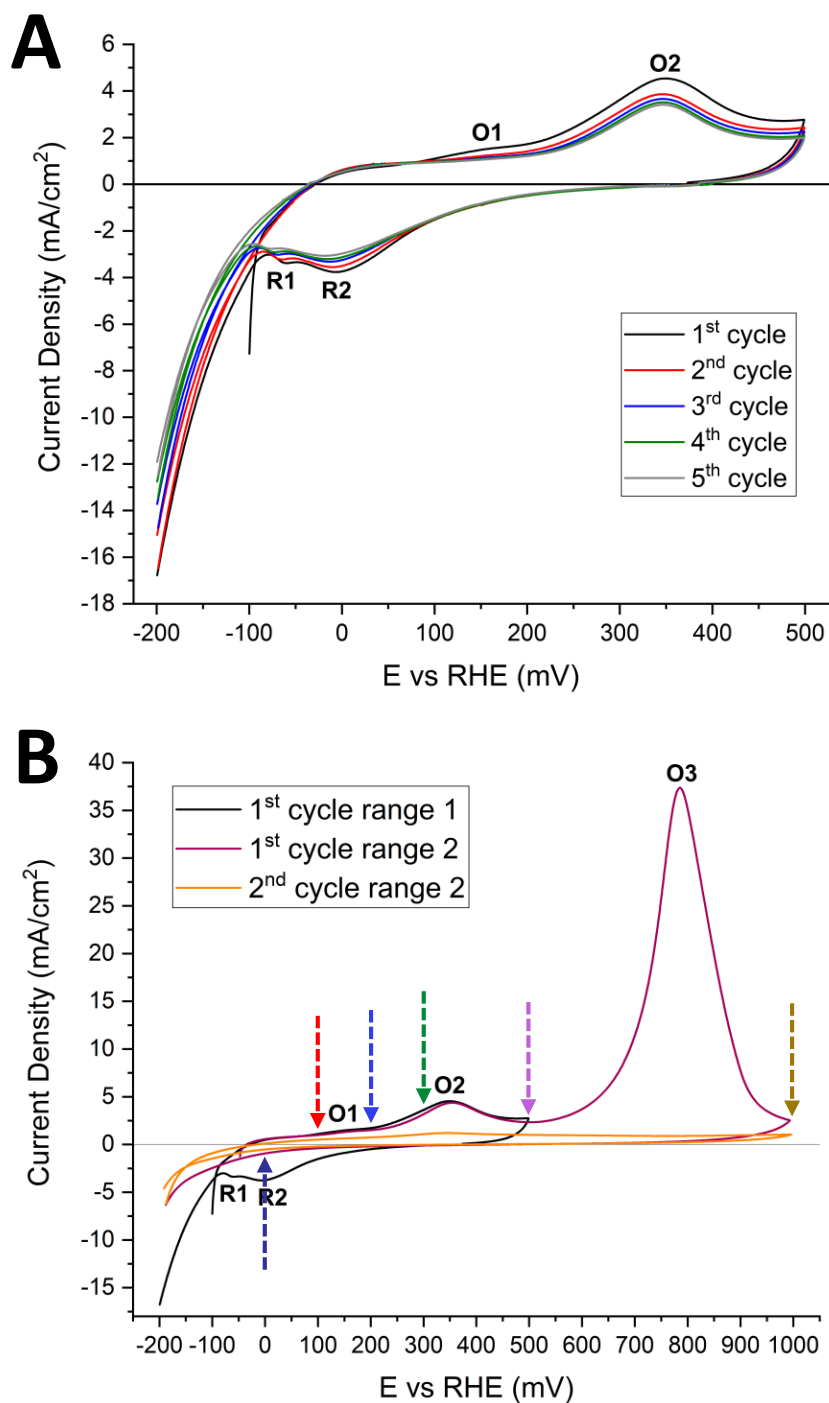


Fig. 7.2: Cyclic voltammograms of a NiMo solgel electrocatalyst, reduced at 600 °C, in 11.6 M KOH at 50 mV/s, with respect to the geometric surface area of 3.14 cm². **A:** α -Ni(OH)₂ region between -200 to 500 mV vs RHE (range 1, repetition of Fig. 5.9), **B:** Operational window of a cathode between -200 to 1000 mV vs RHE (range 2). The arrows indicate where spectroelectrochemical Raman (Fig. 7.4) was conducted.

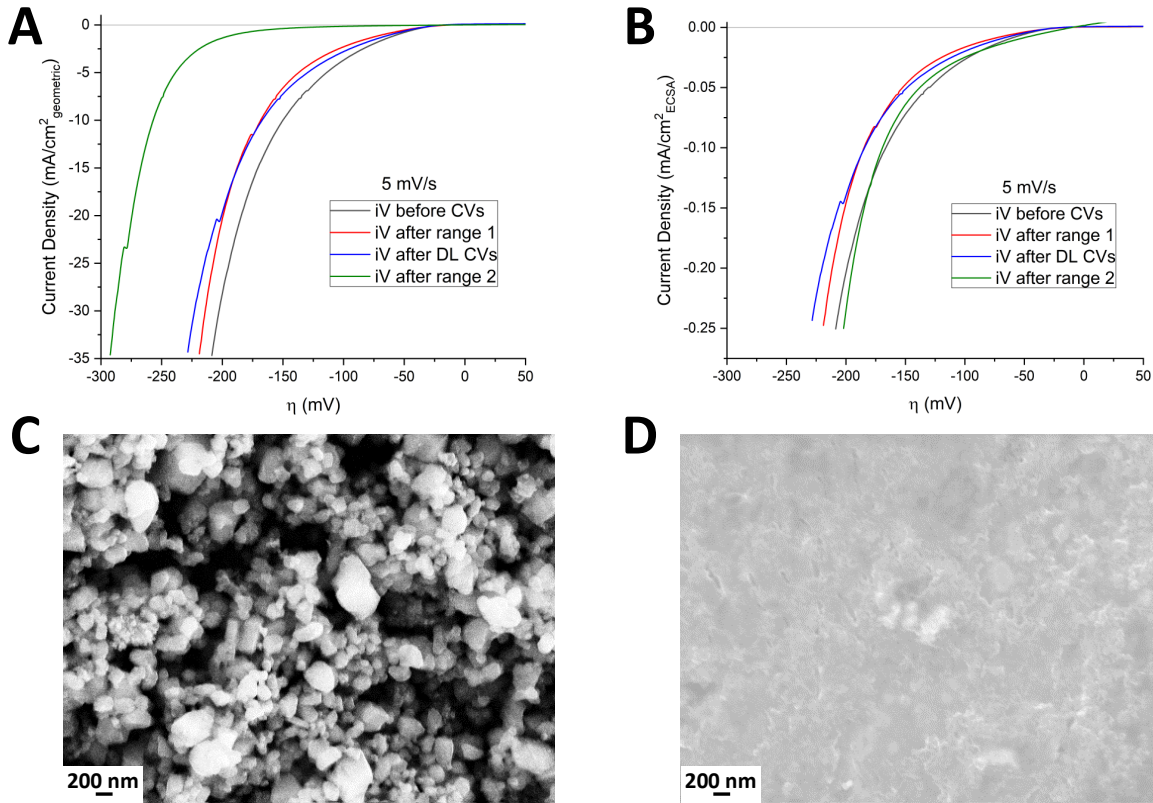


Fig. 7.3: Influence of potential cycling on the HER kinetics in 11.6 M KOH, assessed through the backscans of iR -corrected iV -curves at 5 mV/s. With respect to **A**: The geometric surface area (continuance of Fig. 5.13) and **B**: To the ECSA obtained through an R(RQ)-fitting of an impedance at 10 mA/cm². Curves are recorded initially (before CVs), after measurements of Fig. 7.2A (after range 1), after scans between 50 to 100 mV vs RHE at scan rates of 500 to 5 mV/s to obtain the double layer capacitance (after DL CVs), and after measurements of Fig. 7.2B (after range 2). **C**, **D**: SEM micrographs before and after the test, respectively.

Tab. 7.1: Results from galvanostatic EIS at 10 mA/cm² associated with Fig. 7.3. The fitting results are shown with an R(RQ) equivalent circuit, as the fitting results with an Armstrong equivalent circuit indicated no pseudocapacitive influence. The surface roughness considers a value of 40 μF/cm².

Parameter	Unit	before CVs	after range 1	after DL CVs	after range 2
R_s	Ω	0.560	0.560	0.565	0.568
R_{ct}	Ω	1.514	1.414	1.525	1.209
C_{dl}	μF/cm ²	5537.1	5573.9	5638.4	232.5
R_f	cm ² /cm ²	138.4	139.3	141.0	5.8
ω	Hz	6.0	6.4	5.9	180.2

7.2.2 Results from spectroelectrochemical Raman

Following the findings from Chap. 4 on the concentration-dependent fluorescence influence of KOH, spectroelectrochemical Raman was conducted in 1 M KOH. The sample was polarized at increasing potentials of 100, 200, 300, 500, and 1000 mV vs RHE, followed by 0 mV vs RHE and OCV (see also Fig. 7.2B). The resulting Raman spectra are illustrated in Fig. 7.4.

The unpolarized sample displays monoclinic MoO₂ [74, 195], which remains unchanged at 100 mV vs RHE. At 200 mV vs RHE, additional vibrations at 425 cm⁻¹, 678 cm⁻¹, and 795 cm⁻¹ appear. With further polarization to 300 and 500 mV vs RHE, these vibrations disappear, while a broader vibration at 1350 – 1600 cm⁻¹ appears. Three further vibrations at 614 cm⁻¹ (unidentified), 900 cm⁻¹ (Mo=O symmetric stretching [196]), and 1668 cm⁻¹ (bending of OH in H₂O [161, 197]) can be observed. The vibration at 795 cm⁻¹ is associated with α-Ni(OH)₂ [17, 197, 198]. The vibrations at 425 cm⁻¹ (1 phonon), 678 cm⁻¹ (2 phonons), and 1350 – 1600 cm⁻¹ (2 magnons) stem from NiO [199]. The disappearance of the lower in favor of the higher Raman shift vibrations are a consequential result of the thickness of the NiO layer, as its Raman active vibrations are size-dependent [200–202]. Whilst the phonon-vibrations represent one to a few monolayers of NiO, their disappearance with the associated appearance of the broad 2 magnon vibration connote the growth of the NiO-layer.

With exposure to 1000 mV vs RHE, the MoO₂-vibrations vanish, as a vibration (SU1) at 1540 – 1565 cm⁻¹ can be observed. After decreasing the potential to 0 mV vs RHE, the MoO₂-vibrations reappear under disappearance of the SU1-vibration. Releasing the polarization in a further step, the OCV displays additional vibrations (SU2) at 817 cm⁻¹, 1264 cm⁻¹, and 1348 cm⁻¹. The vibrations SU1 and SU2 may be attributed to MoO₄²⁻_(aq) [203, 204], although an immediate congruence is not given. The published vibrations display a solvent-dependency, e.g. with 897 cm⁻¹ for pH 7 and 841 cm⁻¹ for pH 11 [204]. Hence, the vicinity of the vibrations SU1 and SU2 in 1 M KOH to the published values at pH > 8 (837 cm⁻¹, 897 cm⁻¹) [203] and pH 11 [204] leads to this suspicion. In addition, the disappearance of the MoO₂-vibrations underlines it further. Moreover, it is possible that the Mo=O vibration could potentially stem from MoO₄²⁻_(aq), although this cannot be mentioned with any certainty. This vibration could as well be indexed with the leaching of Mo from the Ni₄Mo alloy, which is described elsewhere [73, 78].

Since the results indicate an adverse effect of the HER underpotential exposure, a

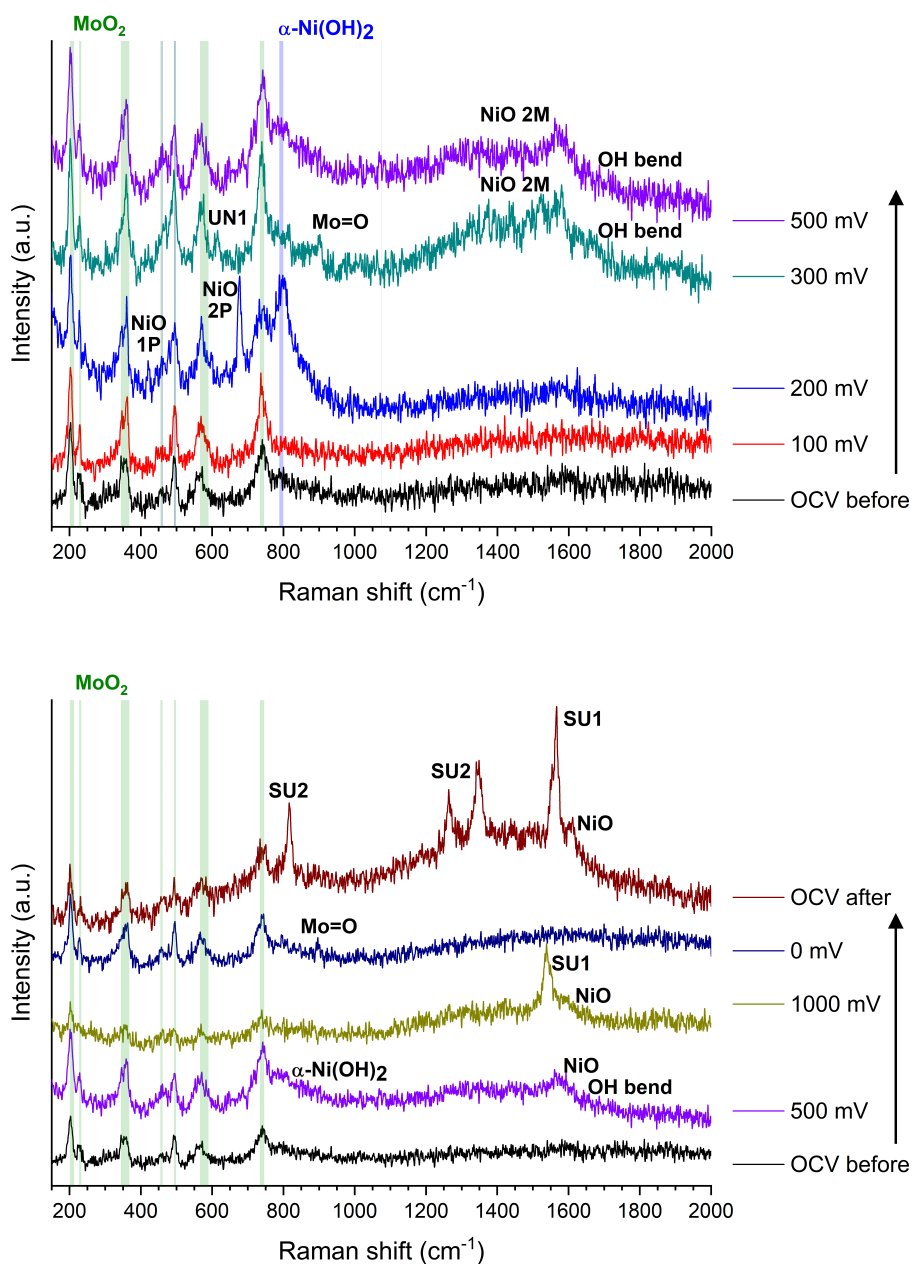


Fig. 7.4: Raman spectra of a NiMo solgel electrocatalyst, reduced at 600 °C, under polarization. Potentials are given versus RHE reference electrode. Green coloring: monoclinic MoO_2 (207, 230, 347, 364, 458, 496, 569, 585, 740 cm^{-1}); blue coloring: $\alpha\text{-Ni(OH)}_2$ (460, 495, 795, 1075 cm^{-1}). Mo=O at 900 cm^{-1} . NiO at 425, 678, 1350–1600 cm^{-1} . UN1: unidentified vibration at 614 cm^{-1} . SU1, SU2: Vibrations suspected from $\text{MoO}_4^{2-}(\text{aq})$ (817, 1264, 1348, 1540–1565 cm^{-1}). OCV before and 500 mV are repeated for comparison in the second plot, as the ordinate scalings differ. Measurements made in 1 M KOH with a 100 mW green laser (532 nm) at 1 % intensity in a Renishaw InVia Spectrometer. Results are 50 times enhanced.

second test was conducted with a fresh sample studying the effects of range 1 in more detail. The results of the second test are presented in Fig. 7.5. Similar to the first test, the second sample shows monoclinic MoO₂ at OCV and at 100 mV vs RHE. In addition, the formation of α -Ni(OH)₂ (795 cm⁻¹) and NiO (678, 1350 – 1600 cm⁻¹) at 200 mV vs RHE repeat. The absence of the 1 phonon vibration while the 2 magnon vibration is visible at this potential indicates a thicker NiO-layer than in the first test at this potential, where the 2 magnon vibration is first identified at 300 mV vs RHE. However, this observation is not controversial. The sample focusing in the second test at 200 mV vs RHE took 3 min. Thus, the formation of NiO-layers is likely time-dependent for potentials \geq 200 mV vs RHE.

To understand the reversibility of the formation of α -Ni(OH)₂ and NiO, the potential was reversed to –100 mV vs RHE. The α -Ni(OH)₂ vibration disappears together with the 2 phonon vibration of NiO, while its 2 magnon vibration remains. Although the reduction of the NiO-layers could potentially, similar to their formation, be time-dependent, it could not be reduced after \approx 5 min at –100 mV vs RHE. An upwards scan to 300 mV vs RHE regenerates the vibrations observed at 200 mV vs RHE and additionally shows the 1 phonon vibration of NiO. Remarkably, the α -Ni(OH)₂ vibration experiences a blue-shift from 795 cm⁻¹ to 814 cm⁻¹ compared to 200 mV vs RHE from the first and the second test. In a second attempt to investigate their reversibility, another measurement was conducted at –100 mV vs RHE. Similar to the previous measurement at this potential, the α -Ni(OH)₂ vibration disappears, while the NiO 2 magnon vibration persists¹.

Lastly, the stability of the electrocatalyst was assessed by an OCV measurement. In the first test, the exposure of up to 1000 mV vs RHE caused the formation of MoO_{4(aq)}²⁻, which redeposited as MoO₂ at 0 mV vs RHE. The OCV afterwards again shows MoO_{4(aq)}²⁻ associated vibrations, indicating that the redeposition was weak. In the second test limited to 500 mV vs RHE², such a step cannot be observed. Neither does MoO_{4(aq)}²⁻ form, nor does the OCV have a detrimental effect on MoO₂. Besides, a Mo=O vibration at 900 cm⁻¹, as seen in the first test, cannot be found in the second test.

¹Remark a horizontal baseline in this measurement. As the broad features at $>$ 1200 cm⁻¹ continue over the displayed abscissa limit of 2000 cm⁻¹, the existence of a broad NiO 2M vibration could be overlooked.

²The spectrum at 500 mV vs RHE is analogous to 300 mV vs RHE and was thus spared in the plot to reduce complexity.

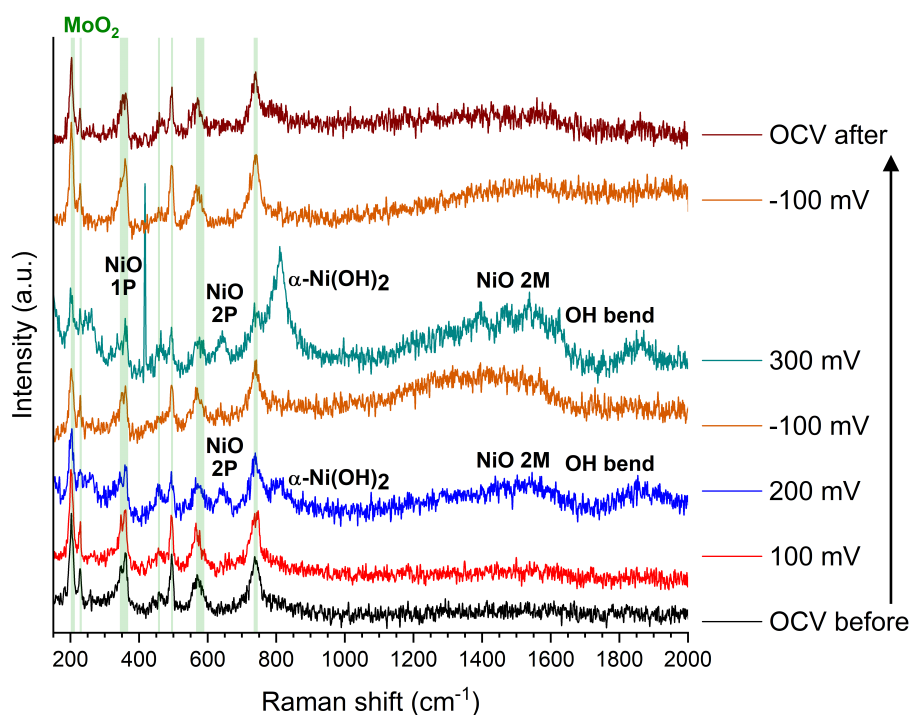


Fig. 7.5: Raman spectra of the second test of a NiMo sol-gel electrocatalyst, reduced at $600\text{ }^{\circ}\text{C}$, under polarization. The electrocatalyst experienced a maximum potential of 500 mV vs RHE. Potentials are given versus RHE reference electrode. Green coloring: monoclinic MoO_2 ($207, 230, 347, 364, 458, 496, 569, 585, 740\text{ cm}^{-1}$). $\alpha\text{-Ni(OH)}_2$ at $795, 814\text{ cm}^{-1}$. NiO at $425, 678, 1350 - 1600\text{ cm}^{-1}$. Measurements made in 1 M KOH with a 100 mW green laser (532 nm) at 1% intensity in a Renishaw InVia Spectrometer. Results are 50 times enhanced.

7.2.3 Importance of spectroelectrochemical Raman studies of NiMo electrocatalysts

For a further assessment of the spectroelectrochemical Raman results, pre- and post-mortem *ex situ* Raman was conducted on the spectroelectrochemical sample (NiMo Raman) as well as on the sample from cyclic voltammetry (NiMo CV) from the first part of the section. The comparison, which is illustrated in Fig. 7.6, confirms the comparability of both samples. The pristine NiMo CV sample displays vibrations of Ni₄Mo/MoO_{3-x} at 187, 341, 370, 819, 891, 940, 947 cm⁻¹ [164]. The pristine NiMo Raman sample displays similar vibrations, which are roughly 14 cm⁻¹ blue-shifted compared to the NiMo CV sample. A similar remark can be made about the post-mortem samples, where a main broad peak at 897 cm⁻¹ in the NiMo CV sample is 7 cm⁻¹ red-shifted in the NiMo Raman sample. Furthermore, the intensity-ratios of the vibrations differ. The latter can be associated to the different substrates. The NiMo Raman sample has a silver-coated substrate, which influences the Raman results through a surface-enhancing effect. The surface-enhancement is identifiable by the different laser-intensities of 5 % (NiMo CV) and of 1 % (NiMo Raman) resulting in comparable signal-intensities. Hence, a SERS-effect was achieved, which influences the intensities of Raman active vibrations compared to conventional Raman [17]. In conclusion, both samples are comparable, but the peak-shifts remain an open question, as they are not necessarily attributed to the different substrates.

In addition to the comparison between the samples, an overview between *ex situ* and *in situ* of the spectroelectrochemical sample is given in Fig. 7.7. The *ex situ* measurements of the dry sample differ remarkably from the wet *in situ* conditions at OCV. While the pristine dry sample consists of Ni₄Mo/MoO_{3-x}, the wetted sample at OCV before electrochemical measurements displays vibrations of monoclinic MoO₂. After the electrochemical measurements, MoO_{4(aq)}²⁻ is additionally visible with the wetted sample. The dissolved permolybdates cannot be found in the dry sample afterwards. Moreover, the MoO₂ changes into presumably mixtures of molybdenum and nickel oxides. In any case, the comparison of *ex situ* to *in situ* clearly indicates the necessity of spectroelectrochemical Raman studies of this type of electrocatalyst. The *ex situ* conditions are not identical to the *in situ* conditions of the electrocatalyst, which could easily guide towards false conclusion.

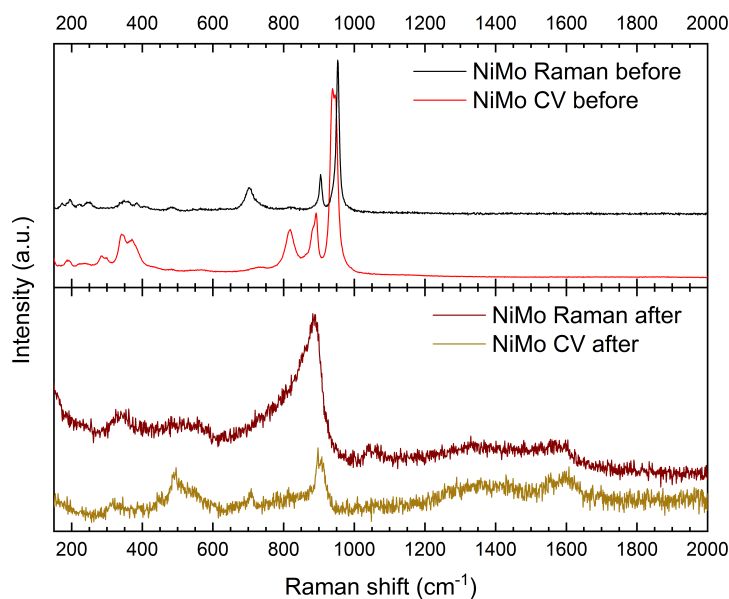


Fig. 7.6: Pre- and post-mortem *ex situ* Raman spectra of the sample from Chap. 7.2.1 (NiMo CV) in comparison to the first spectroelectrochemical sample (NiMo Raman). Measurements made with with a 100 mW green laser (532 nm) at 5 % (NiMo CV) and at 1 % (NiMo Raman) intensity in a Renishaw InVia Spectrometer.

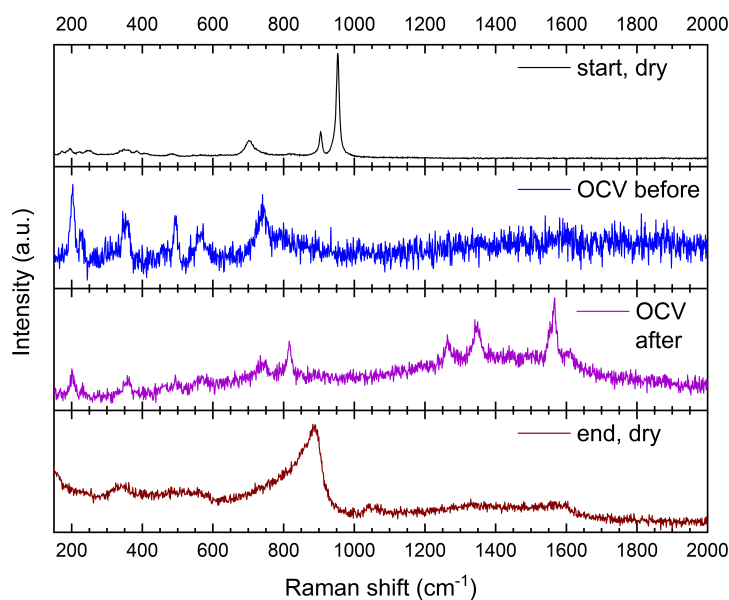


Fig. 7.7: Comparison between pre- and post-mortem Raman on the first spectroelectrochemical sample to the OCV in 1 M KOH. Measurements made with a 100 mW green laser (532 nm) at 1 % intensity in a Renishaw InVia Spectrometer.

7.2.4 Conclusions on the redox processes of a molybdenum oxide supported Ni₄Mo electrocatalysts

Raman spectroscopy on the electrochemical and on the spectroelectrochemical sample confirm their comparability. Based on the findings from the electrochemical tests, spectroelectrochemical Raman in the HER underpotential region unveils the redox processes occurring on a molybdenum oxide supported NiMo electrocatalyst.

The electrocatalyst remains stable at potentials < 100 mV vs RHE. Above this potential, α -Ni(OH)₂ forms. The nickel hydroxide forms reversibly, as it can be reduced at hydrogen evolving potentials. At 200 mV vs RHE and above, NiO is generated. This reaction is time- and potential-dependent and cannot be reduced at hydrogen evolving potentials. On the other hand, further investigations have to show that the found irreducibility of NiO is not an effect of the rather short measurement time, as others find that Ni/NiO heterostructures form β -Ni(OH)₂ at HER underpotentials and eventually reduce to plain Ni in HER conditions over time [161]. Moreover, the assigned NiO 2M vibrations at -100 mV vs RHE could possibly stem from other forms of nickel, e.g. a hydrated nickel oxide phase or nickel hydride. An underlying nickel oxide layer or the formation of a different phase (e.g. α_{compact} [96]) might also explain the blue-shift of the α -Ni(OH)₂ vibration upon reoxidation. However, the true origin remains speculative without additional studies.

In parallel to the thickening of NiO at ≥ 200 mV vs RHE, a Mo=O vibration indicates that the Ni₄Mo potentially leaches Mo. Such a finding was also made by Du et al. [196], who observed the Mo=O vibration at 230 mV vs RHE. Furthermore, the dealloying of Ni_xMo_{1-x} above the equilibrium potential of hydrogen was described previously [73, 78]. Thus, the Mo=O presumably originates from a reaction intermediate during the leaching of Mo from the Ni₄Mo alloy. However, the Mo=O could also be associated to the oxidation of MoO₂. Therefore, its origin remains elusive at this point. In addition, the effect is not much pronounced. The absence of further vibrations associated with MoO_{4(aq)}²⁻ and the absence of the Mo=O vibration in the second test at this potential underline its minor nature. Hence, the impact on the HER kinetics from exposure up to ≤ 500 mV vs RHE, as observed in the electrochemical test, most likely originates from the formation of irreducible NiO.

With polarization above 500 mV vs RHE, an irreversible oxidation of the electrocatalyst occurs. The disappearance of the MoO₂ related vibrations under appearance of

$\text{MoO}_4^{2-}(\text{aq})$ vibrations reveal the electrocatalyst-oxidation. With reversing the potential to 0 mV vs RHE, the permolybdates redeposit on the substrate. However, the OCV thereafter shows that the redeposition is weak, as part of the MoO_2 dissolves without polarization. Electrochemical tests furthermore illustrate the detrimental effect of the MoO_2 -oxidation on the HER kinetics, as 95.8 % of the electrochemical active surface area is lost. The charge of the oxidation peak O3 with 295.9 mC is equal to $62.5 \mu\text{g}/\text{cm}^2$ of MoO_2 , and is thus equal to 16.4 w% of the electrocatalyst. Despite the redeposition of MoO_2 , the amount of active sites was not regained. This can be associated with Ni_4Mo (83.6 w% of the pristine electrocatalyst) as the active part, which does not redeposit onto the MoO_2 supporting structure. Following the electrocatalyst-kinetics normalized to the ECSA, the similar intrinsic kinetics of the partially oxidized Ni-support and of the unaltered electrocatalyst endorse that Ni is the active site in this electrocatalyst. Thereby, the lacking recovery of the kinetics per geometric surface area in spite of the redeposition of MoO_2 is a complementary finding.

The observations on the stability of a molybdenum oxide supported NiMo electrocatalyst coincide with findings by others. Bau et al. [82] and Liu et al. [74] demonstrate the stability of molybdenum oxide supported NiMo electrocatalysts for the alkaline water electrolysis. The potential in these studies did not exceed 300 mV vs RHE and 100 mV vs RHE, respectively. Studies at 0 mV vs RHE indicating the redeposition of molybdenum oxide [82] and over > 7000 s in the HER overpotential region (at ≈ -150 mV vs RHE) [74] validate the stability of these electrocatalysts under HER conditions.

Combining the results from the electrochemical and the spectroelectrochemical tests, a schematic displaying the redox processes of the molybdenum oxide supported Ni_4Mo electrocatalyst is given in Fig. 7.8. Consequentially, four different areas with regards to the electrocatalyst's potential can be defined. As shown in Fig. 7.9, the electrocatalyst remains stable at potentials below 100 mV vs RHE. The formation of $\alpha\text{-Ni}(\text{OH})_2$ is reversible, while the formation of NiO cannot be reversed entirely. This explanation is further guided by the decreasing peak intensities in the cyclic voltammograms of the electrochemical sample in range 1. Beyond 550 mV vs RHE, the molybdenum oxide supporting structure oxidizes to permolybdates. While it can redeposit at lower potentials, the effects on the electrocatalyst-kinetics are irreversibly detrimental. The partly oxidized Ni-support becomes the active site due to the lacking recovery of the highly active nickel sites on molybdenum oxide.

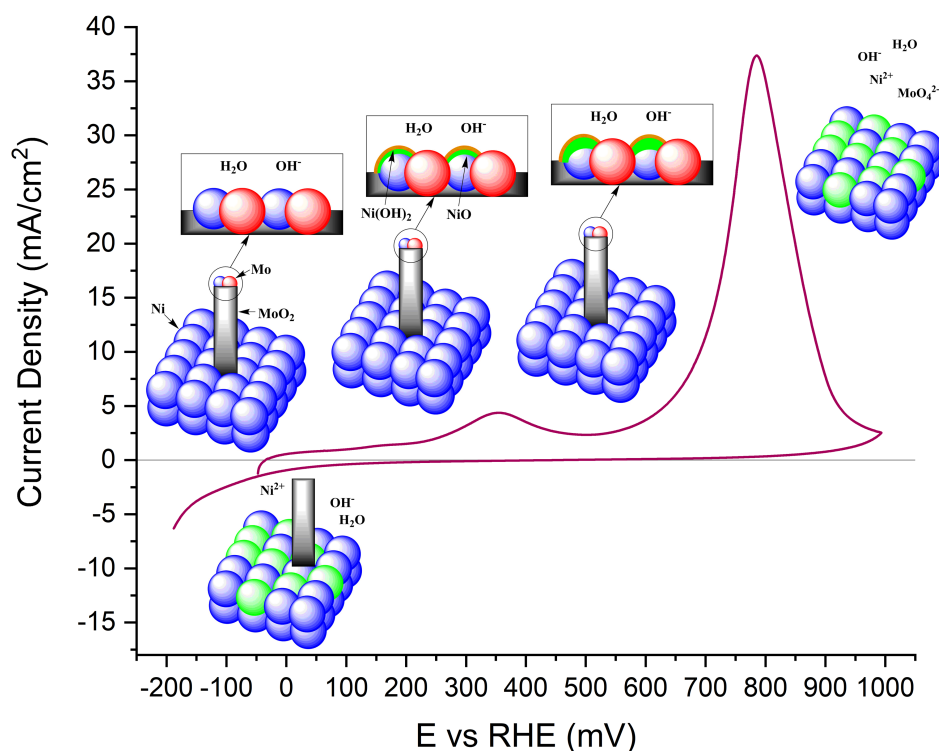


Fig. 7.8: Schematic redox processes of a molybdenum oxide supported NiMo electrocatalyst on Ni-support. Results from spectroelectrochemical Raman with regards to the cyclic voltammogram from Fig. 7.2.

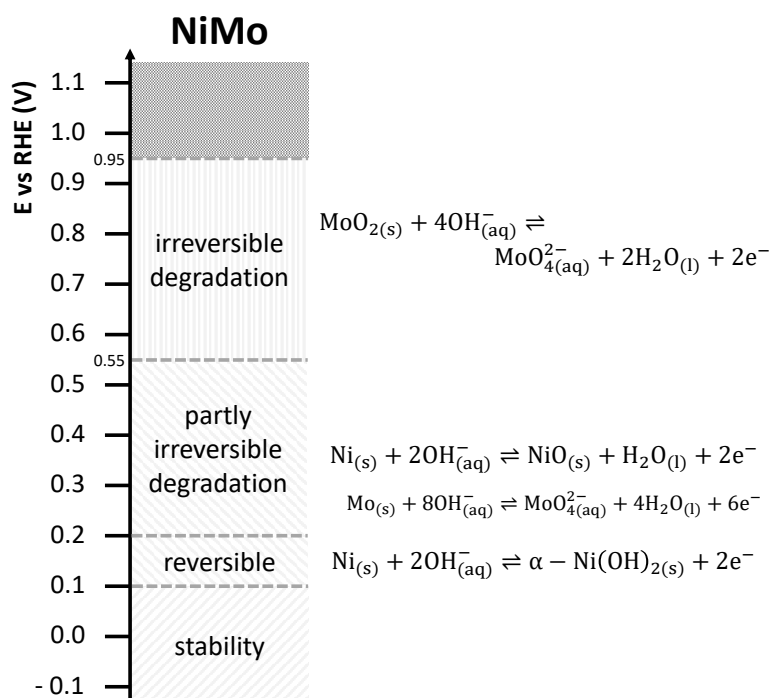


Fig. 7.9: Conclusions about the operational domains and the correlating degradation and redox processes of a molybdenum oxide supported NiMo electrocatalyst.

7.3 Spectroelectrochemical X-ray diffraction of NiFe LDH in the anode operational window

The Ni₈Fe₂ LDH electrocatalyst from Chap. 6 displayed apparent degradation irrespective of the potential, albeit the OER overpotential region appears to be the primary degradation causing environment. As a result, this section covers spectroelectrochemical XRD studies in two segments. Firstly, the study covers a heating sequence from room temperature to 85 °C at an OER overpotential of 200 mV. Secondly, potential cycling at 85 °C simulates the technical application. The combination of XRD patterns with electrochemical tests allows to define structural and stability aspects of the Ni₈Fe₂ LDH electrocatalyst under real operating conditions. Different to the bulk electrocatalyst in Chap. 6, the sonication of the ink resulted in exfoliated electrocatalyst [111] studied in this section.

7.3.1 Stability and performance evolution with temperature

Nickel based layered double hydroxides in their reduced state are electrical insulators, which undergo oxidation above the OER equilibrium potential into their OER active conductive structure [107]. Consequently, the stability evaluation during the heating sequence was conducted just above the oxidation peak by applying an OER overpotential of 200 mV.

The constant-overpotential procedure further serves to determine the activation energy of the electrocatalyst through EIS measurements. The charge transfer resistance was obtained through an LR(RQ)(R_{ct}Q) fitting, as EIS studies at 1000 mV vs RHE showed that the second arc is correlated to the OER (Fig. C.4). The exchange current densities at different temperatures were determined through Eq. (2.17). The OER overpotential was chosen to suffice the potential-requirement for the oxidative activation of the electrocatalyst while simultaneously being at the lowest possible oxygen evolving currents. The calculation of the exchange current densities can only be valid at a constant overpotential and in proximity to the onset-potential of the OER. The results of the XRD patterns and EIS measurements at 25 °C, 45 °C, 55 °C, 65 °C, 75 °C, and 85 °C are illustrated in Fig. 7.10. Based on the YSZ peak at $2\Theta = 30.05^\circ$, which was measured *ex situ* on a platinum-sputtered substrate, the XRD patterns are corrected following Eq. (3.26).

The NiFe LDH electrocatalyst displays peaks at $2\Theta = 19.7^\circ$, 21.8° , and 23.8° , while

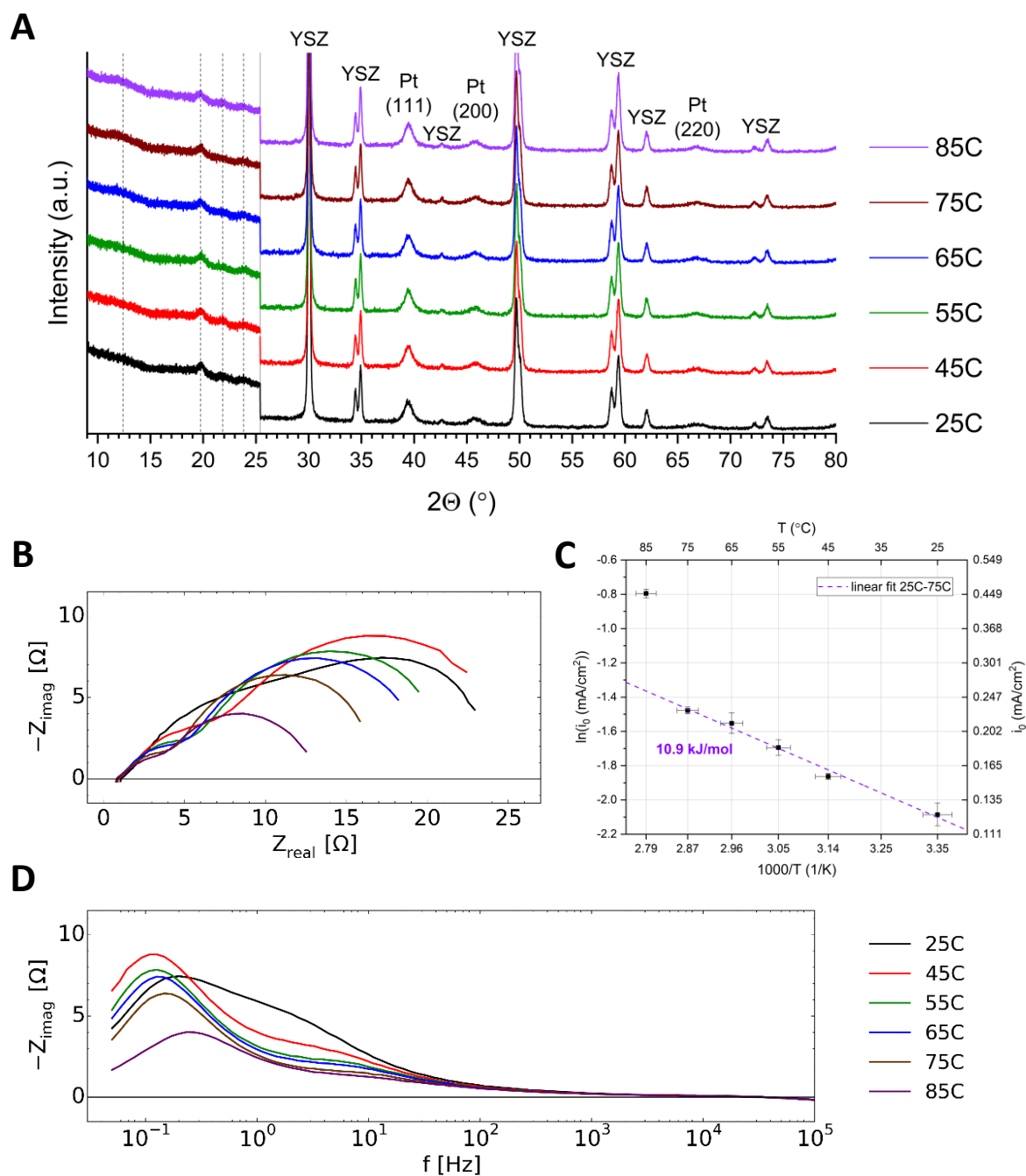


Fig. 7.10: Spectroelectrochemical XRD studies of NiFe LDH with regards to the temperature at an OER overpotential of $\eta = 200$ mV. **A:** GIXRD patterns at an incidence angle of 5° . Dashed lines: NiFe LDH electrocatalyst. **B, D:** Nyquist and $-Z_{\text{Im}}$ over f plots, respectively, of the correlated electrochemical impedance spectra between 100 kHz–50 mHz. **C:** Temperature dependent evolution of the exchange current density, derived through Eq. (2.17) with an LR(RQ)(R_{ct} Q) fitting (see Fig. C.1). Measurements made in 30% KOH within a Rigaku Smartlab diffractometer.

a peak at $2\Theta = 12.4^\circ$ can only be assumed. The peaks are indicated by guiding dashed lines throughout this section. Further electrocatalyst related peaks at higher angles could, not least because of the sample background and the low amount of electrocatalyst, not be found. The correlation of these peaks is a rather complex task. The area at $2\Theta = 9 - 25^\circ$ represents the (003) and (006) planes of LDH as well as brucite-type β -Ni(OH)₂ at 19.3° (ICSD#169978). Furthermore, the positions of the (003) and (006) planes of LDH are, inter alia, dependent on the interlayer anion. For successfully exfoliated LDH, they are absent [111]. Nevertheless, the patterns display oxidized LDH at $\eta = 200$ mV, which presumably differs from unpolarized exfoliated LDH.

Based on the synthesis chemicals of the studied electrocatalyst, the peak at 21.8° can be associated to the (006) plane of a carbonate intercalated LDH [190, 205, 206], while a peak at 19.7° potentially indicates the (006) plane of a nitrate intercalated LDH [190, 205, 206]. However, the latter could as well stem from β -Ni(OH)₂. In fact, the synthesis was conducted in excess of urea to nitrates (2.22:1), which is expected to result in solely carbonate/hydrocarbonate intercalated LDH [190]. Hence, the peak at 19.7° most likely results from brucite-type β -Ni(OH)₂ of polarized exfoliated LDH. The peak at 23.8° might result from the (006) plane of either hydrocarbonate [190] or possibly hydroxide intercalated LDH. Halide intercalated LDH can be excluded due to the purity of the precursor chemicals and the pre-electrolyzed electrolyte.

Upon heating, the electrocatalyst displays no changes with regards to the XRD patterns. Electrochemically, the EIS measurements display an expected decrease of the charge transfer resistance. The calculated exchange current densities result in an activation energy of $E_A = 10.9 \pm 0.6$ kJ/mol ($r^2 = 0.989$), after excluding the result at 85°C . The OER current at this temperature was too high for a valid correlation to OER onset conditions, which is required for the calculation of the exchange current density. The activation energy demonstrates the high performance of this type of OER electrocatalyst, as it sets a benchmark compared to ≈ 26 kJ/mol of electrodeposited NiFe LDH with similar composition reported elsewhere [207], and as it reaches values reported for IrO₂ [208].

7.3.2 Accelerated degradation at 85°C

Since the results from the heating sequence displayed no apparent degradation at steady polarization, dynamic measurements were added at 85°C. Firstly, the polarization was released to study possible implications of OCV conditions. Secondly, the electrocatalyst's potential was swept between 1.0 – 1.559 V vs RHE ($\eta_{\max} = 380$ mV) twice. Due to the stable CVs, the third cycle extended the upper potential limit to 1.679 V vs RHE ($\eta_{\max} = 500$ mV), including a steady polarization step at 1.609 V vs RHE ($\eta = 430$ mV), and at 1.0 V vs RHE on the backscan to conduct XRD measurements. In addition, a steady polarization step at 1.379 V vs RHE ($\eta = 200$ mV) was carried out for an EIS measurement. Thirdly, the potential was swept between 1.0 – 1.729 V vs RHE ($\eta_{\max} = 550$ mV). After the cycling, XRD was carried out at 1.0 V vs RHE, 1.609 V vs RHE ($\eta = 430$ mV), 1.719 V vs RHE ($\eta = 540$ mV), and at OCV. Additionally, another EIS measurement at 1.379 V vs RHE ($\eta = 200$ mV) was performed. The procedure was chosen to simulate the dynamic operation in a technical electrolyzer occurring over several years of operation in a comparably short time-frame. It is also analogous to the procedure from Chap. 6.3.1. The combination of the results from XRD, CV, and EIS is illustrated in Fig. 7.11, with the EIS spectra additionally visualized in Fig. 7.12.

Following the XRD patterns, all observable changes are at the (003) plane of LDH. Peaks from the electrocatalyst at $2\Theta > 24^\circ$ are either absent or undetected due to the background of the sample. The OCV did not result in noticeable changes from the pattern at 1379 mV. The following first, second, and third cycle of the CV in Fig. 7.11B do not indicate significant differences. The XRD measurement on the backscan of the third cycle, however, displays the occurrence of a broad peak at $2\Theta = 12.6^\circ$ at 1609 mV, which shifts to $2\Theta = 11.7^\circ$ at 1000 mV after the reduction peak. The fourth cycle shows a decreased performance and a hysteresis on the backscan. With further cycling, the performance-decrease normalizes. XRD at 1000 mV and at 1609 mV are similar to the patterns after the third cycle. The following patterns at 1719 mV and at OCV present a shift of the (003) plane peak to $2\Theta = 12.7^\circ$ and $2\Theta = 12.8^\circ$, respectively.

As the XRD patterns indicate a change of the electrocatalyst, two additional considerations were added to understand the mechanisms. Firstly, the redox-peaks were analyzed to display the peak positions of the oxidation and reduction peaks per cycle, as well as the area

of the reduction peak between 1.0–1.33 V vs RHE (with a 0 mA baseline) in Fig. 7.11D. The oxidation peak experiences a shift to more negative values with cycling, while the reduction peak remains comparatively unaffected. Integrating the reduction peak results in a linear increase of the area with cycling upon cycle 6, whereafter a stagnant value can be seen. In combination with the XRD patterns, the crystallization of the previously amorphous electrocatalyst appears to be the most plausible cause for the change of the CV-characteristics. The increase of the reduction peak area might further be connected to an increasing amount of higher oxidation states above the oxidation peak with cycling. As such, it is likely that Ni^{4+} [91, 96, 126] and Fe^{4+} [126, 142] form.

Secondly, EIS at 1379 mV (Fig. 7.12) was conducted before CV, after the third and after the 16th cycle. It clearly indicates a decrease of the charge transfer resistance. According to the results from DRT, two main processes exist. These are similar to another after the third and after the 16th cycle, but indicate a frequency shift from the state before CV. The fitting results, as displayed in Fig. 7.11E, confirm the decrease of the charge transfer resistance with cycling. In addition, the double layer capacitance decreases as well.

The rather controversial findings of an apparent performance loss (Fig. 7.11B) while the charge transfer resistance simultaneously decreases can be explained by the findings previously made with XRD (Fig. 7.11A). The electrocatalyst crystallizes, which is further supported by the decreasing double layer capacitance. Hence, the apparent performance loss results from a decreased ECSA through the crystallization process. To confirm this, Fig. 7.11C illustrates the currents of the CVs normalized to the double layer capacitance obtained from EIS. The first, second, and third cycle were normalized to the double layer capacitance before CV. Guided by the similar CVs, the crystallization most likely occurs during the backscan of the third cycle, which is not displayed due to the steady polarization steps for XRD. The fourth cycle was normalized to the capacitance after #1-3 and the remaining fifth and 16th cycle to the capacitance after #4-16. In fact, the so obtained comparison of intrinsic kinetics indicates that the crystallization results in an electrocatalyst with increased kinetics. The apparent performance loss is thereby a result of the decreased ECSA. Considering a value of $81 \mu\text{F}/\text{cm}^2$ for the ECSA of these types of electrocatalysts [107], the amorphous electrocatalyst has an ECSA of $127.7 \text{ cm}^2/\text{mg}$ and the crystallized electrocatalyst of $60.2 \text{ cm}^2/\text{mg}$.

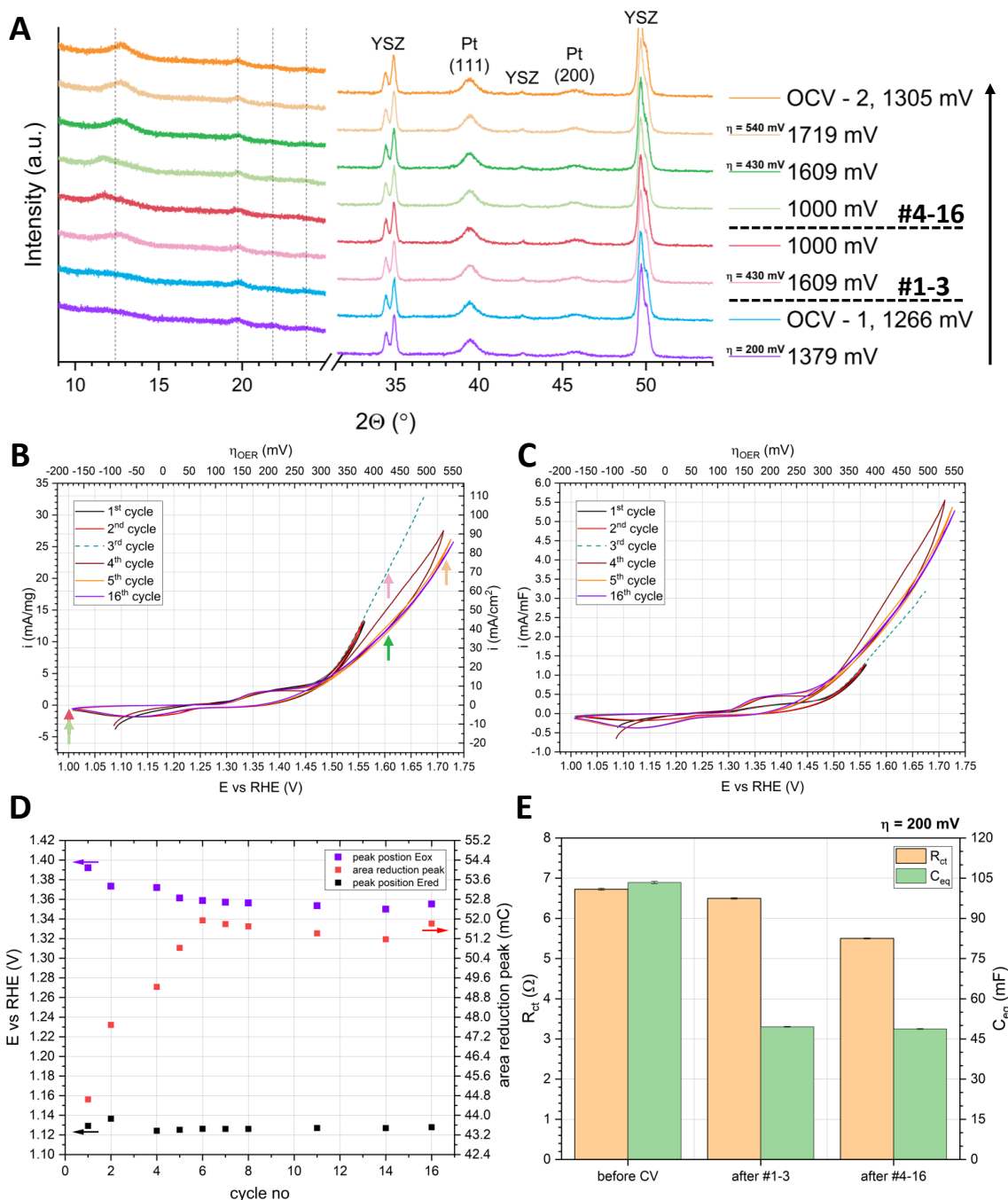


Fig. 7.11: Spectroelectrochemical XRD degradation studies at 85 °C in 30% KOH. **A:** GIXRD patterns at an incidence angle of 5° (see Fig. C.2 for full measurement). Dashed lines: original NiFe LDH electrocatalyst. **B, C:** Correlated CVs at 50 mV/s, 90% iR -corrected from EIS at 1000 mV, with respect to the electrocatalyst mass, geometric surface area, and in correlation to the double layer capacitance at $\eta = 200$ mV derived from EIS. **D:** Peak positions of the redox species and the area of the reduction peak from 1.0 – 1.33 V vs RHE. **E:** Results from EIS at $\eta = 200$ mV before and after CVs (see Fig. 7.12).

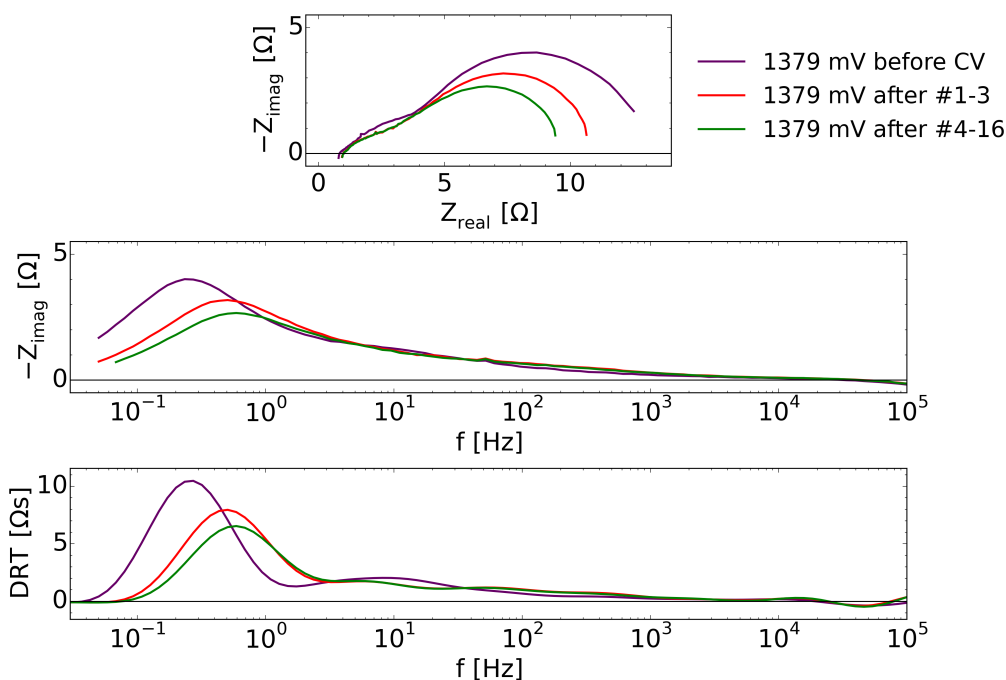


Fig. 7.12: EIS spectra at $\eta = 200$ mV between 100 kHz – 50 mHz of NiFe LDH during spectroelectrochemical XRD studies. Top: Nyquist plots. Middle: $-Z_{Im}$ over f plots. Bottom: DRT plots. Spectra before cyclic voltammograms, after cycle no 3 and after cycle no 16. Fitting results from Fig. 7.11E made with an LR(RQ)(R_{ct}Q) fitting (see Fig. C.3 for fitting). Measurements at 85 °C in 30 % KOH.

An *ex situ* post-mortem XRD measurement of the sample was heavily impacted by dried KOH and carbonate, making an analysis of the electrocatalyst practically impossible. An attempt to wash the electrocatalyst from the surface and to centrifuge it resulted in too little amounts of remaining electrocatalyst to conduct Powder X-ray diffraction. As a result, a comparison of *in situ* to *ex situ* measurements was not possible. Nevertheless, the crystallization of the electrocatalyst upon cycling is an important finding towards the understandings of this type of electrocatalyst under technological relevant conditions.

Based on these results, the crystallization appears to be a result of the upper potential limit. While potential-cycling to $\eta \leq 380$ mV implies that this process does not occur, cycling to $\eta \leq 500$ mV results in the electrocatalyst crystallization. However, since the characteristics of the CV are not divided into such a trend, it is reasonable to assume that this process is potential and time-dependent.

7.3.3 Conclusions on the stability and the active phase of a Ni₈Fe₂ LDH electrocatalysts

Hydrothermally prepared exfoliated Ni₈Fe₂ LDH as OER electrocatalyst demonstrates benchmarking kinetics with an activation energy of $E_A = 10.9 \pm 0.6$ kJ/mol. Furthermore, the electrocatalyst displays stable operation upon heating. Dynamic operation at 85 °C reveals that the as prepared amorphous electrocatalyst crystallizes, which results in a decrease of the electrochemical active surface area to roughly half of the amorphous state. As a result, the apparent performance is reduced, albeit the intrinsic electrocatalyst kinetics increase.

The findings of this work contradict the claims of an unstable electrocatalyst at these conditions concluded by Andronescu et al. [130]. The implications of polarization, dynamic operation and comparable electrolyte and temperature does not indicate a demolished electrocatalyst in this work. The differences between both studies lie in the measurement time of ≈ 8 h (at 85 °C) in this work and 60 h (at 80 °C) in the work from Andronescu et al., as well as the measurement conditions. This work studied spectroelectrochemical XRD under polarization, while Andronescu et al. compare *ex situ* XRD patterns of unpolarized electrocatalysts after aging. Hence, the differences may likely result from the different measurement approaches. Consequently, an at OCV aged electrocatalyst, similar to the work from Andronescu et al., should be studied with spectroelectrochemical XRD after aging to clarify the contradiction.

Furthermore, this work confirms the results of Chen et al. [114]. In both works, an exfoliated Ni₈Fe₂ LDH electrocatalyst was studied. Chen et al. compared a bulk to an exfoliated LDH for 20 h at 500 mA/cm² and 80 °C in 1 M KOH. Whilst the bulk sample deactivated continuously, the exfoliated LDH remained stable. The authors conclude that the interlayer-spacing of the LDH inhibits the successful diffusion of the proton-accepting hydroxide-anions between the LDH layers, which ultimately causes the dissolution of bulk LDH. ICP-MS supports their findings.

Acknowledging the different peak positions at different polarizations, it is possible to make schematic considerations about the active phase of the Ni₈Fe₂ LDH electrocatalyst from this work. Complementary to Chen et al. on the discussions of the interlayer-spacing, changes of the (003) plane of LDH were observed. Layered double hydroxides can be described with either a trigonal crystal system in the space group R3m [106] or with a non-

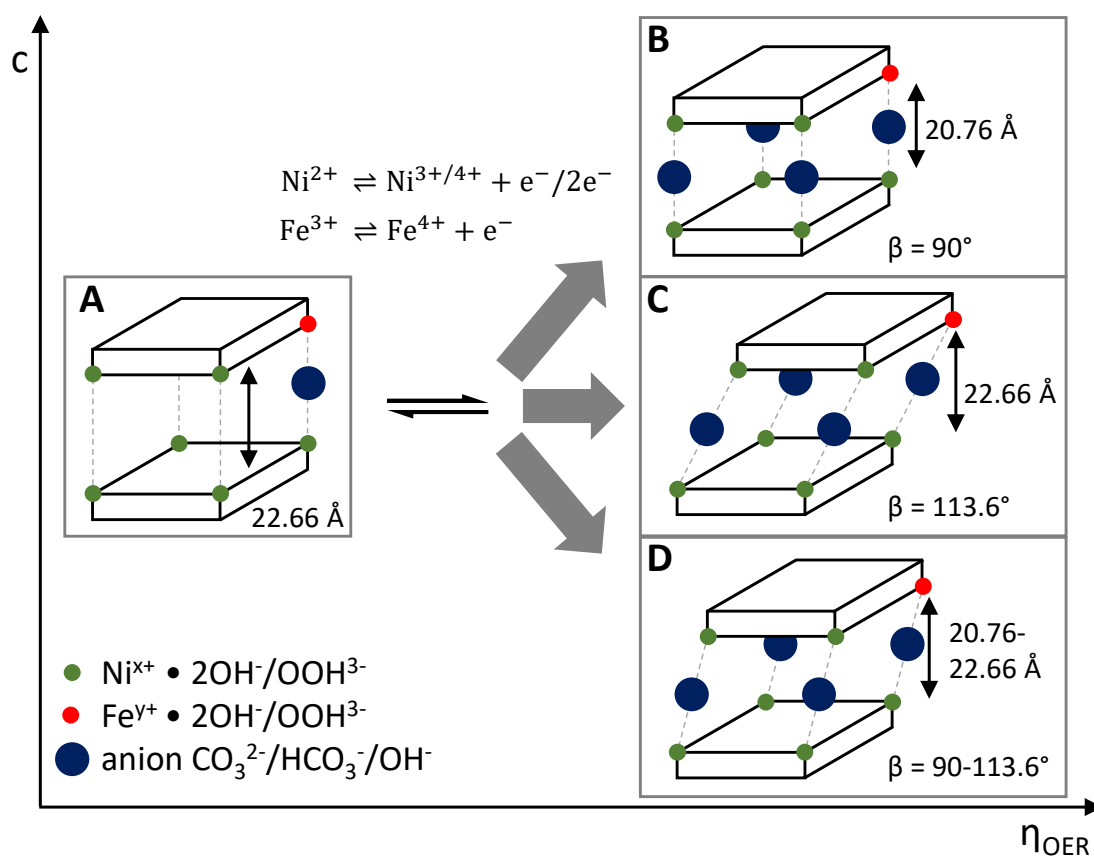
oclinic crystal system in the space group C2/m [105]. Consequently, the peak positions of the (003) planes under polarization can be calculated to the interlayer-spacing and the shear angle. These calculations were made based on Eq. (3.25) for the XRD patterns after the 16th cycle as shown in Tab. 7.2.

For a trigonal crystal system, the shear angle is 90°. Therefore, the change of the peak position of the (003) would result in a contraction of the interlayer-spacing from 22.66 Å to 20.76 Å. Schematically, this mechanism is illustrated in Fig. 7.13 (A to B). It is furthermore possible that the change of the peak position results solely from a shear, which is described by a monoclinic crystal system. In this case, the layers shear to an angle of $\beta = 113.6^\circ$ without a contraction of the interlayer-spacing (Fig. 7.13 A to C). Another possible change could be the combination of contraction and shear for the monoclinic LDH (Fig. 7.13 A to D). The exact mechanism remains elusive, as it would require e.g. calculations of a (hk0) plane, which was not possible due to the sample background. However, it is possible to make concluding considerations about the active phase under operation based on these findings.

The layers of the active LDH phase presumably contract and shear upon polarization. The increased positive charge due to the formation of Ni³⁺/Ni⁴⁺ and Fe³⁺/Fe⁴⁺ requires charge-balancing anions in the interlayer space. Due to the increased electrostatic forces, a layer contraction is conceivable. As this would limit the interlayer-diffusion of OH⁻ between the layers, a solely contracting LDH phase would experience a limiting current density. As this was not the case in this work, it is reasonable to consider a shear of the layers as well. A shear of the layers allows the outer-laying cations of LDH to be the active site with the hydroxide anions of the electrolyte serving as unhindered proton acceptors and charge-balancing anions. As a result of this mechanism, the exfoliated LDH electrocatalyst remains stable under technologically relevant operating conditions, ultimately crystallizing into an α/γ type with time and OER overpotential.

Tab. 7.2: XRD results of the (003) peak after cycles 4-16 from Fig. 7.11A calculated with a trigonal R3m and a monoclinic C2/m model.

E vs RHE [mV]	2 Θ (003) [$^{\circ}$]	spacing d [\AA]	trigonal R3m		monoclinic C2/m	
			c [\AA]	β [$^{\circ}$]	c [\AA]	β [$^{\circ}$]
1000	11.72	7.553	22.66	90.0	22.66	90.0
1609	12.61	7.021	21.06	90.0	22.66	111.6
1719	12.75	6.946	20.84	90.0	22.66	113.1
1305	12.79	6.920	20.76	90.0	22.66	113.6

**Fig. 7.13:** Conclusions on the active α/γ type phase of Ni_8Fe_2 LDH under OER conditions. **A:** uncharged α type LDH structure. **B:** Oxidized trigonal LDH structure, R3m space group, with resulting lattice contraction. **C:** Oxidized monoclinic LDH structure, C2/m space group, with resulting lattice shear. **D:** Combined lattice contraction and shear in oxidized monoclinic LDH, space group C2/m. All oxidized structures incorporate greater amounts of charge-balancing anions. For the purpose of facilitation, interlayer water is, despite its presence, omitted in the figure.

7.4 Discussions on the spectroelectrochemical studies

The spectroelectrochemical studies were supplementary in the understandings about the stability of NiMo and NiFe LDH electrocatalysts. However, these first-principle studies with the homebuilt setup FeliS faced some challenges, which need to be named to overcome them in further studies.

In spectroelectrochemical Raman, it is possible to distinguish that OH_{ad} desorption is not causing the first oxidation peak in the CVs on the molybdenum oxide supported Ni_4Mo electrocatalyst. A vibration at 795 cm^{-1} appeared, which indicates the formation of a layer and thus not a desorption process. However, the correlation to $\alpha\text{-Ni(OH)}_2$ was a complicated task. Firstly, the overlap of nickel hydroxide with monoclinic MoO_2 vibrations narrowed the possibility for distinguishable vibrations, where $\alpha/\beta\text{-Ni(OH)}_2$ were possible to be observed with vibrations at 795 cm^{-1} and at 850 cm^{-1} , respectively, where the absence of the latter represents the absence of $\beta\text{-Ni(OH)}_2$. Nevertheless, an overlap of vibrations might cause suppression of e.g. $\beta\text{-Ni(OH)}_2$ vibrations. Hence, it cannot be guaranteed that this phase does not form. Secondly, the use of a silver-coated substrate gave surface enhancing properties. Accordingly, a different measurement outcome to conventional Raman under SERS conditions is conceivable. Therefore, the Raman studies cannot be determined as encompassing without further tests, especially about the origin of the peak-shifts between conventional Raman and SERS. This includes improvements in the SERS substrate, as the obtained up to 10^1 enhancement underperforms reported 10^2 [209] or 10^5 [210] enhancements reported elsewhere, which additionally raises the question if a true SERS effect was achieved. Furthermore, the strong deviations of the Raman spectra between the dry and the wet state of the electrocatalyst should be addressed in further work.

In spectroelectrochemical XRD, stability aspects and mechanisms of the active phase of Ni_8Fe_2 LDH were possible to deduce. Nevertheless, the small XRD measurement intensities as a result of the small amount of nano-sized electrocatalyst resulted in an unfavorable signal-to-noise ratio. An increased amount of electrocatalyst was purposefully avoided due to the possible bulk-induced degradation and the low conductivity of the electrocatalyst. A stacking of electrocatalyst would cause unpolarized electrocatalyst in distance to the conducting substrate. Thus, a better signal-to-noise ratio can be achieved through optimized substrates such as, for instance, glassy carbon.

For both spectroelectrochemical studies, a time-dependence was observed. During HER underpotential conditions, the molybdenum oxide supported Ni₄Mo electrocatalyst displays a time-depending formation of NiO, and presumably of α -Ni(OH)₂ as well. The crystallization of Ni₈Fe₂ LDH was detectable without time-resolved measurements. However, the exact potential and time relations are to this date not entirely conclusive. Furthermore, a long-term aged electrocatalyst as reported elsewhere [130] was not investigated. Hence, more studies with time-resolved spectroelectrochemical measurements, e.g. with smaller increments of increasing potentials or timely followed CVs, should be added in further tests.

In conclusion, the spectroelectrochemical measurements were successful first-principle studies. In further studies, improvements to the sample preparation and to the substrates are needed. With improved samples, and a possible combination to online ICP measurements in a flowcell approach for an additional level of complementary detail, and more time-resolved measurements, the open points of spectroelectrochemical studies with FeliS can perspectivevely be diminished to a negligible level.

Chapter 8

General Conclusions and Outlook

The alkaline water electrolysis is the most promising technology for the large scale production of green hydrogen because it has no limitations on scale due to scarce elements and because it is already a quite mature technology. For this purpose, the voltage losses through the separator and the electrocatalysts need to be minimized to reach competitive performance at low investment cost and high durability. In this Ph.D. project, high performing electrocatalysts were characterized to address the durability requirement for the industrial application. In light of the literature, which predominantly does not represent industrial conditions, bridging studies between fundamental research and the technical application were conducted.

For NiMo HER electrocatalysts, three main observations can be summarized. Firstly, *in situ* assessments of the electrochemical active surface area are possible via electrochemical impedance spectroscopy. In nickel electrocatalysts, it was shown that the formation of a monolayer of α -Ni(OH)₂ and overpotential impedance modeling of the double layer capacitance deliver similar surface area estimations if a pseudocapacitive contribution is considered. In a conclusion by analogy, the *in situ* method was found to be valid for NiMo electrocatalysts as well, as the double layer capacitance measurements from non-faradaic cyclic voltammetry and overpotential impedance matched. Hence, the *in situ* impedance method was found to be a valuable technique, which does not cause possible degradation from potential cycling or electrolyte pollution through the addition of redox active chemicals. Furthermore, the *in situ* method allows to estimate the electrochemical surface area during operation. On the other hand, a challenge remains in finding the precise value for the correlation between the double layer capacitance and the surface area.

Secondly, Ni_xMo_y , oxide supported Ni_xMo_y , partially oxidized Ni, and surface specific Ni electrocatalysts displayed a similar scaling of the overpotential at 10 mA/cm^2 with surface roughness. Bulk Ni, in contrast, showed a less pronounced reduction of the overpotential at 10 mA/cm^2 with surface roughness. High performance of NiMo electrocatalysts in the literature appears to predominantly result from high electrochemical active surface areas. However, it could be hypothesized that Ni is the active site in NiMo electrocatalysts following this comparison. The active Ni site seems to have a favorable chemical state in these types of electrocatalysts. Hence, future studies need to address the chemical state of Ni in NiMo and Ni electrocatalysts, as this hypothesis is based on a comparably rough categorization of electrocatalysts. Furthermore, additional studies should obtain data through standardized procedures to reduce the scattering of the data. One suggested standardized measurement protocol could be the galvanostatic measurement of the overpotential at 10 mA/cm^2 for 5 min and the assessment of the electrochemical active surface area through overpotential impedance and non-faradaic cyclic voltammetry.

Thirdly, molybdenum oxide supported Ni_4Mo did not show degradation for potentials $< 0.1 \text{ V vs RHE}$. A long-term deactivation process, which is reported in the literature to occur on Ni electrocatalysts through the formation of hydrides, was absent in the studied NiMo electrocatalyst. On the other hand, HER underpotential conditions caused degradation of the NiMo electrocatalyst in this work. The combination of electrochemical tests and spectro-electrochemical Raman showed that partial degradation occurred at $0.1\text{-}0.55 \text{ V vs RHE}$. At these potentials, the reversible formation of $\alpha\text{-Ni(OH)}_2$ was accompanied by the formation of irreducible NiO. Both further indicate that Ni is the active site in this electrocatalyst. The irreducibility of NiO is yet confirmed without additional studies over longer times, but short time measurements at -0.1 V vs RHE were not found to reduce it. Furthermore, the presence of immune NiO coincides with the observed performance loss, which makes its formation a likely degradation nominator in the studied NiMo electrocatalyst. At potentials $> 0.55 \text{ V vs RHE}$, the MoO_2 supporting structure oxidized to permolybdates. Although it could redeposit at 0 V vs RHE , the active sites did not reform. This is attributed to the lack of redepositing Ni_4Mo , which was 83.6 w% of the pristine electrocatalyst according to cyclic voltammetry. This further displays Ni as the active site, which is also underlined by surface area corrected iV -curves.

The observed destruction of the NiMo electrocatalyst in the HER underpotential region agrees with the cell testing, where intermittent operation caused the degradation of the electrocatalyst at a potential of 0.95 V vs RHE. Thus, the molybdenum oxide supported NiMo electrocatalyst is not stable enough to withstand intermittent operation without the addition of corrosion inhibitors as e.g. a sacrificial anode. Although the electrocatalyst could be protected by a small current or stack voltage during shut-downs, power failures or forms of emergency shut-downs are likely to occur over the course of several decades of operation. Therefore, further improvements are needed before implementing the molybdenum oxide supported NiMo electrocatalyst in a technical electrolyzer. Due to the observations similar to those in the literature, it is considerable that the observations on the active Ni site and the stability of NiMo electrocatalysts in this work are general for NiMo electrocatalysts. However, only further studies including alloyed NiMo electrocatalysts, where no supporting oxide structure exists, can confirm this assumption.

For a Ni₈Fe₂ LDH electrocatalysts, two main conclusions can be drawn. Firstly, bulk Ni₈Fe₂ LDH showed vulnerability to the entire technical operation window. Although severe degradation, also during intermittent operation at OCV, was not observed, an *in situ* restructuring was concluded. The Ni₈Fe₂ LDH electrocatalyst is stable after an initial conditioning step during long-term operation under constant polarization. However, the coagulation of the electrocatalyst in combination with the bulk depletion of iron challenges if a bulk NiFe LDH electrocatalyst is durable under these conditions. EDS on the tested electrode and counter electrode confirmed the depletion of iron from the bulk of the anode, while XPS displayed that iron is preserved in the surface. Hence, further studies, including e.g. online ICP measurements, have to address the mechanism of iron depletion.

Secondly, spectroelectrochemical XRD on exfoliated Ni₈Fe₂ LDH revealed that the previously observed degradation is likely an effect of the bulk electrocatalyst. The exfoliated Ni₈Fe₂ LDH was not found to degrade. In fact, the exfoliated Ni₈Fe₂ LDH displayed a benchmarking activation energy of $E_A = 10.9 \pm 0.6$ kJ/mol and did not transform into brucite β -Ni(OH)₂, likewise not at OCV. However, the OCV in the spectroelectrochemical XRD study was different to the electrochemical test in the flowcell, as it was not immersed into circulated electrolyte saturated with oxygen. Hence, no reversing reaction took place and thus this observation may differ in circulated oxygen saturated electrolyte over prolonged

times. Potential cycling at 85 °C in 30 w% KOH revealed that the exfoliated Ni₈Fe₂ LDH crystallizes with potential and time into an α/γ type. The apparent deactivation could be correlated to the decreased electrochemical surface area as a result of the crystallization process. The intrinsic kinetics, on the contrary, increased. This displays that the exfoliated Ni₈Fe₂ LDH electrocatalyst is stable at these conditions for at least the measured 8 h.

The observed degradation of bulk Ni₈Fe₂ LDH and the crystallization of exfoliated Ni₈Fe₂ LDH can be taken as baseline to describe the observed conditioning step of bulk Ni₈Fe₂ LDH. Due to the low conductivity of NiFe LDH, a delamination of unpolarized outer layers and coagulation of conductive inner substrate-near layers could cause a peeling effect of the bulk Ni₈Fe₂ LDH. Eventually, the bulk Ni₈Fe₂ LDH would structurally transform more closely to a surface specific LDH and thus be identical to the exfoliated Ni₈Fe₂ LDH. This is assisted by the presence of iron in the surface of the long-term tested bulk Ni₈Fe₂ LDH. The amount of 14.4 % in the tested compared to 9.9 % in the pristine sample as evaluated by XPS could potentially indicate that iron in the surface and in the electrolyte are in a dynamic equilibrium, whereas the bulk of the electrocatalyst is likely iron depleted following EDS. Although further evidence to support this explanation would be required, it is reasonable to conclude that surface specific NiFe LDH electrocatalysts are superior to bulk NiFe LDH electrocatalysts in terms of stability under technologically relevant conditions.

Overall, the bimetallic bulk materials appear to experience degradation. Thus, a solution for both could be to produce high surface area electrodes with surface specific electrocatalysts, such as alloyed core shell NiMo and exfoliated NiFe LDH electrocatalysts. These considerations are further supported by recent literature. Although this work observed some apparent degradation, it shows promising results towards electrocatalyst stability and guides towards improvements to circumvent degradation.

To conclude, the Ph.D. work presents studies that increase the understandings of high performing NiMo and NiFe LDH electrocatalysts for the technical application. A new tool to shine light on questions about the reaction and degradation mechanisms of electrocatalysts was developed with the spectroelectrochemical cell FeliS, which gave more detailed insights into degradation mechanisms and will also serve in future studies.

Bibliography

- [1] European Commission, A hydrogen strategy for a climate-neutral Europe, European Commission, no. COM(2020) 301 final, 2020.
- [2] G. Kakoulaki et al., Green hydrogen in Europe – A regional assessment: Substituting existing production with electrolysis powered by renewables, *Energy Conversion and Management*, vol. 228, no. July 2020, 2021.
- [3] Z. Abdin et al., Hydrogen as an energy vector, *Renewable and Sustainable Energy Reviews*, vol. 120, no. December 2019, 2020.
- [4] D. M. Santos, C. A. Sequeira, and J. L. Figueiredo, Hydrogen Production By Alkaline Water Electrolysis, *Quim. Nova*, vol. 36, no. 8, pp. 1176–1193, 2013.
- [5] IRENA - International Renewable Energy Agency: Green Hydrogen Cost Reduction: Scaling up Electrolyzers to Meet the 1.5°C Climate Goal, Abu Dhabi, 2020.
- [6] P. C. Vesborg and T. F. Jaramillo, Addressing the terawatt challenge: scalability in the supply of chemical elements for renewable energy, *RSC Advances*, vol. 2, no. 21, pp. 7933–7947, 2012.
- [7] Z. Chehade et al., Review and analysis of demonstration projects on power-to-X pathways in the world, *International Journal of Hydrogen Energy*, vol. 44, no. 51, pp. 27 637–27 655, 2019.
- [8] C. C. L. McCrory et al., Benchmarking hydrogen evolving reaction and oxygen evolving reaction electrocatalysts for solar water splitting devices. *Journal of the American Chemical Society*, vol. 137, no. 13, pp. 4347–57, 2015.
- [9] M. Gong et al., A mini review on nickel-based electrocatalysts for alkaline hydrogen evolution reaction, *Nano Research*, vol. 9, no. 1, pp. 28–46, 2016.
- [10] S. Anantharaj, K. Karthick, and S. Kundu, Evolution of layered double hydroxides (LDH) as high performance water oxidation electrocatalysts: A review with insights on structure, activity and mechanism, *Materials Today Energy*, vol. 6, pp. 1–26, 2017.
- [11] A. J. Bard and L. R. Faulkner: *Electrochemical Methods*, Second Edi, D. Harris et al., Eds. New York, Chichester, Weinheim, Brisbane, Singapore, Toronto: John Wiley & Sons, Inc., 2001.
- [12] J. Hnát, M. Paidar, and K. Bouzek, Hydrogen production by electrolysis, *Current Trends and Future Developments on (Bio-) Membranes*, no. V, pp. 91–117, 2020.
- [13] K. Zeng and D. Zhang, Recent progress in alkaline water electrolysis for hydrogen production and applications, *Progress in Energy and Combustion Science*, vol. 36, no. 3, pp. 307–326, 2010.

- [14] H. Bode, K. Dehmelt, and J. Witte, Zur Kenntnis der Nickelhydroxidelektrode-I. Über das Nickel (II)-Hydroxidhydrat, *Electrochimica Acta*, vol. 11, pp. 1079–1087, 1966.
- [15] M. Grdeń, M. Alsabet, and G. Jerkiewicz, Surface science and electrochemical analysis of nickel foams, *ACS Applied Materials and Interfaces*, vol. 4, no. 6, pp. 3012–3021, 2012.
- [16] D. S. Hall, C. Bock, and B. R. Macdougall, Surface Layers in Alkaline Media: Nickel Hydrides on Metallic Nickel Electrodes, *ECS Transactions*, vol. 50, no. 31, pp. 165–179, 2013.
- [17] D. S. Hall et al., Nickel hydroxides and related materials : a review of their structures, synthesis and properties, *Proc. R. Soc. A*, vol. 471, 2014.
- [18] M. Alsabet, M. Grden, and G. Jerkiewicz, Electrochemical Growth of Surface Oxides on Nickel. Part 1: Formation of α -(NiOH)₂ in Relation to the Polarization Potential, Polarization Time, and Temperature, *Electrocatalysis*, vol. 2, pp. 317–330, 2011.
- [19] M. Alsabet, M. Grden, and G. Jerkiewicz, Electrochemical Growth of Surface Oxides on Nickel. Part 2: Formation of β -Ni(OH)₂ and NiO in Relation to the Polarization Potential, Polarization Time, and Temperature, *Electrocatalysis*, vol. 5, pp. 136–147, 2014.
- [20] M. Alsabet, M. Grdeń, and G. Jerkiewicz, Electrochemical Growth of Surface Oxides on Nickel. Part 3: Formation of β -NiOOH in Relation to the Polarization Potential, Polarization Time, and Temperature, *Electrocatalysis*, vol. 6, pp. 60–71, 2015.
- [21] S. Klaus et al., Effects of Fe electrolyte impurities on Ni(OH)₂/NiOOH structure and oxygen evolution activity, *Journal of Physical Chemistry C*, vol. 119, no. 13, pp. 7243–7254, 2015.
- [22] M. Ďurovič, J. Hnát, and K. Bouzek, Electrocatalysts for the hydrogen evolution reaction in alkaline and neutral media. A comparative review, *Journal of Power Sources*, vol. 493, no. December 2020, 2021.
- [23] N. Mahmood et al., Electrocatalysts for Hydrogen Evolution in Alkaline Electrolytes: Mechanisms, Challenges, and Prospective Solutions, *Advanced Science*, vol. 5, no. 2, 2018.
- [24] W. Sheng et al., Correlating the hydrogen evolution reaction activity in alkaline electrolytes with the hydrogen binding energy on monometallic surfaces, *Energy and Environmental Science*, vol. 6, no. 6, pp. 1509–1512, 2013.
- [25] T. Shinagawa, A. T. Garcia-Esparza, and K. Takanabe, Insight on Tafel slopes from a microkinetic analysis of aqueous electrocatalysis for energy conversion, *Scientific Reports*, vol. 5, no. September, pp. 1–21, 2015.
- [26] D. Strmcnik et al., Improving the hydrogen oxidation reaction rate by promotion of hydroxyl adsorption. *Nature chemistry*, vol. 5, no. 4, pp. 300–6, 2013.
- [27] P. Farinazzo Bergamo Dias Martins et al., Hydrogen evolution reaction on copper: Promoting water dissociation by tuning the surface oxophilicity, *Electrochemistry Communications*, vol. 100, no. November 2018, pp. 30–33, 2019.
- [28] F. Dionigi and P. Strasser, NiFe-Based (Oxy)hydroxide Catalysts for Oxygen Evolution Reaction in Non-Acidic Electrolytes, *Advanced Energy Materials*, vol. 6, no. 23, 2016.

-
- [29] H. Ali-Löytty et al., Ambient-Pressure XPS Study of a Ni-Fe Electrocatalyst for the Oxygen Evolution Reaction, *Journal of Physical Chemistry C*, vol. 120, no. 4, pp. 2247–2253, 2016.
- [30] R. Palaniappan and G. G. Botte, Effect of ammonia on Pt, Ru, Rh, and Ni cathodes during the alkaline hydrogen evolution reaction, *Journal of Physical Chemistry C*, vol. 117, no. 34, pp. 17 429–17 441, 2013.
- [31] A. J. Appleby, G. Crepy, and J. Jacquelin, High efficiency water electrolysis in alkaline solution, *International Journal of Hydrogen Energy*, vol. 3, no. 1, pp. 21–37, 1978.
- [32] J. O. Bockris and E. C. Potter, The mechanism of hydrogen evolution at nickel cathodes in aqueous solutions, *The Journal of Chemical Physics*, vol. 20, no. 4, pp. 614–628, 1952.
- [33] E. A. Franceschini, G. I. Lacconi, and H. R. Corti, Kinetics of the hydrogen evolution on nickel in alkaline solution: New insight from rotating disk electrode and impedance spectroscopy analysis, *Electrochimica Acta*, vol. 159, pp. 210–218, 2015.
- [34] A. Gomez Vidales and S. Omanovic, Evaluation of nickel-molybdenum-oxides as cathodes for hydrogen evolution by water electrolysis in acidic, alkaline, and neutral media, *Electrochimica Acta*, vol. 262, pp. 115–123, 2018.
- [35] C. González-Buch et al., Study of the catalytic activity of 3D macroporous Ni and NiMo cathodes for hydrogen production by alkaline water electrolysis, *Journal of Applied Electrochemistry*, vol. 46, no. 7, pp. 791–803, 2016.
- [36] I. Herraiz-Cardona et al., Assessment of the roughness factor effect and the intrinsic catalytic activity for hydrogen evolution reaction on Ni-based electrodeposits, *International Journal of Hydrogen Energy*, vol. 36, no. 16, pp. 9428–9438, 2011.
- [37] J.-Y. Huot, Hydrogen Evolution and Interface Phenomena on a Nickel Cathode in 30 w/o KOH, *Journal of The Electrochemical Society*, vol. 136, no. 7, p. 1933, 2006.
- [38] J. M. Jakšić, M. V. Vojnović, and N. V. Krstajić, Kinetic analysis of hydrogen evolution at Ni-Mo alloy electrodes, *Electrochimica Acta*, vol. 45, no. 25-26, pp. 4151–4158, 2000.
- [39] M. F. Kibria, M. S. Mridha, and A. H. Khan, Electrochemical Studies of a Nickel Electrode for the Hydrogen Evolution Reaction, *International Journal of Hydrogen Energy*, vol. 20, no. 6, pp. 435–440, 1995.
- [40] G. Kreysa, B. Håkansson, and P. Ekdunge, Kinetic and Thermodynamic Analysis of Hydrogen Evolution at Nickel Electrodes, *Electrochimica Acta*, vol. 33, no. 10, pp. 1351–1357, 1988.
- [41] N. Krstajić et al., On the kinetics of the hydrogen evolution reaction on nickel in alkaline solution: Part II. Effect of temperature, *Journal of Electroanalytical Chemistry*, vol. 512, no. 1–2, pp. 27–35, 2001.
- [42] Z. Liang, H. S. Ahn, and A. J. Bard, A Study of the Mechanism of the Hydrogen Evolution Reaction on Nickel by Surface Interrogation Scanning Electrochemical Microscopy, *Journal of the American Chemical Society*, vol. 139, no. 13, pp. 4854–4858, 2017.
- [43] S. A. Machado and L. A. Avaca, The hydrogen evolution reaction on nickel surfaces stabilized by H-absorption, *Electrochimica Acta*, vol. 39, no. 10, pp. 1385–1391, 1994.

- [44] A. C. Makrides, Hydrogen Overpotential on Nickel in Alkaline Solution, *Journal of The Electrochemical Society*, vol. 109, no. 10, p. 977, 2007.
- [45] A. G. Oshchepkov et al., On the effect of temperature and surface oxidation on the kinetics of hydrogen electrode reactions on nickel in alkaline media, *Electrochimica Acta*, vol. 269, pp. 111–118, 2018.
- [46] M. Grdeń and G. Jerkiewicz, Influence of Surface Treatment on the Kinetics of the Hydrogen Evolution Reaction on Bulk and Porous Nickel Materials, *Electrocatalysis*, vol. 10, no. 2, pp. 173–183, 2019.
- [47] A. G. Oshchepkov, A. Bonnefont, and E. R. Savinova, On the Influence of the Extent of Oxidation on the Kinetics of the Hydrogen Electrode Reactions on Polycrystalline Nickel, *Electrocatalysis*, vol. 11, no. 2, pp. 133–142, 2020.
- [48] A. G. Oshchepkov et al., Exploring the Influence of the Nickel Oxide Species on the Kinetics of Hydrogen Electrode Reactions in Alkaline Media, *Topics in Catalysis*, vol. 59, no. 15-16, pp. 1319–1331, 2016.
- [49] S. L. Medway et al., In situ studies of the oxidation of nickel electrodes in alkaline solution, *Journal of Electroanalytical Chemistry*, vol. 587, no. 1, pp. 172–181, 2006.
- [50] M. Grdeń, K. Klimek, and A. Czerwiński, A quartz crystal microbalance study on a metallic nickel electrode, *Journal of Solid State Electrochemistry*, vol. 8, no. 6, pp. 390–397, 2004.
- [51] Z. Liang, H. S. Ahn, and A. J. Bard, Supporting Information for: A Study of the Mechanism of the Hydrogen Evolution Reaction on Nickel by Surface Interrogation Scanning Electrochemical Microscopy, *Journal of the American Chemical Society*, vol. 139, no. 13, pp. 4854–4858, 2017.
- [52] W. Visscher and E. Barendrecht, Absorption of hydrogen in reduced nickel oxide, *Journal of Applied Electrochemistry*, vol. 10, no. 2, pp. 269–274, 1980.
- [53] A. Pătru et al., Size and strain dependent activity of Ni nano and micro particles for hydrogen evolution reaction, *International Journal of Hydrogen Energy*, vol. 38, no. 27, pp. 11 695–11 708, 2013.
- [54] N. Takano and S. Kaida, Crack Initiation by Cathodic Hydrogen Charging in Nickel Single Crystal, *ISIJ International*, vol. 52, no. 2, pp. 263–266, 2012.
- [55] D. M. Soares et al., Deactivation Mechanism of Nickel Cathodes in Alkaline Media, *Science*, vol. 19, no. 7, 1994.
- [56] D. M. Soares, Hydride Effect on the Kinetics of the Hydrogen Evolution Reaction on Nickel Cathodes in Alkaline Media, *Journal of The Electrochemical Society*, vol. 139, no. 1, p. 98, 2006.
- [57] D. S. Hall, C. Bock, and B. R. MacDougall, The Electrochemistry of Metallic Nickel: Oxides, Hydroxides, Hydrides and Alkaline Hydrogen Evolution, *Journal of The Electrochemical Society*, vol. 160, no. 3, F235–F243, 2013.
- [58] B. Baranowski, Electrochemical formation of nickel hydride in alkaline solutions, *Journal of Electroanalytical Chemistry*, vol. 472, no. 2, pp. 182–184, 1999.
- [59] D. W. Kirk and S. J. Thorpe, Nickel Cathode Passivation in Alkaline Water Electrolysis, *ECS Transactions*, vol. 2, no. 14, pp. 71–76, 2007.

- [60] R. M. Abouatallah, D. W. Kirk, and J. W. Graydon, Long-term electrolytic hydrogen permeation in nickel and the effect of vanadium species addition, *Electrochimica Acta*, vol. 47, no. 15, pp. 2483–2494, 2002.
- [61] R. Juškėnas, R. Giraitis, and V. Pakštas, X-ray diffraction investigation of nickel hydride formation in alkaline solution, *Chemija*, vol. T. 13, no. 1, 2002.
- [62] A. Y. Faid et al., Highly active nickel-based catalyst for hydrogen evolution in anion exchange membrane electrolysis, *Catalysts*, vol. 8, no. 12, 2018.
- [63] B. E. Conway and L. Bai, Determination of the adsorption behaviour of 'overpotential-deposited' hydrogen-atom species in the cathodic hydrogen-evolution reaction by analysis of potential-relaxation transients, *Journal of the Chemical Society, Faraday Transactions 1: Physical Chemistry in Condensed Phases*, vol. 81, no. 8, pp. 1841–1862, 1985.
- [64] J. Zhang et al., Efficient hydrogen production on MoNi₄ electrocatalysts with fast water dissociation kinetics, *Nature Communications*, vol. 8, no. May, pp. 1–8, 2017.
- [65] J. R. McKone et al., Ni-Mo nanopowders for efficient electrochemical hydrogen evolution, *ACS Catalysis*, vol. 3, no. 2, pp. 166–169, 2013.
- [66] S. M. Fernández-Valverde et al., Electrochemical behavior of Ni-Mo electrocatalyst for water electrolysis, *Journal of the Mexican Chemical Society*, vol. 54, no. 3, pp. 169–174, 2010.
- [67] J. Kubisztal, A. Budniok, and A. Lasia, Study of the hydrogen evolution reaction on nickel-based composite coatings containing molybdenum powder, *International Journal of Hydrogen Energy*, vol. 32, no. 9, pp. 1211–1218, 2007.
- [68] Y. Wang et al., A 3D Nanoporous Ni-Mo Electrocatalyst with Negligible Overpotential for Alkaline Hydrogen Evolution, *ChemElectroChem*, vol. 1, no. 7, pp. 1138–1144, 2014.
- [69] J. Wijten et al., Electrolyte Effects on the Stability of Ni-Mo Cathodes for the Hydrogen Evolution Reaction, *ChemSusChem*, cssc.201900617, 2019.
- [70] N. Danilovic et al., Enhancing the alkaline hydrogen evolution reaction activity through the bifunctionality of Ni(OH)₂/metal catalysts, *Angewandte Chemie - International Edition*, vol. 51, no. 50, pp. 12 495–12 498, 2012.
- [71] G. X. Cao et al., Investigation of the correlation between the phase structure and activity of Ni-Mo-O derived electrocatalysts for the hydrogen evolution reaction, *Journal of Materials Chemistry A*, vol. 7, no. 17, pp. 10 338–10 345, 2019.
- [72] M. Schalenbach, O. Kasian, and K. J. Mayrhofer, An alkaline water electrolyzer with nickel electrodes enables efficient high current density operation, *International Journal of Hydrogen Energy*, vol. 43, no. 27, pp. 11 932–11 938, 2018.
- [73] M. Schalenbach et al., Nickel-molybdenum alloy catalysts for the hydrogen evolution reaction: Activity and stability revised, *Electrochimica Acta*, vol. 259, pp. 1154–1161, 2018.
- [74] X. Liu et al., Upraising the O 2p Orbital by Integrating Ni with MoO₂ for Accelerating Hydrogen Evolution Kinetics, *ACS Catalysis*, vol. 9, no. 3, pp. 2275–2285, 2019.
- [75] S. Kabir et al., Platinum group metal-free NiMo hydrogen oxidation catalysts: High performance and durability in alkaline exchange membrane fuel cells, *Journal of Materials Chemistry A*, vol. 5, no. 46, pp. 24 433–24 443, 2017.

- [76] M. Pourbaix: Atlas of Electrochemical Equilibria in Aqueous Solutions, 2nd ed., J. A. Franklin, Ed. Houston, Texas, USA: National Association of Corrosion Engineers, 1974.
- [77] P. M. Csernia et al., Electrochemical Hydrogen Evolution at Ordered Mo₇Ni₇, ACS Catalysis, vol. 7, pp. 3375–3383, 2017.
- [78] E. S. Davydova et al., Stability Limits of Ni-Based Hydrogen Oxidation Electrocatalysts for Anion Exchange Membrane Fuel Cells, ACS Catalysis, vol. 9, pp. 6837–6845, 2019.
- [79] Y. Yu et al., First-principles study of Mo segregation in MoNi(111): Effects of chemisorbed atomic oxygen, Materials, vol. 9, no. 1, pp. 21–23, 2016.
- [80] M. P. Marceta Kaninski et al., Energy consumption and stability of the Ni-Mo electrodes for the alkaline hydrogen production at industrial conditions, International Journal of Hydrogen Energy, vol. 36, no. 15, pp. 8864–8868, 2011.
- [81] D. E. Brown et al., Preparation and characterization of low overvoltage transition metal alloy electrocatalysts for hydrogen evolution in alkaline solutions, Electrochimica Acta, vol. 29, no. 11, pp. 1551–1556, 1984.
- [82] J. A. Bau et al., On the reconstruction of NiMo electrocatalysts by operando spectroscopy, Journal of Materials Chemistry A, pp. 15 031–15 035, 2019.
- [83] J. O. Bockris, Kinetics of activation controlled consecutive electrochemical reactions: Anodic evolution of oxygen, The Journal of Chemical Physics, vol. 24, no. 4, pp. 817–827, 1956.
- [84] E. Fabbri et al., Developments and perspectives of oxide-based catalysts for the oxygen evolution reaction, Catalysis Science and Technology, vol. 4, no. 11, pp. 3800–3821, 2014.
- [85] F. Song et al., An Unconventional Iron Nickel Catalyst for the Oxygen Evolution Reaction, ACS Central Science, vol. 5, no. 3, pp. 558–568, 2019.
- [86] I. C. Man et al., Universality in Oxygen Evolution Electrocatalysis on Oxide Surfaces, ChemCatChem, vol. 3, no. 7, pp. 1159–1165, 2011.
- [87] M. E. Lyons and M. P. Brandon, A comparative study of the oxygen evolution reaction on oxidised nickel, cobalt and iron electrodes in base, Journal of Electroanalytical Chemistry, vol. 641, no. 1-2, pp. 119–130, 2010.
- [88] E. Fabbri and T. J. Schmidt, Oxygen Evolution Reaction - The Enigma in Water Electrolysis, ACS Catalysis, vol. 8, no. 10, pp. 9765–9774, 2018.
- [89] Z. W. She et al., Combining theory and experiment in electrocatalysis: Insights into materials design, Science, vol. 355, no. 6321, 2017.
- [90] D. Friebel et al., Identification of highly active Fe sites in (Ni,Fe)OOH for electrocatalytic water splitting. Journal of the American Chemical Society, vol. 137, no. 3, pp. 1305–13, 2015.
- [91] P. W. T. Lu and S. Srinivasan, Electrochemical-Ellipsometric Studies of Oxide Film Formed on Nickel during Oxygen Evolution, Journal of The Electrochemical Society, vol. 125, no. 9, p. 1416, 1978.
- [92] T. Rauscher et al., The effect of Fe as constituent in Ni-base alloys on the oxygen evolution reaction in alkaline solutions at high current densities, International Journal of Hydrogen Energy, vol. 44, no. 13, pp. 6392–6402, 2019.

-
- [93] D. A. Corrigan, The Catalysis of the Oxygen Evolution Reaction by Iron Impurities in Thin Film Nickel Oxide Electrodes, *Journal of The Electrochemical Society*, vol. 134, no. 2, p. 377, 1987.
- [94] J. Kang et al., Study on the anodic reaction of Ni in an alkaline solution by transient pH detection based on SECM, *Surface and Interface Analysis*, vol. 39, pp. 877–884, 2007.
- [95] M. E. G. Lyons and M. P. Brandon, The Oxygen Evolution Reaction on Passive Oxide Covered Transition Metal Electrodes in Aqueous Alkaline Solution Part I - Nickel, *International Journal of Electrochemical Science*, vol. 3, pp. 1425–1462, 2008.
- [96] S. R. Mellsop et al., Structure and transformation of oxy-hydroxide films on Ni anodes below and above the OER potential in alkaline electrolytes, *Electrochimica Acta*, vol. 168, pp. 356–364, 2015.
- [97] R. D. Smith et al., On How Experimental Conditions Affect the Electrochemical Response of Disordered Nickel Oxyhydroxide Films, *Chemistry of Materials*, vol. 28, no. 16, pp. 5635–5642, 2016.
- [98] J. Mohammed-Ibrahim and S. Xiaoming, Recent progress on earth abundant electrocatalysts for oxygen evolution reaction (OER) in alkaline medium to achieve efficient water splitting – A review, *Journal of Energy Chemistry*, vol. 400, no. February, pp. 111–160, 2019.
- [99] M. Görlin et al., Oxygen evolution reaction dynamics, faradaic charge efficiency, and the active metal redox states of Ni-Fe oxide water splitting electrocatalysts, *Journal of the American Chemical Society*, vol. 138, no. 17, pp. 5603–5614, 2016.
- [100] E. Fabbri et al., Dynamic surface self-reconstruction is the key of highly active perovskite nano-electrocatalysts for water splitting, *Nature Materials*, vol. 16, no. 9, pp. 925–931, 2017.
- [101] S. Jung et al., Benchmarking nanoparticulate metal oxide electrocatalysts for the alkaline water oxidation reaction, *Journal of Materials Chemistry A*, vol. 4, no. 8, pp. 3068–3076, 2016.
- [102] J. B. Gerken et al., A survey of diverse earth abundant oxygen evolution electrocatalysts showing enhanced activity from Ni-Fe oxides containing a third metal, *Energy and Environmental Science*, vol. 7, no. 7, pp. 2376–2382, 2014.
- [103] Z. Lu et al., Three-dimensional NiFe layered double hydroxide film for high-efficiency oxygen evolution reaction, *Chemical Communications*, vol. 50, no. 49, pp. 6479–6482, 2014.
- [104] A. T. Bell: *Electrocatalysis - Understanding the Effects of Composition and Structure on the Oxygen Evolution Reaction (OER) Occurring on NiFeOx Catalysts*, 22nd ed. The Royal Society of Chemistry, 2019, ch. 3, pp. 81–116.
- [105] S. Marappa and P. V. Kamath, Structure of the Carbonate-Intercalated Layered Double Hydroxides: A Reappraisal, *Industrial and Engineering Chemistry Research*, vol. 54, no. 44, pp. 11 075–11 079, 2015.
- [106] G. V. Manohara, S. V. Prasanna, and P. V. Kamath, Structure and composition of the layered double hydroxides of Mg and Fe: Implications for anion-exchange reactions, *European Journal of Inorganic Chemistry*, no. 16, pp. 2624–2630, 2011.

- [107] A. S. Batchellor and S. W. Boettcher, Pulse-Electrodeposited Ni-Fe (Oxy)hydroxide Oxygen Evolution Electrocatalysts with High Geometric and Intrinsic Activities at Large Mass Loadings, *ACS Catalysis*, vol. 5, no. 11, pp. 6680–6689, 2015.
- [108] R. Chen et al., Achieving stable and efficient water oxidation by incorporating NiFe layered double hydroxide nanoparticles into aligned carbon nanotubes, *Nanoscale Horizons*, vol. 1, no. 2, pp. 156–160, 2016.
- [109] A. Mahmood et al., Controllable structure reconstruction of nickel-iron compounds toward highly efficient oxygen evolution, *Nanoscale*, vol. 12, no. 19, pp. 10 751–10 759, 2020.
- [110] M. W. Louie and A. T. Bell, An investigation of thin-film Ni-Fe oxide catalysts for the electrochemical evolution of oxygen, *Journal of the American Chemical Society*, vol. 135, no. 33, pp. 12 329–12 337, 2013.
- [111] F. Song and X. Hu, Exfoliation of layered double hydroxides for enhanced oxygen evolution catalysis, *Nature Communications*, vol. 5, no. 4477, 2014.
- [112] L. J. Enman et al., Effects of Metal Electrode Support on the Catalytic Activity of Fe(oxy)hydroxide for the Oxygen Evolution Reaction in Alkaline Media, *ChemPhysChem*, pp. 1–8, 2019.
- [113] Y. Xu et al., Room-temperature synthetic NiFe layered double hydroxide with different anions intercalation as an excellent oxygen evolution catalyst, *RSC Advances*, vol. 5, no. 68, pp. 55 131–55 135, 2015.
- [114] R. Chen et al., Layered Structure Causes Bulk NiFe Layered Double Hydroxide Unstable in Alkaline Oxygen Evolution Reaction, *Advanced Materials*, vol. 1903909, 2019.
- [115] X. X. Jiang et al., Ultrathin sulfate-intercalated NiFe-layered double hydroxide nanosheets for efficient electrocatalytic oxygen evolution, *RSC Advances*, vol. 10, no. 21, pp. 12 145–12 150, 2020.
- [116] F. Le Formal et al., Influence of Composition on Performance in Metallic Iron-Nickel-Cobalt Ternary Anodes for Alkaline Water Electrolysis, *ACS Catalysis*, pp. 12 139–12 147, 2020.
- [117] J. A. Carrasco et al., Influence of the interlayer space on the water oxidation performance in a family of surfactant-intercalated NiFe-layered double hydroxides, *Chemistry of Materials*, vol. 31, no. 17, pp. 6798–6807, 2019.
- [118] L. Trotochaud et al., Nickel-Iron oxyhydroxide oxygen-evolution electrocatalysts: The role of intentional and incidental iron incorporation, *Journal of the American Chemical Society*, vol. 136, no. 18, pp. 6744–6753, 2014.
- [119] S. Anantharaj, S. Kundu, and S. Noda, "The Fe Effect": A review unveiling the critical roles of Fe in enhancing OER activity of Ni and Co based catalysts, *Nano Energy*, vol. 80, no. October 2020, p. 105 514, 2021.
- [120] M. B. Stevens et al., Reactive Fe-Sites in Ni/Fe (Oxy)hydroxide Are Responsible for Exceptional Oxygen Electrocatalysis Activity, *Journal of the American Chemical Society*, vol. 139, no. 33, pp. 11 361–11 364, 2017.
- [121] S. Klaus et al., Role of Catalyst Preparation on the Electrocatalytic Activity of Ni_{1-x}Fe_xOOH for the Oxygen Evolution Reaction, *Journal of Physical Chemistry C*, vol. 119, no. 32, pp. 18 303–18 316, 2015.

-
- [122] L. Trotochaud et al., Solution-cast metal oxide thin film electrocatalysts for oxygen evolution, *Journal of the American Chemical Society*, vol. 134, no. 41, pp. 17 253–17 261, 2012.
- [123] B. M. Hunter, J. R. Winkler, and H. B. Gray, Iron is the active site in nickel/iron water oxidation electrocatalysts, *Molecules*, vol. 23, no. 4, 2018.
- [124] N. Li et al., Influence of iron doping on tetravalent nickel content in catalytic oxygen evolving films, *Proceedings of the National Academy of Sciences of the United States of America*, vol. 114, no. 7, pp. 1486–1491, 2017.
- [125] M. Gorlin et al., Tracking catalyst redox states and reaction dynamics in ni-fe oxyhydroxide oxygen evolution reaction electrocatalysts: The role of catalyst support and electrolyte pH, *Journal of the American Chemical Society*, vol. 139, no. 5, pp. 2070–2082, 2017.
- [126] H. Xiao, H. Shin, and W. A. Goddard, Synergy between Fe and Ni in the optimal performance of (Ni,Fe)OOH catalysts for the oxygen evolution reaction, *Proceedings of the National Academy of Sciences of the United States of America*, vol. 115, no. 23, pp. 5872–5877, 2018.
- [127] T. Ohligschläger and G. Schwitzgebel, EQCM contributions to the reactions of the nickel oxide electrode, *Physical Chemistry Chemical Physics*, vol. 3, no. 23, pp. 5290–5296, 2001.
- [128] B. S. Yeo and A. T. Bell, In situ raman study of nickel oxide and gold-supported nickel oxide catalysts for the electrochemical evolution of oxygen, *Journal of Physical Chemistry C*, vol. 116, no. 15, pp. 8394–8400, 2012.
- [129] I. J. Godwin and M. E. Lyons, Enhanced oxygen evolution at hydrous nickel oxide electrodes via electrochemical ageing in alkaline solution, *Electrochemistry Communications*, vol. 32, pp. 39–42, 2013.
- [130] C. Andronesco et al., Influence of Temperature and Electrolyte Concentration on the Structure and Catalytic Oxygen Evolution Activity of Nickel–Iron Layered Double Hydroxide, *Chemistry - A European Journal*, vol. 24, no. 52, pp. 13 773–13 777, 2018.
- [131] M. Etzi Coller Pascuzzi et al., Investigation of the stability of NiFe-(oxy)hydroxide anodes in alkaline water electrolysis under industrially relevant conditions, *Catalysis Science and Technology*, vol. 10, no. 16, pp. 5593–5601, 2020.
- [132] Y. Liu et al., Corrosion engineering towards efficient oxygen evolution electrodes with stable catalytic activity for over 6000 hours, *Nature Communications*, vol. 9, no. 1, pp. 1–10, 2018.
- [133] A. Lasia: *Electrochemical Impedance Spectroscopy and its Applications*. New York, Heidelberg, Dordrecht, London: Springer Science+Business Media New York, 2014.
- [134] J. I. Goldstein et al.: *Quantitative Analysis: The SEM/EDS Elemental Microanalysis k-ratio Procedure for Bulk Specimens, Step-by-Step*. 2018, pp. 309–339.
- [135] C. V. Raman and K. S. Krishnan, A New Type of Secondary Radiation, *Nature*, vol. 121, no. 3048, pp. 501–502, 1928.
- [136] R. L. McCreery: *Raman Spectroscopy for Chemical Analysis*, J. D. Winefordner, Ed., 5. Columbus: John Wiley & Sons, Inc., 2000, vol. 157.
- [137] B. B. He: *Two-dimensional X-ray diffraction*. John Wiley & Sons, Inc., 2009.

- [138] J. F. Watts and J. Wolstenholme: *An Introduction to Surface Analysis by XPS and AES*. West Sussex: John Wiley & Sons, Inc., 2003, vol. 3.
- [139] S. M. Alia and B. S. Pivovar, Evaluating hydrogen evolution and oxidation in alkaline media to establish baselines, *Journal of the Electrochemical Society*, vol. 165, no. 7, F441–F455, 2018.
- [140] M. R. Kraglund: *Alkaline membrane water electrolysis with non-noble catalysts*, Ph.D. dissertation, Technical University of Denmark, 2017.
- [141] R. Chen et al., Supporting Information - Layered Structure Causes Bulk NiFe Layered Double Hydroxide Unstable in Alkaline Oxygen Evolution Reaction, *Advanced Materials*, p. 1903909, 2019.
- [142] J. Y. C. Chen et al., Operando Analysis of NiFe and Fe Oxyhydroxide Electrocatalyst for Water Oxidation Detection of Fe⁴⁺ by Moessbauer Spectroscopy, *Journal of the American Chemical Society*, vol. 137, pp. 15090–15093, 2015.
- [143] Y. Deng and B. S. Yeo, Characterization of Electrocatalytic Water Splitting and CO₂ Reduction Reactions using in situ/operando Raman Spectroscopy, *ACS Catalysis*, vol. 7, pp. 7873–7889, 2017.
- [144] M. Fleischmann, A. Oliver, and J. Robinson, In Situ X-ray diffraction studies of electrode solution interfaces, *Electrochimica Acta*, vol. 31, no. 8, pp. 899–906, 1986.
- [145] E. J. Crumlin et al., X-ray spectroscopy of energy materials under in situ/operando conditions, *Journal of Electron Spectroscopy and Related Phenomena*, vol. 200, pp. 264–273, 2015.
- [146] G. Nauer, GIXD (Grazing Incidence X-Ray Diffraction) as a Tool for the In Situ Investigation of Electrochemical Reactions of Metals in Electrolyte Solution The Lead Electrode in 5M Sulphuric Acid, *Materials Science Forum*, vol. 228-231, pp. 387–392, 1996.
- [147] M. Farmand et al., Electrochemical flow cell enabling: Operando probing of electrocatalyst surfaces by X-ray spectroscopy and diffraction, *Physical Chemistry Chemical Physics*, vol. 21, no. 10, pp. 5402–5408, 2019.
- [148] F. Allebrod, C. Chatzichristodoulou, and M. B. Mogensen, Alkaline electrolysis cell at high temperature and pressure of 250 °C and 42 bar, *Journal of Power Sources*, vol. 229, pp. 22–31, 2013.
- [149] F. Allebrod, C. Chatzichristodoulou, and M. B. Mogensen, Foam Based Gas Diffusion Electrodes for Reversible Alkaline Electrolysis Cells, *ECS Transactions*, vol. 64, no. 3, pp. 1029–1038, 2014.
- [150] N. M. Marković et al., Hydrogen electrochemistry on platinum low-index single-crystal surfaces in alkaline solution, *Journal of the Chemical Society, Faraday Transactions*, vol. 92, no. 20, pp. 3719–3725, 1996.
- [151] P. J. Rheinländer et al., Comparing Hydrogen Oxidation and Evolution Reaction Kinetics on Polycrystalline Platinum in 0.1M and 1M KOH, *ECS Transactions*, vol. 50, no. 2, pp. 2163–2174, 2012.
- [152] P. Daubinger et al., Electrochemical characteristics of nanostructured platinum electrodes-A cyclic voltammetry study, *Physical Chemistry Chemical Physics*, vol. 16, no. 18, pp. 8392–8399, 2014.

-
- [153] R. Kizil and J. Irudayaruj: Raman Spectroscopy, G. V. Barbosa-Canovas, Ed. Maslak, Istanbul: Springer Science+Business Media, 2014, ch. five, pp. 103–134.
- [154] G. E. Walraten and R. T. Douglas, Raman spectra from very concentrated aqueous NaOH and from wet and dry, solid, and anhydrous molten, LiOH, NaOH, and KOH, *Journal of Chemical Physics*, vol. 124, no. 11, 2006.
- [155] V. Umapathy et al., Synthesis of NiMoO₄ nanoparticles by sol-gel method and their structural, morphological, optical, magnetic and photocatalytic properties, *Transactions of Nonferrous Metals*, vol. China 27, pp. 1785–1793, 2017.
- [156] J. Divisek, H. Schmitz, and J. Balej, Ni and Mo coatings as hydrogen cathodes, *Journal of Applied Electrochemistry*, vol. 19, no. 4, pp. 519–530, 1989.
- [157] L. B. Albertini, A. C. Angelo, and E. R. Gonzalez, A nickel molybdenite cathode for the hydrogen evolution reaction in alkaline media, *Journal of Applied Electrochemistry*, vol. 22, no. 9, pp. 888–892, 1992.
- [158] L. Birry and A. Lasia, Studies of the hydrogen evolution reaction on Raney nickel-molybdenum electrodes, *Journal of Applied Electrochemistry*, vol. 34, no. 7, pp. 735–749, 2004.
- [159] G. S. Tasic et al., Characterization of the Ni-Mo catalyst formed in situ during hydrogen generation from alkaline water electrolysis, *International Journal of Hydrogen Energy*, vol. 36, no. 18, pp. 11 588–11 595, 2011.
- [160] X. Tang et al., Noble fabrication of Ni-Mo cathode for alkaline water electrolysis and alkaline polymer electrolyte water electrolysis, *International Journal of Hydrogen Energy*, vol. 39, no. 7, pp. 3055–3060, 2014.
- [161] A. Y. Faid et al., Ni/NiO nanosheets for alkaline hydrogen evolution reaction: In situ electrochemical-Raman study, *Electrochimica Acta*, vol. 361, p. 137 040, 2020.
- [162] R. Subbaraman et al., Enhancing Hydrogen Evolution Activity in Water Splitting by Tailoring Li⁺-Ni(OH)₂-Pt Interfaces, *Science*, vol. 334, no. December, pp. 1256–1260, 2011.
- [163] M. Gong et al., Nanoscale nickel oxide/nickel heterostructures for active hydrogen evolution electrocatalysis, *Nature Communications*, vol. 5, pp. 1–6, 2014.
- [164] Y. Y. Chen et al., Self-Templated Fabrication of MoNi₄/MoO_{3-x} Nanorod Arrays with Dual Active Components for Highly Efficient Hydrogen Evolution, *Advanced Materials*, vol. 29, no. 39, pp. 1–7, 2017.
- [165] J. Wang et al., Dominating Role of Ni₀ on the Interface of Ni/NiO for Enhanced Hydrogen Evolution Reaction, *ACS Applied Materials and Interfaces*, vol. 9, no. 8, pp. 7139–7147, 2017.
- [166] M. Schalenbach et al., A perspective on low-temperature water electrolysis - Challenges in alkaline and acidic technology, *International Journal of Electrochemical Science*, vol. 13, no. 2, pp. 1173–1226, 2018.
- [167] D. S. Hall, C. Bock, and B. R. MacDougall, An oxalate method for measuring the surface area of nickel electrodes, *Journal of the Electrochemical Society*, vol. 161, no. 12, H787–H795, 2014.
- [168] H. Wang and L. Gao, Recent developments in electrochemical hydrogen evolution reaction, *Current Opinion in Electrochemistry*, vol. 7, pp. 7–14, 2018.

- [169] R. B. Patil et al., Direct observation of Ni – Mo catalyst formation via thermal reduction of nickel molybdate nanorods, *ChemRxiv*, vol. 2, 2020.
- [170] L. Bai, D. A. Harrington, and B. E. Conway, Behavior of Overpotential-deposited species in faradaic reactions-II ac Impedance Measurements on H₂ Evolution Kinetics at activated and unactivated Pt Cathodes, *Electrochimica Acta*, vol. 32, no. 12, pp. 1713–1731, 1987.
- [171] C. Fan, D. L. Piron, and P. Paradis, Hydrogen evolution on electrodeposited nickel-cobalt-molybdenum in alkaline water electrolysis, *Electrochimica Acta*, vol. 39, no. 18, pp. 2715–2722, 1994.
- [172] Y. Dong et al., First-Principles Determination of Active Sites of Ni Metal-Based Electrocatalysts for Hydrogen Evolution Reaction, *ACS Applied Materials and Interfaces*, vol. 10, no. 46, pp. 39 624–39 630, 2018.
- [173] V. Mahalingam et al., Inception of Molybdate as “Pore Forming Additive” to Enhance the Bifunctional Electrocatalytic Activity of Nickel and Cobalt based Mixed Hydroxides for Overall Water Splitting, *Nanoscale*, 2019.
- [174] S. Machado et al., The Influence of H-Absorption on the Cathodic Response of High Area Nickel, *Electrochimica Acta*, vol. 39, no. 11, pp. 1757–1761, 1994.
- [175] V. Ganesh and V. Lakshminarayanan, Preparation of high surface area nickel electrodeposit using a liquid crystal template technique, *Electrochimica Acta*, vol. 49, no. 21, pp. 3561–3572, 2004.
- [176] K. I. Siwek et al., 3D nickel foams with controlled morphologies for hydrogen evolution reaction in highly alkaline media, *International Journal of Hydrogen Energy*, vol. 44, no. 3, pp. 1701–1709, 2019.
- [177] V. Pérez-Herranz et al., Modification of porous nickel electrodes with silver nanoparticles for hydrogen production, *Journal of Electroanalytical Chemistry*, vol. 808, no. March 2017, pp. 420–426, 2018.
- [178] L. Wang et al., Ni nanoparticles supported on graphene layers: An excellent 3D electrode for hydrogen evolution reaction in alkaline solution, *Journal of Power Sources*, vol. 347, pp. 220–228, 2017.
- [179] M. Zhiani and S. Kamali, Preparation and Evaluation of Nickel Nanoparticles Supported on the Polyvinylpyrrolidone-Graphene Composite as a Durable Electrocatalyst for HER in Alkaline Media, *Electrocatalysis*, vol. 7, no. 6, pp. 466–476, 2016.
- [180] P. J. Rheinländer et al., Kinetics of the Hydrogen Oxidation/Evolution Reaction on Polycrystalline Platinum in Alkaline Electrolyte Reaction Order with Respect to Hydrogen Pressure, *Journal of The Electrochemical Society*, vol. 161, no. 14, F1448–F1457, 2014.
- [181] A. Kellenberger, N. Vaszilcsin, and W. Brandl, Roughness factor evaluation of thermal arc sprayed skeleton nickel electrodes, *Journal of Solid State Electrochemistry*, vol. 11, no. 1, pp. 84–89, 2006.
- [182] R. Karimi Shervedani and A. Reza Madram, Electrocatalytic activities of nanocomposite Ni₈₁P₁₆C₃ electrode for hydrogen evolution reaction in alkaline solution by electrochemical impedance spectroscopy, *International Journal of Hydrogen Energy*, vol. 33, no. 10, pp. 2468–2476, 2008.

-
- [183] J. Divisek, J. Mergel, and H. Schmitz, Advanced Water Electrolysis and Catalyst Stability under Discontinuous Operation, *International Journal of Hydrogen Energy*, vol. 15, no. 2, pp. 105–114, 1990.
- [184] R. Hagedorn and G. Fuhr, Steady state electrolysis and isoelectric focusing, *Electrophoresis*, vol. 11, no. 4, pp. 281–289, 1990.
- [185] E. A. Hernández-Pagán et al., Resistance and polarization losses in aqueous buffer-membrane electrolytes for water-splitting photoelectrochemical cells, *Energy and Environmental Science*, vol. 5, no. 6, pp. 7582–7589, 2012.
- [186] J. Divisek, R. Jung, and D. Britz, Potential distribution and electrode stability in a bipolar electrolysis cell, *Journal of Applied Electrochemistry*, vol. 20, no. 2, pp. 186–195, 1990.
- [187] A. E. Mauer, D. W. Kirk, and S. J. Thorpe, The role of iron in the prevention of nickel electrode deactivation in alkaline electrolysis, *Electrochimica Acta*, vol. 52, no. 11, pp. 3505–3509, 2007.
- [188] J. O. Bockris and T. Otagawa, The Electrocatalysis of Oxygen Evolution on Perovskites, *Journal of Electrochemical Society*, vol. 131, no. 2, pp. 290–302, 1984.
- [189] S. R. Mellsop, A. Gardiner, and A. T. Marshall, Electrocatalytic oxygen evolution on nickel oxy-hydroxide anodes: Improvement through rejuvenation, *Electrochimica Acta*, vol. 180, pp. 501–506, 2015.
- [190] X. Wu et al., Fabrication of NiFe layered double hydroxides using urea hydrolysis - Control of interlayer anion and investigation on their catalytic performance, *Catalysis Communications*, vol. 50, no. 3, pp. 44–48, 2014.
- [191] M. Bernardini et al., Formation of nickel hydrides by hydrogen evolution in alkaline media: Effect of temperature, *Journal of Electroanalytical Chemistry*, vol. 457, no. 1-2, pp. 205–219, 1998.
- [192] B. E. Conway and G. Jerkiewicz, Thermodynamic and electrode kinetic factors in cathodic hydrogen sorption into metals and its relationship to hydrogen adsorption and poisoning, *Journal of Electroanalytical Chemistry*, vol. 357, no. 1-2, pp. 47–66, 1993.
- [193] C. A. Melendres and M. Pankuch, On the composition of the passive film on nickel: a surface-enhanced Raman spectroelectrochemical study, *Journal of Electroanalytical Chemistry*, vol. 333, no. 1-2, pp. 103–113, 1992.
- [194] J. D. Benck et al., Substrate selection for fundamental studies of electrocatalysts and photoelectrodes: Inert potential windows in acidic, neutral, and basic electrolyte, *PLoS ONE*, vol. 9, no. 10, 2014.
- [195] M. Dieterle and G. Mestl, Raman spectroscopy of molybdenum oxides: Part II. Resonance Raman spectroscopic characterization of the molybdenum oxides Mo₄O₁₁ and MoO₂, *Physical Chemistry Chemical Physics*, vol. 4, no. 5, pp. 822–826, 2002.
- [196] W. Du et al., Unveiling the In Situ Dissolution and Polymerization of Mo in Ni₄ Mo Alloy for Promoting the Hydrogen Evolution Reaction, *Angewandte Chemie*, vol. 133, no. 13, pp. 7127–7131, 2021.
- [197] D. S. Hall et al., Raman and infrared spectroscopy of α and β phases of thin nickel hydroxide films electrochemically formed on nickel, *Journal of Physical Chemistry A*, vol. 116, no. 25, pp. 6771–6784, 2012.

- [198] C. Johnston and P. R. Graves, In situ Raman spectroscopy study of the nickel oxyhydroxide electrode (NOE) system, *Applied Spectroscopy*, vol. 44, no. 1, pp. 105–115, 1990.
- [199] K. Varunkumar et al., Effect of calcination temperature on Cu doped NiO nanoparticles prepared via wet-chemical method: Structural, optical and morphological studies, *Materials Science in Semiconductor Processing*, vol. 66, no. August, pp. 149–156, 2017.
- [200] A. Sunny and K. Balasubramanian, Raman Spectral Probe on Size-Dependent Surface Optical Phonon Modes and Magnon Properties of NiO Nanoparticles, *Journal of Physical Chemistry C*, vol. 124, no. 23, pp. 12 636–12 644, 2020.
- [201] N. Mironova-Ulmane et al., Raman scattering in nanosized nickel oxide NiO, *Journal of Physics: Conference Series*, vol. 93, no. 1, 2007.
- [202] N. Mironova-Ulmane et al., Structural and Magnetic Properties of Nickel Oxide Nanopowders, *Solid State Phenomena*, vol. 168-169, pp. 341–344, 2011.
- [203] H. Hu and I. E. Wachs, Surface structures of supported molybdenum oxide catalysts. Characterization by Raman and Mo L3-edge XANES, *Journal of physical chemistry*, vol. 99, no. 27, pp. 10 897–10 910, 1995.
- [204] G. Mestl and T. K. Srinivasan: Raman Spectroscopy of Monolayer-Type Catalysts: Supported Molybdenum Oxides, 4. 1998, vol. 40, pp. 451–570.
- [205] D. Zhou et al., Effects of redox-active interlayer anions on the oxygen evolution reactivity of NiFe-layered double hydroxide nanosheets, *Nano Research*, vol. 11, no. 3, pp. 1358–1368, 2018.
- [206] B. M. Hunter et al., Effect of interlayer anions on [NiFe]-LDH nanosheet water oxidation activity, *Energy and Environmental Science*, vol. 9, no. 5, pp. 1734–1743, 2016.
- [207] J. R. Swierk et al., Electrochemical Study of the Energetics of the Oxygen Evolution Reaction at Nickel Iron (Oxy)Hydroxide Catalysts, *Journal of Physical Chemistry C*, vol. 119, no. 33, pp. 19 022–19 029, 2015.
- [208] L. M. Da Silva et al., Surface, kinetics and electrocatalytic properties of Ti/(IrO₂ + Ta₂O₅) electrodes, prepared using controlled cooling rate, for ozone production, *Electrochimica Acta*, vol. 49, no. 22-23 SPEC. ISS. Pp. 3977–3988, 2004.
- [209] Y. W. Alsmeyer and R. L. McCreery, Surface-Enhanced Raman Spectroscopy of Carbon Electrode Surfaces Following Silver Electrodeposition, *Analytical Chemistry*, vol. 63, no. 13, pp. 1289–1295, 1991.
- [210] Y. Xia et al., Electrodeposition of High Density Silver Nanosheets with Controllable morphologies Served as Effective and Reproducible SERS Substrates, *Langmuir*, vol. 32, no. 14, pp. 3385–3392, 2016.

List of Figures

1.1	The three different types of water electrolyzers: PEMEC, SOEC, and AWE.	2
1.2	Comparison of the current status and the development potential of water electrolysis between the three different techniques.	3
1.3	The overpotential of various electrocatalysts at a geometric current density of 10 mA/cm^2 after a polarization time of 2 hours.	5
2.1	Schematic illustration of the losses in a water electrolyzer on the reversible cell voltage summing up to the operating cell voltage.	12
2.2	Illustration of the Butler-Volmer and the Tafel equation.	14
2.3	The hydroxides and oxyhydroxides of nickel according to the Bode diagram.	15
2.4	Reported Tafel-slopes for the HER on polycrystalline nickel in alkaline electrolyte at room temperature with respect to the measurement pH.	18
2.5	Reported exchange current densities for the HER on polycrystalline nickel in alkaline electrolyte at room temperature with respect to the measurement pH.	19
2.6	Overpotential at 10 mA/cm^2 for the HER on polycrystalline nickel in alkaline electrolyte at room temperature with respect to the measurement pH.	19
2.7	Calculated exchange current densities of the HER over reciprocal temperature for bare and partially oxidized Nickel.	22
2.8	Cyclic voltammograms of a nickel electrode with increasing upper potential limit, reported vs Ag/AgCl (1 M KCl) in 0.01 M KOH.	22
2.9	The measured current of the hydrogen evolution reaction at -1.20 V by Surface Interrogation Scanning Electrochemical Microscopy in relation to the upper potential limit from Fig. 2.8.	22
2.10	XRD pattern of a nickel electrode, 20 minutes after being polarized at 300 mA/cm^2 for 2 h.	24
2.11	XRD pattern of a) fresh nickel, b) after 141 h at 500 mA/cm^2 in 1 M NaOH, c) after 66.5 h at 500 mA/cm^2 in 30 % KOH.	24
2.12	Model of the influence from overpotentially deposited hydrogen on the total capacitance of a nickel electrode in the HER region.	25
2.13	Current densities of various Ni_xMo_y electrocatalysts at an HER overpotential of 400 mV in 1 M NaOH at room temperature.	27
2.14	Ni/Mo-ratio in the precursor solution and the resulting Ni/Mo-ratio in the electrocatalyst with the respective overpotential at 10 mA/cm^2 in 1 M NaOH.	27
2.15	Current density per true electrochemical surface area, evaluated through the hexaaminruthenium (II/III) redox couple, at -300 mV in 1 M NaOH.	28

2.16	Calculated hydrogen adsorption energy at the equilibrium potential of MoO ₂ -Ni, MoO ₂ , and Ni.	29
2.17	High resolution XPS spectra at UHV, as well as in hydrogen and in humidified hydrogen environment of a Ni and a NiMo electrocatalyst.	29
2.18	Potential-pH-diagram of the molybdenum-water-system at 25 °C.	30
2.19	Cyclic voltammograms close to the HER equilibrium potential of a Ni and a Ni _{0.92} Mo _{0.08} electrocatalyst.	31
2.20	Leaching of Mo from Ni ₃ Mo with respect to the applied potential.	33
2.21	Dissolution of molybdenum in Mo, NiMo, Ni ₂ Mo, Ni ₃ Mo, Ni ₄ Mo, and Ni ₆ Mo in correlation to the applied potential and the elapsed time.	33
2.22	Segregation energies of Mo in NiMo (111) with regards to the atomic layers, with respect to the degree of chemisorbed monolayers of atomic oxygen. . . .	33
2.23	Operando Raman spectra recorded at 0 V vs RHE and at OCV on a NiMo electrode in 0.1 M KOH.	34
2.24	Mechanism of the alkaline OER.	37
2.25	Crystal structures of brucite β-Ni(OH) ₂ and NiFe LDH.	39
2.26	Influence of the Fe content in electrodeposited NiFe LDH on the kinetics of the alkaline OER.	40
2.27	OER overpotentials subtracted with the minimum reported overpotential in a literature source in regards to the iron content of NiFe LDH.	40
2.28	The influence of Fe impurities and co-deposited Fe on the OER kinetics of Ni(OH) ₂ /NiOOH electrocatalyst films.	41
2.29	Extended model of the nickel phases in alkaline media describing to the Bode diagram additional α and β phases.	43
2.30	Cyclic voltammograms, linear sweep voltammetry and Raman spectra of α/γ Ni and β/β Ni.	43
2.31	XRD patterns and Raman spectra of a NiFe LDH electrocatalyst before and after aging for 60 h in 1 M and in 7.5 M KOH.	45
3.1	Illustrating the correlation of the imaginary and real part of impedance by a vector R and its modulus $ R $ in the complex plane and the resulting Lissajous curves.	48
3.2	The three-dimensional plotting of impedance.	50
3.3	Electric circuit models with resistive, capacitive and inductive contributions in Boukamp notation.	50
3.4	Cyclic sweeping of the electrode potential with time and resulting cyclic voltammogram.	52
3.5	Correlation between the energy of incoming photons, the excited electronic state and the virtual state.	55
3.6	The electrocatalyst testing setup FlexCell at DTU Energy.	59
3.7	The laboratory flowcell setup at DTU Energy.	60
4.1	A choice of setups for different spectroelectrochemical approaches published in the literature.	64
4.2	The first approach towards spectroelectrochemistry.	67

4.3	The second approach towards spectroelectrochemistry.	67
4.4	Electrochemical impedance spectra at OCV and at 200 mV HER overpotential and iV -curves of approach 2.	68
4.5	The third approach towards spectroelectrochemistry.	69
4.6	The schematic cross-section of the spectroelectrochemical cell FeliS.	71
4.7	Assembly of the spectroelectrochemical cell FeliS.	72
4.8	The final spectroelectrochemical testing setup and correlated electrochemical verification through electrochemical impedance spectroscopy, cyclic voltammetry and iV -curves.	74
4.9	FeliS Raman working electrode lid.	75
4.10	The operation of FeliS within the Renishaw InVia Raman spectrometer and <i>in situ</i> measurement of a hydrothermally synthesized Ni ₇ Fe ₃ LDH electrocatalyst.	77
4.11	Raman measurement of 1 M and 11.6 M KOH electrolyte.	78
4.12	First X-ray working electrode lid of FeliS.	79
4.13	The operation of FeliS within the Rigaku Smartlab X-ray diffractometer with the first X-ray working electrode lid and operando XRD measurement.	81
4.14	The second X-ray working electrode lid of FeliS.	82
4.15	Comparison between the first and second X-ray working electrode lid of FeliS.	83
4.16	GIXRD patterns of a plasma coated silver-YSZ electrode and at 600 °C thermochemically reduced NiMo solgel electrocatalyst with the second X-ray working electrode lid.	84
4.17	FeliS in flowcell configuration through the cell.	86
4.18	FeliS in flowcell configuration over the working electrode.	87
4.19	Concept of a mounting-tool to ensure a flat working electrode of FeliS.	88
5.1	Powder X-ray diffraction of the precursors by hydrothermal and solgel synthesis.	95
5.2	The R(RQ) electric equivalent circuit for electrocatalyst modeling.	96
5.3	Correlation of the double layer capacitance to the HER overpotential at room temperature in 45 w% KOH.	96
5.4	Results from electrochemical impedance spectroscopy of the hydrothermal 400 °C electrocatalyst.	98
5.5	Results from electrochemical impedance spectroscopy of the solgel 700 °C electrocatalyst.	98
5.6	Kramers-Kronig tests of the hydrothermal 400 °C and of the solgel 700 °C electrocatalyst.	100
5.7	Armstrong's electric circuit.	101
5.8	Correlation of the double layer capacitance obtained from two different fitting models to the HER overpotential.	102
5.9	Cyclic voltammograms of the NiMo solgel 600 °C electrocatalyst between -200 - +500 mV vs RHE.	104
5.10	Cyclic voltammograms in the non-faradaic region of the solgel 600 °C electrocatalyst and the resulting double layer capacitance.	105
5.11	Relative ratio between the double layer capacitance obtained by galvanostatic EIS, through an R(RQ) and an Armstrong fitting, in relation to the double layer capacitance from the non-faradaic region.	107

5.12	Evaluation of the quality of the results from Fig. 5.11.	107
5.13	Influence of the cyclic voltammograms on the kinetics of the NiMo solgel 600 °C electrocatalyst.	109
5.14	Correlation between surface area estimates on a nickel foil in 1 M and 11.6 M (~ 45 w%) KOH.	110
5.15	The geometric performance at 10 mA/cm ² after 5 min of a variety of nickel, partially oxidized/activated nickel and nickel-molybdenum electrocatalysts in correlation to the surface roughness factor.	112
5.16	Repetition of Fig. 5.15, with additional nickel samples, samples made by electrodeposition and a variety of nickel and nickel-molybdenum samples from the literature.	116
5.17	Repetition of Fig. 5.16, divided into nickel and nickel-molybdenum plus active nickel electrocatalysts.	117
5.18	Repetition of Fig. 5.16, including the semi-logarithmic fittings and corre- sponding Student-t (95 %) statistical evaluations.	124
5.19	Repetition of Fig. 5.18 considering surface area estimates by double layer capacitance by 20 μF/cm ²	126
6.1	Schematic evolution of the galvani-potential and the pH over a zero-gap water electrolyzer, including a pH-sensitive reference electrode behind the cathode and behind the anode.	135
6.2	Electrochemical impedance at 1 mA/cm ² and 80 °C on the <i>Ni-PP vs NiFe</i> <i>LDH/PP</i> cell	138
6.3	Electrochemical impedance at 1 mA/cm ² and 80 °C on the <i>NiMo/PP vs NiFe</i> <i>LDH/PP</i> cell.	139
6.4	Fitting of the full cell electrochemical impedance at 1 mA/cm ² and 80 °C of the <i>NiMo/PP vs NiFe LDH/PP</i> cell with a LR(RQ)(RQ) fitting.	139
6.5	Polarization curves of the <i>Ni-PP vs Ni-PP</i> , the <i>Ni-PP vs NiFe LDH/PP</i> , and the <i>NiMo/PP vs Ni/PP</i> cell at 80 °C in 30 w% KOH.	141
6.6	Repetition of Fig. 6.5, focused on the kinetic segment up to 20 mA/cm ² and additional plotting of the summation of the single electrode overpotentials.	143
6.7	Polarization curves of electrodes with perforated plate-support at 80 °C in 30 w% KOH.	146
6.8	Polarization curves of electrodes with felt-support at 80 °C in 30 w% KOH.	147
6.9	Cyclic voltammograms of the <i>Ni-PP vs Ni-PP</i> cell at 50 mV/s and 80 °C in 30 w% KOH.	150
6.10	Cyclic voltammograms of the <i>Ni-PP vs NiFe LDH/PP</i> cell at 50 mV/s and 80 °C in 30 w% KOH.	150
6.11	Cyclic voltammograms of the <i>NiMo/PP vs Ni-PP</i> cell at 50 mV/s and 80 °C in 30 w% KOH.	151
6.12	Single electrode potentials vs both reference electrodes, and their bias, during cyclic voltammetry on the <i>Ni-PP vs NiFe LDH/PP</i> cell.	152
6.13	Evolution of the cell voltage, the cathode and the anode electrode potential vs RHE at open-circuit voltage.	154

6.14	Influence of cyclic voltammetry and open-circuit on the kinetics of the <i>Ni-PP vs Ni-PP</i> cell at 80 °C in 30 w% KOH.	156
6.15	Electrochemical impedance spectra of the <i>Ni-PP vs Ni-PP</i> cell at 1 mA/cm ² and 80 °C in 30 w% KOH.	157
6.16	Fitting results of the electrochemical impedance of the <i>Ni-PP vs Ni-PP</i> cell at 1 mA/cm ² and 80 °C in 30 w% KOH with an LR(RQ)(RQ) equivalent circuit.	157
6.17	Influence of cyclic voltammetry and open-circuit on the kinetics of the <i>Ni-PP vs NiFe LDH/PP</i> cell at 80 °C in 30 w% KOH.	160
6.18	Electrochemical impedance spectra of the <i>Ni-PP vs NiFe LDH/PP</i> cell at 1 mA/cm ² and 80 °C in 30 w% KOH.	161
6.19	Fitting results of the electrochemical impedance of the <i>Ni-PP vs NiFe LDH/PP</i> cell at 1 mA/cm ² and 80 °C in 30 w% KOH with an LR(RQ)(RQ) equivalent circuit.	161
6.20	Influence of cyclic voltammetry and open-circuit on the kinetics of the <i>NiMo/PP vs Ni-PP</i> cell at 80 °C in 30 w% KOH.	164
6.21	Electrochemical impedance spectra of the <i>NiMo/PP vs Ni-PP</i> cell at 1 mA/cm ² and 80 °C in 30 w% KOH.	165
6.22	Fitting results of the electrochemical impedance of the <i>NiMo/PP vs Ni-PP</i> cell at 1 mA/cm ² and 80 °C in 30 w% KOH with an LR(RQ)(RQ) equivalent circuit.	165
6.23	SEM images of the cathode of the <i>NiMo/PP vs Ni-PP</i> cell	167
6.24	SEM images of the anode of the <i>Ni-PP vs NiFe LDH/PP</i> cell	169
6.25	Results from accelerated degradation testing about the operational domains of a NiMo HER electrocatalyst and a NiFe LDH OER electrocatalyst, with respect to the influence of the electrode potential vs RHE on the kinetic performance.	171
6.26	Dynamic operation of the <i>NiMo/felt vs NiFe LDH/felt</i> cell at 80 °C in 30 w% KOH.	174
6.27	Repetition of Fig. 6.26, with cut-outs between 8 h – 118 h, 124 h – 178 h and 293 h – 347 h.	175
6.28	Polarization curve results from the long-term test on the <i>NiMo/felt vs NiFe LDH/felt</i> cell at 80 °C in 30 w% KOH.	180
6.29	Electrochemical impedance spectroscopy at the start and at the end of the long-term test on the <i>NiMo/felt vs NiFe LDH/felt</i> cell at 80 °C in 30 w% KOH.	181
6.30	Fitting of the electrochemical impedance spectroscopy at the beginning and at the end of the long-term test on the <i>NiMo/felt vs NiFe LDH/felt</i> cell at 80 °C in 30 w% KOH. LR(RQ)(RQ) equivalent circuit.	181
6.31	Cell voltage, cathode electrode potential and anode electrode potential at 1 mA/cm ² and at 10 mA/cm ²	184
6.32	SEM images of the cathode of the <i>NiMo/felt vs NiFe LDH/felt</i> cell.	186
6.33	SEM images of the anode of the <i>NiMo/felt vs NiFe LDH/felt</i> cell.	188
6.34	XRD patterns and XPS spectra of the pristine and 357 h tested NiFe LDH anode.	191

6.35	Conclusions about the operational domains of a NiMo HER electrocatalyst and a NiFe LDH OER electrocatalyst, with respect to the influence of the electrode potential vs RHE on the kinetic performance.	197
7.1	Grazing incidence at 5° incidence angle and Powder X-ray diffraction of the NiMo solgel electrocatalyst reduced at 600°C	203
7.2	Cyclic voltammograms of a NiMo solgel electrocatalyst, reduced at 600°C , in 11.6 M KOH at 50 mV/s, with respect to the geometric surface area of 3.14 cm^2	206
7.3	Influence of potential cycling on the HER kinetics in 11.6 M KOH, assessed through the backscans of iV -curves at 5 mV/s and correlated SEM micrographs of the electrocatalyst.	207
7.4	Raman spectra of a NiMo solgel electrocatalyst, reduced at 600°C , under polarization.	209
7.5	Raman spectra of the second test of a NiMo solgel electrocatalyst, reduced at 600°C , under polarization.	211
7.6	Pre- and post-mortem <i>ex situ</i> Raman spectra of the sample from Chap. 7.2.1 in comparison to the first spectroelectrochemical sample.	213
7.7	Comparison between pre- and post-mortem Raman on the first spectroelectrochemical sample to the OCV in 1 M KOH.	213
7.8	Schematic redox processes of a molybdenum oxide supported NiMo electrocatalyst on Ni-support.	216
7.9	Conclusions about the operational domains and the correlating degradation and redox processes of a molybdenum oxide supported NiMo electrocatalyst.	216
7.10	Spectroelectrochemical XRD studies of NiFe LDH with regards to the temperature at an OER overpotential of $\eta = 200\text{ mV}$ in 30 % KOH.	218
7.11	Spectroelectrochemical XRD degradation studies at 85°C	222
7.12	EIS spectra at $\eta = 200\text{ mV}$ of NiFe LDH during spectroelectrochemical XRD studies at 85°C	223
7.13	Conclusions on the active α/γ type phase of Ni_8Fe_2 LDH under OER conditions.	226
B.1	Spectrum of the monocrystalline Si calibration sample. Measurements made with a 100 mW green laser (532 nm) at 10 % intensity in a Renishaw InVia Spectrometer.	XXXIII
B.2	Light sensitivity of the sample from Chap. 7.2.1. Measurements made with a 100 mW green laser (532 nm). <u>Left</u> : 10%. <u>Middle</u> : 5%. <u>Right</u> : 1% intensity.	XXXIV
B.3	Repetition of Fig. 7.4. Additional visualization of $\beta - \text{Ni}(\text{OH})_2$ vibrations revealing the absence of this phase.	XXXIV
C.1	EIS fitting from Fig. 7.10 with an LR(RQ)(R_{ct} Q) fitting.	XXXVI
C.2	Full pattern of the GIXRD measurements in Fig. 7.11.	XXXVII
C.3	EIS fittings of the EIS spectra from Fig. 7.12 with an LR(RQ)(R_{ct} Q) fitting.	XXXVII
C.4	EIS spectra in correlation to the XRD patterns after cycles 4-16 from Fig. 7.11.	XXXVIII

List of Tables

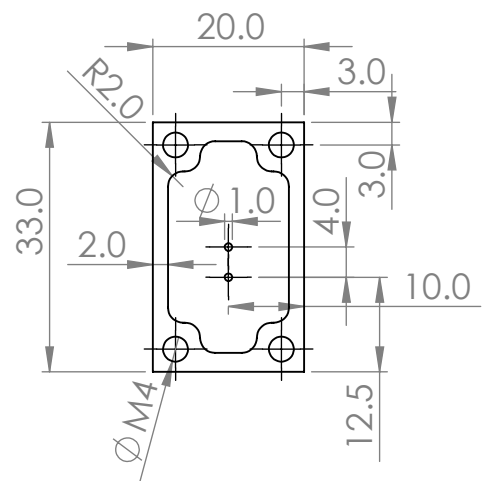
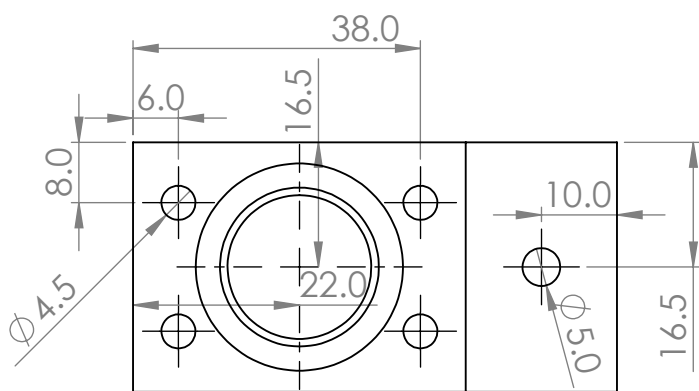
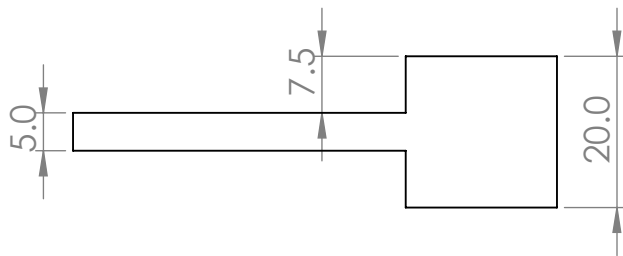
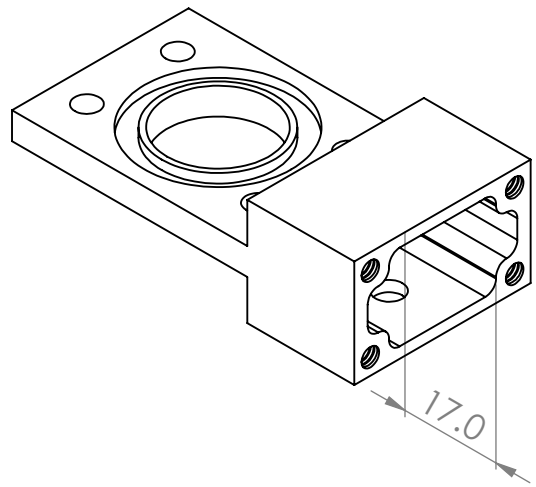
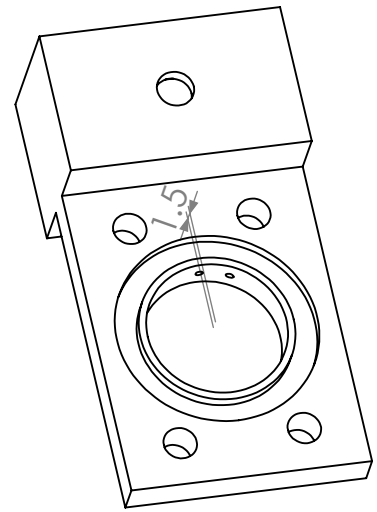
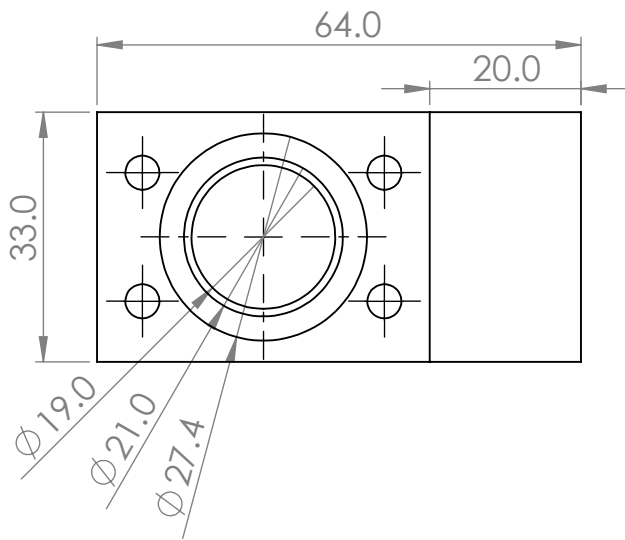
2.1	The reaction steps of the HER in alkaline electrolyte and the correlated Tafel-slopes.	16
2.2	Kinetic values for the alkaline HER on nickel, obtained from the literature and used in Fig. 2.4, 2.5, and 2.6. Bold marked values represent literature sources that considered the electrochemical active surface area.	20
2.3	The reaction steps of the OER in alkaline electrolyte and the correlated Tafel-slopes.	36
3.1	Elements for equivalent electric circuits and their impedance function and equivalent/coefficient functions. Reproduced from [133].	51
4.1	Summarized stipulations for the spectroelectrochemical cell.	62
4.2	A choice of setups published in the literature and represented in Fig. 4.1.	65
5.1	Electrocatalyst samples and substrates (written as electrocatalyst / substrate), as presented in Fig. 5.15.	113
5.2	Additional Ni (top), NiMo electrodeposited (middle) and NiMo in the literature (bottom) samples presented in Fig. 5.16.	118
5.3	NiMo in the literature (top, continued) and Ni in the literature (bottom) samples presented in Fig. 5.16.	119
5.4	Ni in the literature (top, continued) and Ni nano/micro in the literature (bottom) samples presented in Fig. 5.16.	120
5.5	Ni nano/micro in the literature (top, continued) and Pt (bottom) samples presented in Fig. 5.16.	121
5.6	Fitting and Student-t (95%) statistical parameters for Ni and NiMo / active Ni from Fig. 5.18. Based on the fitting equation $\eta_{10,geometric} = slope \cdot \log(\text{Surface Roughness Factor}) + intercept$. The same parameters including only the samples from this work in 11.6 M KOH (see Fig. 5.15) are shown for comparison. All surface area estimates from the double layer capacitance considered a value of $40 \mu\text{F}/\text{cm}^2$	125
5.7	Fitting and Student-t (95%) statistical parameters for Ni and NiMo / active Ni from Fig. 5.19. Based on the fitting equation $\eta_{10,geometric} = slope \cdot \log(\text{Surface Roughness Factor}) + intercept$. All surface area estimates from the double layer capacitance considered a value of $20 \mu\text{F}/\text{cm}^2$	126

6.1	Kinetics of the <i>Ni-PP vs Ni-PP</i> cell at 1 mA/cm^2 , before and after accelerated degradation. Charge transfer resistances and equivalent capacities as fitting results from EIS with an LR(RQ)(RQ) equivalent circuit. *: erroneous. . . .	156
6.2	Kinetics of the <i>Ni-PP vs NiFe LDH/PP</i> cell at 1 mA/cm^2 , before and after accelerated degradation. Charge transfer resistances and equivalent capacities as fitting results from EIS with an LR(RQ)(RQ) equivalent circuit.	160
6.3	Kinetics of the <i>NiMo/PP vs Ni-PP</i> cell at 1 mA/cm^2 , before and after accelerated degradation. Charge transfer resistances and equivalent capacities as fitting results from EIS with an LR(RQ)(RQ) equivalent circuit.	164
6.4	EDS results from the pristine and aged cathode of the <i>NiMo/PP vs Ni-PP</i> cell shown in Fig. 6.23, as well as the tested anode. Elemental compositions are given as atomic-%.	167
6.5	EDS results from the pristine and aged anode of the <i>Ni-PP vs NiFe LDH/PP</i> cell shown in Fig. 6.24, as well as the tested cathode. Elemental compositions are given as atomic-%.	169
6.6	Kinetics of the <i>NiMo/felt vs NiFe LDH/felt</i> cell at 1 mA/cm^2 (top) and 10 mA/cm^2 (bottom) at 80°C in 30 w% KOH. Results from 0 h (beginning), 353 h 40 min (lowest kinetic performance), and 356 h 24 min (ending).	180
6.7	Kinetics of the <i>NiMo/felt vs NiFe LDH/felt</i> cell at 1 mA/cm^2 and 80°C in 30 w% KOH. Results from electrochemical impedance spectroscopy at the start and at the end of the test. Charge transfer resistances and equivalent capacities (surface roughness factor 40 and $60 \mu\text{F/cm}^2$ for cathode and anode, respectively), calculated as non-blocking electrodes, as fitting results with an LR(RQ)(RQ) equivalent circuit. Note that the fitting is considered erroneous.	182
6.8	EDS results from the cathode of the <i>NiMo/felt vs NiFe LDH/felt</i> cell shown in Fig. 6.32. Elemental compositions are given as atomic-%.	187
6.9	EDS results from the anode of the <i>NiMo/felt vs NiFe LDH/felt</i> cell shown in Fig. 6.33. Elemental compositions are given as atomic-%.	189
7.1	Results from galvanostatic EIS at 10 mA/cm^2 associated with Fig. 7.3. The fitting results are shown with an R(RQ) equivalent circuit, as the fitting results with an Armstrong equivalent circuit indicated no pseudocapacitive influence. The surface roughness considers a value of $40 \mu\text{F/cm}^2$	207
7.2	XRD results of the (003) peak after cycles 4-16 from Fig. 7.11A calculated with a trigonal R3m and a monoclinic C2/m model.	226

Appendix A

Drawings of the spectroelectrochemical cell FeliS

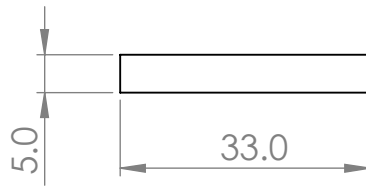
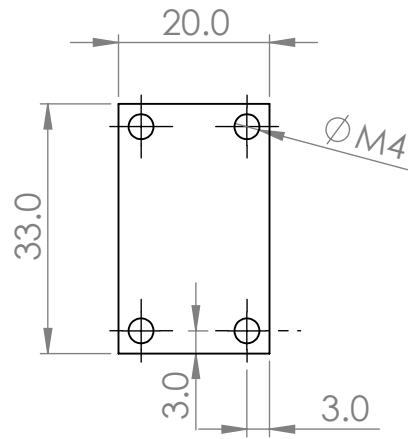
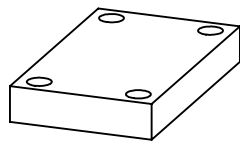
This chapter includes the drawings of the first (stationary application) and the second (flow-cell) generation of FeliS. Please refer to this work when using these drawings.



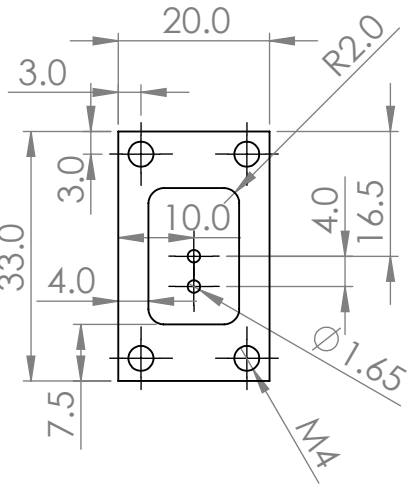
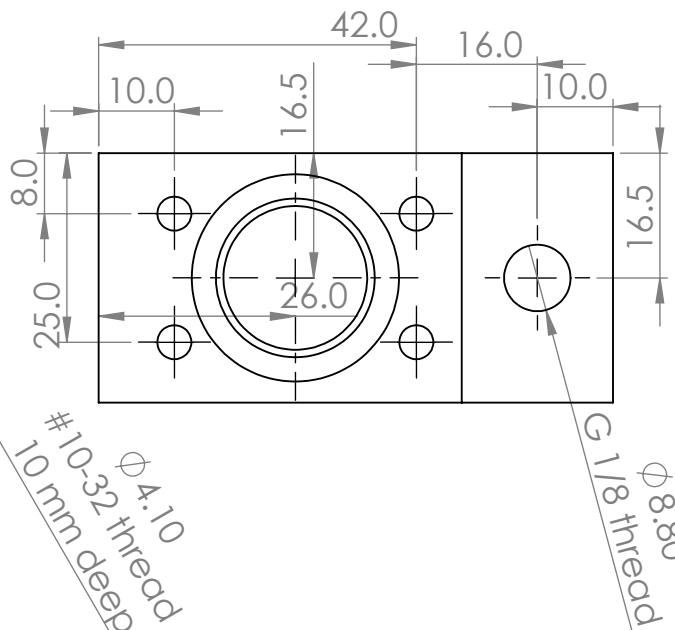
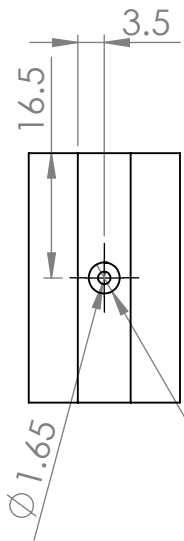
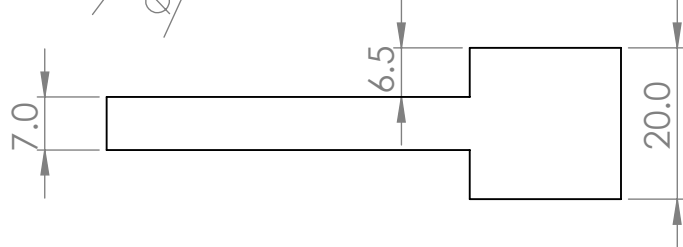
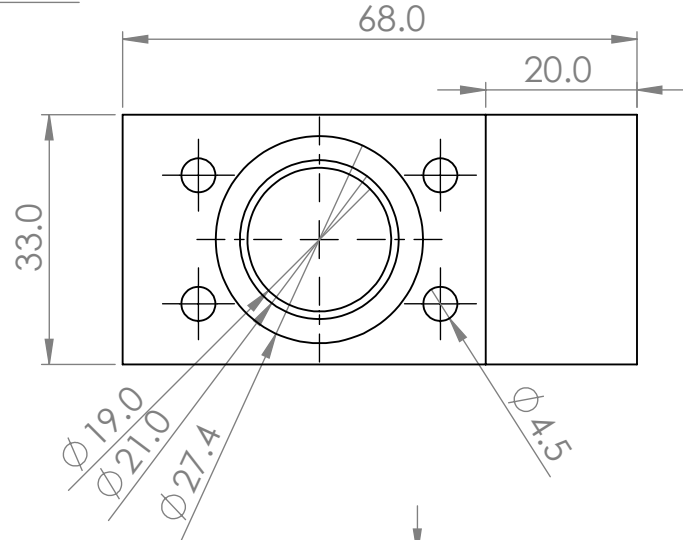
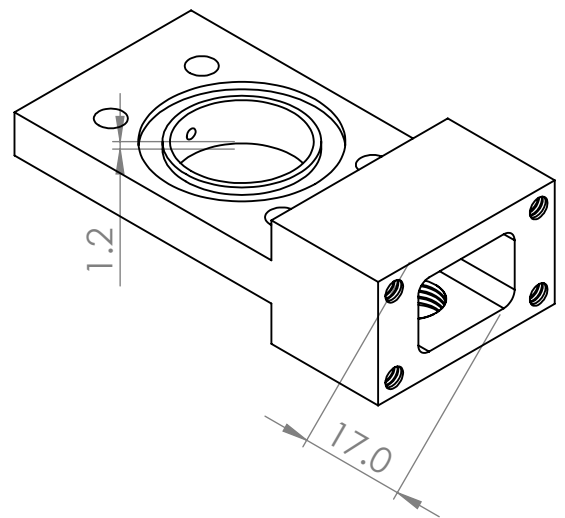
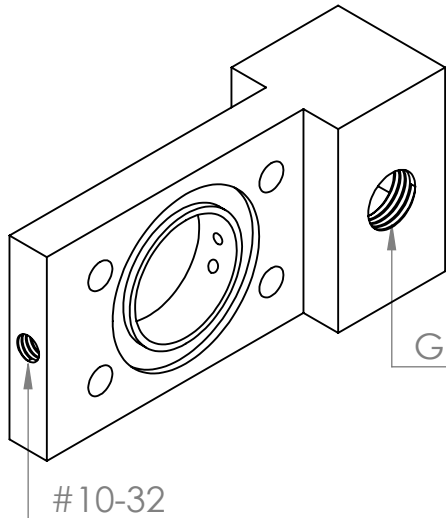
4 3 2 1

F
E
D
C
B
A

F
E
D
C
B
A



4 3 2 1



Florian Gellrich

UNLESS OTHERWISE SPECIFIED:
DIMENSIONS ARE IN MILLIMETERS

DO NOT SCALE DRAWING

Name

FeliS2-main

SCALE:1:1

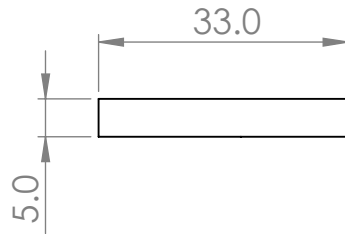
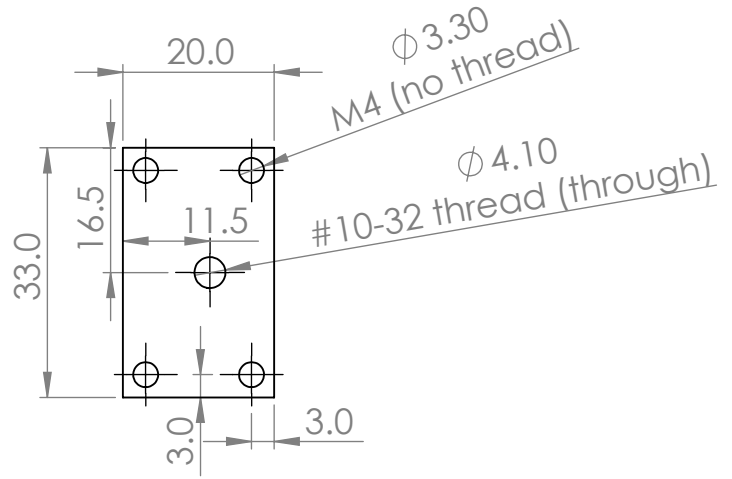
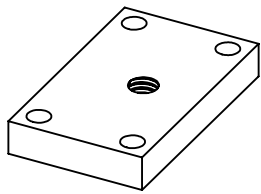
SHEET 1 OF 1

A4

4 3 2 1

F
E
D
C
B
A

F
E
D
C
B
A



Florian Gellrich

UNLESS OTHERWISE SPECIFIED:
DIMENSIONS ARE IN MILLIMETERS

DO NOT SCALE DRAWING

Name

Felis2-lid

SCALE:1:1

SHEET 1 OF 1

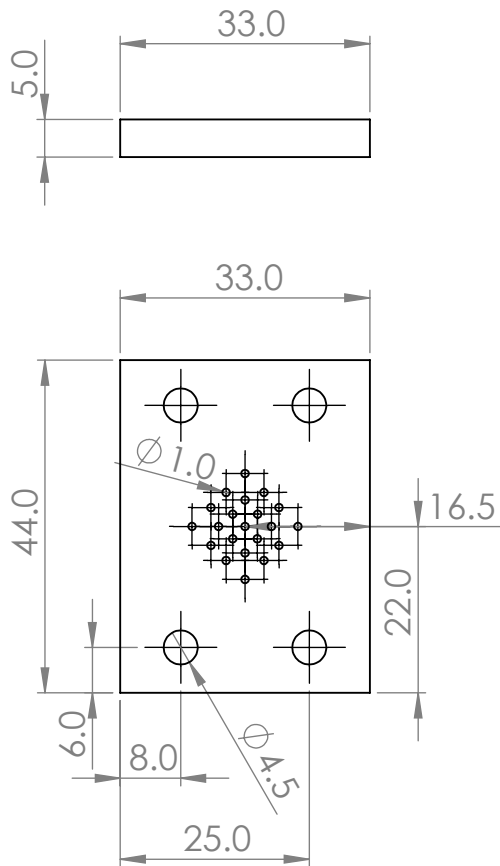
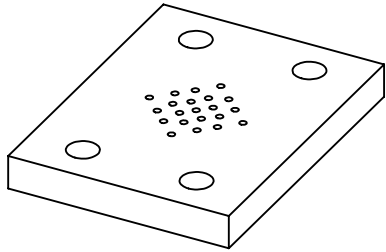
A4

4 3 2 1

4 3 2 1

F
E
D
C
B
A

F
E
D
C
B
A



Florian Gellrich

UNLESS OTHERWISE SPECIFIED:
DIMENSIONS ARE IN MILLIMETERS

DO NOT SCALE DRAWING

Name

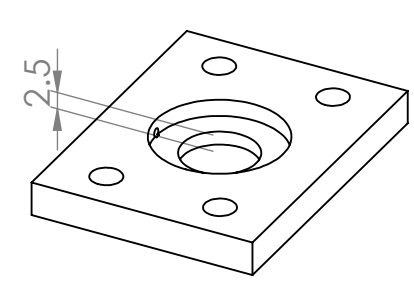
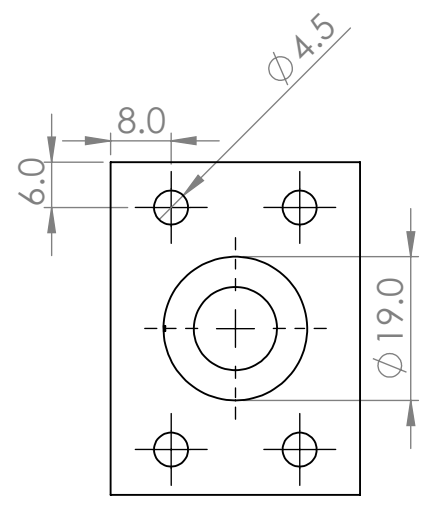
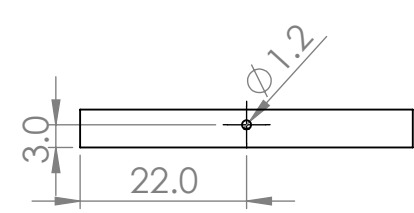
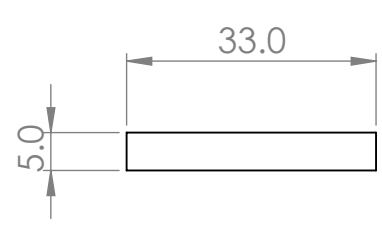
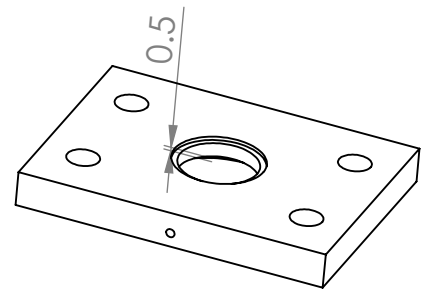
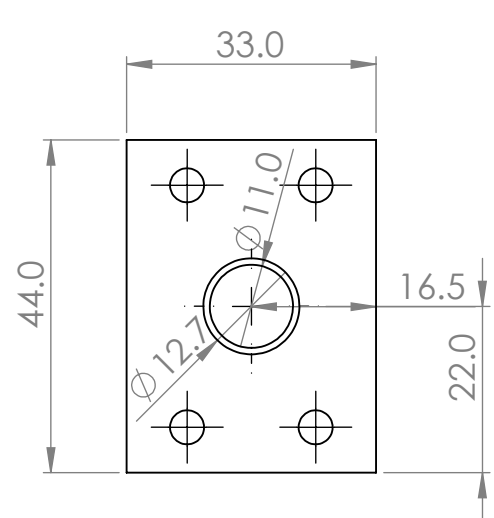
FeliS-counter-lid

SCALE:1:1

SHEET 1 OF 1

A4

4 3 2 1



Florian Gellrich

UNLESS OTHERWISE SPECIFIED:
DIMENSIONS ARE IN MILLIMETERS

DO NOT SCALE DRAWING

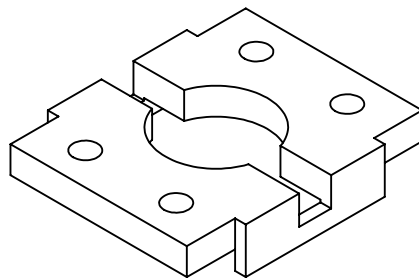
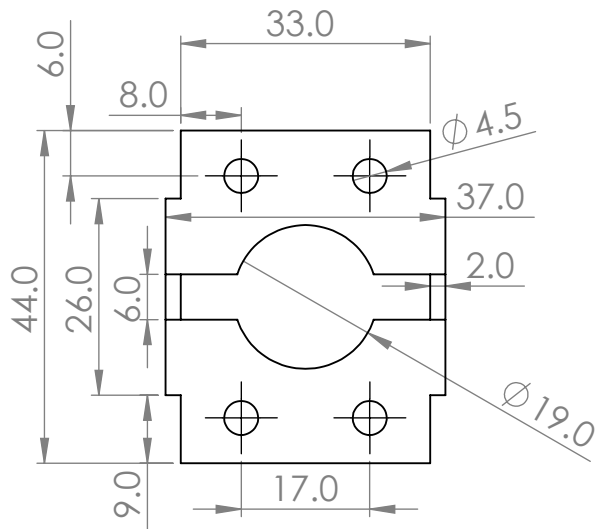
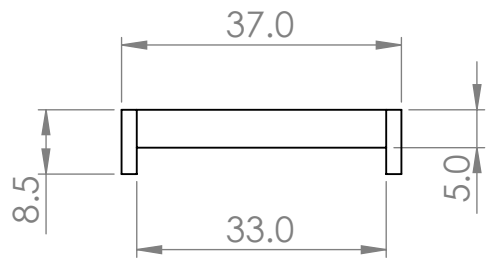
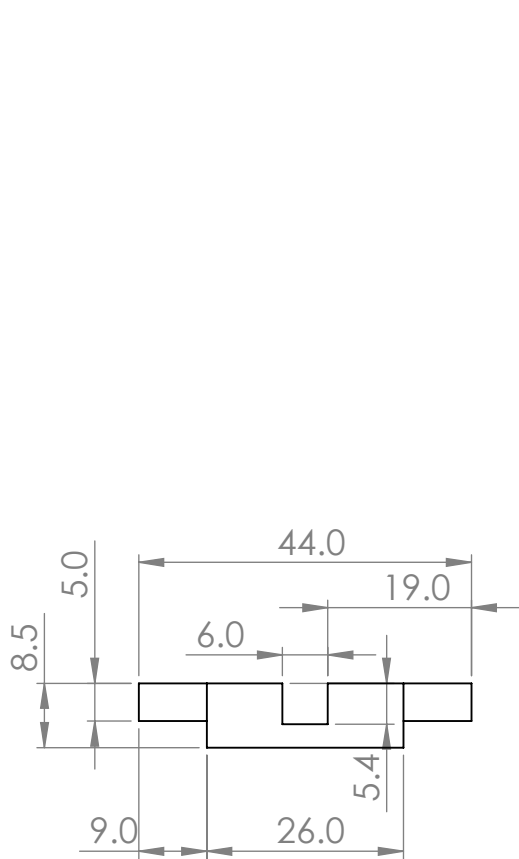
Name

FeliS-Raman

SCALE:1:1

SHEET 1 OF 1

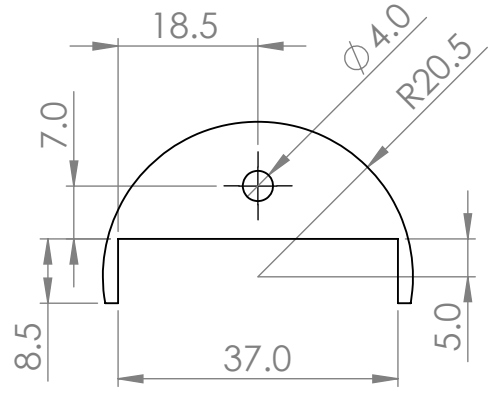
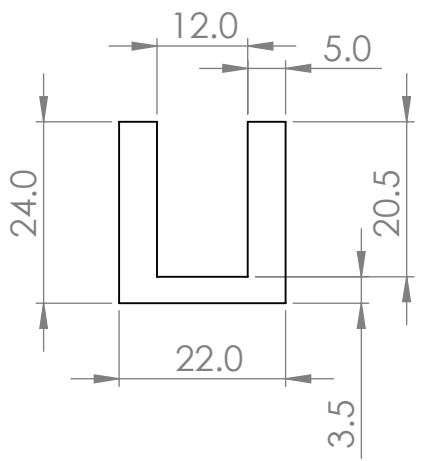
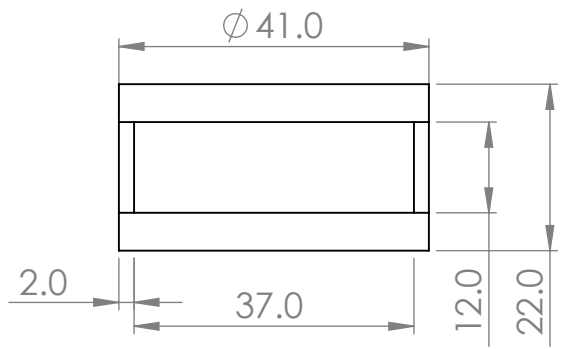
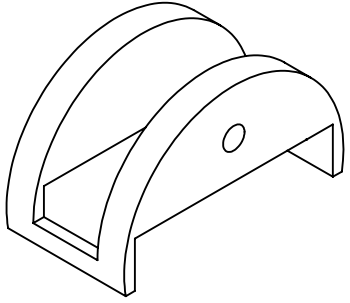
A4



4 3 2 1

F
E
D
C
B
A

F
E
D
C
B
A



Florian Gellrich

UNLESS OTHERWISE SPECIFIED:
DIMENSIONS ARE IN MILLIMETERS

DO NOT SCALE DRAWING

Name

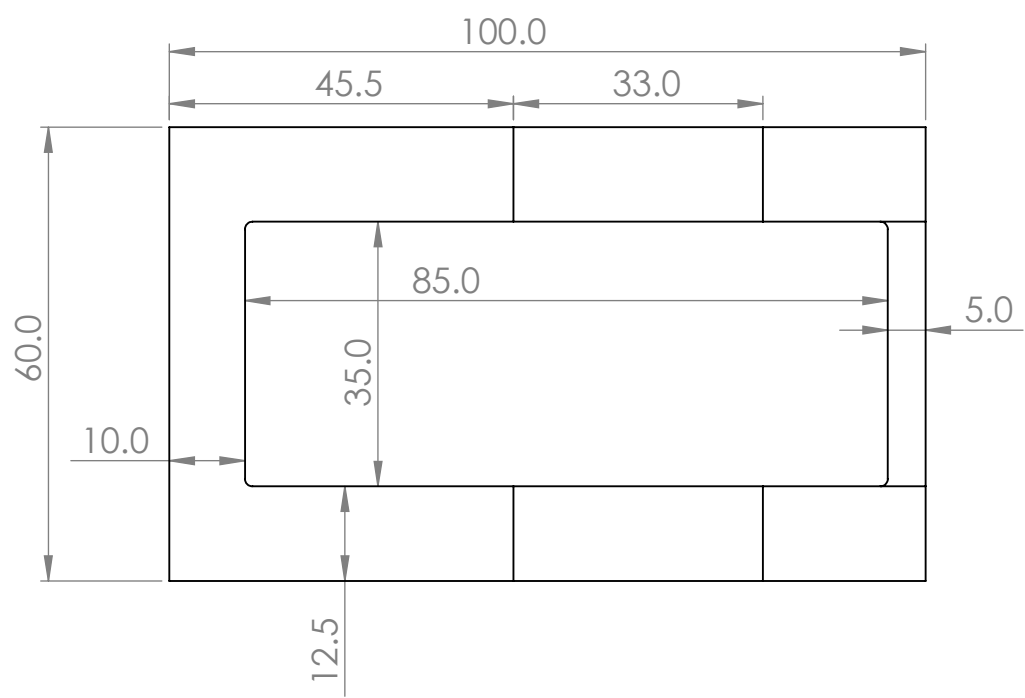
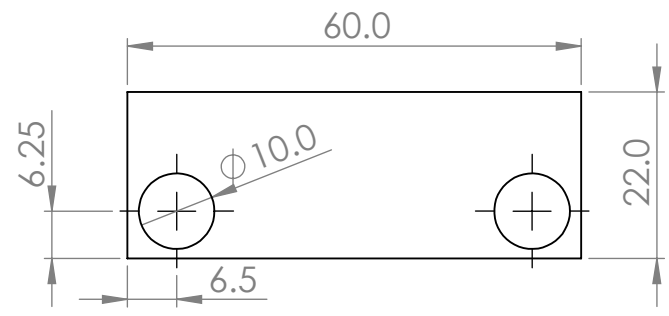
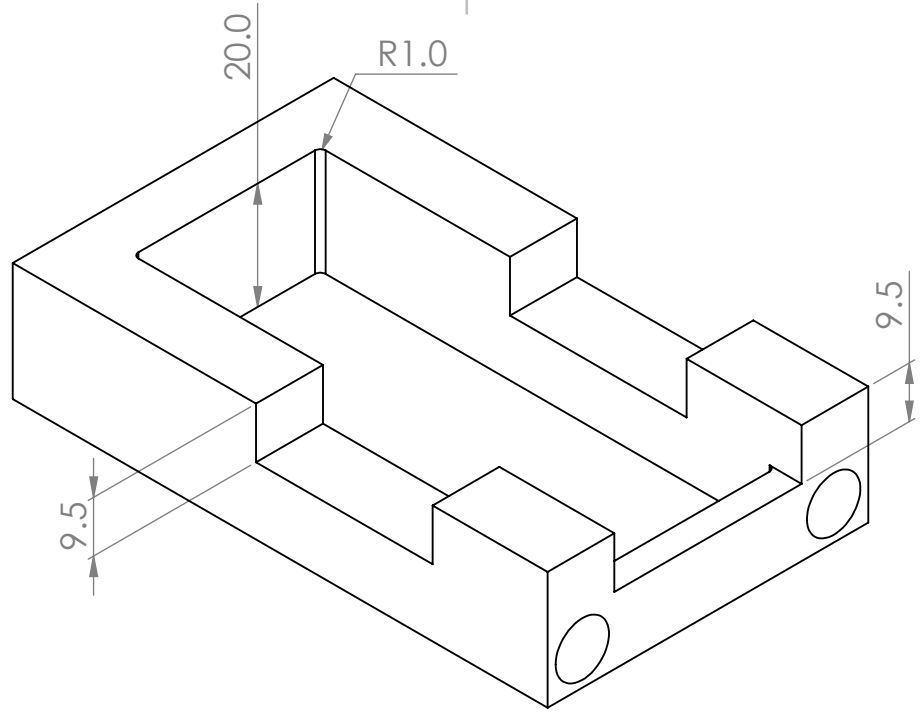
FeliS-dome

SCALE:1:1

SHEET 1 OF 1

A4

4 3 2 1



Florian Gellrich

UNLESS OTHERWISE SPECIFIED:
DIMENSIONS ARE IN MILLIMETERS

DO NOT SCALE DRAWING

Name

FeliS-stage

SCALE:1:1

SHEET 1 OF 1

A4

Appendix B

Supplementary Raman results

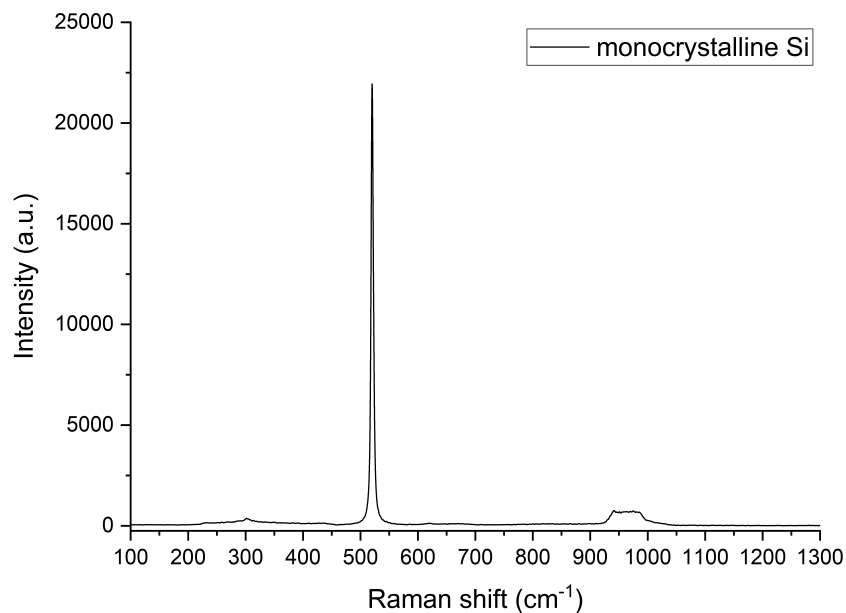


Fig. B.1: Spectrum of the monocrystalline Si calibration sample. Measurements made with a 100 mW green laser (532 nm) at 10 % intensity in a Renishaw InVia Spectrometer.

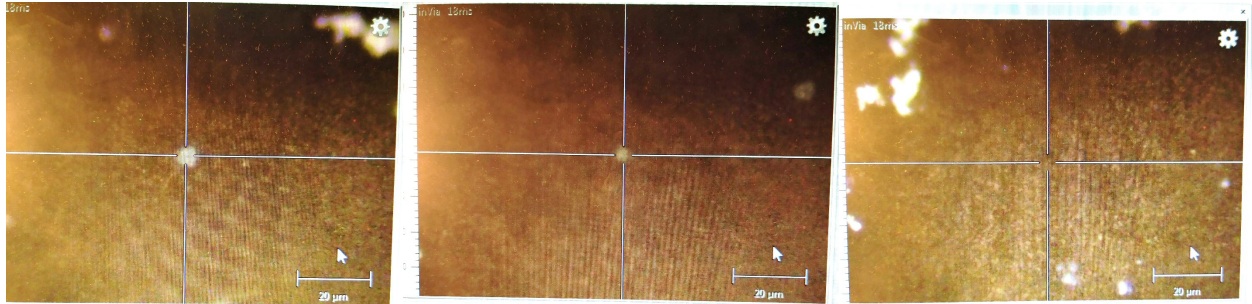


Fig. B.2: Light sensitivity of the sample from Chap. 7.2.1. Measurements made with a 100 mW green laser (532 nm). Left: 10%. Middle: 5%. Right: 1% intensity.

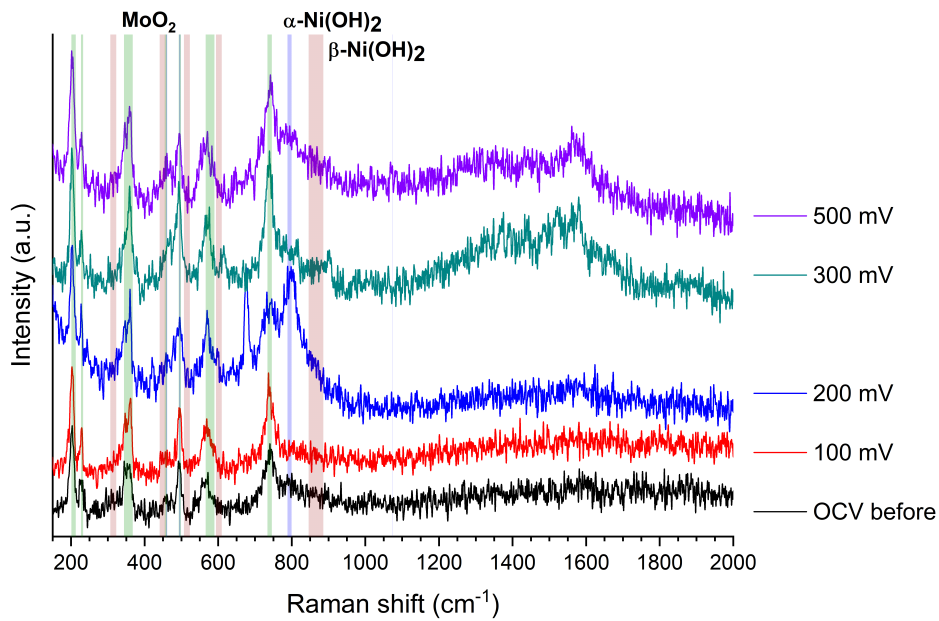


Fig. B.3: Repetition of Fig. 7.4. Additional visualization of β -Ni(OH)₂ vibrations revealing the absence of this phase.

Appendix C

Supplementary X-ray diffraction results

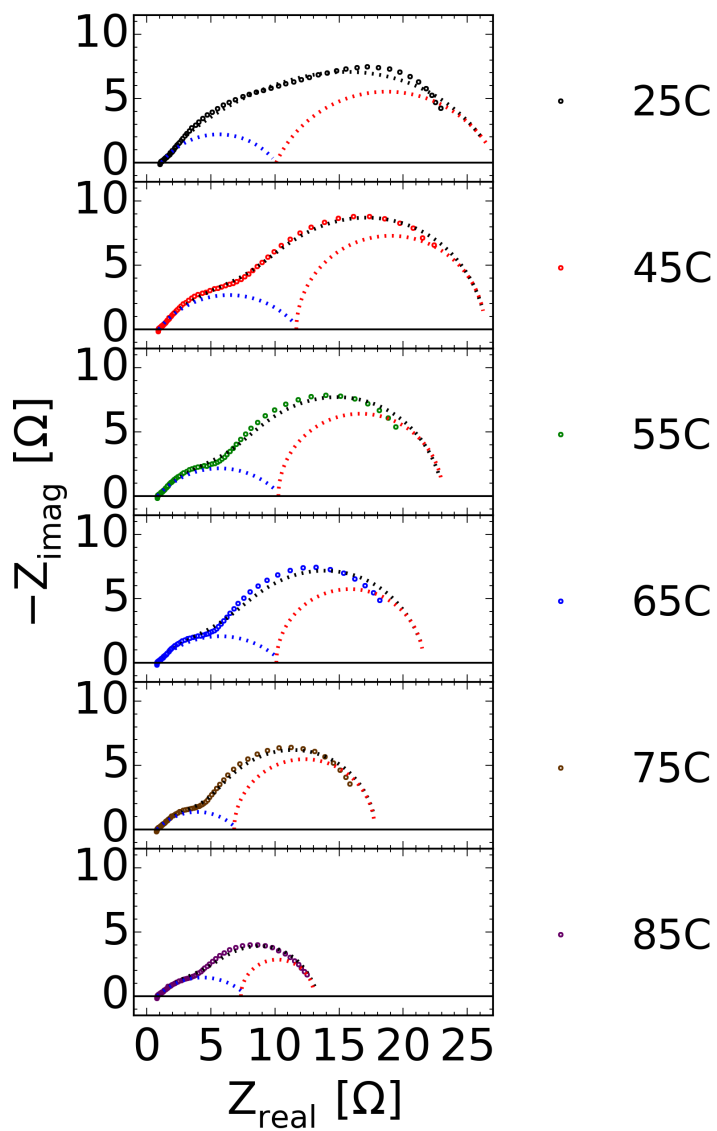


Fig. C.1: EIS fitting from Fig. 7.10 with an LR(RQ)(R_{ct}Q) fitting.

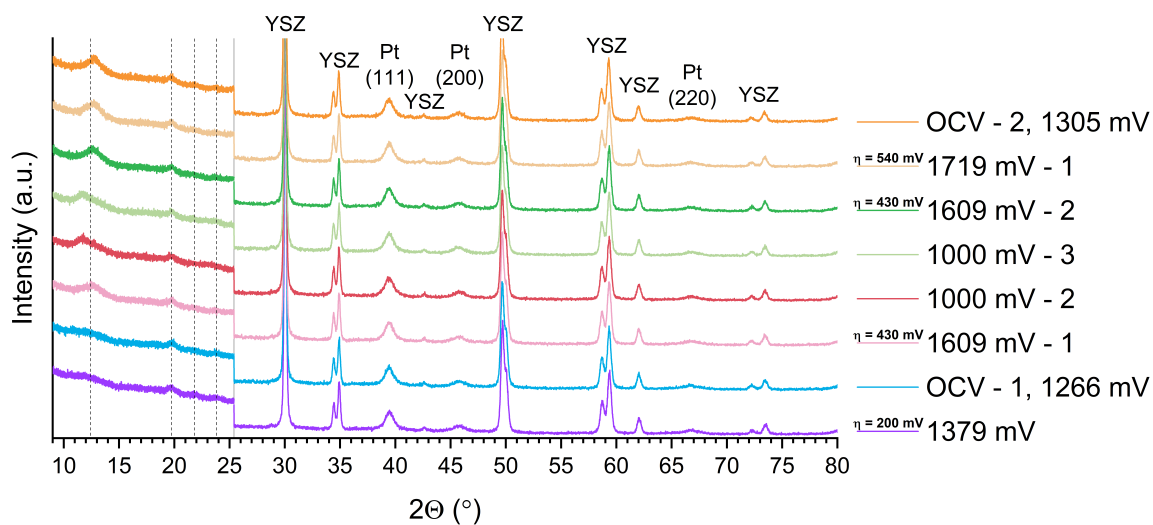


Fig. C.2: Full pattern of the GIXRD measurements in Fig. 7.11.

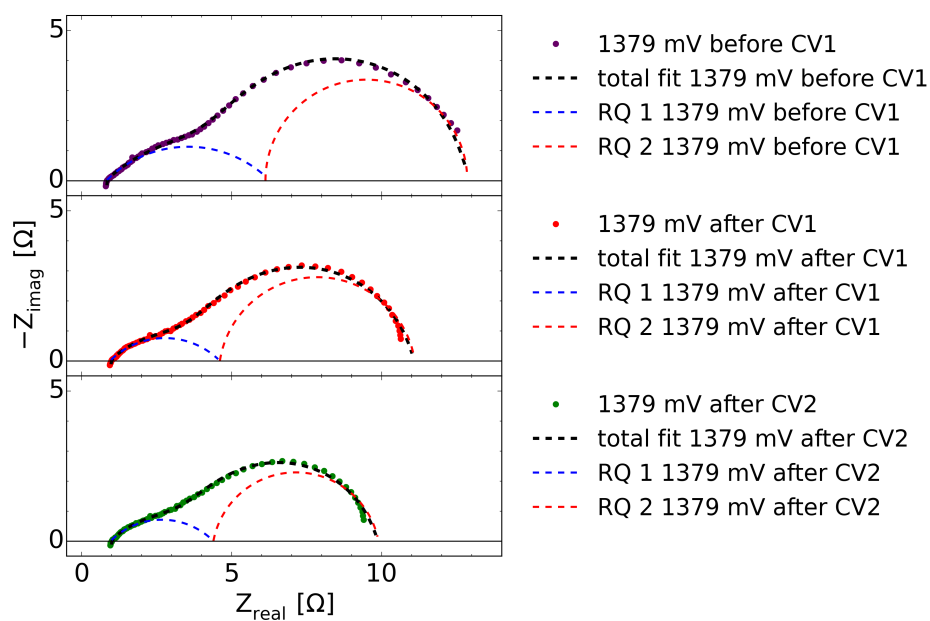


Fig. C.3: EIS fittings of the EIS spectra from Fig. 7.12 with an LR(RQ)(R_{ct}Q) fitting.

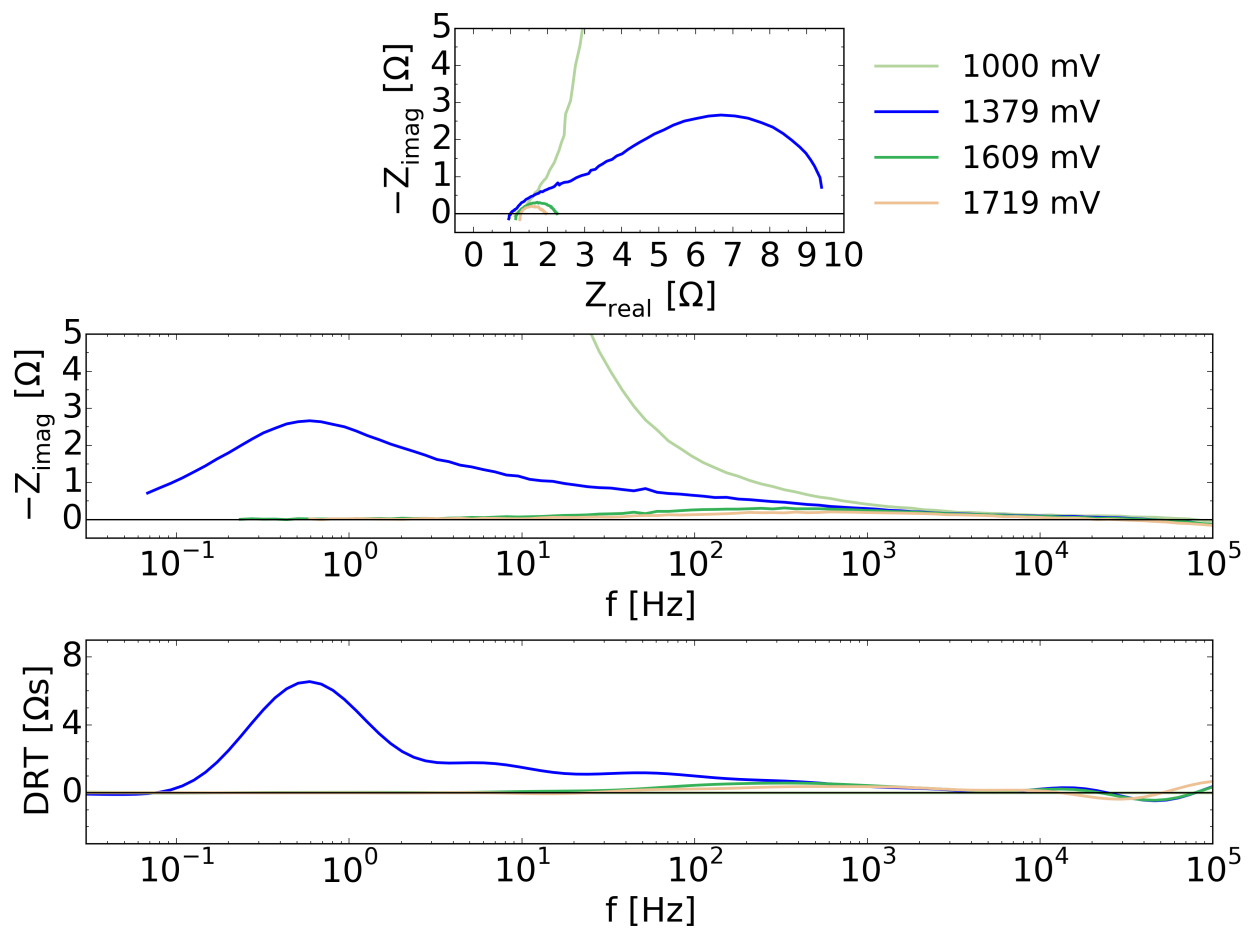


Fig. C.4: EIS spectra in correlation to the XRD patterns after cycles 4-16 from Fig. 7.11.

It always seems impossible until it's done.

Nelson Mandela